ABSTRACT

Title of Dissertation: RELATIVISTIC ELECTRON DYNAMICS IN PETAWATT LASER FIELDS WITH APPLICATIONS TO FUNDAMENTAL MEASUREMENTS

Smrithan Ravichandran
Doctor of Philosophy, 2026

Dissertation Directed by: Professor Wendell T. Hill, III
Institute for Physical Science and Technology

Multi-petawatt lasers provide unprecedented access to test nearly century-old predictions of nonlinear quantum electrodynamics (QED). Realizing laser-based precision measurements of nonlinear QED effects, however, requires overcoming various critical challenges, including (i) reliably characterizing the focal volume in real time at full power and (ii) minimizing the presence of real particles in the focal volume that can have adverse effects.

This dissertation demonstrates that both challenges can be addressed by exploiting the dynamics of electrons liberated from residual gas in the focal volume and subsequently expelled at acute angles relative to the direction of laser propagation. Through a series of experiments and numerical simulations, it is shown that the spatial distribution of these ejected electrons provides critical information about the peak intensity, aberrations, and the presence of deleterious particles in the focal volume. These results establish a practical pathway toward state-of-the-art measurements of nonlinear QED effects in the near future.

RELATIVISTIC ELECTRON DYNAMICS IN PETAWATT LASER FIELDS WITH APPLICATIONS TO FUNDAMENTAL MEASUREMENTS

by

Smrithan Ravichandran

Dissertation submitted to the Faculty of the Graduate School of the
University of Maryland, College Park in partial fulfillment
of the requirements for the degree of
Doctor of Philosophy
2026

Advisory Committee:
Professor Wendell T. Hill, III, Chair/Advisor
Professor Howard Milchberg
Professor Julius Goldhar
Professor Ki-Yong Kim
Professor William Fox

© Copyright by
Smrithan Ravichandran
2026

Dedication

To the taxpayer who made this work possible.

Acknowledgments

I am grateful for the role played by my Ph.D. advisor, Wendell T. Hill, III, in shaping me into the confident scientist that I am today – by allowing me to be my candid self through my trials and tribulations, and treating me throughout my Ph.D. like the scientist he wanted me to grow into. Having direct access to his vast experience and knowledge through one-on-one mentorship has taught me invaluable lessons that I will carry with me in my career. I am also indebted to our close collaborators, Robert Fedosejevs and Luis Roso, for their mentorship throughout my Ph.D. I want to thank them for their insightful advise and extensive support in my pursuit of postdoctoral opportunities. In addition, I am highly appreciative of the mentorship from members of my advisory committee, Howard Milchberg, Julius Goldhar, Ki-Yong Kim, William Fox.

Scientific research, and the benefits it brings to society, are in turn only possible with adequate funding to support such work. I therefore acknowledge with gratitude the organizations and agencies that provided funding for this research. The material presented in this dissertation is based upon work supported by the U.S. National Science Foundation under Award No. PHY2010392, PHY2308905, PHY2207771 and the Mid-scale Research Infrastructure Program under Award No. PHY2329970; the U.S. Department of Energy under Award No. DE-SC0025340; the U.S. Department of Energy (National Nuclear Security Administration) University of Rochester "National Inertial Confinement Fusion Program" under Award No. DE-

NA0004144; the U.S. Department of Energy's Office of Science Fusion Energy Sciences program under Award No. DE-SC0021231: the LaserNetUS initiative at the Scarlet Laser Facility; the Natural Sciences and Engineering Research Council of Canada under Grant No. RGPIN-2019-05013; the Ministerio de Ciencia e Innovación of Spain under Grant No. PID2022-140593NB-C22; the European Union's Horizon 2020 research and innovation program under grant agreement no. 871124 Laserlab-Europe; the ZEUS facility supported by the National Science Foundation under Award No. 2126181. I also express my gratitude to the University of Maryland (UMD), the American Physical Society, the X-lites Network and LaserNetUS for awarding fellowships and travel grants that provided essential support during my doctoral studies.

The work presented in this dissertation would not have been possible without the invaluable efforts of my peers and collaborators – Calvin He, Andrew Longman, Nathan McLane, Anthony Raymond, Rohan Mahnot, Elise Fiala and Lionel Ngassiki. One of my favorite things about conducting experiments at various research facilities is the ability to meet, work with, and learn from a massive network of scientists and technical experts. I would like to acknowledge the critical roles played by people I met and/or interacted with at the University of Alberta: Channprit Kaur, Matthew Gjevre, and Caleb Guthrie; Centro de Láseres Pulsados: Marine Huault, Roberto Lera, Michael Ehret, Cruz Méndez, José Antonio, Jon Apiñaniz, Teresa Cebriano, José Luis and Juan Hernández; The Ohio State University: Douglass Schumacher, German Tiscareno, Nick Czapla, David Hanggi, Pedro Spingola, Rebecca Daskalova, and Lili Manzo; University of Rochester: Seung-Whan Bahk, Chad Mileham, Ildar Begishev, Shao Qin, Noah Dauphin, Jarrett Shamlian, and Hans Rinderknecht; University of Michigan: Karl Krushelnick, Louise Willingale, Paul Campbell, Luke Tower, Jeremy Rebenstock, Yong Ma, John Nees, Anatoly Maksimchuk, Galina Kalinchenko, Gregg Sucha, and Lauren Weinberg. I am also grateful for the technical support I

received from members of UMD: Lester Putnam, for imparting a wealth of knowledge about designing and machining components that were critical for all the experiments; Alessandro Restelli, for his wizardry with electronics that enabled me to employ a working ion detector during my first research campaign; and Matias Calderon, for machining components on short notice and providing crucial assistance when needed. In addition, I acknowledge the UMD supercomputing resources made available for conducting the research in this dissertation.

I deeply value the words of encouragement I received from several leading scientists around the world, such as Scott Wilks, Farhat Beg, Dino Jaroszynski, Jon Zuegel, Mike Campbell, Dustin Froula, Arianna Gleason, Robbie Scott, and Enam Chowdhury, during interactions outside of research campaigns. I thank them for the essential role they play in inspiring early-career researchers like myself. I am especially grateful to Antonino Di Piazza for taking the time to share his expertise on nonlinear quantum electrodynamics, which strengthened my ability to articulate the motivation for the work presented in this dissertation. I also thank my long-term mentors, Sivarama Krishnan and Suresh Govindarajan, for championing my research career from an early stage and encouraging me to remain on this path; Praveen Bhallamudi, for his generous support with my graduate school applications; and the lovely folks at AG Pohl including Randolf Pohl, Stefan Schmidt, Marcel Willig, Jan Haack, Rishi Horn, who gave me my first break and helped me realize that I, too, can pursue scientific research.

I am grateful for all the support I received from various members of UMD including course instructors: Kaustubh Agashe, John Weeks, Victor Yakovenko, Pratyush Tiwary, Sarah Eno, Sylvester James Gates Jr. and Rosina Bierbaum; administrative staff: Souad Nejjar, Teri Schuler, Johnathan Long, Maritza Montelara, Pranjali Manerikar, Sokhan Min and Akshay Kanamarlapudi; and, in particular, Stacey Bremerman, for her caring presence; Jessica Crosby, for her

meticulous efforts and her fish tank, which inspired my award-winning three-minute thesis presentation; Robyn Kotzker, for consistently bringing great news whenever I received an award or fellowship from the Graduate School; and Dean Stephen Roth, for his kind words of encouragement on many occasions.

On the personal front, I was fortunate to have an excellent support system in my dearest friends, Akashnathan Aranganathan, Anmol Sikka, Emma Huckestein, Kishalay Mahato, Manodheepak Lakshmanan, Samyak Gothi, Sashank Sridhar, Shravan Nagarajan, Sreejith Santosh and Vishal Sannuthi; in particular, Adarsh Venkataraman, for his ever-reliable friendship; Allen Mathews, for his perpetual readiness to split a Popeyes meal; Chandrahas Tanguturi, for sharing my passion for photography; Greeshma Oruganti, for being my on-call therapist at work and the closest thing I had to a sister during these years; Jacob Asherman and Ritu Agarwal, for turning my housing arrangement into a place I called home; Priyanka Bharadwaj, for enabling my dad humor; Raghul Rajasekar, for trusting my ability to plan trips despite questionable moments; and Samay Narasimhamurthy, for being someone I could always learn from. I also thank the U.S. National Park Service for preserving and maintaining the National Park System, and for making this invaluable public resource accessible to all; it has, on many occasions, helped me find perspective and satisfaction in life.

The past five years would not have been the same without the love and care from my partner, Sahana Kumar. I am deeply grateful for her ability to bring color to my life, for the positive impact she has had on my emotional growth, and for sharing my goals and aspirations. I am, and always will be, incredibly fortunate to have her by my side as we navigate life's challenges together.

Finally, I thank my family in what feels like an impossible attempt to express my gratitude for their unwavering support and for giving me everything that I could have asked for. I

thank my dad, Ravichandran Beerappa, for his abundant love and patience with my tantrums; my mom, Malarvizhi Ethirajan, for her unconditional adoration and interest in hearing about my work, which helped me immensely improve my ability to communicate my research to a general audience; and my younger brother, Sai Sharan Ravichandran, for being the exceptional person that he is and for holding down the fort at home while I lived halfway across the world.

Despite my best efforts, it is impossible to fully acknowledge everyone who has had a meaningful impact on my life during my Ph.D. I am deeply grateful to those whose names I may have unintentionally omitted and thank them sincerely for their support.

Table of Contents

Dedication ii

Acknowledgements iii

Table of Contents viii

List of Tables xi

List of Figures xii

List of Abbreviations xx

Nomenclature xxii

Chapter 1: Motivation 1
- 1.1 Petawatt-Class Lasers and Their Applications . . . 1
- 1.2 Tests of Nonlinear QED in Novel Regimes . . . 8
  - 1.2.1 Key Experimental Constraints for Laser-Based Tests . . . 12
  - 1.2.2 Relativistic Electron Dynamics as a Diagnostic Tool . . . 13
- 1.3 Overview of Contents . . . 14

Chapter 2: Introduction 16
- 2.1 Liberation of Electrons Through Ionization in Strong Fields . . . 16
- 2.2 Treating Electrons as Single Particles Influenced by an External Laser Field . . . 18
- 2.3 Motion in Non-Relativistic Laser Fields . . . 22
- 2.4 Motion in Relativistic Laser Fields . . . 23

Chapter 3: Simulating Electron Trajectories in the Single-Particle Regime 28
- 3.1 Outline . . . 28
  - 3.1.1 Particle Initialization and Ionization . . . 29
  - 3.1.2 Solving Equations of Motion . . . 33
- 3.2 Field Equations . . . 34
- 3.3 Simulating Multiple Laser Pulses . . . 35
- 3.4 Parameter Optimization . . . 38
  - 3.4.1 Size of Initial Box of Atoms . . . 38
  - 3.4.2 Terminating the Program . . . 40

Chapter 4: Electron Dynamics Under Various Conditions 45
4.1 Dependence on Peak Intensity . . . 45
4.1.1 Simulation . . . 46
4.1.2 Experiment . . . 47
4.1.3 Comparing Measurements with Theory . . . 54
4.2 Dependence on Pulse Duration . . . 57
4.2.1 Simulation . . . 58
4.2.2 Experiment . . . 62
4.3 Dependence on F-Number . . . 65
4.3.1 Simulation . . . 65
4.3.2 Experiment . . . 67
4.4 Ultra-Relativistic Regime (Intensities Beyond 10^{22} $\mathrm{W/cm^2}$) . . . 71

Chapter 5: Applications to Enabling Nonlinear QED Measurements 75
5.1 Measuring the Peak Intensity . . . 75
5.1.1 Detecting Highly Charged Ions . . . 76
5.1.2 Detecting Relativistic Electrons (With Scintillators) . . . 82
5.2 Diagnosing Laser Aberrations . . . 85
5.3 Creating an Electron-Free Volume Through Ponderomotive Expulsion . . . 89
5.3.1 Overview of Clearing Mechanism . . . 90
5.3.2 Observing Electron Clearing . . . 91
5.3.3 Time Taken to Clear the Focal Volume . . . 100
5.3.4 Role of High-Z Gases . . . 104

Chapter 6: Summary and Outlook 109
6.1 Summary . . . 109
6.2 Outlook . . . 112
6.2.1 Improving Measurements of Peak Intensity with Electron Dynamics . . . 112
6.2.2 Next Steps for Measuring Aberrations with Electron Distributions . . . 113
6.2.3 Quantifying Ponderomotive Clearing Efficiency . . . 113

Appendix A: Tables of Ionization Intensities Assuming BSI 115
A.1 Hydrogen . . . 115
A.2 Helium . . . 115
A.3 Nitrogen . . . 116
A.4 Oxygen . . . 116
A.5 Argon . . . 117
A.6 Krypton . . . 118
A.7 Xenon . . . 119

Appendix B: Details of Computational Approach Used for Simulations 120
B.1 Characterizing the System . . . 120
B.2 Methods to Solve Equations of Motion . . . 121
B.3 Comparing Results From Different Methods for Various Test Cases . . . 122
B.3.1 Constant Magnetic Field . . . 122

B.3.2 Focused Laser Field with $a_0 = 10$ and $a_0 = 200$ . . . 125
B.4 Summary . . . 130

Appendix C: Details of experimental setup 132
C.1 Focal Spot Diagnostics . . . 132
C.1.1 Focal Spot Image File Format . . . 132
C.1.2 Choosing the Appropriate Exposure Level . . . 133
C.1.3 Establishing Image Orientation . . . 135
C.1.4 Evaluating Energy Delivered to the Focal Plane for an Apodized Beam . . . 136
C.2 Image Plate Handling . . . 138
C.2.1 Preparing an Image Plate . . . 138
C.2.2 Analyzing an Image Plate . . . 140
C.3 Time of Flight Detector . . . 142
C.3.1 Assembling the Extraction and Deflection Modules . . . 142
C.3.2 Deflection Circuit . . . 144
C.4 Two-beam setup . . . 147

References 151

List of Tables

1.1 Lasers ordered by pulse energy (> 25 kJ) delivered on target as of January 2026. 2
1.2 Lasers ordered by peak power (> 1 PW) per laser beam as of January 2026. . . . 4

4.1 Summary of experimental conditions used for measurements with the image plates. The U and τ reported here is the average value obtained over the corresponding sequence of shots. The techniques used to measure U and τ are detailed in Section 4.1.2.1. 51
4.2 Summary of experimental conditions used for measurements with the image plates. 62
4.3 Summary of experimental conditions used for measurements with the energy spectrometer. 69

5.1 Summary of experimental parameters used for the TOF detector. 78
5.2 Summary of experimental conditions used for measurements with the scintillation electron detectors. The U and τ reported here is the average value obtained over the corresponding sequence of shots. The techniques used to measure U and τ are detailed in Section 4.1.2.1. 83
5.3 Summary of experimental conditions used for measurements with varying laser aberrations. The nominal parameters applicable to all the measurements are f/2.8, $\lambda_0 = 1.05$ μm, $\tau \approx 700$ fs and $d = 25$ mm. All measurements were single shot. The Zernike index used here is based on the Fringe indexing scheme. 86

A.1 I_{th} for H. 115
A.2 I_{th} for He. 115
A.3 I_{th} for N. 116
A.4 I_{th} for O. 116
A.5 I_{th} for Ar. 117
A.6 I_{th} for Kr. 118
A.7 I_{th} for Xe. 119

B.1 Summary of B_0 and γ_0 used for simulating an electron in a constant magnetic field, with corresponding R_G and T_G calculated analytically. 123
B.2 Summary of initial conditions for the representative electron trajectories presented. 126
B.3 Summary of results from simulations with varying $\mathrm{d}t$ and Tol for the representative electron trajectories presented. 127

List of Figures

1.1 Parametric map of lasers with highest pulse energy (Table 1.1) and highest peak power (Table 1.2). Opaque red diamonds represent lasers whose performance on target was recorded as previously demonstrated through a peer-reviewed article. Translucent red diamonds represent lasers whose parameters were claimed as their current capability through press release and/or conference abstract and/or peer-reviewed article. Circles represent future capabilities of existing or new lasers that are either being planned or in development. 3

1.2 Parametric map of various physical phenomena made accessible by focusing petawatt-class lasers. Red diamonds represent lasers that held the world record for peak intensity since 1994, and whose performance on target was previously demonstrated through a peer-reviewed article and/or scientific report. The horizontal dashed lines represent the intensity thresholds corresponding to various physical phenomena as labeled (see text for detailed description). 6

2.1 One-dimensional model of strong-field ionization. The orange dashed, blue dotted and green solid lines represent the Coulomb potential, instantaneous perturbation due to the laser field and the total potential V_{tot} (see Eq. (2.1)), respectively. 17

2.2 A cartoon showing the motion of an electron (purple dot) once liberated from the parent atom (green dot) at non-relativistic laser intensities. 22

2.3 A cartoon showing the motion of an electron (purple dot) once liberated from the parent atom (green dot) at relativistic laser intensities. 23

3.1 Demonstration of the time scale used for ionization with a $\lambda_0 = 800$ nm laser pulse. Timing sequence (see Eqs. (3.5) and (3.6)) for ionization with $w_0 = 10$ μm, $\alpha_z = 4$ is shown using (a) $\tau = 30$ fs and (b) $\tau = 500$ fs. Vertical lines with no markers represent the boundaries of the box, $z = \pm\alpha_z z_R$. Vertical lines with circle and triangle markers represent the position of the pulse at $t = t_{ion,start}$ and $t = t_{ion,stop}$, respectively. Time resolution (see Eq. (3.7)) for ionization is represented using $\tau = 30$ fs in (c), where the red line and dark red circles represent the continuous field and the samples used when stepping through the pulse during ionization, respectively. 31

3.2 Location of a $\lambda_0 = 800$ nm, $w_0 = 10$ μm laser pulse along the axis of propagation at $t = t_{end}$ (see Eq. (3.11)) is shown with $\alpha_z = 4$, $\alpha_t = 50$ for (a) $\tau = 30$ fs and (b) $\tau = 500$ fs, represented by the vertical line with square markers. Vertical lines with no markers represent the boundaries of the box, $z = \pm\alpha_z z_R$. 33

3.3 Timing sequence (see Eqs. (3.25)–(3.27)) used for two copropagating pulses with $\lambda_{01} = \lambda_{02} = 800$ μm, $\tau_1 = \tau_2 = 40$ fs, $w_0 = 10$ μm, $\alpha_z = 4$ and $\Delta t = +300$ fs. Pulse 1 (Pulse 2) is represented by the shaded (unshaded) gaussian envelope. Vertical lines with no markers represent the boundaries of the box, $z = \pm\alpha_z z_R$. Vertical lines with circle, triangle and square markers represent the position of the pulse at $t = t_{ion,start}$, $t = t_{ion,stop}$ and $t = t_{end}$, respectively. 38
3.4 Intensity contours of a Gaussian beam shown in normalized units for $I_{th} = 10^{-9} I_0$, $10^{-6} I_0$, $10^{-3} I_0$, $10^{-1} I_0$ by the blue solid, green dash-dotted, dark-yellow dashed and maroon dotted lines, respectively. 39
3.5 Initial positions of electrons ejected at $\theta \leq 50^\circ$ with $\gamma_f - 1 \geq 1$ from a variably-sized initial box (see Conditions (3.1)–(3.3)) containing Ar atoms with (a) $\alpha_{xy} = 2$, $\alpha_z = 2$, (b) $\alpha_{xy} = 4$, $\alpha_z = 2$, and (c) $\alpha_{xy} = 4$, $\alpha_z = 6$. Simulations performed with $I_0 = 5 \times 10^{20}$ W/cm^2, $w_0 = 5$ μm, $P = 10^{-6}$ mbar. Color bar represents $\gamma_f - 1$. Thick magenta (thin black) edges of the box represent faces that clip (do not clip) the distribution of electrons of interest. 41
3.6 Maximum possible fraction of the peak intensity that an electron born at $z = 0$ can experience at some $t = t_{end}$ when (a) $w_0 = 10$ μm and $\tau = 40$ fs, (b) $w_0 = 10$ μm and $\tau = 400$ fs, (c) $w_0 = 5$ μm and $\tau = 40$ fs, and (d) $w_0 = 5$ μm and $\tau = 400$ fs. The blue solid, green dash-dotted, dark-yellow dashed and maroon dotted lines represent $\gamma_f = 2, 4, 10, 500$, respectively. 42

4.1 Simulated $\gamma_f - 1$ and θ for all electrons of interest generated from $P = 10^{-5}$ mbar of Ar by a $w_0 = 8$ μm, $\tau = 30$ fs laser pulse with (a) $a_0 = 4$, (b) $a_0 = 8$ and (c) $a_0 = 12$. Each translucent black dot represents an electron. The orange dashed line represents Equation (2.23). Simulated θ_c (see text) for varying a_0 in (d) with black square (yellow circle) markers representing Ar (N_2) and corresponding error bars denoting $\pm 1\sigma$ in evaluating θ_c. 46
4.2 Experimental setup (not to scale) for image plate at CLPU in (a) and OSU in (b). Image plates are mounted after, and facing, the focal spot at a fixed distance, d. The laser pulse is traveling along $-\hat{z}$ and is linearly polarized with E_x along $\hat{x}$. In (b), the maroon dashed lines represent (not to scale) the outline of the laser beam when the circular aperture was used. The maroon dotted lines represent the transverse beam profile. The magenta dotted lines with arrows represent the directions in which the three plates that are not perpendicular to $\vec{k}$ are unfolded when scanned. 48
4.3 Representative set of focal spot images captured at low power with the VEGA-3 laser, shown in (a)–(c), and the Scarlet laser after using the circular aperture (see text), shown in (d). 48
4.4 Scaled image plate data captured under conditions detailed in Table 4.1, where 1 on the color scale corresponds to peak PSL values (see text) of 7.06, 6.82, 31.88 and 4.57 within a 50×50 μm^2 pixel for (a)–(d), respectively. The laser is polarized along the $\vec{x}$-axis and $\vec{k}$ points into the page. 50

4.5 The ϕ-averaged line profile, $h(\theta)$ (see text), is shown for data in Figs. 4.4a–4.4c represented by red (far-right), yellow and dark blue (far-left) curves respectively. The dot-dashed magenta (blue) curve indicates the signal floor for the BAS-SR (BAS-MS) plates (see text). The shaded regions are the uncertainties in the signal floor estimated from [150]. The dashed lines represent the exponential fit used to determine θ_c, given by the intersection with the signal floor and shown by the black dots with error bars obtained by accounting for the uncertainty in positioning the plate. 52
4.6 Comparison of measured θ_c at the inferred a_0, simulated θ_c for varying a_0, with the theory. Green solid and red dotted curves, represent Equation (2.27) with $\eta = 1$ and $\sqrt{2}$, respectively. Black square markers represent simulations performed with Ar (see Section 4.1.1). Blue dot (maroon cross) markers represent measurements in Figures 4.4a–4.4c (Figure 4.4d). Horizontal (vertical) error bars represent the uncertainty in inferring (measuring) a_0 (θ_c). The blue dashed line represents a numerical fit of the data from Figures 4.4a–4.4c to $\tan\theta_c = 2\eta/a_0$, where $\eta = 2.02^{+0.26}_{-0.22}$. The shaded region around the dashed curve represents the uncertainty in η. 54
4.7 Setup (not to scale) for simulations and experiments measuring the spatial distribution of electrons under varying pulse duration. Electrons ejected from the focus as the origin are recorded on the plane with $z = -d$ and another with $x = +d_s$. The laser pulse is traveling along $-\hat{z}$ and is linearly polarized along $\hat{x}$ ($\hat{y}$) in the simulation (experiment). 57
4.8 Simulated $\gamma_p - 1$ in (a) and θ_c in (b), under varying τ for three different a_0 with $I_{th} = I_0/10$. Blue circles, yellow triangles and orange squares represent $a_0 = 2.16$, 6.84 and 21.6, which correspond to $I_0 = 10^{19}$, 10^{20}, 10^{21} W/cm^2, respectively. Error bars denote the standard deviation in evaluating γ_p and θ_c. Solid (dashed) lines correspond to $\gamma_p - 1 = a_0^2/4$ ($a_0^2/2$) in (a) and $\tan\theta_c = \sqrt{8}/a_0$ ($2/a_0$) in (b). 58
4.9 Spatial distribution of electrons generated by $a_0 = 6.84$ is shown when (a) $\tau = 30$ fs and (c) $\tau = 600$ fs on a plane with $d = 25$ mm. The color scale denotes the number of electrons in each 1×1 mm^2 pixel across the plane. Electric field sampled by the most energetic electron from (a) and (c) in (b) and (d), respectively, normalized to the peak field. 59
4.10 Spatial distribution of electrons generated by $a_0 = 4$ for (a) N_2 and $\tau = 30$ fs, (b) N_2 and $\tau = 600$ fs, (c) Ar and $\tau = 30$ fs, and (d) $\tau = 600$ fs. The color scale denotes the number of electrons in each 1×1 mm^2 pixel across the plane. The laser is polarized along the $\vec{x}$-axis with $\vec{k}$ pointing into the page. The plane with $x = +60$ mm is saturated for (b) and (d) to increase contrast for the electrons appearing on the $z = -25$ mm plane that exhibit characteristic features discussed in the text. 61

4.11 Scaled image plate data captured under conditions detailed in Table 4.2, where 1 on the color scale corresponds to peak PSL values of 79.1, 0.12, 57.6, 0.41 within a $50 \times 50\ \mu\mathrm{m}^2$ pixel for (a)–(d), respectively. The white text specifies the thickness of additional Al filtering used in different quadrants of the plane with $z = -25\ \mathrm{mm}$ and the bottom section of the plane with $x = +55\ \mathrm{mm}$ in (b) and (d). The laser is polarized along the $\vec{x}$-axis in (a) and (c), and along the y-axis in (b) and (d), with $\vec{k}$ pointing into the page. 64
4.12 Simulated $\gamma_f - 1$ and θ for all electrons of interest generated from Ar with an effective pressure of $P = 10^{-5}\ \mathrm{mbar}$ by an $a_0 = 15$, $\tau = 30\ \mathrm{fs}$ laser pulse with (a) $w_0 = 8\ \mu\mathrm{m}$, (b) $w_0 = 5\ \mu\mathrm{m}$ and (c) $w_0 = 2\ \mu\mathrm{m}$. The color scale represents the number of electrons within each two-dimensional bin of $\Delta\theta = 0.8^\circ$ and $\Delta(\gamma_f - 1) = 0.2$, and the orange dashed line represents Equation (2.23). Energy distributions at three specific θ from the electron distribution in (a)–(c) are shown in (d)–(f), respectively, where histograms from left to right correspond to $\theta \in [49.6^\circ, 50.4^\circ)$ (red), $\theta \in [39.6^\circ, 40.4^\circ)$ (yellow) and $\theta \in [29.6^\circ, 30.4^\circ)$ (blue). The black dashed line from left to right represent the analytical γ from Equation (2.23) for $\theta = 50^\circ, 40^\circ$ and 30°, respectively. 66
4.13 Experimental setup (not to scale) for measuring electron-energy distributions at UM in (a). Electrons ejected from the focus along the $\vec{B}_L$–$\vec{k}$ plane with some θ are captured by an electron energy spectrometer containing a magnetic field, $\vec{B}_S$ that deflects electrons based on their energy as shown by the three-quarter view in (b). Their final positions are recorded by an image plate at the rear surface of the spectrometer as shown by a sample measurement in (c) with corresponding horizontal and vertical line profiles (see text). The color scale denotes the PSL value within each $50 \times 50\ \mu\mathrm{m}^2$ pixel. The white circle represents the collimated aperture. The white dashed lines represent the aperture width projected onto the rear surface of the spectrometer, obtained by extending rays from the focus through the aperture diameter. 68
4.14 The cumulative vertical line profile, $h(y)$ (see text), is shown for spectrometer measurements performed for Ar with (a) $\mathrm{f}/5$ and (b) $\mathrm{f}/1.8$. The blue (far-left), yellow and red (far-right) curves represent measurements with the spectrometer centered at $\theta = (35^\circ, 40^\circ, 45^\circ)$ in (a) and $(35^\circ, 42.5^\circ, 50^\circ)$ in (b), respectively. Measurement conditions detailed in Table 4.3. 70
4.15 Initial positions of the most energetic electrons generated from $P = 10^{-6}\ \mathrm{mbar}$ of Xe by a $\tau = 30\ \mathrm{fs}$, $w_0 = 5\ \mu\mathrm{m}$ laser pulse with (a) $a_0 = 4.83$, (b) $a_0 = 48.3$ and (c) $a_0 = 216$, with color scale representing $\gamma_f - 1$. A representative sample of trajectories of electrons from (a)–(c) shown in (d)–(f), respectively, with color scale representing $\gamma(t) - 1$. The corresponding time dependence of $\gamma(t') - 1$ for the most energetic electron obtained is shown in (g)–(i), respectively. 72

5.1 A schematic of the ion TOF detector comprising of an extraction module, deflection module and an MCP separated by field-free drift regions. A cartoon of trajectories for an ion of interest and an unwanted ion is shown by the solid and dashed orange lines, respectively. The laser focus is considered the origin, which is in between plates 2 and 3 of the extraction module. See Appendix C.3 for details about various components of the TOF detector 76
5.2 Analytically expected TOF in (a) for H^+, all ions of N and O shown by blue dotted, orange solid and green dashed lines, respectively, with the ionization stage decreasing from left to right starting with N^{7+} and O^{8+}. The starting point of each line represents the ionization intensity assuming BSI (Appendix A). Measured TOF signal (b) for a single laser shot with $U \approx 24$ J and deflection module turned off, and (c) averaged over 60 (26) shots with $U \approx 9.1$ J (0.96 J) shown by the black (gray) curve and deflection module turned on. Vertical lines denote the TOF of relevant ions (see text). 80
5.3 Experimental setup of the scintillation detector for electrons in (a), with individual components of the detector shown using a quarter-section view in (b). A representative measurement of the photon signal recorded by the MPPC for a single shot is shown in (c). The area under the curve (orange shaded region) represents the signal integral for the shot. 82
5.4 Scintillation detector data from the Ar gas measurements in (a). The low (high) energy data are shown by green (blue) squares (dots), the average at each measurement position shown by "×" ("*") and corresponding standard deviations marked by the error bars. The dashed (solid) orange and black lines are sigmoid fits to the small and large angle falloff, respectively, for the low (high) energy measurement. Normalized and background subtracted sigmoid fits for the small angle falloff of measurements performed with N_2 (violet), Ar (orange) and Xe (yellow) in (b). The dashed (solid) curves correspond to low (high) energy measurements. The experimental conditions used for all measurements with the scintillation detector are given in Table 5.2. 84
5.5 Image plate data captured for varying Astigmatism introduced at $45°$ to the polarization axis where the left, middle and right plots represent an aberration magnitude of $-\lambda_0/2, 0$ and $+\lambda_0/2$ in peak-to-peak wavefront distortion, while the top and bottom row represent measurements performed with N_2 and Ar, respectively. The color scale denotes the the PSL deposited in each 50×50 μm^2 pixel across the plane. Polarization axis is along the vertical direction in each measurement. . 87
5.6 Image plate data captured for varying Coma introduced along the polarization axis where the left, middle and right plots represent an aberration magnitude of $-\lambda_0/2, 0$ and $+\lambda_0/2$ in peak-to-peak wavefront distortion, while the top and bottom row represent measurements performed with N_2 and Ar, respectively. The color scale denotes the the PSL deposited in each 50×50 μm^2 pixel across the plane. Polarization axis is along the vertical direction in each measurement. . . . 88
5.7 A cartoon representing the minimum angle of ejection for the (a) strong pulse, $\theta_{c,s}$ and (b) weak pulse, $\theta_{c,w}$. 90

5.8 Spatial distribution of ejected electrons simulated when the (a) strong pulse and (b) weak pulse leads the other by 300 fs with perfect overlap of focal volumes. Distributions simulated 30 mm after the focus on a plane perpendicular to the laser axis passing through the origin. The color scale denotes the number of electrons in each 1×1 mm^2 pixel across the plane. The average number of electrons for varying distance from the laser axis is shown by the solid and dashed lines in (c) for simulations in (a) and (b), respectively. 93
5.9 Schematic of the experimental setup (a) and typical isolated focal-spot images of the strong (b) and weak (c) pulses. The laser pulses propagate along $-\hat{z}$, polarized predominantly along $\hat{x}$ and separated in time by $\pm|\Delta t|$. The circular blue-white dashed line represents the full width at half maximum (≈ 13.4 μm) in (b) and (c). A pair of image plates are loaded onto the image-plate holder that can rotate about the vertical axis indicated in orange. 94
5.10 Spatial distribution of ejected electrons measured when the (a) strong pulse and (b) weak pulse leads the other by 300 fs. Distributions measured 30 mm after the focus on a plane perpendicular to the laser axis passing through the origin. The color scale denotes the the PSL deposited in each 50×50 μm^2 pixel across the plane. The average number of electrons for varying distance from the laser axis is shown by the solid and dashed lines in (c) for measurements in (a) and (b), respectively. 97
5.11 Spatial distribution of ejected electrons simulated when the (a) strong pulse and (b) weak pulse leads the other by 300 fs with randomized relative spatial separation of $\leq 2w_0$ between the laser axes. Distributions simulated 30 mm after the focus on a plane perpendicular to the laser axis passing through the origin. The color scale denotes the number of electrons in each 1×1 mm^2 pixel across the plane. The average number of electrons for varying distance from the laser axis is shown by the solid and dashed lines in (c) for simulations in (a) and (b), respectively. 99
5.12 Spatial distribution of ejected electrons measured when the (a) strong pulse and (b) weak pulse leads the other by 150 fs. Distributions measured 30 mm after the focus on a plane perpendicular to the laser axis passing through the origin. The color scale denotes the PSL deposited in each 50×50 μm^2 pixel across the plane. The average number of electrons for varying distance from the laser axis is shown by the solid and dashed lines in (c) for measurements in (a) and (b), respectively. . 100
5.13 Spatial distribution of ejected electrons simulated with $l = 0,\ p = 0$ Laguerre-Gauss mode beams with (a) strong pulse leading and (b) weak pulse leading the other by 150 fs. Corresponding distributions when the weak pulse is replaced with an $l = 0,\ p = 1$ mode in (c) and (d), respectively. Color scale denotes number of electrons deposited in each 1×1 mm^2 pixel. Trajectories of the electrons with some of the smallest θ (see text) in (c) and (d) shown in (e) and (f), respectively. Birth positions denoted by black points. Color scale denotes the instantaneous $\gamma - 1$ through their trajectory. 102

5.14 Spatial distribution of ejected electrons measured when the (a) strong pulse and (b) weak pulse leads the other by 600 fs. Distributions measured 30 mm after the focus on a plane perpendicular to the laser axis passing through the origin. The color scale denotes the PSL deposited in each $50 \times 50\ \mu\text{m}^2$ pixel across the plane. The average number of electrons for varying distance from the laser axis for $\phi \in (2\pi/3, 4\pi/3]$ is shown by the solid and dashed lines in (c) for measurements in (a) and (b), respectively. 105

5.15 Spatial distribution of ejected electrons simulated with a single beam ($a_0 = 4.84,\ \tau = 40$ fs) and sharp ionization threshold $I_{th} = \delta_{th} I_0$ for (a) $w_0 = 5\ \mu\text{m},\ \delta_{th} = 0.75$, (b) $w_0 = 5\ \mu\text{m},\ \delta_{th} = 0.95$, (c) $w_0 = 5\ \mu\text{m},\ \delta_{th} = 0.99$, (d) $w_0 = 3\ \mu\text{m},\ \delta_{th} = 0.75$, (e) $w_0 = 3\ \mu\text{m},\ \delta_{th} = 0.95$ and (f) $w_0 = 3\ \mu\text{m},\ \delta_{th} = 0.99$. Color scale denotes number of electrons deposited in each $0.5 \times 0.5\ \text{mm}^2$ pixel per mbar. 107

B.1 Numerical solutions to the equations of motion for an electron in a constant magnetic field ($B_0 = 40$ T). The top, middle and bottom row correspond to $\gamma = 10, 20$ and 50, while the left and right columns represent simulations performed using the Vay pusher algorithm and the ode45 solver, respectively. The violet (orange) curve plotted on the primary (secondary) axis represents $x(t)$ ($y(t)$). The horizontal dashed violet (orange) lines represent the analytically estimated peak-to-peak amplitude, i.e., $2R_G$. The vertical black dotted lines are plotted to represent integral multiples of the gyration period T_G. 124

B.2 Variation of γ over time due to numerical computation error for an electron in a constant magnetic field ($B_0 = 40$ T). The top, middle and bottom row correspond to $\gamma = 10, 20$ and 50, while the left and right columns represent simulations performed using the Vay pusher algorithm and the ode45 solver, respectively. . . . 125

B.3 Normalized kinetic energy $(\gamma(t') - 1)$ as a function of time after birth t' for an electron in a Gaussian laser field with $a_0 = 10,\ \lambda_0 = 0.8\ \mu\text{m},\ w_0 = 8\ \mu\text{m},\ \tau = 40$ fs, solved using the Vay pusher with (a) $\text{d}t = T_L/100$, (b) $\text{d}t = T_L/1000$ and (c) $\text{d}t = T_L/2000$, and the ode45 solver with (d) $\text{Tol} = 10^{-6}$, (e) $\text{Tol} = 10^{-8}$ and (f) $\text{Tol} = 10^{-10}$. 128

B.4 Normalized kinetic energy $(\gamma(t') - 1)$ as a function of time after birth t' for an electron in a Gaussian laser field with $a_0 = 200,\ \lambda_0 = 0.8\ \mu\text{m},\ w_0 = 8\ \mu\text{m},\ \tau = 40$ fs, solved using the Vay pusher with (a) $\text{d}t = T_L/100$, (b) $\text{d}t = T_L/1000$ and (c) $\text{d}t = T_L/2000$, and the ode45 solver with (d) $\text{Tol} = 10^{-6}$, (e) $\text{Tol} = 10^{-8}$ and (f) $\text{Tol} = 10^{-10}$. 129

C.1 Representative focal spot images captured across three different laser shots with an 8-bit camera for varying gain of (a) 15 dB, (b) 19 dB and (c) 24 dB. The color scale represents the raw value stored in each pixel. Three-dimensional view of (a)–(c) is shown in (d)–(f) where the height corresponds to the pixel value. The yellow and magenta planes represent the fixed value used to subtract the background and the maximum possible value, which are 3 and 255 here, respectively. The transparent plane with a black dashed outline represents the maximum pixel value stored in the corresponding image. 134

C.2 Intensity profile of a super-Gaussian beam (Eq. (C.1)) with radius ρ_B for order (a) $\kappa = 1$, (b) $\kappa = 4$, (c) $\kappa = 10$, and (d) $\kappa = 100$. The red (gray) shaded region represents the part of the beam transmitted past (discarded by) a circular apodizer with radius ρ_A centered on the beam. 137
C.3 Image plates used to measure (a) the spatial distributions of electrons in CLPU, April 2024 (Section 5.3) and (b) energy distribution through the magnetic spectrometer in ZEUS, June 2024 (Section 4.3.2). 139
C.4 Image plate placed on a scanner tray in (a) and a representative scan in (b) where the color axis represents the raw value recorded in each $50 \times 50\ \mu\mathrm{m}^2$ pixel, when $\mathcal{S} = 4000$ and $\mathcal{L} = 5$ (see text). PSL values corresponding to a range of raw values stored in a $50 \times 50\ \mu\mathrm{m}^2$ pixel shown for (c) $\mathcal{L} = 4$ and (d) $\mathcal{L} = 5$. The blue, green and yellow lines marked by the downward triangle, diamond and upward triangle correspond to $\mathcal{S} = 10000, 4000$ and 1000, respectively. 141
C.5 Components of the TOF detector. The fully constructed extraction module is shown in (a) and a deconstructed close-up view is shown in (b). The laser focus is between plates 2 and 3. The deflection module is shown in (c). 143
C.6 Wiring connected to (a) a plate on the extraction module, (b) a plate on the deflection module and (c) the flange on the vacuum chamber. 144
C.7 Operation of the deflection circuit. Components are shown in (a), input and output signals are shown in (b), and timing schematic (not to scale) for the signals is shown in (c), where time increases to the right, i.e., $t_b > t_a$. 145
C.8 Schematic diagram of the deflection circuit. 146
C.9 Schematic diagram of the two-beam setup (not to scale) employed in CLPU, April 2024, for the ponderomotive-expulsion experiment (Section 5.3) in (a). The black dashed boundary represents the Mach-Zehnder setup. Plane mirrors are marked 'M1' through 'M5', beam splitters are marked 'BS1' and 'BS2'. The two beams resulting from BS1 are represented by the red dashed and dotted rays, which overlap following BS2. The blue dotted boundary around M1 and M2 represents a motorized translation stage. The 6-cm apodizer was placed between M3 and M4. Pointing fluctuation on the focal plane in the target chamber is shown for the strong (b) and weak (c) beams over a series of 20 shots per beam imaged at low power. 148

List of Abbreviations

ADK	Ammosov-Delone-Krainov
BELLA	Berkeley Lab Laser Accelerator
BSI	barrier suppression ionization
CAEP	China Academy of Engineering Physics
CALA	Center for Advanced Laser Applications
CEA	Commissariat à l'énergie atomique et aux énergies alternatives
CLF	Central Laser Facility
CLPU	Centro de Láseres Pulsados
CoReLS	Center for Relativistic Laser Science
CPA	chirped pulse amplification
CUOS	Center for Ultrafast Optical Science
dB	decibel
ELI-BL	Extreme Light Infrastructure – Beamlines
ELI-NP	Extreme Light Infrastructure – Nuclear Physics
eV	electron-volt
f/#	f-number
FWHM	full width at half maximum
HPLS	High Power Laser System
LBNL	Lawrence Berkeley National Laboratory
LLE	Laboratory for Laser Energetics
LLNL	Lawrence Livermore National Laboratory
LMJ	Laser Mégajoule
LMJ-PETAL	Laser Mégajoule - Petawatt Aquitaine Laser
LWFA	laser wakefield acceleration
MCP	microchannel plate
MPPC	multi-pixel photon counter

NIF	National Ignition Facility
ODE	ordinary differential equation
OSU	The Ohio State University
PSL	photostimulated luminescence
PSLM	programmable spatial light modulator
QED	quantum electrodynamics
QVAC	quantum vacuum
RAL	Rutherford Appleton Laboratory
RTS	relativistic Thomson scattering
SEL	Station of Extreme Light
SIOM	Shanghai Institute of Optics and Fine Mechanics
SULF	Shanghai Super-intense Ultra-fast Laser Facility
Ti:Sa	titanium-doped sapphire
TOF	time of flight
UM	University of Michigan
UR	University of Rochester
XCELS	eXawatt Center for Extreme Light Studies
XFEL	x-ray free electron laser
ZEUS	Zetawatt-Equivalent Ultrashort pulse laser System

Nomenclature

Latin Symbols

a_0	normalized vector potential corresponding to the peak intensity
$\vec{A}$	vector potential
$\mathcal{A}$	area of a focused laser spot
A_{pix}	area of a camera pixel in physical units
$\vec{B}$	magnetic field vector with components B_x, B_y, B_z
B	magnetic field magnitude
c	speed of light in vacuum
C_{pk}	peak signal value stored in a focal spot image
C_{sum}	total signal stored in a focal spot image
d	distance between focal spot and image plate perpendicular to laser propagation direction
e	elementary charge
e^-	electron
e^+	positron
$\vec{E}$	electric field vector with components E_x, E_y, E_z
E	electric field magnitude
E_0	peak electric field magnitude within a laser pulse
E_{Coul}	coulombic field magnitude
$f(t)$	temporal profile of a laser pulse
$\vec{F}$	force vector
$\vec{F}_B$	force due to a magnetic field
$\vec{F}_E$	force due to an electric field
h	Planck's constant
I	intensity of a laser
I_0	peak intensity of a laser
I_{th}	intensity threshold for ionization

$\vec{k}$	wave vector
k	angular wavenumber of light
k_B	Boltzmann constant
K	proportionality constant multiplied with peak power to infer the peak intensity
l	azimuthal index of a Laguerre-Gauss mode
m	mass
n_p	density of particles
N_b	number of bits
N_p	number of particles
N_e	number of electrons
N_{th}	maximum attainable ionization stage of a particle
$\vec{p}$	momentum vector with components p_x, p_y, p_z
p	radial index of a Laguerre-Gauss mode
$p_\perp$	transverse momentum of an electron as $t \to \infty$
$p_\parallel$	longitudinal momentum of an electron as $t \to \infty$
P	pressure
P_0	peak power of a laser pulse
P_x	transverse canonical momentum of an electron in a plane wave
q	charge of a particle
$\vec{r}$	position vector with components r_x, r_y, r_z
r	magnitude of position vector
r_e	inter-electron spacing in a volume of ionized gas
r_{ion}	inter-ion spacing in a volume of ionized gas
R_G	radius of gyration
t	time
t_{end}	time instant when a simulation is terminated
$t_{ion,start}$	time instant when ionization routine starts in a simulation
$t_{ion,step}$	step size for time increments within ionization routine in a simulation
$t_{ion,stop}$	time instant when ionization routine stops in a simulation
T	temperature
T_{gas}	temperature of a gas
T_G	gyration period

T_L	field oscillation period
U	laser pulse energy
$\mathcal{U}$	fraction of laser energy transmitted past an apodizer
U_{ion}	kinetic energy of an ion in a time of flight detector
U_{Loss}	energy lost by a laser pulse in accelerating a group of electrons
U_{th}	ionization energy for an electron in an atom
$\vec{v}$	velocity vector with components v_x, v_y, v_z
v	magnitude of velocity vector
V	electric potential
w_0	Gaussian beam waist
$w(z)$	Gaussian beam radius at z
W_D	separation between plates in the deflection module of time of flight detector
W_{MCP}	diameter of the active area of a microchannel plate detector
x	coordinate along the x-axis
$\hat{x}$	unit vector along the x-axis
y	coordinate along the y-axis
$\hat{y}$	unit vector along the y-axis
z	coordinate along the z-axis
$\hat{z}$	unit vector along the z-axis
z_R	Rayleigh length
Z	ionization stage
$\mathcal{Z}$	complex beam parameter

Greek Symbols

α_t	temporal scaling factor used for the end time of a simulation
α_{xy}	transverse scaling factor used for the initial box size used in a simulation
α_z	longitudinal scaling factor used for the initial box size used in a simulation
β	ratio of the speed of a particle to the speed of light in vacuum
γ	Lorentz factor

δ_I random number $\in (0.5, 2.0)$ used to smooth the onset of ionization

ϵ_0 permittivity of free space
ε field strength parameter relative to the Schwinger limit

η dimensionless scaling factor that represents a fraction of the normalized vector potential

θ polar angle, measured relative to the direction of laser propagation
θ_c characteristic ejection cutoff angle

κ order of a super-Gaussian

λ_0 wavelength of light
λ_D Debye shielding length

ν frequency of light

ρ radial distance

τ laser pulse duration
τ_p plasma oscillation period

ϕ azimuthal angle, measured on the transverse plane

χ quantum parameter

ψ_p^l spatial profile of a Laguerre-Gauss beam with mode numbers l and p

ω_0 angular frequency of light
ω_p plasma frequency

Subscripts

e related to the electron

f final value

i initial value
ion related to the ion

L related to the laser

ph photon

s related to the strong pulse in a two-beam setup

th threshold
tot total

w related to the weak pulse in a two-beam setup

x component along the x-axis

y component along the y-axis

z component along the z-axis

Prefixes

δ related to uncertainty
Δ related to an interval or range

Chapter 1: Motivation

1.1 Petawatt-Class Lasers and Their Applications

Advances in laser-based techniques have enabled novel pathways to explore a wide range of physical phenomena. The invention of Q-switching [1] in 1962 allowed the delivery of joule-level laser energy in nanosecond pulses ($1\ \mathrm{ns} = 10^{-9}\ \mathrm{s}$) and mode-locking [2] in 1964 allowed the creation of laser pulses on picosecond ($1\ \mathrm{ps} = 10^{-12}\ \mathrm{s}$) and femtosecond ($1\ \mathrm{fs} = 10^{-15}\ \mathrm{s}$) timescales. Together with the advent of chirped-pulse amplification (CPA) [3] in 1985, which enabled the amplification of laser pulses to kilojoule level energies, these techniques collectively enabled access to regimes of physical phenomena characterized by extreme laser energy U ($\gtrsim 10^3$ J), peak power P_0 ($\gtrsim 10^{15}$ W), and peak intensity I_0 ($\gtrsim 10^{18}\ \mathrm{W/cm^2}$). For a laser pulse whose energy is distributed over an area $\mathcal{A}$ within some pulse duration τ, these parameters are related as

$$I_0 \sim \frac{P_0}{\mathcal{A}} \sim \frac{U}{\tau \mathcal{A}}. \tag{1.1}$$

The invention of CPA led to the development of several state-of-the-art laser systems [4–6], which can generally be classified into two categories: high pulse energy lasers (Table 1.1) and high peak

power lasers (Table 1.2). Figure 1.1 shows an overview of the parameter space covered by these two categories of lasers that enable the exploration of notably different physical regimes.

Table 1.1: Lasers ordered by pulse energy (> 25 kJ) delivered on target as of January 2026.

Laser (Refs.)	**Host (Country)**	**Current**			**No.**
		U (kJ)	τ (ns)	P_0 (TW)	
NIF [7]	LLNL (US)	2200	~ 3 to 20	≈ 500	1
LMJ [8]	CEA (FR)	1500	~ 0.3 to 25	≈ 370	2
SG-III [9, 10]	CAEP (CN)	181	≈ 3	≈ 60	3
OMEGA [11]	LLE, UR (US)	37	≈ 0.75	≈ 50	4
SG-II UP [12]	SIOM (CN)	25	≈ 3.3	≈ 7.6	5

Lasers with high pulse energy (Table 1.1) allow us to deposit $\sim$ a few kJ to MJ of laser energy within a few ns (top-right corner of Figure 1.1), timescales shorter than the characteristic material response times of the system. The rapid deposition of laser energy in a material system can lead to very high energy density ($> 10^{11}$ J/m^3), producing transient states of extreme pressure (> 1 Mbar) and temperature ($> 10^4$ K) [32]. This allows us to create and study matter under extreme conditions within a laboratory, which may only otherwise be present in planetary cores or stars.

In 2022, the National Ignition Facility (NIF) [7] at the Lawrence Livermore National Laboratory (LLNL), which holds the record for the laser system with the highest pulse energy in the world, achieved scientific breakeven in laboratory fusion for the first time in history. Here, scientific breakeven refers to the condition in which the energy released by the fusion reactions exceeds the laser energy delivered to the fusion fuel. This marked a monumental achievement that will further enable the quest for a nearly limitless source of energy. The NIF and other high-energy lasers such as the OMEGA laser [11] at the Laboratory for Laser Energetics (LLE)

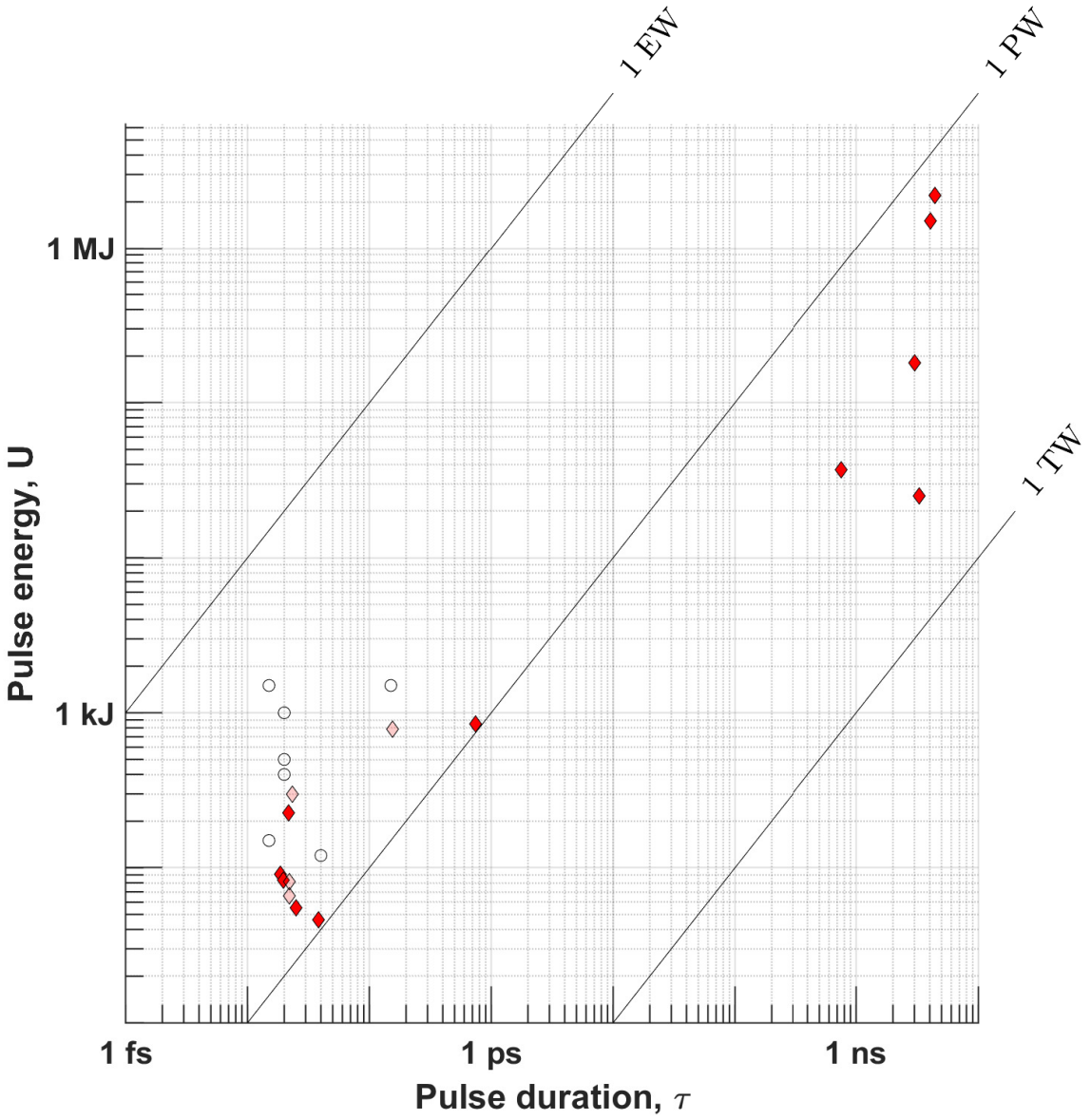


Figure 1.1: Parametric map of lasers with highest pulse energy (Table 1.1) and highest peak power (Table 1.2). Opaque red diamonds represent lasers whose performance on target was recorded as previously demonstrated through a peer-reviewed article. Translucent red diamonds represent lasers whose parameters were claimed as their current capability through press release and/or conference abstract and/or peer-reviewed article. Circles represent future capabilities of existing or new lasers that are either being planned or in development.

Table 1.2: Lasers ordered by peak power (> 1 PW) per laser beam as of January 2026.

Laser (Refs.)	**Host (Country)**	**Current Parameters**				**Future/Planned**		
		U (J)	τ (fs)	P_0 (PW)	**No.**	U (J)	τ (fs)	P_0 (PW)
Systems currently operational								
HPLS [13]	ELI-NP (RO)	225	22	10	$= 1$	-	-	-
SULF [14, 15]	SIOM (CN)	300	24	10†	$= 1$	-	-	-
SILEX-II [16]	CAEP (CN)	91	19	5	$= 3$	-	-	-
ATON [17, 18]	ELI-BL (CZ)	786	154	5†	$= 3$	1500	150	10
CoReLS [19]	CoReLS (KR)	83	20	4	5	-	-	-
F1 [20, 21]	Apollon (FR)	81	22	3.7†	6	150	15	10
ATLAS 3000 [22]	CALA (DE)	66	22	3†	7	-	-	-
ZEUS [23]	ZEUS, UM (US)	55	25	2.2	8	120	40	3
BELLA [24]	LBNL (US)	46	38	1.2	$= 9$	-	-	-
LMJ-PETAL [25]	CEA (FR)	850	740	1.15	$= 9$	-	-	-
Systems in development or planned								
SEL [26–28]	SIOM (CN)	-	-	-	-	1500	15	100
XCELS 600PW [29]	XCELS (RU)	-	-	-	-	1000	20	50
NSF-OPAL [30]	LLE, UR (US)	-	-	-	-	500	20	25
Vulcan 20-20 [6, 31]	CLF, RAL (UK)	-	-	-	-	400	20	20

†Note: Current capability claimed through press release and/or conference abstract and/or peer-reviewed article, performance on target yet to be recorded through a peer-reviewed research article as previously demonstrated.

have led to several other achievements that have widespread applications. Some examples include (i) the creation of exotic phases of matter in a controlled environment, which enhances our understanding of various planetary bodies including rocky planets [33–35], icy planets [36] and gas giants [37], (ii) the discovery of novel acceleration mechanisms such as target normal sheath acceleration [38–40], which can produce beams of protons and ions accelerated to multi-MeV energies and other specialized properties [41], and (iii) the exploration of how fundamental properties of materials, such as chemical bonding, may change under extreme conditions [42].

While high-energy lasers are an excellent and unique resource for investigating phenomena that rely on the rapid deposition of extreme energies in material systems, the attainable peak

electric field within the laser field is limited. This can be attributed to the following reasons. First, the massive energy contained within the laser pulse will far exceed damage thresholds of the optical components if compressed to $\tau \ll 1$ ns. Second, laser systems like the NIF and OMEGA deliver such high laser energies with the use of several lower-energy laser beams (192 for NIF and 60 for OMEGA) that are timed with sub-ns precision but are not phase-locked. Thus, the effective field strength is reduced compared to the sum of field strengths of all individual beams. High-peak power lasers (Table 1.2) circumvent this problem by typically employing a single laser beam with pulse energies of a few J to a few 100 J, compressed to $\tau \sim$ a few 10 to 100 fs (bottom-left corner of Figure 1.1). These lasers have facilitated the exploration of a distinct set of phenomena in the sub-ps regime with extraordinary applications, such as laser wakefield acceleration (LWFA) [43] for example. Researchers have used LWFA to produce highly collimated beams of electrons (divergence $<$ a few mrad) with energies up to 10 GeV [44, 45]. These electrons can also be used to generate high-energy photons in the keV to MeV range. The comparatively small footprint of LWFA setups enables access to relatively low-cost particle and radiation sources that can complement expensive large-scale facilities, such as conventional accelerators and x-ray free electron lasers (XFELs), for applications in x-ray imaging, gamma-ray radiography, and more [46].

Lasers with high peak power offer the unique possibility to achieve extreme electric fields in a laboratory environment when the laser field is focused to spots with area $\mathcal{A} \sim$ a few μm^2 resulting in large I_0. This is because

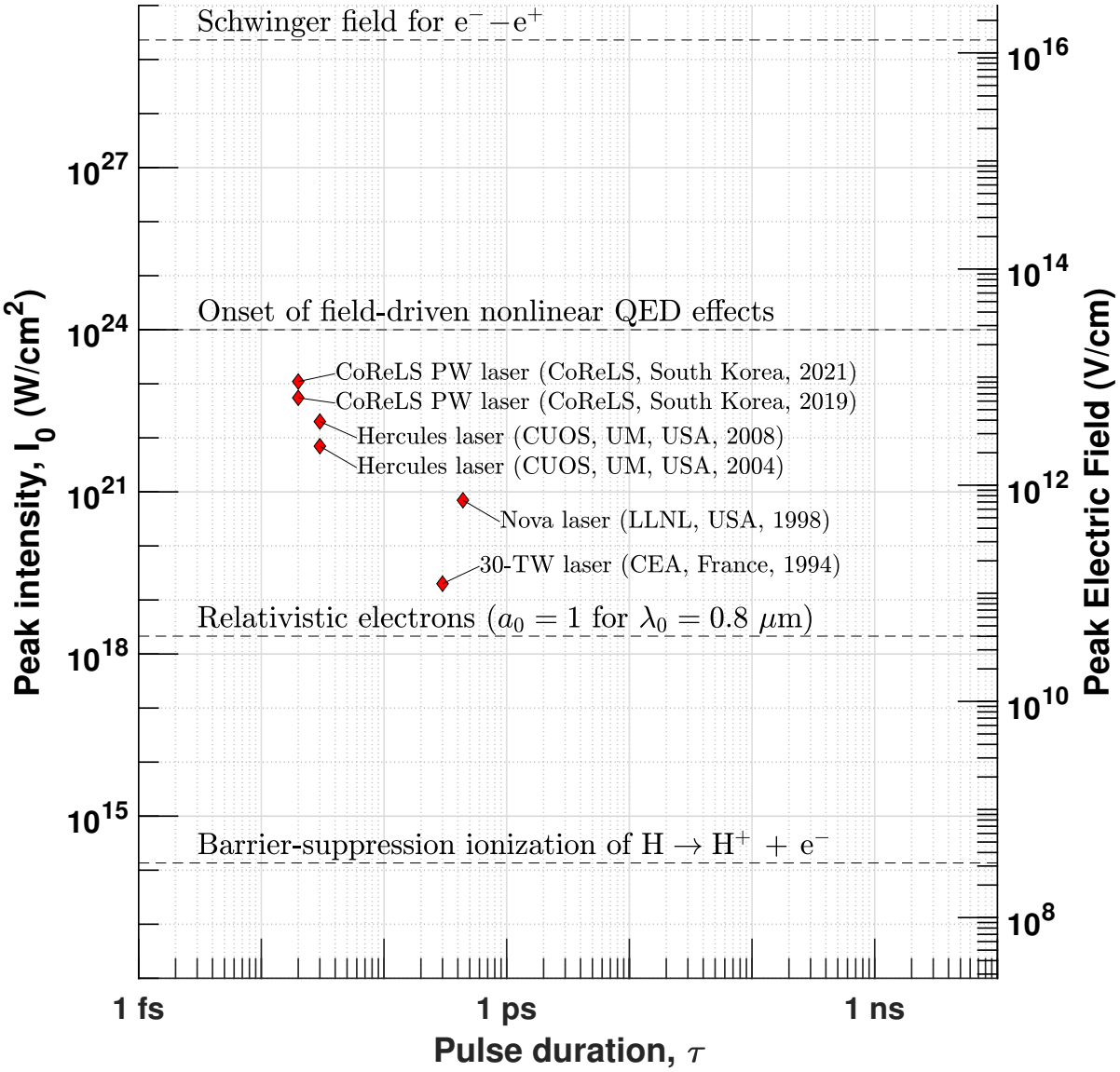


Figure 1.2: Parametric map of various physical phenomena made accessible by focusing petawatt-class lasers. Red diamonds represent lasers that held the world record for peak intensity since 1994, and whose performance on target was previously demonstrated through a peer-reviewed article and/or scientific report. The horizontal dashed lines represent the intensity thresholds corresponding to various physical phenomena as labeled (see text for detailed description).

$$E_L\,(\mathrm{V/cm}) = \sqrt{\frac{2I_0}{c\epsilon_0}} \approx 27.5\sqrt{I_0\,(\mathrm{W/cm^2})}, \tag{1.2}$$

where c ($= 2.997\,924\,58 \times 10^8$ m/s) is the speed of light in vacuum and ϵ_0 ($= 8.854\,187\,812\,8 \times 10^{-12}$ C^2/(N m^2)) is the permittivity of free space. Although there is a lack of an official survey that records the historic progression of the peak laser intensity, we attempted to summarize the progress after the invention of CPA in 1985 to the best of our ability through extensive research of literary sources. We found that in 1994, a CEA laboratory in France attained $I_0 \approx 2 \times 10^{19}$ W/cm^2 [47, 48], which was higher than that referred to by other world-class lasers at the time such as the Vulcan laser at Rutherford Appleton Laboratory in the UK ($I_0 \sim 6$ to 9×10^{18} W/cm^2 [49, 50]), the tabletop terawatt or T^3 laser at SLAC in the US ($I_0 \approx 10^{18}$ W/cm^2 [51]), and the laser at the Center for Ultrafast Optical Science (CUOS), University of Michigan (UM), in the US ($I_0 \sim 4$ to 6×10^{18} W/cm^2 [52]). There is general consensus (see Figure 1.3 in [53]) regarding the record peak intensity following the commissioning of the world's first petawatt laser at LLNL, Nova, due to the significant increase to $I_0 \approx 7 \times 10^{20}$ W/cm^2 in 1998 [54]. CUOS then attained $I_0 \approx 7 \times 10^{21}$ W/cm^2 in 2004 [55] and 2×10^{22} in 2008 [56]. More recently, the CoReLS facility in South Korea attained 5.5×10^{22} W/cm^2 in 2019 [57], and 1.1×10^{23} W/cm^2 in 2021 [19], which currently stands as the record in early 2026. Figure 1.2 summarizes the historic progression of record peak intensity (and corresponding peak electric field) in addition to the variety of physical phenomena made accessible when high peak-power lasers are focused to achieve high intensities.

When $I_0 \approx 1.4 \times 10^{14}$ W/cm^2, the corresponding electric field is large enough to suppress

the atomic potential barrier in the H atom, allowing the liberation of an electron, e^-. With increasing intensity, the laser field ionizes various atomic species with higher ionization potentials to higher ionization stages. We discuss this phenomenon known as barrier-suppression ionization [58] in greater detail in Section 2.1.

When $I_0 \approx 2.14 \times 10^{18}\ \mathrm{W/cm^2}$, electrons are accelerated to relativistic speeds within one oscillation period of a laser field with wavelength $\lambda_0 = 0.8\ \mu\mathrm{m}$, which is typical for many high-power lasers that employ titanium-doped sapphire (Ti:Sa) crystals as the gain medium. More generally, this occurs when the normalized vector potential $a_0 \propto \lambda_0\sqrt{I_0}$, which is a convenient parameter to represent the intensity, approaches or exceeds unity. Electrons are accelerated to higher kinetic energies as a_0 increases. We discuss this in greater detail in Section 2.4.

When $I_0 \gg 10^{18}\ \mathrm{W/cm^2}$ or $a_0 \gg 1$, these lasers enable the exploration of physical processes predicted by quantum electrodynamics (QED), the fundamental theory that describes the interaction between light and charged particles, in regimes that have remained experimentally challenging to access for nearly a century since their theoretical prediction. We discuss this in greater detail in Section 1.2.

1.2 Tests of Nonlinear QED in Novel Regimes

In the late 1920s and early 1930s, Paul Dirac predicted the existence of antiparticles, specifically, the positron (e^+) [59, 60], which has the same mass but opposite charge as the electron and was experimentally observed in 1932 [61]. A positron can annihilate with an electron to release energy, and conversely, sufficient energy can create an $\mathrm{e}^- - \mathrm{e}^+$ pair. These pairs can be created as real pairs naturally in extreme astrophysical environments, such as the magnetospheres of mag-

netars [62, 63] and pulsars [64], or exist, as suggested by Dirac, even in a vacuum devoid of real particles as fleeting virtual pairs [60, 65] that momentarily appear and disappear. Studying the creation and dynamics of such pairs is therefore essential for understanding the physics of extreme environments in the universe.

In a laboratory environment, it may be possible to create $e^- - e^+$ pairs through collisions of high-energy particles without necessarily employing a strong laser field. Examples include the linear Breit-Wheeler process [66], in which two high-energy photons are annihilated; the Bethe-Heitler process [67], in which a high-energy photon converts into a pair in the presence of the Coulomb field of an ion; and the linear trident process [68–70], in which an electron interacting with an external field (such as the Coulomb field of an ion) produces an additional $e^- - e^+$ pair. Some of these processes can be realized in conventional accelerators and particle colliders [71, 72], which are large, expensive facilities that are few in number. In contrast, the relatively compact footprint of petawatt-class lasers offers a more accessible alternative to explore pair production through strong-field, nonlinear QED processes [73, 74].

Pair production in nonlinear QED can occur through multiple processes that are broadly classified into two categories, namely, particle-seeded and field-driven. Particle-seeded processes involve a strong electromagnetic field interacting with real particles, including massive particles such as electrons as well as massless particles such as photons. Field-driven processes are induced purely by a strong electromagnetic field in vacuum devoid of real particles. In this case, nonlinear effects are governed by virtual particle-antiparticle pairs, which are brief quantum fluctuations that appear and disappear in the vacuum.

The rate of particle-seeded pair production in nonlinear QED is conveniently characterized by the dimensionless quantum parameter χ [75], which quantifies the relative strength of the

field experienced by a particle to the QED critical field $E_S \approx 1.3 \times 10^{16}\ \mathrm{V/cm}$, also called the Schwinger field [76–78]. Pair production occurs when $\chi \gtrsim 1$ [73]. For a photon-seeded process, such as the nonlinear Breit-Wheeler [75, 79–84], a high-energy photon with energy $h\nu_{ph}$ interacts with a strong laser field. Here, h $(= 6.626\,070\,15 \times 10^{-34}\ \mathrm{J\,s})$ is the Planck constant. For an electron-seeded process, such as the nonlinear trident [85–87], an electron with mass m_e and kinetic energy $(\gamma - 1)m_e c^2$ interacts with a strong laser field either directly through a one-step process or through a two-step process that involves nonlinear Compton scattering [88, 89] to generate a high-energy photon, followed by nonlinear Breit-Wheeler. In the counter-propagating geometry, which maximizes the probability of the interaction, the quantum parameter may be approximated for both these processes as [73, 90]

$$\chi_{ph} \simeq \frac{2h\nu_{ph}}{m_e c^2}\frac{E_L}{E_S}, \tag{1.3}$$

$$\chi_e \simeq 2\gamma\frac{E_L}{E_S}, \tag{1.4}$$

respectively, where γ is the Lorentz factor of the electron. Here E_L is the magnitude of the electric field of the laser in the lab frame. This implies that increasing the electron or photon energy decreases the required peak intensity of the laser in the lab frame. This is because the effective laser intensity in the boosted frame of the particle increases for higher energy particles. Notably, the E144 experiment at SLAC leveraged this approach to achieve pair production in the late 1990s [51, 90] by colliding a ~ 46 to $49\,\mathrm{GeV}$ electron beam against a laser with $I_0 \approx 0.5 \times 10^{18}\ \mathrm{W/cm^2}$. Using Equations (1.2) and (1.4), it is thus straightforward to show that for a laser with $I_0 = 5 \times 10^{21}\,\mathrm{W/cm^2}$ it is possible to achieve the same quantum parameter

as in the SLAC E144 experiment with an electron beam of energy as low as $500\,\mathrm{MeV}$. As discussed in Section 1.1, these parameters are well within reach of current petawatt-class laser facilities, both in terms of the peak intensity and electron beams made accessible by laser-enabled technologies such as LWFA. Several studies have proposed approaches to achieve pair production using particle-seeded methods enabled by petawatt-class lasers in various configurations [91–98].

In contrast, producing pairs solely with a strong electromagnetic field in the absence of real particles – through the process commonly known as Schwinger pair production – requires $\varepsilon = E/E_S \sim 1$. This implies that the magnitude of the electric field of the laser must be comparable to the Schwinger field, corresponding to a required peak intensity of $I_0 \approx 2.3 \times 10^{29}\,\mathrm{W/cm^2}$, several orders of magnitude higher than the current record peak intensity, as shown in Figure 1.2. Achieving spontaneous pair production from vacuum in the laboratory is thus unlikely in the near future.

However, observing signatures of certain field-driven nonlinear QED processes in the perturbative regime ($\varepsilon \ll 1$) may soon be feasible, specifically quantum vacuum (QVAC) effects where the vacuum behaves as a polarizable medium due to virtual $\mathrm{e^-}-\mathrm{e^+}$ pairs. For example, efforts are underway at XFELs to observe vacuum birefringence [99–101], a phenomenon in which the polarized vacuum acts as a birefringent medium. In addition, these pairs can mediate photon-photon scattering [77, 102, 103], remarkably enabling photons to interact with one another in free space. Several studies have proposed investigating this effect [104–111], which is expected to become observable at intensities $\sim 10^{24}\ \mathrm{W/cm^2}$ [112]. Such intensities may be achievable with multi-petawatt lasers that are either under construction or planned, such as the SEL and NSF-OPAL, paving the way for all-optical probes of field-driven nonlinear QED [113].

1.2.1 Key Experimental Constraints for Laser-Based Tests

Precision measurements of QVAC effects such as photon-photon scattering typically rely on focusing multiple petawatt-class laser beams to overlap in space and time. These experiments are challenging for several reasons including, but not limited to:

1. the lack of diagnostics that can characterize the focal volume in real time at full power
2. the difficulty of creating a volume of space that is void of real particles.

The first challenge arises from the fact that current methods for determining the conditions of the field of a focused petawatt laser pulse, such as the peak intensity or spatiotemporal quality, rely on measurements that sample the field at reduced intensities. Common approaches include using an attenuated beam or the main beam at low power to (i) image the focal spot (at $z = 0$) and/or the wavefront far from the focus ($z \to \infty$), (ii) measure the pulse energy, and (iii) measure the pulse duration [55, 114–116]. The peak intensity is then calculated using Equation (1.1), while aberrations are qualified using phase measurements after the focus with wavefront sensors. Although novel methods have valuably enabled more advanced characterization of the field in space and time [117], it is not possible to employ a detector directly within the focal volume at full power. This is due to the fact that laser pulses with $\tau \gtrsim 1\,\mathrm{fs}$ and $I_0 \gtrsim 10^{16}\ \mathrm{W/cm^2}$ far exceed the damage threshold for material systems, i.e., no detector can withstand the peak laser intensity in the focus. Thus, current methods that rely on extrapolations made from optical measurements made at reduced intensity are not sensitive to true conditions within the focal volume at full power. Therefore, there is a need to develop complementary diagnostic tools that can directly sample the peak laser intensity and aberrations in the focal volume in real time at full power.

The second challenge arises from the fact that while an ultrahigh vacuum pressure $\sim 10^{-14}$ mbar may be achievable in vacuum chambers with particularly designed vacuum technologies [118], such a pressure is not feasible in chambers that are regularly exposed to the atmosphere. This is because the presence of water vapor in the atmosphere prevents chambers that undergo frequent ventilation in high-power laser facilities from reaching a pressure $\lesssim 10^{-7}$ mbar, corresponding to a particle density of $\sim 3 \times 10^{9}/\mathrm{cm}^3$. This can lead to a significant level of ordinary electron-light scattering and seeded electron-positron pair production in the presence of focused multi-petawatt laser fields, which can interfere with laser-based tests of the QVAC [113].

1.2.2 Relativistic Electron Dynamics as a Diagnostic Tool

As the conditions in the focal volume cause irreversible damage to material systems, addressing the first challenge in Section 1.2.1 necessitates the use of charged particles such as ions and electrons. Several approaches to exploit the dynamics of charged particles at intensities $> 10^{18}$ W/cm^2 have been suggested. These include measuring the radiation associated with relativistic Thomson scattering (RTS) [115, 119–121], appearance intensity of ionization stages of tenuous gases [122, 123] and ejection of relativistic electrons from the focal volume [124–127].

For widespread use as a diagnostic, it is important that the method be straightforward to implement, minimally intrusive to the principal scientific study, sensitive to beam conditions and distortions, and capable of single-shot deployment. Radiation from RTS for $I_0 \sim 10^{18}$ to 10^{19} W/cm^2 produces Doppler-shifted 2$^{\mathrm{nd}}$ harmonic radiation that is detectable with a gated spectrometer [115]. However, this approach has limitations in deployment for $I_0 > 10^{19}$ W/cm^2 as it becomes difficult to distinguish between higher harmonic orders that begin to overlap. Al-

though it is possible to monitor the fundamental frequency, this requires mid-infrared detection, which is challenging. Ionization is single-shot capable but provides limited information on the spatiotemporal quality of the focus. In addition, ionization thresholds tend to be clumped together for certain ranges of intensities, with large gaps between thresholds at other intensities.

While measuring electrons ejected from the laser focus shows promise as a diagnostic suited for widespread use, experimental investigation under various conditions is required to improve our understanding of, and ability to model, the dynamics of these electrons. In addition, the expulsion of electrons from the focal volume plays an important role in suppressing sources of unwanted signals in laser-based tests of the QVAC. Thus, to address the challenges discussed in Section 1.2.1, we investigate the dynamics of electrons created via ionization in the focal volume and subsequently ejected by petawatt-class lasers through experiment and computation.

1.3 Overview of Contents

The remainder of this dissertation is organized as follows:

In Chapter 2, we introduce relevant theoretical concepts that are required for understanding the experiments detailed in this study. This includes concepts related to how the electrons of interest are generated, the forces applied on the electrons, and theoretical models that describe their motion in simplistic scenarios.

In Chapter 3, we describe our method to simulate the dynamics of electrons in petawatt-class laser fields, which informs our experimental approach and interpretation of data.

In Chapter 4, we present the experiments we performed in various petawatt-class laser facilities to study electron dynamics under various conditions and compare our data with simulations.

In Chapter 5, we describe how our exploration of electron dynamics may be applied to address challenges faced by laser-based tests of the QVAC.

In Chapter 6, we present a summary of the contents of this dissertation and an outlook for potential developments in the future.

Chapter 2: Introduction

In this chapter, we first review the relevant processes by which electrons of interest are generated, in Section 2.1, followed by a discussion of the relevant forces acting on these electrons once they are generated, in Section 2.2. We then review a simplistic description of electron motion in non-relativistic laser fields in Section 2.3. In Section 2.4, we review electron motion in relativistic laser fields and provide relationships between the kinetic energy and ejection angle of the electron, and the laser intensity, which is relevant for the rest of this dissertation.

2.1 Liberation of Electrons Through Ionization in Strong Fields

Electrons are liberated from their host atoms within a gas when they gain sufficient energy to escape the atomic binding potential. An external electromagnetic field facilitates this process through multiple mechanisms. When the photon energy of the electromagnetic field is sufficiently large, i.e., $h\nu_{ph} \geq U_{th}$, it may be absorbed by the atom through the process commonly known as photoionization. Here, U_{th} is the ionization energy. When $h\nu_{ph} < U_{th}$, electrons may still be liberated if the applied field is sufficiently strong to distort the atomic potential. In this regime, ionization may proceed via tunneling through the field-lowered barrier or if the potential barrier is completely eliminated, via barrier-suppression ionization (BSI) [58]. Such conditions are readily achieved in petawatt-class laser fields focused to high intensities.

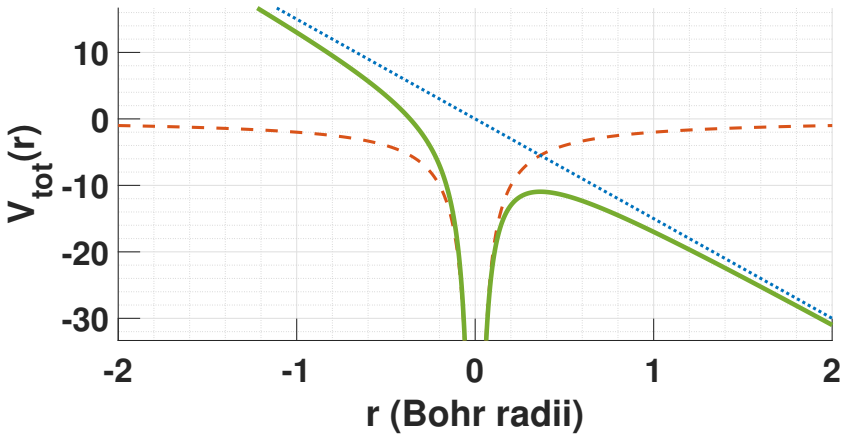


Figure 2.1: One-dimensional model of strong-field ionization. The orange dashed, blue dotted and green solid lines represent the Coulomb potential, instantaneous perturbation due to the laser field and the total potential V_{tot} (see Eq. (2.1)), respectively.

We can estimate the intensity required to ionize a given atomic species to some ionization stage Z as follows. We assume that the laser wavelength $\lambda_0 \gg$ the characteristic atomic length scale (dipole approximation). Under this assumption, the electric field of the laser E_L may be treated as spatially uniform over the atom. This is often the case for the petawatt-class lasers employed here as $\lambda_0 \sim 0.8\ \mu\text{m}$ to $1\ \mu\text{m}$. Using a simple one-dimensional model for an electron bound by the Coulomb potential ($-Z/|r|$) of a nucleus at $r = 0$, we can then write the net potential in the presence of a laser field as

$$V_{tot}(r) = -\frac{Z}{|r|} - rE_L, \tag{2.1}$$

in atomic units, where r is the distance in Bohr radii from the nucleus. As shown in Figure 2.1, $V_{tot}(r)$ has a local maximum at some $r = r_p$. Setting $\partial V/\partial r = 0$, we find $r_p = \sqrt{Z/E_L}$. Equating the local maxima of the suppressed potential, i.e., $V_{tot}(r = r_p)$, to the ionization potential for

obtaining a specific ion, V_{th}, we get

$$E_L = \frac{V_{th}^2}{4Z}. \tag{2.2}$$

Therefore, the laser intensity required to ionize an atom to some stage Z assuming BSI is

$$\begin{aligned} I_{th}(\text{a.u.}) &= \frac{V_{th}^4}{16Z^2}, \\ I_{th}(\text{W/cm}^2) &= 4.00 \times 10^9 \, \frac{[U_{th}(\text{eV})]^4}{Z^2}. \end{aligned} \tag{2.3}$$

We tabulate I_{th} for various atomic species of interest in Appendix A directly using U_{th} values obtained from the Atomic Spectra Database of the National Institute of Standards and Technology [128], which compiles ionization energies from experimental measurements or robust atomistic calculations that do not rely on the hydrogen-like approximation. Therefore, the U_{th} and I_{th} values listed in Appendix A and used for this dissertation account for electron shielding and do not assume a hydrogen-like Coulomb barrier despite the simplistic model used to derive Equation (2.3).

2.2 Treating Electrons as Single Particles Influenced by an External Laser Field

Once an electron is liberated from its parent atom, the Lorentz force governs the dynamics of the electron under the influence of an electric field, $\vec{E}$, and magnetic field, $\vec{B}$, which may each comprise contributions from multiple sources, given by

$$\vec{F} = \vec{F}_E + \vec{F}_B = -e(\vec{E} + \vec{v} \times \vec{B}), \tag{2.4}$$

where e ($= 1.602\,176\,634 \times 10^{-19}$ C) is the elementary charge, $\vec{F}_E$ ($= -e\vec{E}$) is the force due to the electric field, $\vec{F}_B$ ($= -e\vec{v} \times \vec{B}$) is the force due to the magnetic field and $\vec{v}$ is the velocity of the electron traveling with speed $v = |\vec{v}|$. The electric and magnetic fields experienced by an individual electron generally arise from two sources: the applied electromagnetic field, such as that of the laser, and the fields due to other charged particles in its vicinity. We can compare the magnitude and the effect of these fields as follows.

As we employ laser fields focused to peak intensities $I_0 \gg 10^{18}$ W/cm^2, we obtain a lower bound for the magnitude of the electric field of the laser using Equation (1.2) as $E_L \gtrsim 2.75 \times 10^{12}$ V/m. To estimate an upper bound of the Coulomb field acting on the electron, we assume that the laser fully ionizes Xe ($Z = 54$) gas at a maximum pressure of $P = 10^{-3}$ mbar at room temperature, i.e., $T_{gas} = 300$ K. Assuming the ideal gas law, this results in an electron number density

$$n_e = \frac{ZP}{k_B T_{gas}} \approx 1.3 \times 10^{21}/\mathrm{m}^3, \tag{2.5}$$

where k_B ($= 1.380\,649 \times 10^{-23}$ J/K) is the Boltzmann constant. This corresponds to a plasma frequency

$$\omega_p = \sqrt{\frac{n_e e^2}{\epsilon_0 m_e}} \approx 2.03 \times 10^{12}\ \mathrm{rad/s}, \tag{2.6}$$

where m_e ($= 9.109\,383\,701\,5 \times 10^{-31}$ kg) is the rest mass of the electron. This implies that the charges collectively reorganize by virtue of their interparticle interactions on a timescale of $\tau_p = 2\pi/\omega_p \approx 3$ ps. As the time period of oscillation of the laser field is ≈ 2.67 fs, we can thus neglect any collective response of the charges immediately following ionization on the timescale of a laser oscillation. We can then find the total field due to a static and uniform density n_p of particles each with charge q, assuming the fields add constructively, by integrating over a spherical shell of radius r and thickness $\mathrm{d}r$, given by

$$\begin{aligned} |E_{\mathrm{Coul}}| &= \int \frac{q}{4\pi\epsilon_0 r^2}\,(n_p 4\pi r^2)\mathrm{d}r, \\ &= \int_{r_{min}}^{r_{max}} \frac{n_p q}{\epsilon_0}\mathrm{d}r = \frac{n_p q}{\epsilon_0}\left(r_{max} - r_{min}\right), \end{aligned} \tag{2.7}$$

where we assume r_{min} as the nearest neighbor distance for an ion or an electron and $r_{max} \sim 2w_0$ as a characteristic length scale of interest for the ionization volume due to a laser with beam waist w_0. Within the ideal gas assumption, we know the mean inter-ion spacing is $r_{ion} \sim (k_B T_{gas}/P)^{1/3}$ and inter-electron spacing is $r_e \sim [k_B T_{gas}/(ZP)]^{1/3}$. Here, $r_{ion} \approx 0.35\ \mu$m and $r_e \approx 0.09\ \mu$m. Thus, using a generously large w_0 to obtain an upper bound on the Coulomb field, $w_0 \approx 10\ \mu\mathrm{m} \gg r_{ion}$ and $\gg r_e$, we see that the contribution due to ions $|E_{ion}| \approx |E_e|$, where $|E_e|$ is the contribution due to electrons. This is because the product of the number density and charge $n_p q$ is the same for ions and electrons, as the number density of ions is $n_{ion} = n_e/Z$ and the

charge on a fully stripped ion is $q_{ion} = Ze$. Therefore, assuming an absolute worst case scenario where the fields add to give $2|E_{ion}|$, we see

$$|E_{\text{Coul}}| < 4w_0 \frac{n_e e}{\epsilon_0} \approx 9.4 \times 10^8 \text{ V/m} \ll E_L. \tag{2.8}$$

Thus, the dynamics of the electrons are predominantly influenced by the laser field and collective effects may be ignored, i.e., $\vec{E} \approx \vec{E_L}$ and $\vec{B} \approx \vec{B_L}$ in Equation (2.4). Further, we note that for a typical petawatt-class laser with $\lambda_0 = 800$ nm and pulse energy $U \gtrsim 1$ J focused to a beam waist $w_0 \lesssim 10$ μm (resulting in Rayleigh length $z_R \gtrsim 393$ μm), even assuming that all electrons within a cylindrical volume of $10 z_R \pi w_0^2$ are unrealistically accelerated to 10 MeV, the total energy lost by the pulse is

$$U_{\text{Loss}} \lesssim n_e (10 z_R \pi w_0^2)(10 \text{ MeV}) \approx 2.6 \times 10^{-3} \text{ J} \ll U. \tag{2.9}$$

This implies that the laser pulse is not significantly influenced by the energy transferred to electrons generated from the focal volume in tenuous gas ($\lesssim 10^{-3}$ mbar).

Therefore, for the work presented in this dissertation, we treat the interaction between the electrons and the laser pulse as single particles solely influenced by an externally applied laser field that is independent of the positions of all the charged particles at any given time.

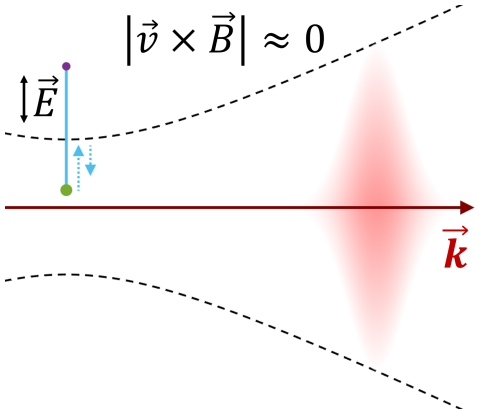


Figure 2.2: A cartoon showing the motion of an electron (purple dot) once liberated from the parent atom (green dot) at non-relativistic laser intensities.

2.3 Motion in Non-Relativistic Laser Fields

The equations of motion that describe the position $\vec{r}(t) = x(t)\hat{x}+y(t)\hat{y}+z(t)\hat{z}$ and velocity $\vec{v}(t) = v_x(t)\hat{x} + v_y(t)\hat{y} + v_z(t)\hat{z}$ of an electron for varying time following ionization are

$$\frac{\mathrm{d}\vec{r}(t)}{\mathrm{d}t} = \vec{v}(t), \tag{2.10}$$

$$m_e\frac{\mathrm{d}\vec{v}(t)}{\mathrm{d}t} = -e\left[\vec{E}\left(\vec{r}(t),t\right) + \vec{v}(t)\times\vec{B}\left(\vec{r}(t),t\right)\right]. \tag{2.11}$$

We know that for an electromagnetic wave propagating in vacuum, $E = B/c$, where $E = |\vec{E}|$, $B = |\vec{B}|$. As $\beta = v/c \ll 1$ in the non-relativistic intensity regime ($I_0 \ll 10^{18}$ W/cm^2 for optical photons), we can see that $|\vec{F}_E| \gg |\vec{F}_B|$. Therefore, the net force on the electron is $\approx \vec{F}_E$ and the electron predominantly moves along $\hat{E}$ $(= \vec{E}/E)$. For a focused laser field where I $(\propto E^2)$ decreases radially outward, this results in the expulsion of electrons perpendicular to the wave vector, $\vec{k}$, as shown in Figure 2.2.

2.4 Motion in Relativistic Laser Fields

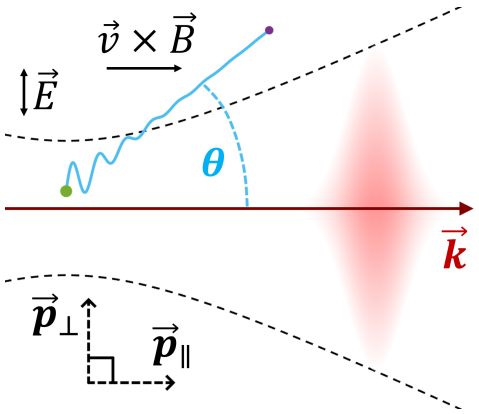


Figure 2.3: A cartoon showing the motion of an electron (purple dot) once liberated from the parent atom (green dot) at relativistic laser intensities.

In the relativistic regime, the equations of motion are written in the general form as follows

$$\frac{\mathrm{d}\vec{r}(t)}{\mathrm{d}t} = \frac{\vec{p}(t)}{\gamma(t)m_e}, \tag{2.12}$$

$$\frac{\mathrm{d}\vec{p}(t)}{\mathrm{d}t} = -e\left[\vec{E}\left(\vec{r}(t),t\right) + \frac{\vec{p}(t)}{\gamma(t)m_e} \times \vec{B}\left(\vec{r}(t),t\right)\right]. \tag{2.13}$$

where $\vec{p}(t) = \gamma(t)m_e\vec{v}(t)$ is the instantaneous momentum and $\gamma(t) = 1/\sqrt{1-(v(t)/c)^2}$ is the instantaneous Lorentz factor of the electron. An electron is considered relativistic once its kinetic energy, $(\gamma(t)-1)m_ec^2$, is comparable to or exceeds its rest mass energy, m_ec^2. Electrons in a laser field are accelerated to relativistic energies when the normalized vector potential of the laser, defined as

$$a_0 = \frac{eE\lambda_0}{2\pi m_e c^2} \approx 0.855\lambda_0(\mu\text{m})\sqrt{I_0(\text{W/cm}^2)/10^{18}}, \tag{2.14}$$

exceeds 1. Here, λ_0 is the central wavelength of the laser. For lasers with the commonly used Ti:Sa crystal as the gain medium, $\lambda_0 = 0.8\ \mu\text{m}$. Thus, the relativistic intensity regime may be defined as $I \gtrsim 2.14 \times 10^{18}\ \text{W/cm}^2$ for a Ti:Sa laser. At these intensities, $\beta \to 1$. Therefore, $|\vec{F}_B|$ becomes comparable to $|\vec{F}_E|$. This results in the electrons gaining momentum along $\vec{k}$ due to the $\vec{v} \times \vec{B}$ term in Equation (2.4). For a focused laser field with an intensity gradient predominantly in the radially outward direction, this implies that relativistic electrons are expelled from the laser focus at an acute angle, θ, relative to $\vec{k}$, as shown in Figure 2.3, where θ is a function of their steady-state kinetic energy, $(\gamma_f - 1)m_e c^2$, and $\gamma_f = \gamma(t \to \infty)$.

Although it is complicated to establish an explicit relationship between a_0, γ_f and θ for an arbitrary ultrashort laser pulse, we can derive analytical relationships under the paraxial approximation. For simplicity, we consider a Gaussian spatial profile and approximate the field near the peak as a plane wave to employ the plane-wave model [129] for linearly polarized light with

$$\vec{E} = -\frac{\partial \vec{A}}{\partial t} = E_0 \cos(\omega_0 t - kz)\hat{x}, \tag{2.15}$$

$$\vec{B} = \vec{\nabla} \times \vec{A} = \frac{E_0}{c} \cos(\omega_0 t - kz)\hat{y}, \tag{2.16}$$

where $\omega_0 = ck$, $k = 2\pi/\lambda_0$ and the corresponding vector potential is given by

$$\vec{A} = A_x\hat{x} = -\frac{E_0}{\omega_0}\sin(\omega_0 t - kz)\hat{x}. \tag{2.17}$$

We note that for a particle in a plane wave, the transverse Canonical momentum, $P_x = p_x(t) + eA_x(z,t)$, and $\gamma(t) - p_z(t)/(m_e c)$ are conserved in the laboratory frame. Recognizing that electrons of interest are generated at some instant t_i in the focal volume with $\gamma(t = t_i) \approx 1 \ll \gamma_f$, we can write $P_x \approx 0$ and $p_z(t = t_i) \approx 0$. This implies $p_x(t) = -eA_x$ and $\gamma(t) - p_z(t)/(m_e c) = 1$. Therefore, using Equations (2.14) and (2.17), we can approximate the transverse and longitudinal momentum components of an electron in the vicinity of the peak field as

$$p_x(t) = m_e c a_0 \sin(\omega_0 t - kz), \tag{2.18}$$

$$p_z(t) = m_e c\left(\gamma(t) - 1\right). \tag{2.19}$$

Using the definition of $\gamma(t)$ and noting that $p_y = 0$ in a plane wave, we can write

$$\gamma(t) = \sqrt{1 + \left(\frac{|\vec{p}(t)|}{m_e c}\right)^2}, \tag{2.20}$$

$$= \sqrt{1 + (\gamma(t) - 1)^2 + a_0^2 \sin^2(\omega_0 t - kz)}, \tag{2.21}$$

$$\implies \gamma(t) = 1 + \frac{a_0^2}{2}\sin^2(\omega_0 t - kz). \tag{2.22}$$

Combining Equation (2.22) with Equations (2.18) and (2.19), we can thus obtain the ejection

angle of an electron relative to $\vec{k}$ in the paraxial regime as [130]

$$\tan\theta = \frac{p_\perp}{p_\parallel} = \sqrt{\frac{2}{\gamma_f - 1}}, \tag{2.23}$$

where $p_\perp$ and $p_\parallel$ are the transverse and longitudinal momentum components of the electron as $t \to \infty$, which correspond to $p_x(t \to \infty)$ and $p_z(t \to \infty)$, respectively, in this situation. Equation (2.23) implies that electrons with a higher final energy, or γ_f, are ejected at smaller θ. In three-dimensional space, the electrons are ejected along a cone with apex angle θ with $\vec{k}$ as the axis, due to the presence of longitudinal field components for a focused laser beam. For an ideal Gaussian, theoretical studies predict a uniform and symmetric distribution of electrons along the cone of ejection [131], which produces a ring-like pattern when projected on a plane perpendicular to $\vec{k}$.

In addition, Equation (2.22) gives us a first-order approximation of $\gamma(t)$ in terms of a_0 in the vicinity of the peak field in a focused Gaussian beam. This implies that the maximum possible γ_f with which electrons can be ejected is

$$\gamma_{max} = 1 + \frac{a_0^2}{2}. \tag{2.24}$$

Alternatively, we can also make a heuristic argument that the most energetic electrons generated from this interaction may lose some fraction of their energy while traversing regions of lower intensities as they drift outward from the peak field in the focal volume. In that vein, we can take

the cycle-averaged value of Equation (2.22), which gives us

$$\gamma_{RMS} = 1 + \frac{a_0^2}{4}. \tag{2.25}$$

Therefore, in general, we can assume that the most energetic electrons have some $\gamma_f = \gamma_p$ of the form

$$\gamma_p = 1 + \frac{1}{2}\left(\frac{a_0}{\eta}\right)^2. \tag{2.26}$$

This allows us to write the ejection angle of the most energetic electrons obtained from this interaction explicitly in terms of a_0 as

$$\tan\theta_c = \frac{2\eta}{a_0}, \tag{2.27}$$

where θ_c is defined as the characteristic ejection cutoff angle. This implies that as a_0 increases, electrons are accelerated to higher energies, and thus ejected at smaller θ. Although there exist longitudinal components in a focused laser pulse, the relative strength of the longitudinal to the transverse component goes as $\approx 1/(kw_0)$ [132]. Therefore, the plane-wave model may be used as a first-order approximation to a paraxial beam where $1/(kw_0)$ is small. In the following chapters, we provide details of simulations and experiments that we performed to test the relationships between a_0, γ_f and θ under various conditions.

Chapter 3: Simulating Electron Trajectories in the Single-Particle Regime

In this chapter, we present our methods to model the interaction between the laser pulse and electrons liberated from rarefied gas within the focal volume. As a first-order approach to understand electron dynamics with a simplistic field, we employ a Gaussian beam with a Gaussian temporal profile, unless specified otherwise. The laser pulse is therefore characterized by beam parameters such as central wavelength λ_0, angular frequency $\omega_0 = 2\pi c/\lambda_0$, beam waist w_0, Rayleigh length $z_R = \pi w_0^2/\lambda_0$, and full width at half maximum pulse duration τ. We first provide an outline that summarizes the processes involved, followed by details such as the field equations used, our approach to incorporate multiple laser beams, and optimization procedures for critical simulation parameters.

3.1 Outline

The objective of our simulation is to calculate $\vec{r}(t)$ and $\vec{p}(t)$ of electrons under the influence of a focused laser field for varying time, t, starting from their time of birth until they reach steady state. We achieve this through a two-step process: (1) particle initialization and ionization, followed by (2) solving the equations of motion, as detailed below. We ignore radiation reaction and collective effects between charged particles, which are negligible for the interaction studied herein.

3.1.1 Particle Initialization and Ionization

We begin with a uniformly random population of particles, each with some initial position (x_i, y_i, z_i), in a cuboid such that

$$-\alpha_{xy} w_0 < x_i < +\alpha_{xy} w_0, \tag{3.1}$$

$$-\alpha_{xy} w_0 < y_i < +\alpha_{xy} w_0, \tag{3.2}$$

$$-\alpha_z z_R < z_i < +\alpha_z z_R, \tag{3.3}$$

for a laser pulse propagating along the z-axis. We use scaling factors $\alpha_{xy} \in (0, \infty)$ and $\alpha_z \in (0, \infty)$ along the transverse and longitudinal axes, respectively, to vary the size of the initial box of particles in characteristic length scales of w_0 and z_R. This is so that for a given a_0, fixing α_{xy} and α_z keeps the fractional intensities sampled within the focal volume the same under varying w_0. This allows us to sample various laser intensities proportionally in the focal volume when comparing simulations under different focusing conditions. The number of particles, N_p, contained within the box defined by Conditions (3.1)–(3.3) is thus determined by the desired gas pressure P using the ideal gas law as

$$N_p = \frac{8\alpha_{xy}\alpha_z w_0^2 z_R P}{k_B T} \approx \frac{7.58 \times 10^5}{\lambda_0(\mu\mathrm{m})} \alpha_{xy}\alpha_z w_0^4(\mu\mathrm{m}^4) P(\mathrm{mbar}). \tag{3.4}$$

at room temperature of $T = 300$ K, where k_B is the Boltzmann constant. We note that due to

the absence of collective effects in this interaction, and thus our modeling approach, the pressure may be set to arbitrarily high values for increased sampling. This does not affect the physics involved in this computational approach. For example, a single simulation with $P = 10$ mbar will effectively yield the same statistical result as 10^6 simulations with $P = 10^{-5}$ mbar if all other parameters are fixed. In addition, these particles that give rise to electrons remain stationary for the entirety of these simulations as the motion of neutral atoms and ions is negligible over durations $\ll 1$ ns for laser intensities $\ll 10^{24}$ W/cm^2, as is the case here. Further, while it is straightforward to model a heterogeneous gaseous mixture by adding particles that ionize at different intensities using the above approach for various partial pressures, we assume a fixed atomic species for all particles for simplicity.

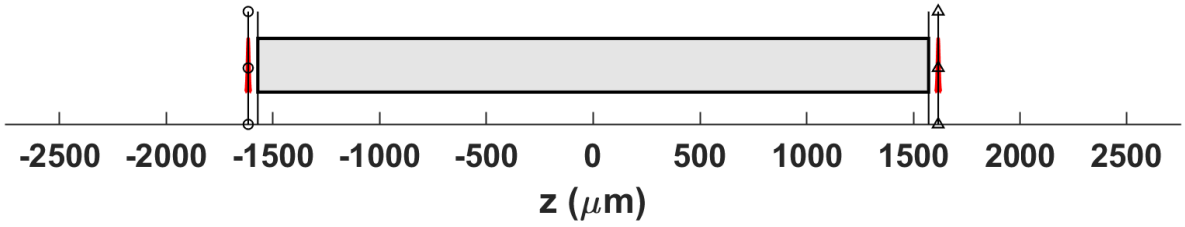
We now evaluate the time of birth, t_i, of each electron that can be ionized from each stationary atom. We provide I_{th} assuming BSI for all ionization stages of several species of interest in Appendix A. To determine t_i for each electron, we parse the laser pulse through the box of atoms from a start to stop time of

$$t_{ion,start} = -\frac{\alpha_z z_R}{c} - 5\tau, \tag{3.5}$$

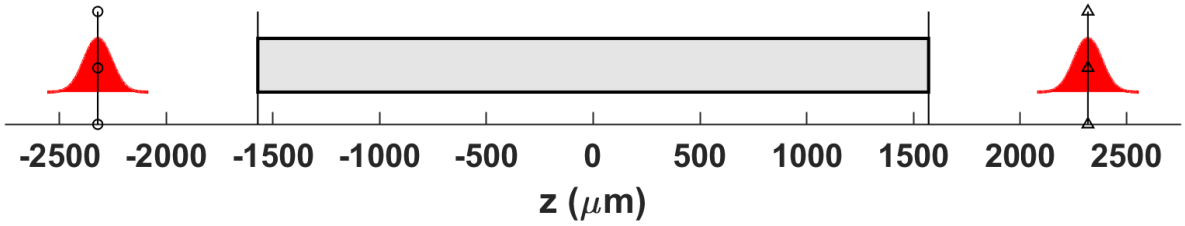
$$t_{ion,stop} = +\frac{\alpha_z z_R}{c} + 5\tau, \tag{3.6}$$

respectively, with a time resolution of

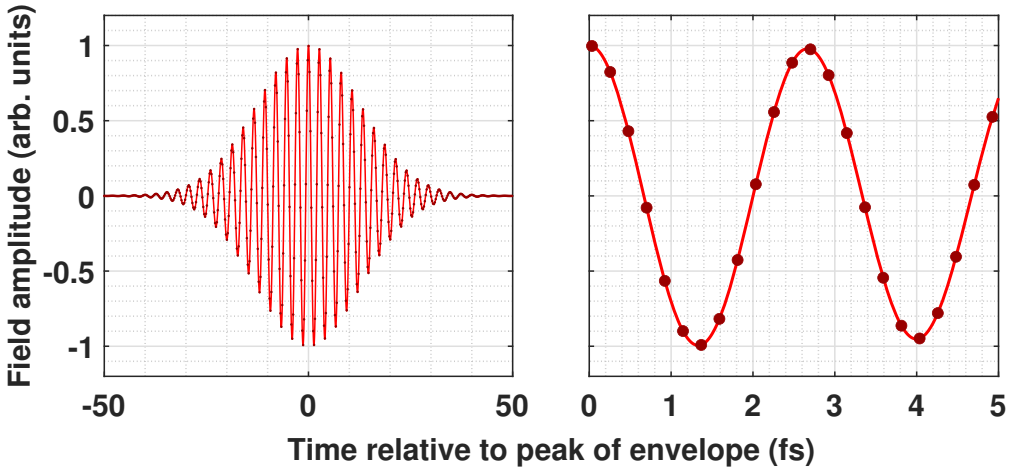
$$t_{ion,step} = \frac{1}{12}\left(\frac{2\pi}{\omega_0}\right). \tag{3.7}$$



(a)



(b)



(c)

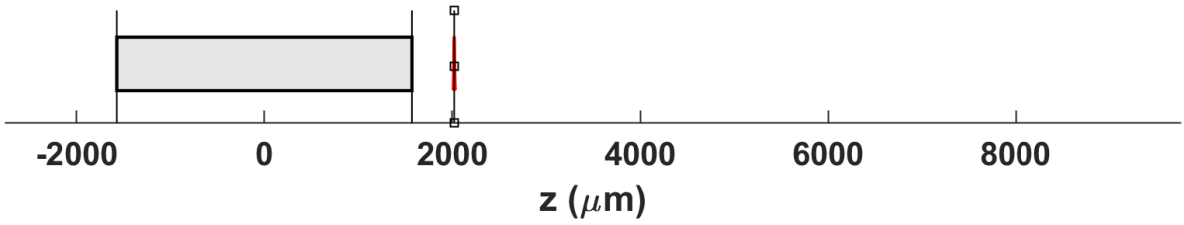
Figure 3.1: Demonstration of the time scale used for ionization with a $\lambda_0 = 800$ nm laser pulse. Timing sequence (see Eqs. (3.5) and (3.6)) for ionization with $w_0 = 10$ μm, $\alpha_z = 4$ is shown using (a) $\tau = 30$ fs and (b) $\tau = 500$ fs. Vertical lines with no markers represent the boundaries of the box, $z = \pm\alpha_z z_R$. Vertical lines with circle and triangle markers represent the position of the pulse at $t = t_{ion,start}$ and $t = t_{ion,stop}$, respectively. Time resolution (see Eq. (3.7)) for ionization is represented using $\tau = 30$ fs in (c), where the red line and dark red circles represent the continuous field and the samples used when stepping through the pulse during ionization, respectively.

This allows us to sample the field at every one-twelfth an oscillation, while starting and stopping the ionization process with the laser pulse sufficiently far from the box to avoid an abrupt turn on or turn off of ionization. We chose to displace the laser pulse by $5c\tau$ from the ends of the box for this purpose as $I(|t| = \alpha_z z_R/c + 5\tau) \approx 10^{-30} I(|t| = \alpha_z z_R) \approx 0$. Figure 3.1 provides a graphic representation of Equations (3.5)–(3.7). We note that $t_{ion,step}$ is used only to evaluate t_i with reasonable precision and that it is not the time step used to solve the equations of motion. We evaluate the field for all (x_i, y_i, z_i) at each time step to find the earliest instant when the intensity at that location exceeds the barrier for a specific ionization stage of the atom. Specifically, each atom at some position (x_i, y_i, z_i) creates an electron at the same location at the earliest instant $t = t_i$ when

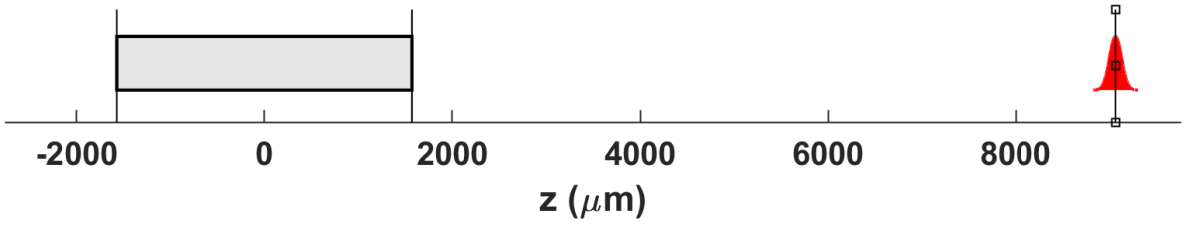
$$I(x_i, y_i, z_i, t_i) \geq \delta_I I_{th}, \tag{3.8}$$

where δ_I is a random number $\in (0.5, 2.0)$ used to smooth the onset of ionization. We employed this simplistic approach to avoid introducing phase-dependent artifacts during ionization, as petawatt-class laser systems typically do not have a fixed carrier-envelope phase, while circumventing the need for sophisticated ionization models. This results in a number of electrons $N_e \leq N_p N_{th}$ for a gas species with a maximum attainable ionization stage of N_{th} in a given simulation. We set the initial momenta of the electrons $p_{x,i} = p_{y,i} = p_{z,i} = 0$ as they are born with non-relativistic kinetic energies that are negligible relative to their final kinetic energies.

3.1.2 Solving Equations of Motion



(a)



(b)

Figure 3.2: Location of a $\lambda_0 = 800$ nm, $w_0 = 10$ μm laser pulse along the axis of propagation at $t = t_{end}$ (see Eq. (3.11)) is shown with $\alpha_z = 4$, $\alpha_t = 50$ for (a) $\tau = 30$ fs and (b) $\tau = 500$ fs, represented by the vertical line with square markers. Vertical lines with no markers represent the boundaries of the box, $z = \pm\alpha_z z_R$.

Once we have $(\vec{r}_i, \vec{p}_i, t_i)$ for each electron, we numerically solve the Lorentz force equation in three dimensions to find $\vec{r}(t)$ and $\vec{p}(t)$. For an electron in a laser field with electric and magnetic fields $\vec{E}_L$ and $\vec{B}_L$, respectively, the relativistic equations of motion may be written explicitly in terms of $\vec{r}(t)$ and $\vec{p}(t)$ as

$$\frac{\mathrm{d}\vec{r}(t)}{\mathrm{d}t} = \frac{c\vec{p}(t)}{\sqrt{|\vec{p}(t)|^2 + m_e^2 c^2}}, \tag{3.9}$$

$$\frac{\mathrm{d}\vec{p}(t)}{\mathrm{d}t} = -e\left[\vec{E}_L\left(\vec{r}(t), t\right) + \frac{c\vec{p}(t) \times \vec{B}_L\left(\vec{r}(t), t\right)}{\sqrt{|\vec{p}(t)|^2 + m_e^2 c^2}}\right]. \tag{3.10}$$

Equations (3.9) and (3.10) represent a system of six coupled ordinary differential equations (ODE). We compute $\vec{r}(t)$ and $\vec{p}(t)$ using a native ODE solver in MATLAB® known as ode45 [133] that is based on an explicit Runge-Kutta (4,5) algorithm [134, 135] with a variable time step (see Appendix B for more details). We note that the electrons, once born, are not confined to the initial box of particles and may thus travel to any point in space as governed by Equations (3.9) and (3.10) until some desired end time

$$t_{end} = +\frac{\alpha_z z_R}{c} + \alpha_t \tau, \tag{3.11}$$

where $\alpha_t \gtrsim 50\tau$ to allow sufficient time for the electrons born at the end of the box ($+\alpha_z z_R$) to reach steady state. This gives us $\vec{r}_f = \vec{r}(t = t_{end}) = x_f\hat{x} + y_f\hat{y} + z_f\hat{z}$ and $\vec{p}_f = \vec{p}(t = t_{end}) = p_{x,f}\hat{x} + p_{y,f}\hat{y} + p_{z,f}\hat{z}$. We can then obtain steady state values of observables of interest as

$$\theta = \tan^{-1}\left(\frac{\sqrt{p_{x,f}^2 + p_{y,f}^2}}{p_{z,f}}\right), \tag{3.12}$$

$$\gamma_f = \sqrt{1 + \frac{p_{x,f}^2 + p_{y,f}^2 + p_{z,f}^2}{m_e^2 c^2}}. \tag{3.13}$$

3.2 Field Equations

We use the description of field components prescribed in [132, 136], which we consider a good fit for modeling paraxial beams [137]. For reference, the spatial and temporal profiles of a Gaussian beam, i.e., Laguerre-Gauss $l = 0,\ p = 0$ mode, traveling along $\hat{z}$ are given by

$$\psi_{p=0}^{l=0}(x,y,z) = \frac{w_0}{w(z)} \exp\left[-\frac{k(x^2+y^2)}{2\mathcal{Z}}\right] \exp\left(-i \tan^{-1}\frac{z}{z_R}\right), \tag{3.14}$$

$$f(t) = \exp\left[-\frac{2\ln(2)\,(kz-\omega_0 t)^2}{\omega_0^2 \tau^2}\right] \exp[i(kz-\omega_0 t)], \tag{3.15}$$

respectively, where $w(z) = w_0\sqrt{1+z^2/z_R^2}$ is the beam radius and $\mathcal{Z} = z_R + iz$ is the complex beam parameter. The field components are then given by

$$\vec{E}_L(x,y,z,t) = E_0\left[\hat{x} + \frac{xy}{2\mathcal{Z}^2}\,\hat{y} - i\,\frac{x}{\mathcal{Z}}\,\hat{z}\right] \psi_p^l(x,y,z)\, f(t), \tag{3.16}$$

$$\vec{B}_L(x,y,z,t) = \frac{E_0}{c}\left[\frac{xy}{2\mathcal{Z}^2}\,\hat{x} + \hat{y} - i\,\frac{y}{\mathcal{Z}}\,\hat{z}\right] \psi_p^l(x,y,z)\, f(t). \tag{3.17}$$

3.3 Simulating Multiple Laser Pulses

To incorporate multiple laser pulses, we use the superposition principle and simply replace $\vec{E}_L$ and $\vec{B}_L$ in Equation (3.10) with the total electric and magnetic fields due to N_L number of pulses given by $\vec{E}_{tot} = \sum_{j=1}^{N_L} \vec{E}_{Lj}$ and $\vec{B}_{tot} = \sum_{j=1}^{N_L} \vec{B}_{Lj}$, respectively, where $\vec{E}_{Lj}$ and $\vec{B}_{Lj}$ are the electric and magnetic fields of each laser pulse. While it is straightforward to incorporate different beam geometries with the help of three-dimensional rotation matrices, we consider here a special case that is relevant for Section 5.3, which involves two copropagating laser pulses with a relative time delay, Δt.

When using multiple laser pulses, it is critical to ensure that the first (last) pulse to enter (exit) the box of atoms is sufficiently far from the box at the beginning (end) of ionization to

prevent an abrupt turn on (off) of a pulse inside the box. For two pulses copropagating along $\hat{z}$ with the form $\vec{E}_{L1} \propto f(t)$ and $\vec{E}_{L2} \propto f(t + \Delta t)$, and pulse durations τ_1 and τ_2, the position of their temporal center at some time t is given as

$$z_1 = ct, \tag{3.18}$$

$$z_2 = c(t + \Delta t), \tag{3.19}$$

respectively. Therefore, pulse 2 leads pulse 1 when $\Delta t > 0$, and vice versa. Using this, we can evaluate the time at which either pulse is $5c\tau_j$ behind the box as

$$t_1 = -\frac{\alpha_z z_R}{c} - 5\tau_1, \tag{3.20}$$

$$t_2 = -\frac{\alpha_z z_R}{c} - 5\tau_2 - \Delta t, \tag{3.21}$$

respectively. Therefore, we start ionization at

$$t_{ion,start} = -\frac{\alpha_z z_R}{c} - \max(5\tau_1,\ 5\tau_2 + \Delta t). \tag{3.22}$$

Repeating this exercise to evaluate the time at which either pulse is $5c\tau_j$ and $\alpha_t c\tau$ past the box, we get

$$t_{ion,stop} = +\frac{\alpha_z z_R}{c} + \max(5\tau_1,\ 5\tau_2 - \Delta t), \tag{3.23}$$

$$t_{end} = +\frac{\alpha_z z_R}{c} + \max(\alpha_t\tau_1,\ \alpha_t\tau_2 - \Delta t), \tag{3.24}$$

respectively. It is possible to extend this for arbitrary beam geometries by modifying Equations (3.18) and (3.19) to account for each beam traveling along some unit vector in three-dimensional space. However, this is not required for our special case that is relevant for Section 5.3 where we also have $\tau_1 \approx \tau_2 = \tau$, which further simplifies Equations (3.22)–(3.24) as

$$\Delta t_{ion,start} = \begin{cases} -\frac{\alpha_z z_R}{c} - 5\tau & \text{if } \Delta t \leq 0 \\ -\frac{\alpha_z z_R}{c} - 5\tau - \Delta t & \text{if } \Delta t > 0 \end{cases}, \tag{3.25}$$

$$\Delta t_{ion,stop} = \begin{cases} +\frac{\alpha_z z_R}{c} + 5\tau - \Delta t & \text{if } \Delta t < 0 \\ +\frac{\alpha_z z_R}{c} + 5\tau & \text{if } \Delta t \geq 0 \end{cases}, \tag{3.26}$$

$$\Delta t_{end} = \begin{cases} +\frac{\alpha_z z_R}{c} + \alpha_t\tau - \Delta t & \text{if } \Delta t < 0 \\ +\frac{\alpha_z z_R}{c} + \alpha_t\tau & \text{if } \Delta t \geq 0 \end{cases}. \tag{3.27}$$

Figure 3.3 shows the timing sequence for two copropagating pulses with $\tau_1 = \tau_2 = 40$ fs and $\Delta t = +300$ fs.

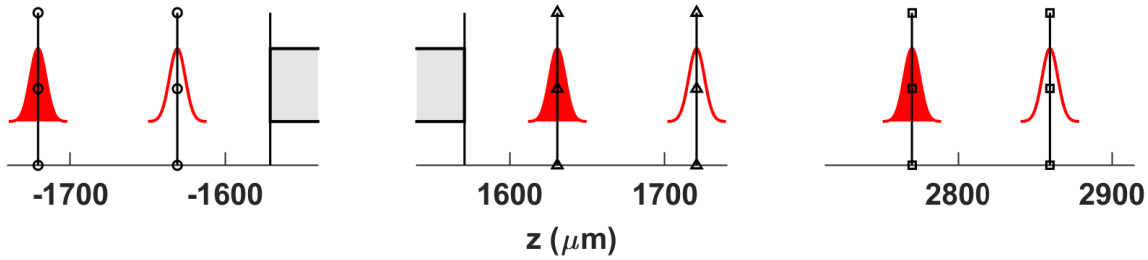


Figure 3.3: Timing sequence (see Eqs. (3.25)–(3.27)) used for two copropagating pulses with $\lambda_{01} = \lambda_{02} = 800\ \mu$m, $\tau_1 = \tau_2 = 40$ fs, $w_0 = 10\ \mu$m, $\alpha_z = 4$ and $\Delta t = +300$ fs. Pulse 1 (Pulse 2) is represented by the shaded (unshaded) gaussian envelope. Vertical lines with no markers represent the boundaries of the box, $z = \pm\alpha_z z_R$. Vertical lines with circle, triangle and square markers represent the position of the pulse at $t = t_{ion,start}$, $t = t_{ion,stop}$ and $t = t_{end}$, respectively.

3.4 Parameter Optimization

A major requirement to obtain useful information from this computational model is to achieve sufficient sampling of the region of interest within the focal volume using finite computational resources. It is therefore important to identify the optimal range for the computational parameters related to the size of the initial box, namely, α_{xy} and α_z in Conditions (3.1)–(3.3), and the time at which the program is terminated, namely, α_t in Equation (3.11). Below, we discuss how we obtain the minimum values of these parameters required to accurately model the interaction, and thus maximize computational efficiency.

3.4.1 Size of Initial Box of Atoms

For a Gaussian beam (Eq. (3.14)) with peak intensity I_0, it is straightforward to plot the boundaries that enclose $I(x, y, z) > I_{th}$. We show this in Figure 3.4 for $I_{th} = 10^{-9} I_0$, $10^{-6} I_0$, $10^{-3} I_0$, $10^{-1} I_0$ in normalized units of w_0 and z_R along the transverse and longitudinal direction, respectively. For a laser pulse with $I_0 \sim 10^{22}$ W/cm^2, it is thus impractical, and often extraneous,

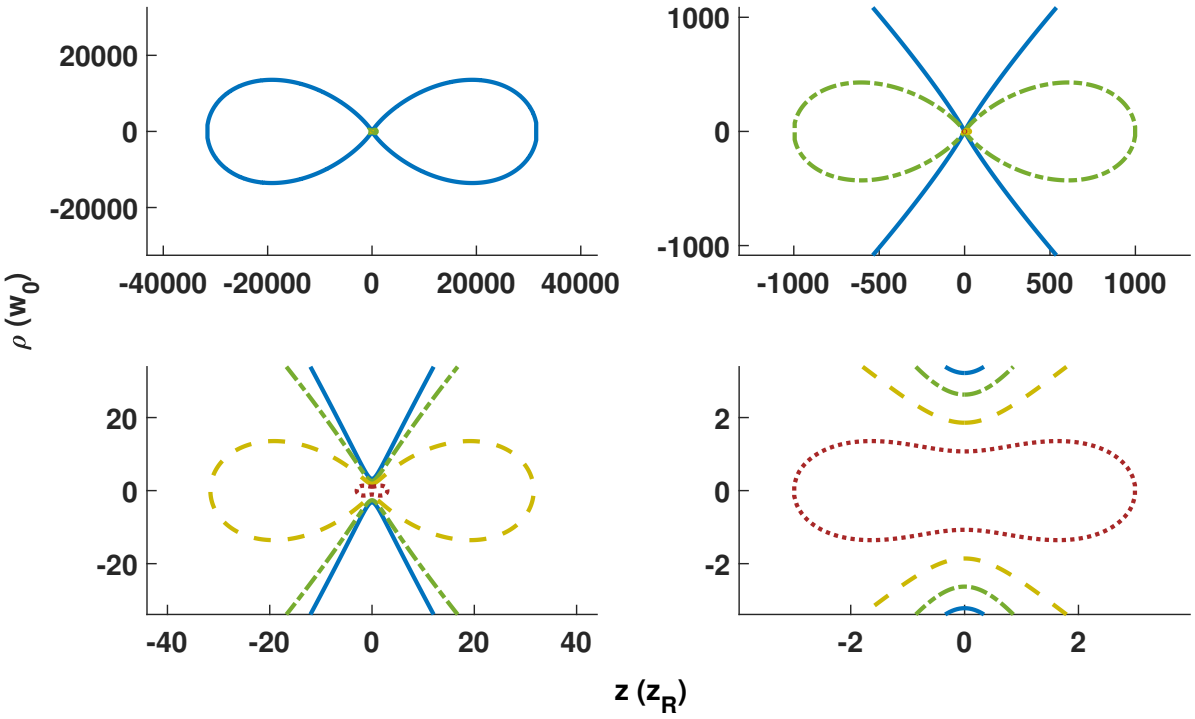


Figure 3.4: Intensity contours of a Gaussian beam shown in normalized units for $I_{th} = 10^{-9}I_0$, $10^{-6}I_0$, $10^{-3}I_0$, $10^{-1}I_0$ by the blue solid, green dash-dotted, dark-yellow dashed and maroon dotted lines, respectively.

to simulate the entire volume over which the lower ionization stages such as Ar^{1+} ($I_{th} \approx 2.5 \times 10^{-8} I_0$) or Xe^{1+} ($I_{th} \approx 9 \times 10^{-9} I_0$) are generated. Instead, the minimum size of the initial box of atoms required for efficient sampling must be evaluated based on the range of θ and γ_f that is of interest for a given study.

We achieve this through an iterative process prior to executing simulations of a nominal pressure. We start by performing our simulation for an arbitrary box size of sub-nominal pressure with all other parameters set to desired values. Then, we plot the initial positions of all electrons of interest to identify whether the boundaries of the box artificially clip the initial distribution of electrons. If this is true, we use larger α_{xy} and/or α_z as required to enclose the full initial distribution of the electrons of interest. For example, we see in Figure 3.5 that $\alpha_{xy} \leq 2$ and $\alpha_z \leq 2$ are insufficient to model electrons ejected at $\theta \leq 50^\circ$ with $\gamma_f - 1 \geq 1$ by a pulse with $I_0 = 5 \times 10^{20}$ W/cm^2. We can also employ this approach in the converse scenario to reduce α_{xy} and/or α_z and thus improve sampling efficiency when the box size is significantly larger than required.

3.4.2 Terminating the Program

To determine an appropriate value of t_{end} for an electron born at $z = z_i$ we can evaluate when the intensity that the electron experiences at $t = t_{end}$ becomes negligible relative to the peak intensity at the focus, i.e.,

$$\frac{I_e(z_i, t_{end})}{I_0} \ll 1. \tag{3.28}$$

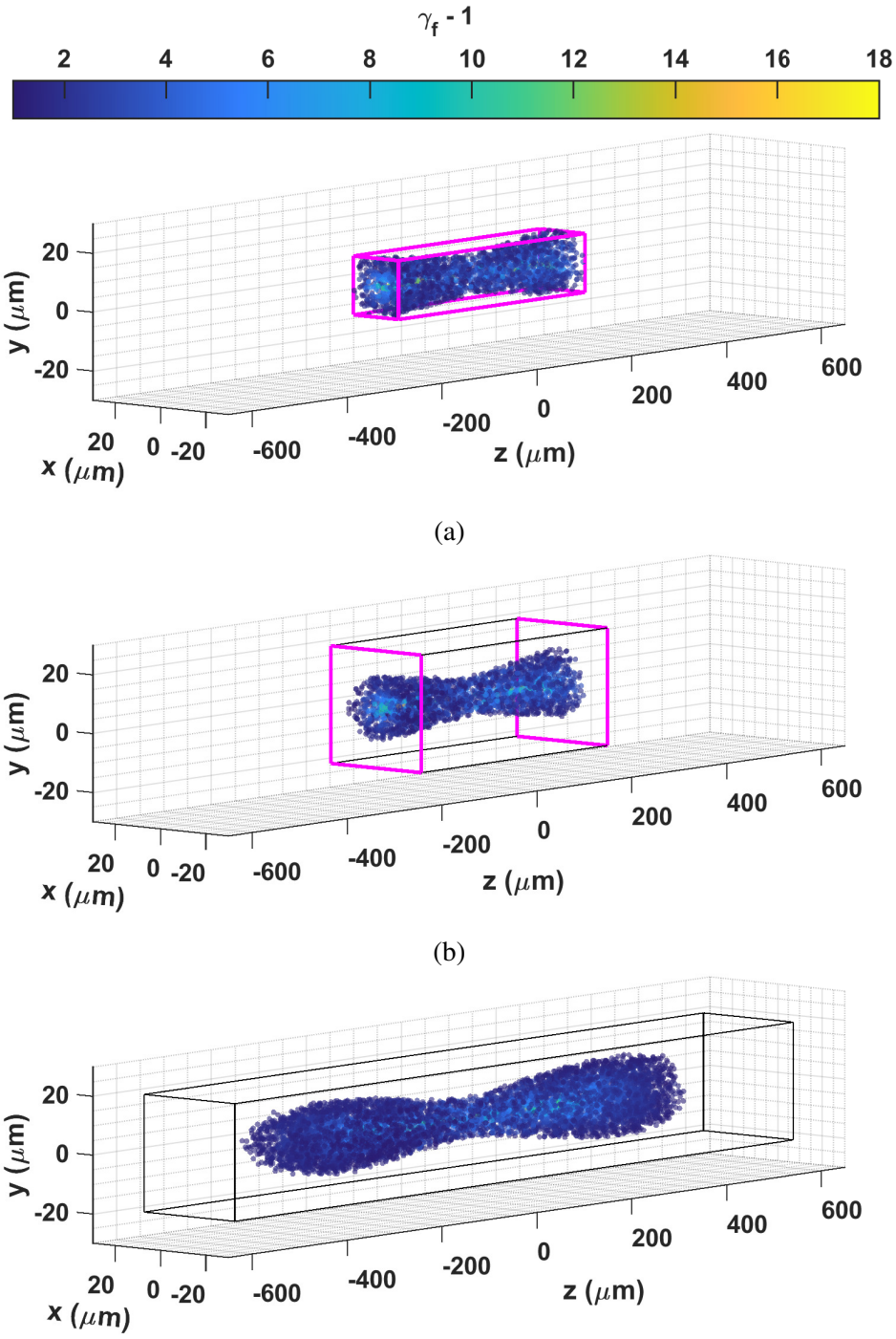


Figure 3.5: Initial positions of electrons ejected at $\theta \leq 50^\circ$ with $\gamma_f - 1 \geq 1$ from a variably-sized initial box (see Conditions (3.1)–(3.3)) containing Ar atoms with (a) $\alpha_{xy} = 2$, $\alpha_z = 2$, (b) $\alpha_{xy} = 4$, $\alpha_z = 2$, and (c) $\alpha_{xy} = 4$, $\alpha_z = 6$. Simulations performed with $I_0 = 5 \times 10^{20}$ W/cm^2, $w_0 = 5$ μm, $P = 10^{-6}$ mbar. Color bar represents $\gamma_f - 1$. Thick magenta (thin black) edges of the box represent faces that clip (do not clip) the distribution of electrons of interest.

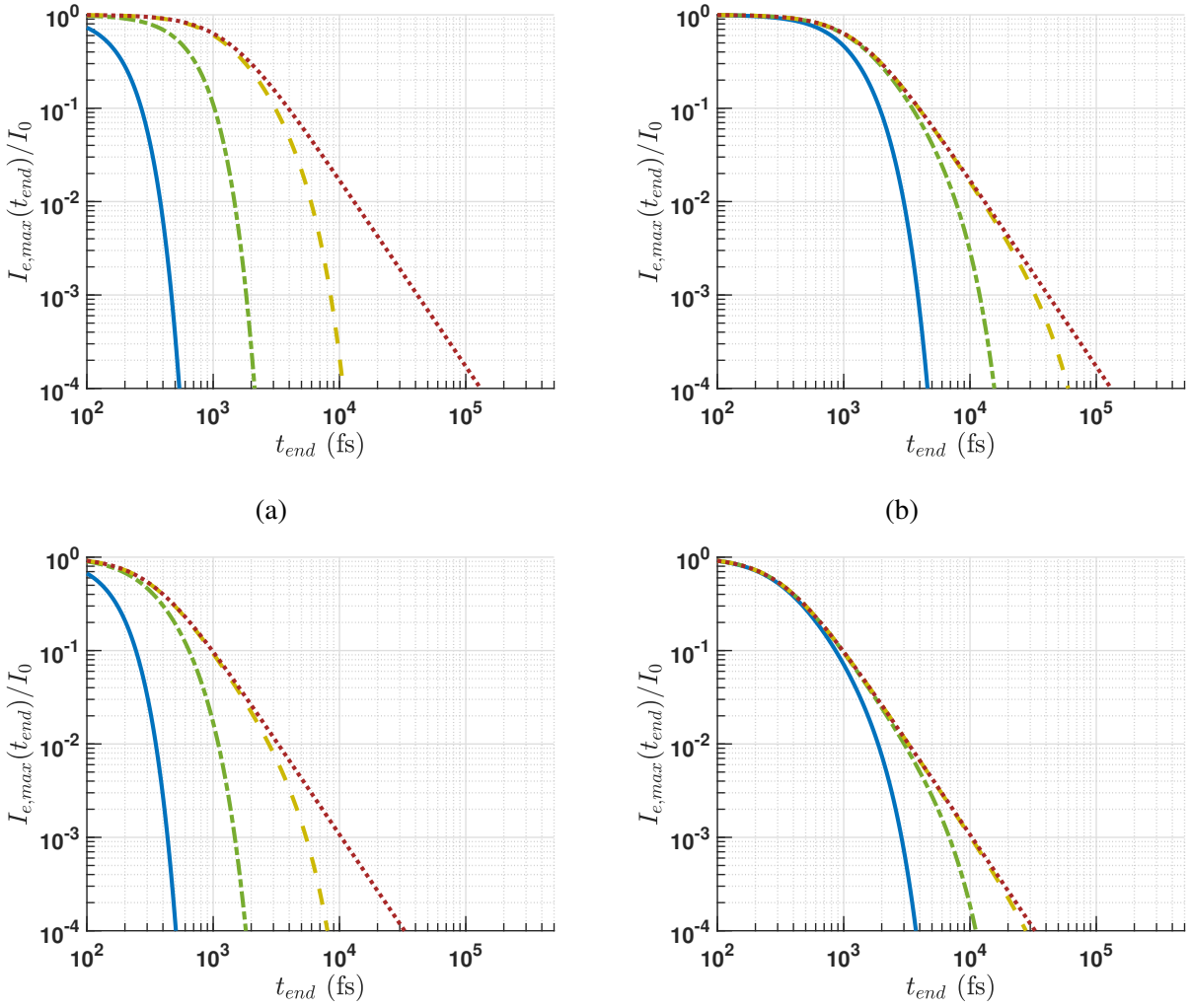


Figure 3.6: Maximum possible fraction of the peak intensity that an electron born at $z = 0$ can experience at some $t = t_{end}$ when (a) $w_0 = 10\ \mu$m and $\tau = 40$ fs, (b) $w_0 = 10\ \mu$m and $\tau = 400$ fs, (c) $w_0 = 5\ \mu$m and $\tau = 40$ fs, and (d) $w_0 = 5\ \mu$m and $\tau = 400$ fs. The blue solid, green dash-dotted, dark-yellow dashed and maroon dotted lines represent $\gamma_f = 2$, 4, 10, 500, respectively.

It is straightforward to calculate an upper bound for $I_e(z_i, t_{end}) \leq I_{e,max}(z_i, t_{end})$ as follows. For simplicity, we assume that the electron is born at $x_i = y_i = 0$ with $\gamma_f = 1/\sqrt{1 - v_f^2/c^2}$ and drifts along the direction of laser propagation. The position of the laser pulse and such an electron at $t = t_{end}$ is given by

$$z_L = ct_{end}, \tag{3.29}$$

$$z_e = z_i + v_f \left(t_{end} - \frac{z_i}{c} \right), \tag{3.30}$$

This gives the spatial separation between the electron and the laser pulse as

$$\Delta z_{L,e} = c \left(1 - \frac{v_f}{c} \right) \left(t_{end} - \frac{z_i}{c} \right) \tag{3.31}$$

$$= c \left(1 - \sqrt{1 - \frac{1}{\gamma_f^2}} \right) \left(t_{end} - \frac{z_i}{c} \right). \tag{3.32}$$

We note that the maximum intensity of a Gaussian laser pulse at $z = ct_{end}$ (using Eq. (3.14)) is

$$I(z = ct_{end}) = \frac{I_0}{1 + \left(\frac{ct_{end}}{z_R} \right)^2}. \tag{3.33}$$

Therefore, by accounting for the temporal lag of the electron from the peak, $\Delta t_{L,e} = \Delta z_{L,e}/c$, and using Equations (3.15), (3.32) and (3.33), we get

$$\frac{I_{e,max}(z_i, t_{end})}{I_0} = \frac{I(z = ct_{end})}{I_0} \exp \left[-\frac{4 \ln(2) (\Delta t_{e,L})^2}{\tau^2} \right] \tag{3.34}$$

$$= \frac{\exp \left[-\frac{4 \ln(2)}{\tau^2} \left(1 - \sqrt{1 - \frac{1}{\gamma_f^2}} \right)^2 \left(t_{end} - \frac{z_i}{c} \right)^2 \right]}{1 + \left(\frac{c}{z_R} t_{end} \right)^2}. \tag{3.35}$$

As the most energetic electrons of interest are typically born near $z = 0$, we show $I_{e,max}(0, t_{end})$ in Figure 3.6. This allows us to determine a suitable t_{end} and thus α_t (see Eq. (3.11)) for our simulations depending on the required value of the ratio $I_{e,max}(z_i, t_{end})/I_0$ and the approximate range of γ_f for the electrons of interest.

Chapter 4: Electron Dynamics Under Various Conditions

Portions of this chapter are adapted from:

- S. Ravichandran, M. Huault, R. Lera, C. Z. He, A. Longman, R. Fedosejevs, L. Roso, and W. T. Hill. "Imaging electron angular distributions to assess a full-power petawatt-class laser focus". *Physical Review A* 108.5 (Nov. 2023), p. 053101. *Copyright 2023 by the American Physical Society.*
- A. Longman, S. Ravichandran, L. Manzo, C. Z.He, R. Lera, N. McLane, M. Huault, G. Tiscareno, D. Hanggi, P. Spingola, N. Czapla, R. L. Daskalova, L. Roso, R. Fedosejevs, and W. T. Hill III. "Toward direct spatial and intensity characterization of ultrahigh-intensity laser pulses using ponderomotive scattering of free electrons". *Physics of Plasmas* 30.8 (Aug. 2023), p. 082110, *with the permission of AIP Publishing.*
- A. E. Raymond, S. Ravichandran, S.-W. Bahk, A. Longman, L. Roso, R. Fedosejevs, C. Mileham, I. A. Begishev, S. Qin, N. Dauphin, J. Shamlian, W. T. Hill III, and H. G. Rinderknecht. "Laser aberration signatures in expelled electrons from a tenuous gas". *Physics of Plasmas* 32.6 (June 2025), p. 062101, *with the permission of AIP Publishing.*

In this chapter, we present our investigation of the distribution of ejected electrons under varying conditions in the laser focus through simulation and experiment. Sections 4.1, 4.2 and 4.3 elucidate how the peak laser intensity, pulse duration and focusing conditions, respectively, affect electron dynamics. We then briefly discuss features of electron dynamics at intensities beyond 10^{22} $\mathrm{W/cm^2}$ in Section 4.4.

4.1 Dependence on Peak Intensity

Here we present our investigation of the electron distribution for varying a_0 through simulation (Section 4.1.1) and experiment (Section 4.1.2), followed by a discussion where we compare the results of our simulations and measurements with the analytical model presented in Section 2.4.

4.1.1 Simulation

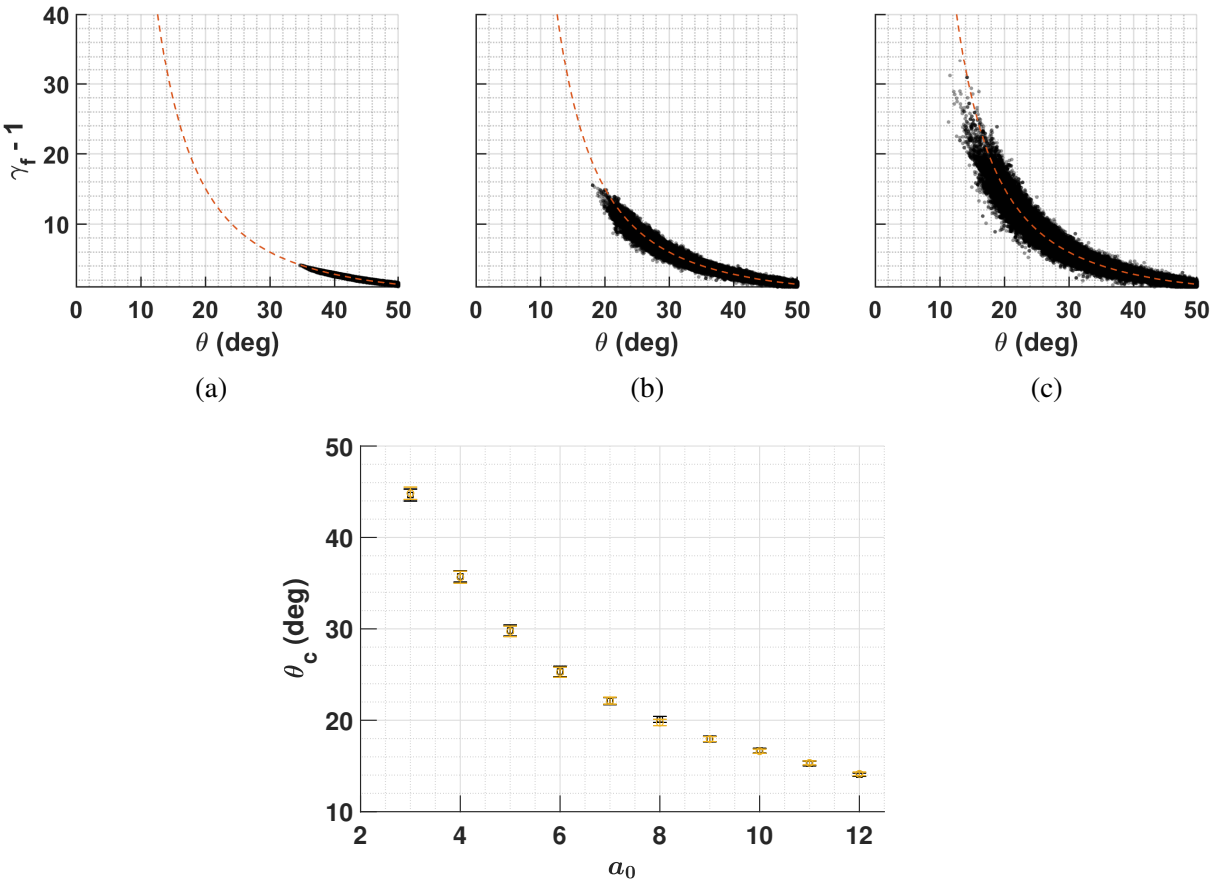


Figure 4.1: Simulated $\gamma_f - 1$ and θ for all electrons of interest generated from $P = 10^{-5}$ mbar of Ar by a $w_0 = 8$ μm, $\tau = 30$ fs laser pulse with (a) $a_0 = 4$, (b) $a_0 = 8$ and (c) $a_0 = 12$. Each translucent black dot represents an electron. The orange dashed line represents Equation (2.23). Simulated θ_c (see text) for varying a_0 in (d) with black square (yellow circle) markers representing Ar (N_2) and corresponding error bars denoting $\pm 1\sigma$ in evaluating θ_c.

We performed simulations for varying a_0 ($= 3$ to 12) and fixed λ_0 ($= 0.8$ μm), w_0 ($= 8$ μm), and τ ($= 30$ fs) with two different gas species – Ar and N_2. We note that to simulate N_2, we approximate the N_2 molecule as two atoms of N at each location for simplicity. In reality, the ionization sequence of the N_2 molecule is more complex due to the presence of a covalent triple bond, but this approximation is sufficient for a first-order approach as part of our simplistic

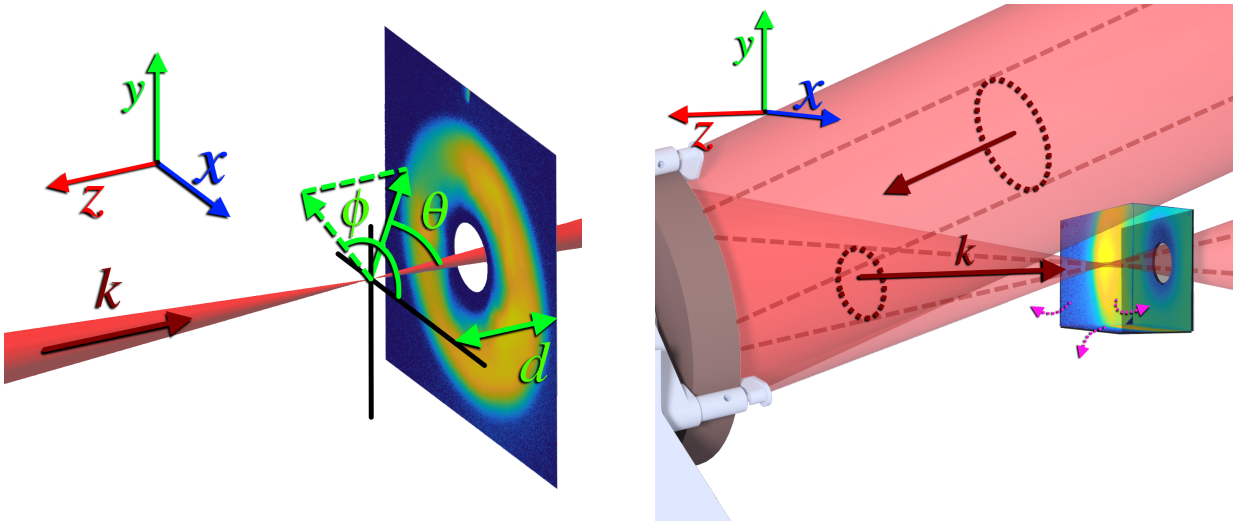
ionization model (detailed in Section 3.1.1). Figures 4.1a–4.1c show the cumulative γ_f and θ data for electrons generated by a representative set of a_0, each with 20 runs of 5×10^{-7} mbar of Ar leading to an effective pressure of 10^{-5} mbar. For these simulations, we used $\alpha_{xy} = 2.5$, $\alpha_z = 3.5$ and $\alpha_t = 100$, which we determined was sufficient to capture the dynamics of the electrons with $\gamma_f > 2$ and $\theta < 50°$ using the approach detailed in Section 3.4. For each a_0 and gas species, this results in $\sim (5 \text{ to } 8) \times 10^6$ electrons generated from the initial box of atoms. We then define the simulated θ_c as the average θ of the 100 smallest-θ electrons for each a_0 with the standard deviation σ representing the uncertainty in the simulated θ_c. We show the simulated θ_c for varying a_0 with both Ar and N_2 in Figure 4.1d.

4.1.2 Experiment

We performed experiments [138, 139] with the VEGA-3 laser [140, 141] at the Centro de Láseres Pulsados (CLPU) in Spain and the Scarlet laser [142, 143] at The Ohio State University (OSU), USA, to test Equation (2.27) as follows. First, we obtain an inferred a_0, $a_{0,infer}$, from low power measurements (Section 4.1.2.1). Then, we obtain θ_c for varying $a_{0,infer}$ (Section 4.1.2.2) that allows us to compare with the a_0 predicted in Equation (2.27). We provide a diagram of the experimental setup in Figure 4.2.

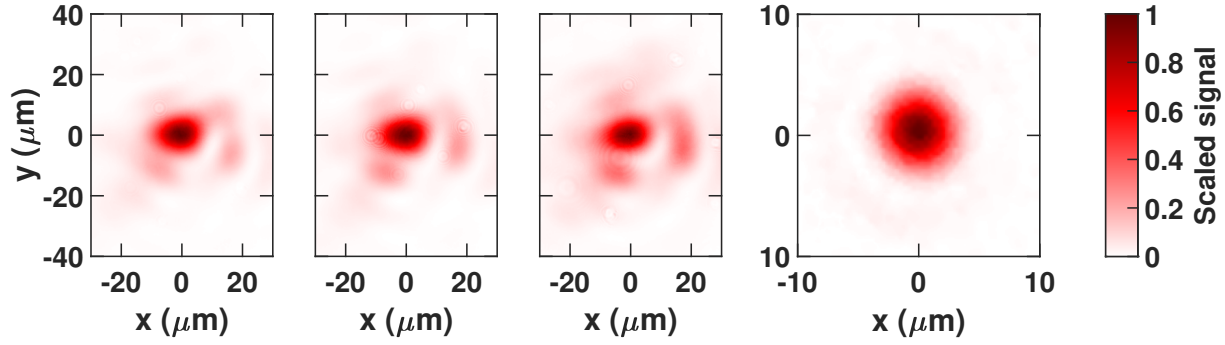
4.1.2.1 Inferring the Intensity

Our approach to infer the peak intensity, and thus a_0, involves estimating the laser energy delivered on the focal plane, U, measuring the temporal pulse duration τ, imaging the focal spot distribution at low power. We estimate U using a leaky mirror to measure a fraction of



(a) (b)

Figure 4.2: Experimental setup (not to scale) for image plate at CLPU in (a) and OSU in (b). Image plates are mounted after, and facing, the focal spot at a fixed distance, d. The laser pulse is traveling along $-\hat{z}$ and is linearly polarized with E_x along $\hat{x}$. In (b), the maroon dashed lines represent (not to scale) the outline of the laser beam when the circular aperture was used. The maroon dotted lines represent the transverse beam profile. The magenta dotted lines with arrows represent the directions in which the three plates that are not perpendicular to $\vec{k}$ are unfolded when scanned.



(a) (b) (c) (d)

Figure 4.3: Representative set of focal spot images captured at low power with the VEGA-3 laser, shown in (a)–(c), and the Scarlet laser after using the circular aperture (see text), shown in (d).

the energy of the full beam before the compressor and τ by diverting a small portion of the beam near its edge into a second-harmonic autocorrelator. We then obtain the intensity profile by distributing the peak power U/τ over the focal spot by scaling the peak signal in the image to $I_{infer} = KU/\tau$. The proportionality constant K is determined by the focal spot distribution as $K = C_{pk}/(C_{sum}A_{pix})$ where C_{pk} corresponds to the peak signal in the image, C_{sum} is the total signal and A_{pix} is the area of the camera pixel in physical units (cm^2, when I_{infer} is expressed in $\mathrm{W/cm}^2$). We then use the maximum value of I_{infer} in Equation (2.14) to obtain a_0. We note that this approach does not approximate a focal spot distribution to any analytical form but rather provides a two-dimensional map of the intensity profile based on the focal spot image. A detailed description of our approach is given in the Appendix of Ref. [115].

By considering the systematic uncertainties in the calibration process and factoring in losses for U (in the compressor and subsequent focusing optics) and dispersion for τ (in beam transport through a fused silica viewport of thickness 5 mm and ≈ 1 m of air), we estimated the overall uncertainty in measuring U and τ to be $\approx 10\ \%$ and $20\ \%$ respectively. A representative set of focal spot images taken at low power over different days with the VEGA-3 laser (f/10 focusing) is shown in Figures 4.3a–4.3c and a focal spot image of the Scarlet laser (f/6 focusing) is shown in Figure 4.3d. The fluctuation in this distribution contributes to an additional uncertainty $\approx 8\ \%$ in the inferred intensity for fixed U and τ. With the Scarlet laser, we placed a circular aperture before the focusing mirror that created a more symmetric spot, shown in Figure 4.2b, with an effective f/6 focusing.

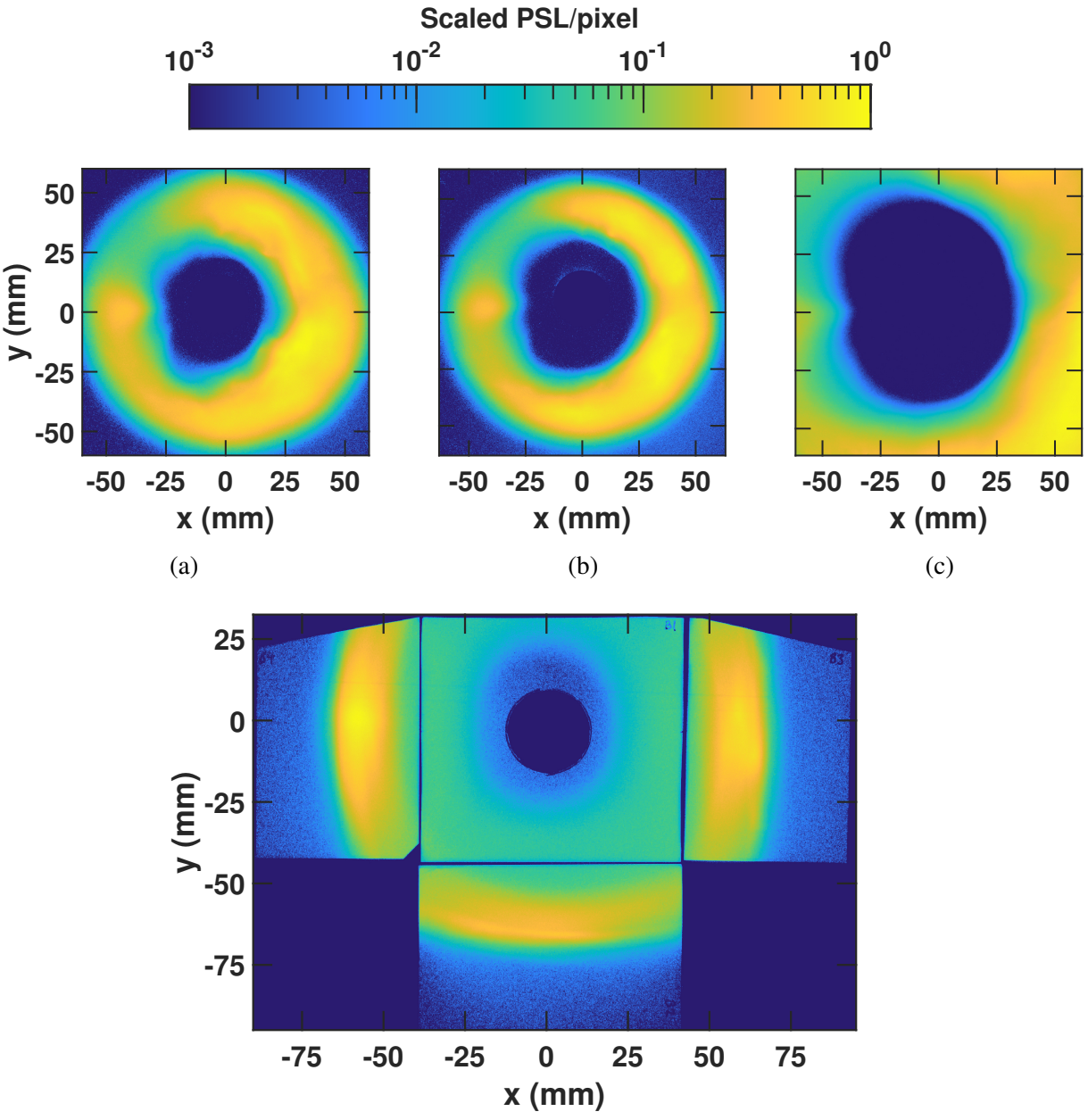


Figure 4.4: Scaled image plate data captured under conditions detailed in Table 4.1, where 1 on the color scale corresponds to peak PSL values (see text) of 7.06, 6.82, 31.88 and 4.57 within a 50×50 μm^2 pixel for (a)–(d), respectively. The laser is polarized along the $\vec{x}$-axis and $\vec{k}$ points into the page.

Table 4.1: Summary of experimental conditions used for measurements with the image plates. The U and τ reported here is the average value obtained over the corresponding sequence of shots. The techniques used to measure U and τ are detailed in Section 4.1.2.1.

Fig.	**Laser**	**f/#**	**Plate Type**	**No. of Shots**	**U (J) [±10%]**	**τ (fs) [±20%]**	**$a_{0,infer}$ [±12%]**	**Pressure (mbar)**	**Gas**
4.4a	VEGA-3	f/10	SR	100	23.0	35.4	9.1	4×10^{-5}	N_2
4.4b	VEGA-3	f/10	SR	100	23.4	55.4	7.3	7×10^{-5}	N_2
4.4c	VEGA-3	f/10	MS	96	8.8	34.7	5.7	9×10^{-5}	N_2
4.4d	Scarlet	f/6	MS	70	1.07	38.7	7.0	8×10^{-5}	Ar

4.1.2.2 Measuring θ_c

To find θ_c, we first imaged the spatial distribution of ejected electrons for varying experimental conditions specified in Table 4.1 using commercially available image plates – Fujifilm BAS-MS and BAS-SR. Image plates consist of a high-emission, photo-stimulable phosphor layer that contains F-centers, which trap electrons excited within the phosphor layer by incident radiation, which in this case is electrons ejected from the laser focus. A phosphorimager device then reads the stored information by exposing the image plate to visible light, which then releases the trapped electrons [144–146]. After correcting for the signal fading in time [147] before the plate is read, the corresponding measurements are shown in Figure 4.4 in photostimulated luminescence (PSL) units [148], which is linearly proportional to the energy deposited on the plate. We provide more details about preparing and processing image plates in Appendix C.2. For the VEGA-3 (Scarlet) laser, we mounted the plates perpendicular to $\vec{k}$ at $\approx 40 \pm 2$ mm (35 ± 2 mm) after, and facing, the focus as shown in Figure 4.2, with a hole of diameter ≈ 20 mm (25 mm) to allow the laser to pass. For the Scarlet laser, we modified the plate geometry (see Figure 4.2b) to accommodate the beam geometry in the chamber. We covered the plates with a layer of Al foil

(thickness 12 μm at VEGA-3, 16 μm at Scarlet) to block scattered laser light. In the case of Figures 4.4a and 4.4b, we placed an additional Al shield (thickness 520 μm) directly in front of the plates to block abundant low-energy electrons and enhance contrast for the most energetic electrons of interest. This increases the detection threshold to ~ 0.5 MeV [149] and thus suppresses electrons beyond $\sim 55^\circ$ according to Equation (2.23).

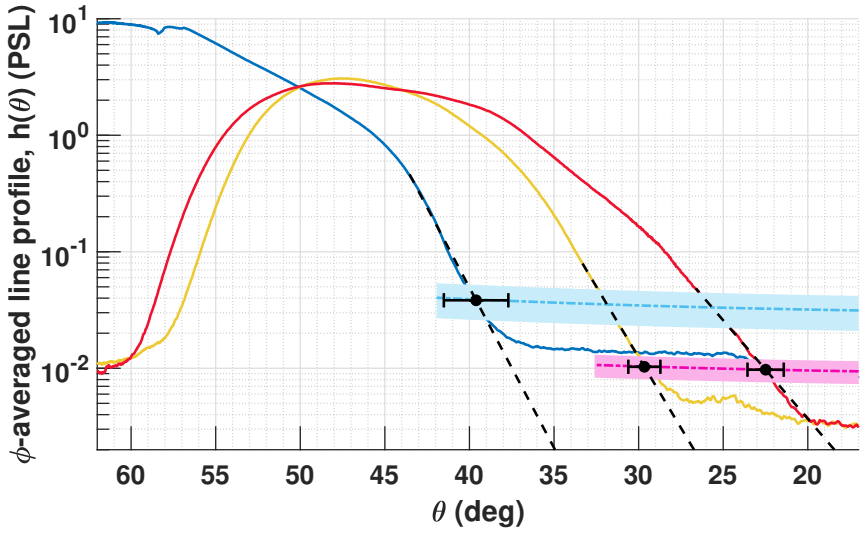


Figure 4.5: The ϕ-averaged line profile, $h(\theta)$ (see text), is shown for data in Figs. 4.4a–4.4c represented by red (far-right), yellow and dark blue (far-left) curves respectively. The dot-dashed magenta (blue) curve indicates the signal floor for the BAS-SR (BAS-MS) plates (see text). The shaded regions are the uncertainties in the signal floor estimated from [150]. The dashed lines represent the exponential fit used to determine θ_c, given by the intersection with the signal floor and shown by the black dots with error bars obtained by accounting for the uncertainty in positioning the plate.

We extracted θ_c from the measurements in Figures 4.4a–4.4c by obtaining an average line profile for varying θ that is representative of each image, to then find the smallest θ at which the signal falls to the PSL level that a single electron would deposit. In the case of Figure 4.4d, we adopt a modified approach and analyze a single horizontal lineout as detailed in Section IV.A of Ref. [139]. For measurements in Figures 4.4a–4.4c, we first remove extraneous noise from the recorded image using a median filter in units of 3×3 squares of 50 μm $\times$ 50 μm pixels. We

visually centered the data using the large-angle falloff in Figures 4.4a and 4.4b, which is accurate to ± 1 mm on the x–y plane. As the electron distribution in Figure 4.4c extends beyond the image plate, we chose the center in this case in the vicinity of that in Figures 4.4a and 4.4b relative to the hole cut in the plate, as we used the same alignment procedure for all three measurements. We extended the uncertainty to ± 5 mm for the measurement in Figure 4.4c. We define $g(\theta, \phi)$ as the PSL value stored in each pixel of the image, located at a given θ $(= \tan^{-1}(\sqrt{x^2 + y^2}/d))$ and ϕ $(= \tan^{-1}(y/x))$ from the laser focus (as shown in Figure 4.2a). A ϕ-averaged line profile, given by $h(\theta) = \int_0^{2\pi} g(\theta, \phi) d\phi \; / \int_0^{2\pi} d\phi$, for the measurements in Figures 4.4a–4.4c is shown in Figure 4.5. We then obtain a θ_c that is representative of the recorded image by finding the smallest θ where $h(\theta) =$ the PSL value that a single electron in the MeV energy range would deposit on average in a single pixel on the image plate. This is $\approx (9 \pm 2) \times 10^{-3}$ PSL for BAS-SR and $\approx (3 \pm 1) \times 10^{-2}$ PSL for BAS-MS [150] at normal incidence. To account for the incident angle dependence of the deposited PSL, we then multiplied this value by $1/\cos(\theta)$ to obtain a signal floor as shown in Figure 4.5. We used the point of intersection of $h(\theta)$ and the corresponding floor as a first estimate to then apply an exponential fit to $h(\theta)$ from this point to an added 4° (toward the left in Figure 4.5). We then found θ_c by extending the fit data to smaller θ to find where it crosses the shaded region, as shown in Figure 4.5. To account for the uncertainty in positioning the plate, We repeated the same procedure by randomly varying the position of the center and the distance of the plate from the focus within the limits of uncertainty in positioning. This dominates the contribution from the uncertainty in estimating the signal floor. Thus, $\theta_c = 22^\circ \pm 1^\circ$, $30^\circ \pm 1^\circ$ and $39^\circ \pm 2^\circ$ for Figures 4.4a–4.4c, respectively.

4.1.3 Comparing Measurements with Theory

We present a summary of the analytical model (Eq. (2.27)), our simulations (Section 4.1.1) and measurements (Section 4.1.2) in Figure 4.6. From our simulations, we chose to display only the Ar data to avoid cluttering the plot, as the simulation results were nearly identical for Ar and N_2 (Figure 4.1d).

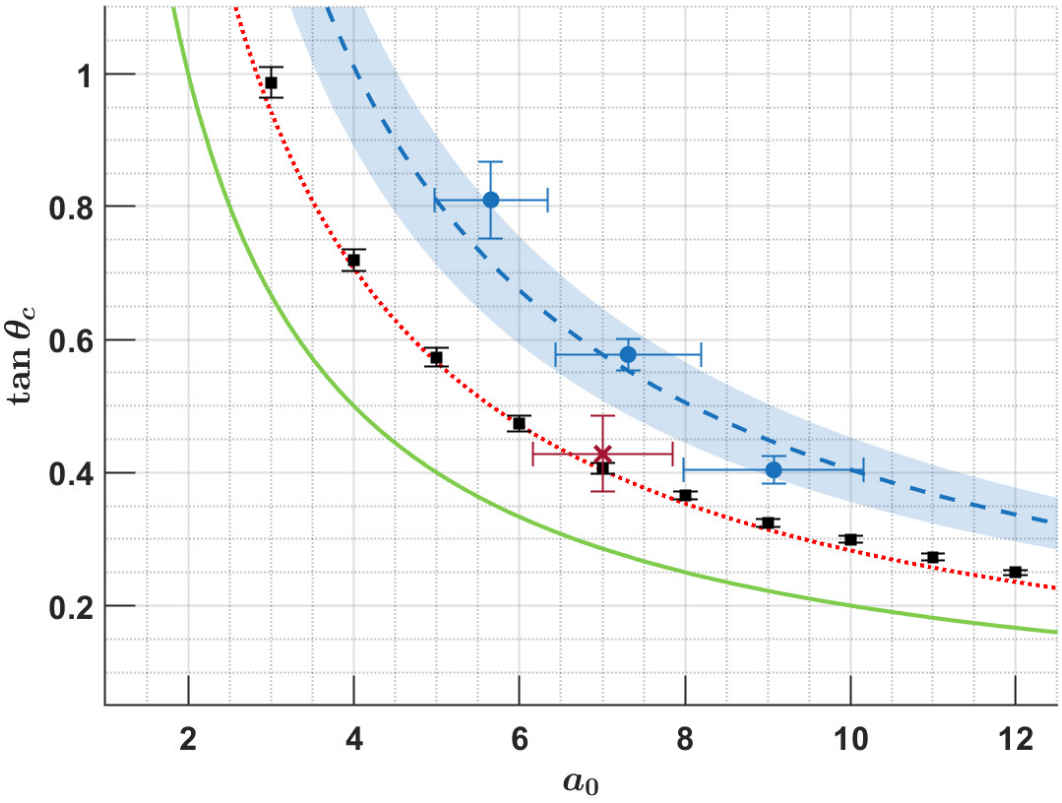


Figure 4.6: Comparison of measured θ_c at the inferred a_0, simulated θ_c for varying a_0, with the theory. Green solid and red dotted curves, represent Equation (2.27) with $\eta = 1$ and $\sqrt{2}$, respectively. Black square markers represent simulations performed with Ar (see Section 4.1.1). Blue dot (maroon cross) markers represent measurements in Figures 4.4a–4.4c (Figure 4.4d). Horizontal (vertical) error bars represent the uncertainty in inferring (measuring) a_0 (θ_c). The blue dashed line represents a numerical fit of the data from Figures 4.4a–4.4c to $\tan\theta_c = 2\eta/a_0$, where $\eta = 2.02^{+0.26}_{-0.22}$. The shaded region around the dashed curve represents the uncertainty in η.

We first point out that the simulation data and the measurements in Figures 4.4a–4.4c scale

statistically consistent with $\tan\theta_c \propto 1/a_0$, while the measurement in Figure 4.4d is in better agreement with the simulation data than the rest of the measurements. Specifically, we see that the simulation is in agreement with $\eta = \sqrt{2}$ in Equation (2.27), which implies that $\gamma_p = 1 + a_0^2/4$ (Eq. (2.25)) is a good approximation for a near-ideal paraxial Gaussian laser pulse with $\tau = 30$ fs. However, we also see that $\eta > \sqrt{2}$ for measurements in Figures 4.4a–4.4c. In the following, we discuss possible reasons for this, followed by a discussion of why the measurement in Figure 4.4d appears to be consistent with $\eta = \sqrt{2}$.

First, to obtain η for our measurements in Figures 4.4a–4.3c, we fit the resultant θ_c (see Figure 4.5) to the function $\tan\theta_c = 2\eta/a_x$, with the measured data at $a_x = a_0$ (shown by the blue dashed line in Figure 4.6), $a_x = a_0 + \delta a_0$ and $a_x = a_0 - \delta a_0$ (represented by the boundaries of the shaded region in Figure 4.6). This gives $\eta = 2.02^{+0.26}_{-0.22}$. There could be several reasons why $\eta > \sqrt{2}$ in this case: (A) the inferred a_0 might not correspond to the peak intensity present in the focus, (B) the measured θ_c may not reflect the peak intensity in the focus, and (C) a more robust theoretical model of the dynamics in a focused laser pulse may be required. Below, we discuss some factors that could likely contribute to each of these possibilities.

To address the possibility of (A), we note that the focal spot may not behave the same way at high power as it did at low power, and might possibly expand in size or have a larger proportion of energy distributed farther away from the central spot. For example, it is straightforward to show that for a Gaussian beam, since $a_0 \propto 1/w_0$, the beam waist at full power would only have to expand by a factor of $\sqrt{2}$ or 2 relative to that at low power to reduce the full power estimate of a_0 by the same factor, which would then be a closer fit to the simulations and the analytical model (Eq. (2.27) with $\eta = \sqrt{2}$). Further, if there were a pulse front tilt, the effective pulse duration would be longer. For example, Figure 1 of [151] shows that a tilt of only 0.2 fs/mm for a beam

of 25-cm diameter (as in the VEGA-3 laser) results in a reduction of the intensity by a factor of ≈ 3.2. Additionally, other aberrations such as astigmatism or coma that might cause the focal spot to be oval-like or teardrop-like (such as in the central region of Figs. 4.3a–4.3c), could also contribute to lowering the intensity delivered in the focus. Such spatial and temporal aberrations are not uncommon in petawatt-class lasers as the heat-transfer between the laser pulse and the optics can often induce deformation to the optics, which affects the spatiotemporal quality of the focus. This is especially true for gratings in the pulse compressor where even a peak-to-peak deformation of $\sim 1\lambda_0$ across the surface can lead to several spatiotemporal aberrations that severely affect the peak intensity [152].

To address the possibility of (B), we note that we measured θ_c by finding the smallest θ at which the ϕ-averaged pixel response over ≈ 100 laser shots meets the PSL level that a single electron would deposit on average in a pixel from [150]. We found that this intersection was well above the noise (see Figure 4.5), implying that more than one electron irradiated the image plate on average (for all ϕ) for $\theta > \theta_c$. However, if one performs the measurement with more laser shots, it is possible that the ϕ-averaged pixel response could reach the single-electron PSL level at some $\theta < \theta_c$. Therefore, the measured θ_c here acts as a reasonable upper bound for the smallest ejection angle of electrons that presumably reflects the peak intensity.

Additional experiments with robust simulations are required to address the possibility of (C), which is an ongoing project that is partially covered by Sections 4.2 and 4.3.

Finally, we address the reason why θ_c from the measurement in Figure 4.4d is more consistent with simulations and $\eta = \sqrt{2}$. We see from Figure 4.3 that the focal spot of the Scarlet laser (see Figure 4.3d) is more symmetric than the more aberrated focal spot of the VEGA-3 laser (see Figures 4.3a–4.3c). We show in Section 5.2 and in Refs. [153, 154] that this results in

a relatively symmetric spatial distribution of electrons for the measurement in Figure 4.4d than those in Figures 4.4a–4.4c. This likely leads to a more favorable environment for acceleration in the focal volume due to reduced intensity degradation from aberrations at full power. Therefore, the measured θ_c from a relatively uniform focal spot appears closer to the near-ideal simulations than those from highly aberrated beams.

4.2 Dependence on Pulse Duration

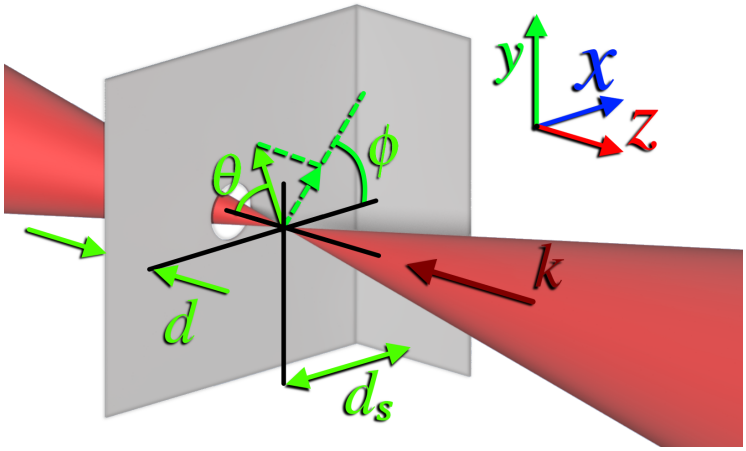
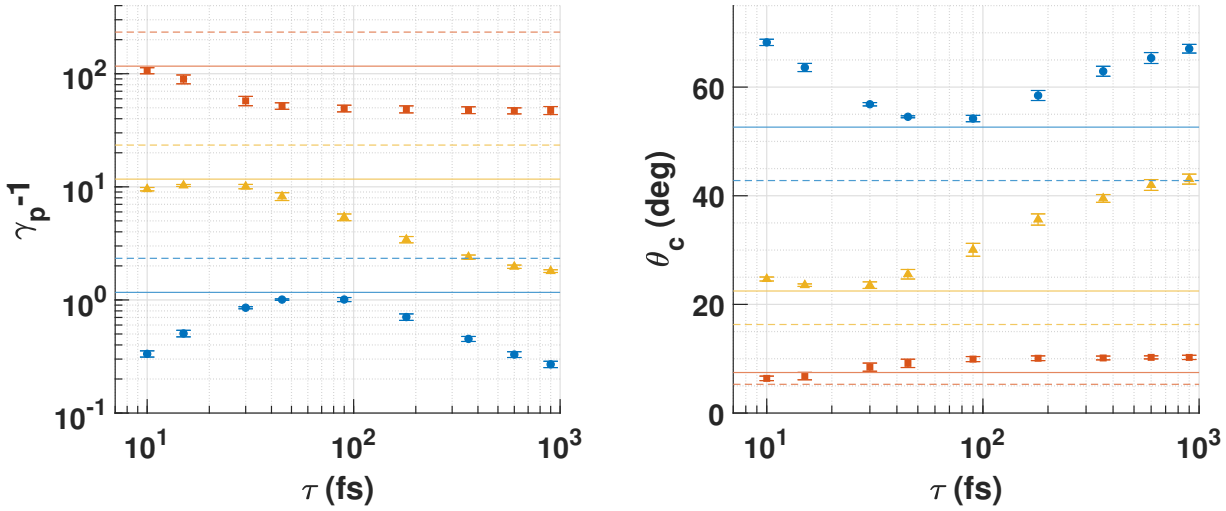


Figure 4.7: Setup (not to scale) for simulations and experiments measuring the spatial distribution of electrons under varying pulse duration. Electrons ejected from the focus as the origin are recorded on the plane with $z = -d$ and another with $x = +d_s$. The laser pulse is traveling along $-\hat{z}$ and is linearly polarized along $\hat{x}$ ($\hat{y}$) in the simulation (experiment).

The temporal structure of a laser pulse may affect the effective interaction time between an electron and the laser pulse. Therefore, it is essential to consider the dependence of γ_p and θ_c on the pulse duration. In this section, we present our investigation of electron dynamics under varying τ from $\sim$ 10 fs to $\sim$ 100 fs through simulation (Section 4.2.1) and experiment (Section 4.2.2).

4.2.1 Simulation

We performed simulations for varying τ ($=$ 15 to 900 fs) and fixed λ_0 ($=$ 0.8 μm), w_0 ($=$ 8 μm) with three different a_0 ($=$ 2.16, 6.84, 21.6, which correspond to $I_0 = 10^{19}$, 10^{20}, 10^{21} W/cm^2, respectively). To isolate the role of pulse duration on γ_p and θ_c, we used an artificial atom with a single ionization stage $I_{th} = I_0/10$, at an effective pressure of 2×10^{-5} mbar for each set of laser parameters. We show the average γ (θ) of the 100 largest-γ (smallest-θ) electrons obtained for each simulation in Figure 4.8a (Figure 4.8b).



(a) (b)

Figure 4.8: Simulated $\gamma_p - 1$ in (a) and θ_c in (b), under varying τ for three different a_0 with $I_{th} = I_0/10$. Blue circles, yellow triangles and orange squares represent $a_0 = 2.16$, 6.84 and 21.6, which correspond to $I_0 = 10^{19}$, 10^{20}, 10^{21} W/cm^2, respectively. Error bars denote the standard deviation in evaluating γ_p and θ_c. Solid (dashed) lines correspond to $\gamma_p - 1 = a_0^2/4$ ($a_0^2/2$) in (a) and $\tan\theta_c = \sqrt{8}/a_0$ ($2/a_0$) in (b).

We observe for all a_0 that for $\tau > 100$ fs, γ_p decreases (θ_c increases). This is due to the slow temporal rise in intensity, which results in electrons being ejected from the finite spatial extent of the laser pulse prior to the arrival of the peak intensity. Therefore, this results in a smaller γ_p (larger θ_c) that does not reflect the peak intensity. For shorter τ, the sudden rise in

peak intensity results in an increased likelihood of interaction between the electron and the peak intensity, which results in better agreement with analytical estimates. However, for $a_0 = 2.16$, we observe that $\gamma_p - 1$ (θ_c) also decreases (increases) for $\tau < 45$ fs. This is because the interaction time between the electrons and the relativistic part of pulse is reduced as $I_{th} = I_0/10$, which implies that electrons are ionized at a sub-relativistic intensity $I_{th} = 10^{18}$ W/cm^2.

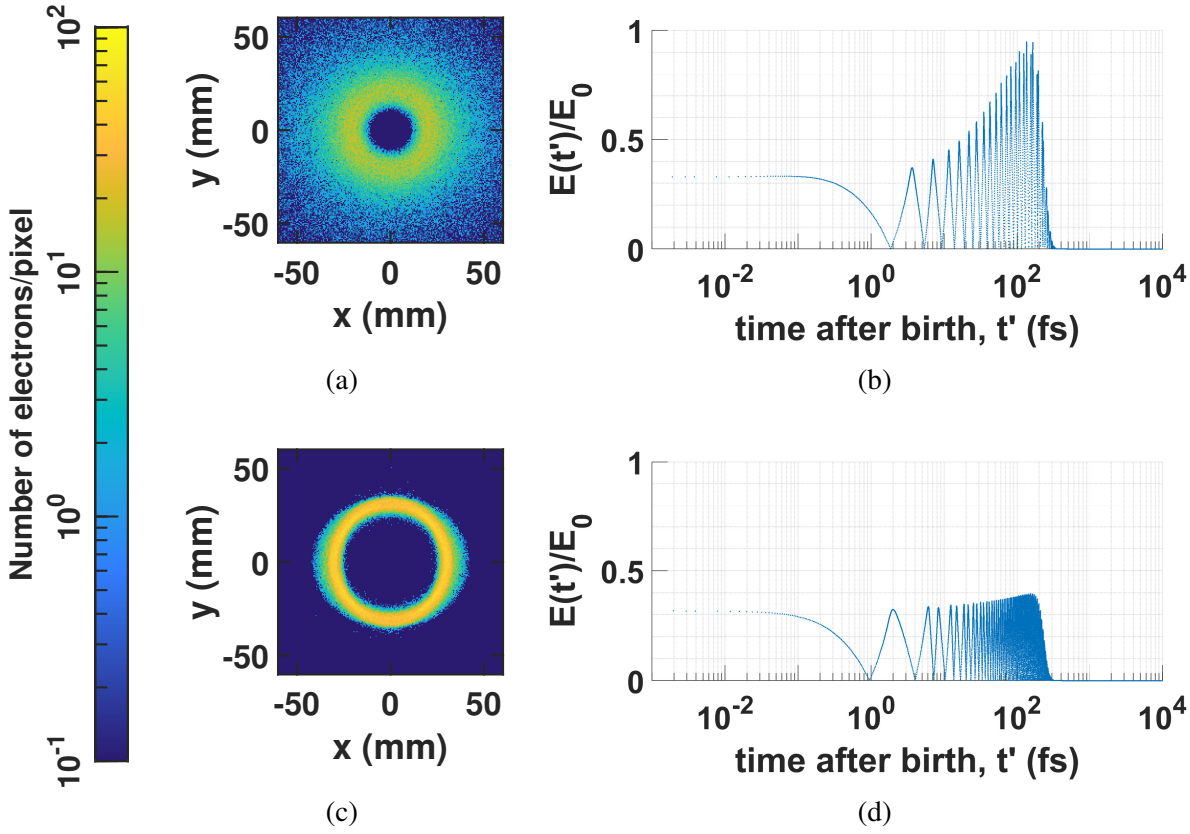


Figure 4.9: Spatial distribution of electrons generated by $a_0 = 6.84$ is shown when (a) $\tau = 30$ fs and (c) $\tau = 600$ fs on a plane with $d = 25$ mm. The color scale denotes the number of electrons in each 1×1 mm^2 pixel across the plane. Electric field sampled by the most energetic electron from (a) and (c) in (b) and (d), respectively, normalized to the peak field.

Due to the correlation between γ_p and θ_c, it is possible to observe the role played by the temporal intensity gradient on γ_p by recording the spatial distribution of electrons as shown in Figures 4.9a and 4.9c for $\tau = 30$ and 600 fs, respectively. We see that when $\tau = 30$ fs, the sharp

increase in intensity results in electrons being ejected over a wide range of θ depending on the intensities sampled within the laser pulse. When $\tau = 600$ fs, however, electrons are ejected over a smaller range of θ due to the more gradual rise in intensity that limits the range of intensities that can be sampled. This is further demonstrated by Figures 4.9b and 4.9d, which show the field sampled by the most energetic electron in Figures 4.9a and 4.9c that are ejected at $\theta \approx 23°$ and $41°$, respectively. We see that the electron experiences $E(t')/E_0 \approx 0.32$ for $t' \to 0$ as it is ionized at $I_{th}/I_0 = 0.1 = E^2(t' = 0)/E_0^2$ and samples a maximum of $\approx 0.95a_0$ when $\tau = 30$ fs and only $\approx 0.4a_0$ when 600 fs (note $a_0 \propto E_0$). Here, t' is the time after the birth of the electron. This implies that for large τ ($\gg 30$ fs), electrons are accelerated by a maximum of $I \gtrapprox I_{th}$, which may be $\ll I_0$ if $I_{th} \ll I_0$, due to the gradual rise in intensity.

While it may not be possible to employ an atom with a single ionization stage of $I_{th} = I_0$, it is possible to observe this effect for certain a_0 using appropriate gas species. For example, N (Table A.3) is ionized up to N^{5+} by $I \lesssim 10^{16}$ W/cm^2 while N^{6+} and N^{7+} appear only when $I \sim 10^{19}$ W/cm^2. Therefore, for a laser pulse with $I_0 \gtrsim 10^{19}$ W/cm^2 and $\tau \gtrsim 100$ fs, the $2s$ and $2p$ electrons of N collectively experience similar intensities $I \ll I_0$ while the $1s$ electrons experience $I \sim I_0$. Meanwhile, for a species such as Ar (Table A.5), although $I_0 \gtrsim 10^{19}$ W/cm^2 is insufficient to ionize the $1s$ electrons that appear at $I \sim 10^{21}$ W/cm^2, a similar structure exists in that the $3s$ and $3p$ electrons appear at $I \lesssim 10^{16}$ W/cm^2 while the $2s$ and $2p$ electrons only appear at $I \sim 10^{18}$ W/cm^2. Therefore, while there may be a separation in the range of intensities the electrons experience, it is less distinct than in the case of N. We performed simulations using N_2 and Ar for $\tau = 30$ and 600 fs with fixed $a_0 = 4$ ($I_0 \approx 3.4 \times 10^{19}$ W/cm^2), λ_0 ($= 0.8$ μm) and w_0 ($= 8$ μm). We show the resultant spatial distribution of electrons in Figure 4.10.

For simulations with $\tau = 30$ fs, we see that the distributions for N_2 (Figure 4.11a) and Ar

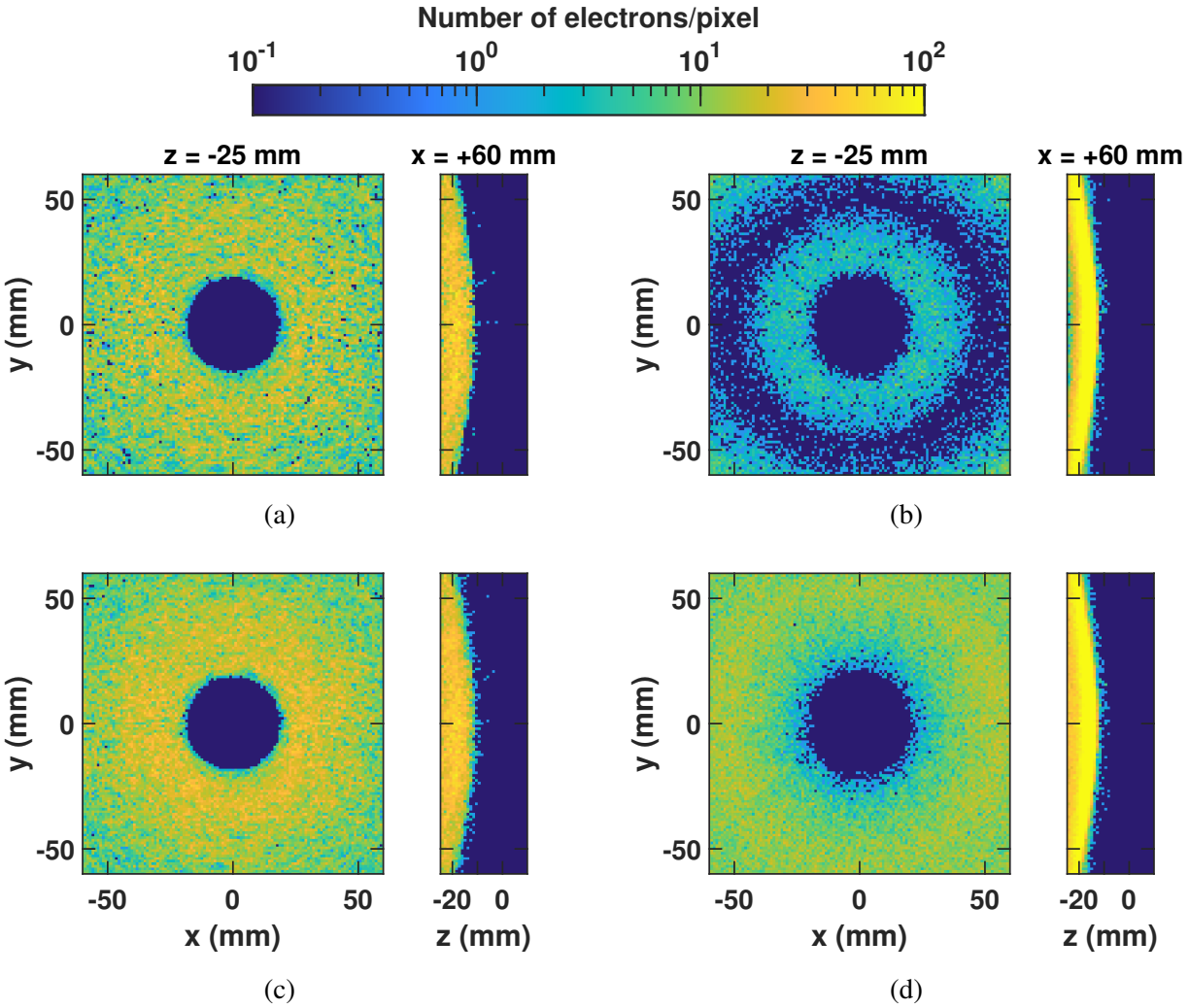


Figure 4.10: Spatial distribution of electrons generated by $a_0 = 4$ for (a) N_2 and $\tau = 30$ fs, (b) N_2 and $\tau = 600$ fs, (c) Ar and $\tau = 30$ fs, and (d) $\tau = 600$ fs. The color scale denotes the number of electrons in each 1×1 mm^2 pixel across the plane. The laser is polarized along the $\vec{x}$-axis with $\vec{k}$ pointing into the page. The plane with $x = +60$ mm is saturated for (b) and (d) to increase contrast for the electrons appearing on the $z = -25$ mm plane that exhibit characteristic features discussed in the text.

(Figure 4.11c) appear similar except for a difference in the signal strength, which simply depends on the accessibility of ionization stages with $a_0 = 4$. For simulations with $\tau = 600$ fs, however, we observe that the simulated distributions (Figures 4.11a and 4.11c) are significantly different. We see that for N_2, electrons are ejected in two distinct ring-shaped structures. This is due to the slow increase in intensity that leads to the interaction of the $2s$ and $2p$ electrons of N with 10^{16} W/cm$^2 \lesssim I \ll I_0$, resulting in barely-relativistic energies and large θ, which form the outer ring. Meanwhile, the $1s$ electrons ionized at $I \sim 10^{19}$ close to the peak are accelerated to higher energies with notably smaller θ, forming the inner ring. This effectively results in two distinct ring-shaped structures. We see that for Ar, although a similar structure appears, the inner ring is notably larger and spans a wider range of θ, nearly overlapping with the outer ring. This is a consequence of the relatively small difference between the range of ionization intensities for electrons in the $n = 3$ and $n = 2$ shells.

4.2.2 Experiment

Table 4.2: Summary of experimental conditions used for measurements with the image plates.

Fig.	**Laser**	**Gas**	τ **(fs)**	**Pressure (mbar)**	**No. of Shots**	f/#	**U (J)**	λ_0 **(μm)**	a_0	d **(mm)**	d_s **(mm)**
4.11a	VEGA-3	N_2	40	1.7×10^{-4}	20	f/10	22.2	0.8	8.4	40	N/A
4.11b	MTW	N_2	700	6.67×10^{-4}	1	f/2.8	6.9	1.05	6.1	25	55
4.11c	VEGA-3	Ar	40	1.1×10^{-4}	50	f/10	21.9	0.8	8.4	40	N/A
4.11d	MTW	Ar	700	1.13×10^{-3}	1	f/2.8	7.9	1.05	6.6	25	55

We performed experiments with the VEGA-3 laser [140, 141] at CLPU and the MTW laser [155] at LLE, to test the behavior of the spatial distribution of electrons predicted in Figure 4.10. For both experiments, we used Fujifilm BAS-MS image plates covered with a layer of Al foil

(thickness 12 μm) in a slightly modified version of the setup shown in Figure 4.7 as follows. With the VEGA-3 laser ($\tau \sim 40$ fs), we only used a plate perpendicular to $\vec{k}$ as the low-energy electrons at large angles are not critical for the short-pulse scenario. With the MTW laser ($\tau \sim 700$ fs), we used additional layers of Al placed directly in contact with the image plate surface facing the laser focus to filter out electrons of varying energy in different regions. On the plate parallel to the x–y plane and perpendicular to the laser passing through the origin, we used square-shaped Al layers with thicknesses 102, 204, 306 μm to cover the second, third and fourth quadrants, which effectively suppress electrons with kinetic energy $\sim 0.15, 0.25, 0.35$ MeV, respectively. On the plate parallel to the z–y plane, we used a rectangular Al layer with thickness 254 μm placed near the bottom, which suppresses electrons with kinetic energy ~ 0.3 MeV. We provide the experimental parameters in Table 4.2 for the measurements in Figure 4.11.

We see from Figure 4.11 that for $\tau \sim 40$ fs, we obtain a continuous distribution across the image plate whereas for $\tau \sim 700$ fs, ring-shaped structures appear as predicted in Figure 4.10. Specifically, we observe the distinct double-ring structure for N_2 (Figure 4.11b) comprised of an outer ring with predominantly low-energy (< 0.3 MeV) electrons, likely from the $n = 2$ shell, and an inner ring with predominantly high-energy (> 0.35 MeV) electrons, likely from the $n = 1$ shell. We see that this double-ring structure is less distinct with Ar (Figure 4.11d) in that the inner ring spans a wider range of angles (see first quadrant on $z = -25$ mm plane and the upper part of the $x = +55$ mm plane in Figure 4.11d). This is likely due to the relatively closely spacing between the ionization intensities of the $n = 2$ and $n = 3$ shell electrons in Ar (Table A.5) compared to that of the $n = 1$ and $n = 2$ shell electrons in N_2 (Table A.3) as discussed in Section 4.2.1. These measurements collectively indicate that for $\tau \gtrsim 100$ fs, electrons interact with $I \gtrsim I_{th}$ due to the gradual rise in intensity and thus $I \ll I_0$ if $I_{th} \ll I_0$, whereas for

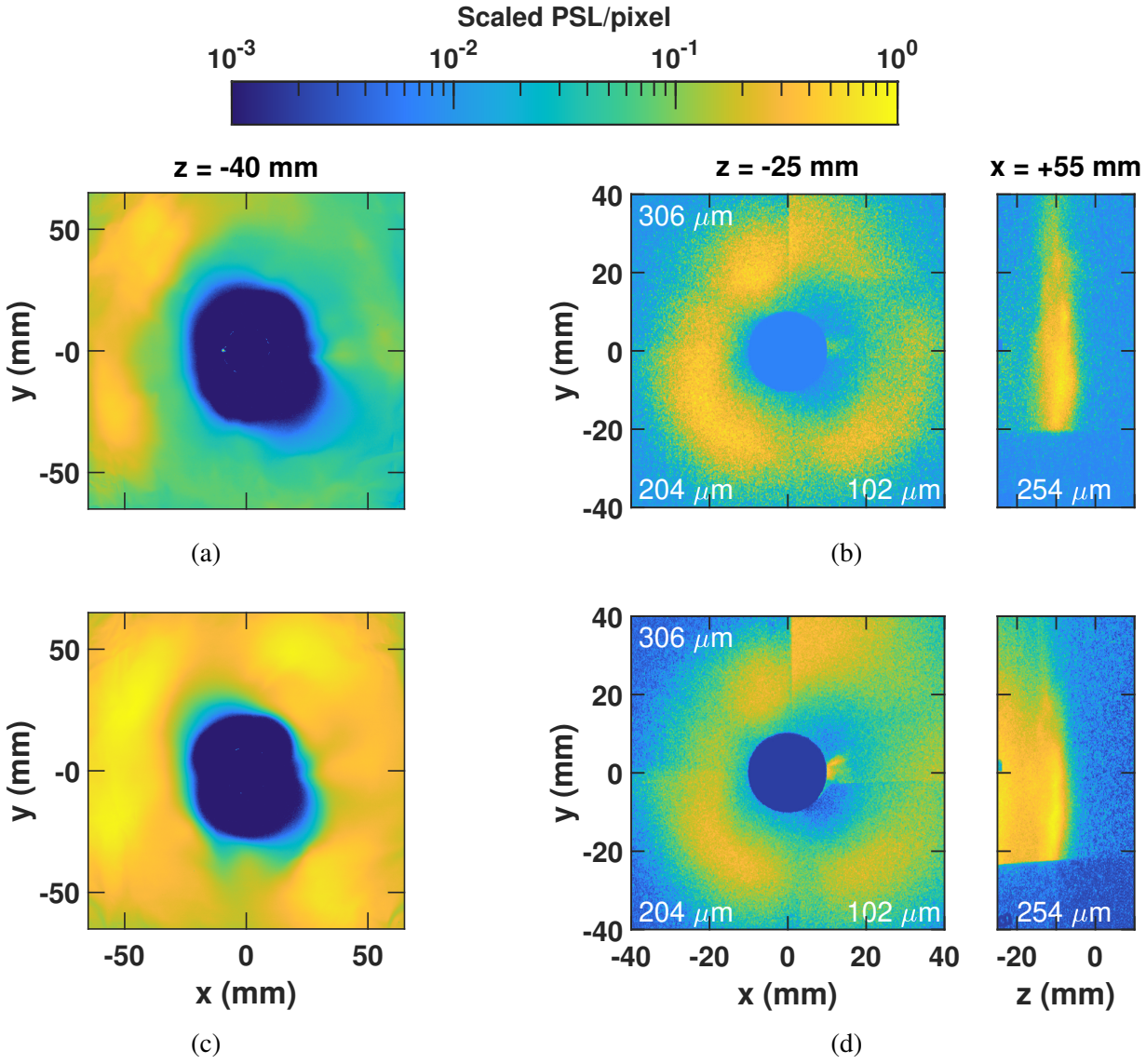


Figure 4.11: Scaled image plate data captured under conditions detailed in Table 4.2, where 1 on the color scale corresponds to peak PSL values of 79.1, 0.12, 57.6, 0.41 within a 50×50 μm^2 pixel for (a)–(d), respectively. The white text specifies the thickness of additional Al filtering used in different quadrants of the plane with $z = -25$ mm and the bottom section of the plane with $x = +55$ mm in (b) and (d). The laser is polarized along the $\vec{x}$-axis in (a) and (c), and along the y-axis in (b) and (d), with $\vec{k}$ pointing into the page.

$\tau < 100$ fs, electrons may interact with $I \gg I_{th}$ due to the sharp rise in intensity and thus $I \lesssim I_0$ even if $I_{th} \ll I_0$.

4.3 Dependence on F-Number

While we predominantly considered electron dynamics in the paraxial regime thus far, it is worth noting that laser facilities aiming to achieve higher peak intensities with fixed peak power typically employ tight focusing conditions (focusing optics with low f-number) that are non-paraxial in nature. It is therefore important to investigate the role of the f-number ($\mathrm{f}/\#$) on electron dynamics. In this section, we present our investigation of electron dynamics for varying $\mathrm{f}/\#$ through simulation (Section 4.3.1) and experiment (Section 4.3.2).

4.3.1 Simulation

We performed simulations for varying w_0 ($= 8, 5$ and 2 μm) and fixed λ_0 ($= 0.8$ μm), τ ($= 30$ fs), a_0 ($= 15$, which corresponds to $I_0 \approx 4.8 \times 10^{20}$ W/cm^2). As the $\mathrm{f}/\#$ for a Gaussian beam is $\approx \pi w_0/(2\lambda_0)$, $w_0 = 8, 5$ and 2 μm correspond to $\sim \mathrm{f}/16, \mathrm{f}/10,$ and $\mathrm{f}/4$, respectively. We simulated Ar gas with an effective pressure of $P = 10^{-5}$ mbar in each case to maintain a quantitative comparison of the number of electrons generated with varying focal volume due to the change in w_0. We show the resultant distribution of the electrons of interest for the three cases with a bivariate histogram of θ and γ in Figures 4.12a–4.12c and energy distributions for specific intervals of θ in Figures 4.12d–4.12f, respectively.

In Figures 4.12a–4.12c, we observe that as w_0 decreases, the total number of electrons generated also decreases under fixed pressure. This is consistent with the fact that for a Gaussian

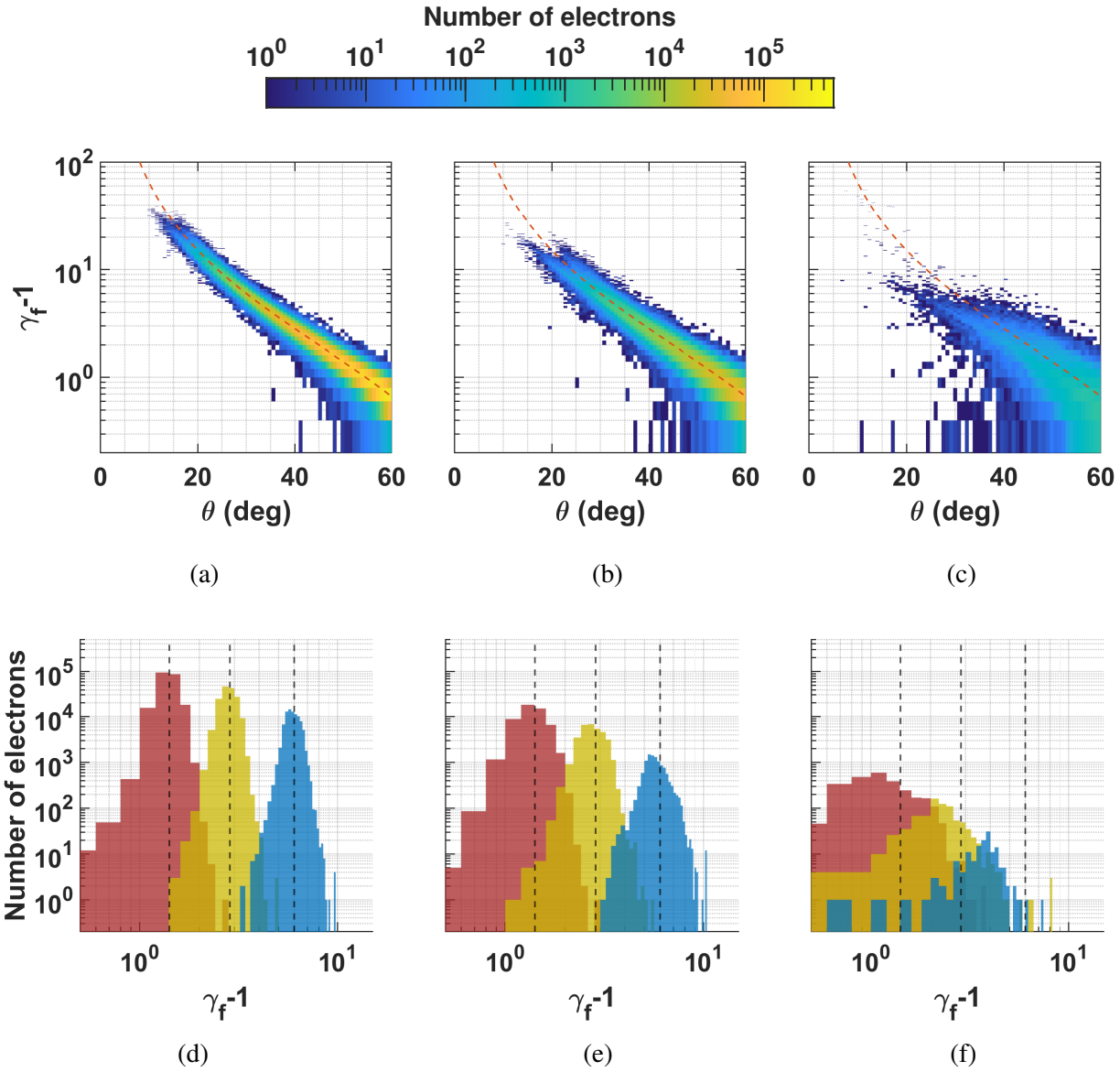
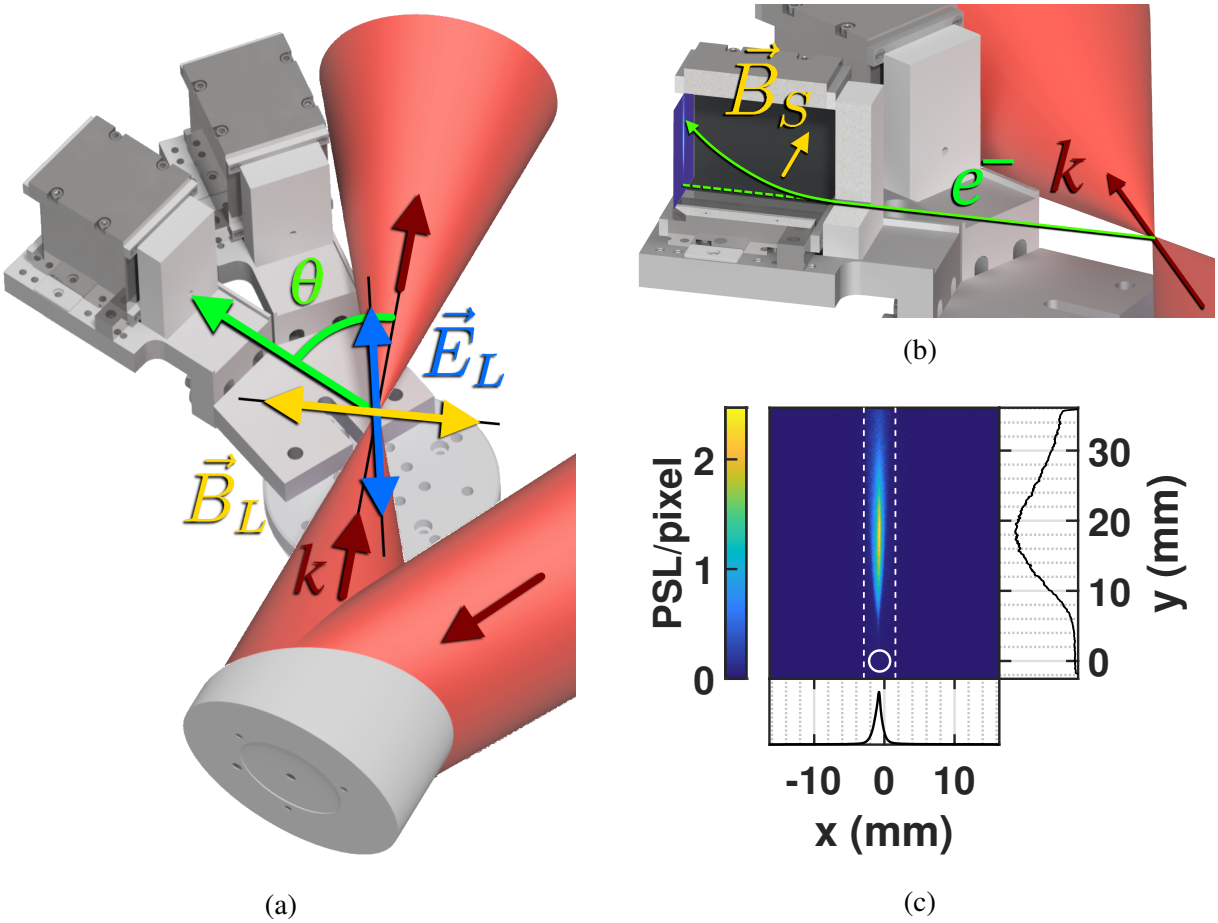


Figure 4.12: Simulated $\gamma_f - 1$ and θ for all electrons of interest generated from Ar with an effective pressure of $P = 10^{-5}$ mbar by an $a_0 = 15$, $\tau = 30$ fs laser pulse with (a) $w_0 = 8$ μm, (b) $w_0 = 5$ μm and (c) $w_0 = 2$ μm. The color scale represents the number of electrons within each two-dimensional bin of $\Delta\theta = 0.8°$ and $\Delta(\gamma_f - 1) = 0.2$, and the orange dashed line represents Equation (2.23). Energy distributions at three specific θ from the electron distribution in (a)–(c) are shown in (d)–(f), respectively, where histograms from left to right correspond to $\theta \in [49.6°, 50.4°)$ (red), $\theta \in [39.6°, 40.4°)$ (yellow) and $\theta \in [29.6°, 30.4°)$ (blue). The black dashed line from left to right represent the analytical γ from Equation (2.23) for $\theta = 50°, 40°$ and $30°$, respectively.

beam, the focal volume scales $\propto w_0^4$ as the transverse axes each scale $\propto w_0$ and the longitudinal axis scales $\propto w_0^2$. We also see that the γ_f-θ distribution follows the analytical equation (Eq. (2.23)) relatively closely for higher w_0 and undergoes broadening for decreasing w_0. Figures 4.12d–4.12f further illustrate these features. We see that for $w_0 = 8\ \mu\mathrm{m}$, the energy spectra appear symmetric around the analytical estimate of $\gamma_f - 1$ whereas the most probable $\gamma_f - 1$ consistently decreases with decreasing w_0 along with a reduction in the number of electrons per $\Delta(\gamma_f - 1)$. In addition, we see from Figures 4.12a–4.12c that although the maximum γ_f as part of the cluster of electrons decreases with decreasing w_0, a few high-energy electrons ($\gamma_f - 1 \gtrsim 40$) persist for $w_0 = 2\ \mu\mathrm{m}$ (Figure 4.12c). However, we note that measuring these electrons requires significantly higher sampling as these electrons are grouped within a fixed $\Delta\theta$ for all ϕ whereas a typical energy spectrometer has a finite solid angle of acceptance with some fixed $\Delta\phi$ in addition to a fixed $\Delta\theta$.

4.3.2 Experiment

We performed an experiment with the ZEUS laser [23] at UM, to measure the energy distribution of electrons ejected at various θ for varying $\mathrm{f}/\#$. The setup is shown in Figure 4.13. To vary the $\mathrm{f}/\#$, we apodized the beam (not pictured) by adopting an approach similar to that in Figure 4.2b to switch between the native $\mathrm{f}/1.8$ of the focusing optic to an $\mathrm{f}/5$. We estimated that the apodizer transmitted $\approx 16\%$ of the laser energy incident on it as detailed in Appendix C.1.4. Although this results in a different a_0 for different w_0 due to the fixed peak power before the apodizer, which results in weaker signals for the $\mathrm{f}/5$ case, we can still measure the energy distribution for $35^\circ \leq \theta \leq 50^\circ$ to compare with the general trends observed in Figure 4.12. To



(a) (b) (c)

Figure 4.13: Experimental setup (not to scale) for measuring electron-energy distributions at UM in (a). Electrons ejected from the focus along the $\vec{B}_L$–$\vec{k}$ plane with some θ are captured by an electron energy spectrometer containing a magnetic field, $\vec{B}_S$ that deflects electrons based on their energy as shown by the three-quarter view in (b). Their final positions are recorded by an image plate at the rear surface of the spectrometer as shown by a sample measurement in (c) with corresponding horizontal and vertical line profiles (see text). The color scale denotes the PSL value within each 50×50 μm^2 pixel. The white circle represents the collimated aperture. The white dashed lines represent the aperture width projected onto the rear surface of the spectrometer, obtained by extending rays from the focus through the aperture diameter.

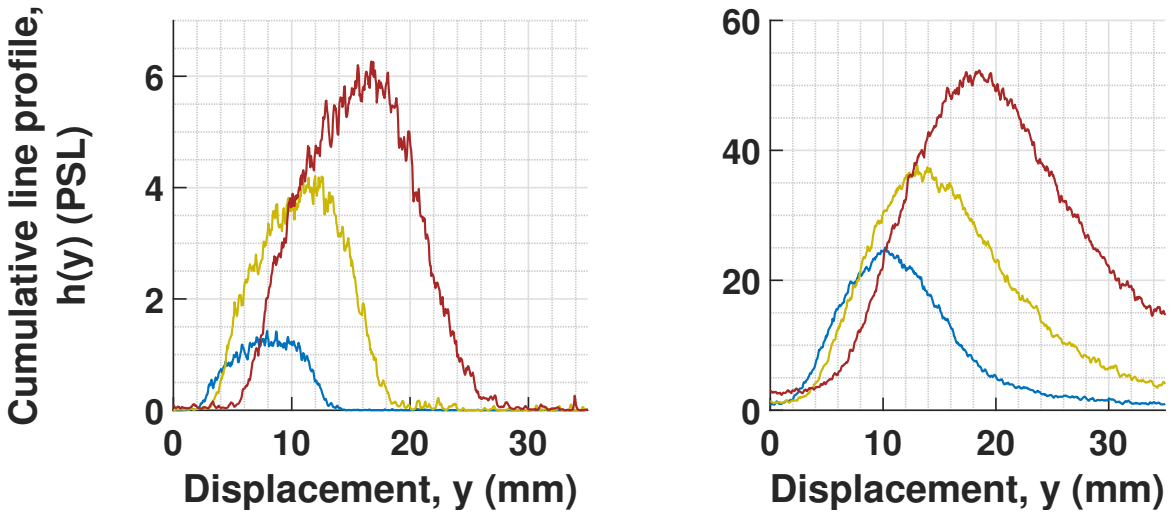
achieve this, we employed an electron energy spectrometer mounted on a rotation plate to record energy spectra for varying θ along the $\vec{B}_L$–$\vec{k}$ plane at a fixed distance from the focus as shown in Figure 4.13a. We used a tungsten aperture (thickness $12.7\ \mathrm{mm}$) with a collimated hole (diameter $3\ \mathrm{mm}$) placed directly in front of the spectrometer cartridge to limit the acceptance angle to the spectrometer. The rear surface of the aperture was $\approx 113.3\ \mathrm{mm}$ away from the focus, resulting in a maximum acceptance of $\Delta\theta = 1.5^\circ$ along the $\vec{B}_L$–$\vec{k}$ plane. Within the spectrometer cartridge, electrons encounter a magnetic field $\vec{B}_S$ due to two parallel magnets, which results in a deflection that depends on their kinetic energy as shown by the three-quarter view of a cartridge in Figure 4.13b. We used a Fujifilm BAS-MS image plate placed on the rear surface of the spectrometer cartridge to record their final positions. We show a sample measurement in Figure 4.13c. We provide the experiment conditions for various measurements in Table 4.3.

Table 4.3: Summary of experimental conditions used for measurements with the energy spectrometer.

Fig.	**Laser**	**Gas**	**f/#**	**Meas. Angle**	**Pressure (mbar)**	**No. of Shots**	**U (J)**	**τ (fs)**	**a_0**
4.14a	ZEUS	Ar	f/5	$\theta = 35^\circ$	1.43×10^{-3}	200	3.46	25	5.3
4.14a	ZEUS	Ar	f/5	$\theta = 40^\circ$	1.36×10^{-3}	200	3.42	25	3.8
4.14a	ZEUS	Ar	f/5	$\theta = 45^\circ$	1.37×10^{-3}	200	3.42	25	5.1
4.14b	ZEUS	Ar	f/1.8	$\theta = 35^\circ$	1.37×10^{-3}	200	3.43	25	14.8
4.14b	ZEUS	Ar	f/1.8	$\theta = 42.5^\circ$	1.33×10^{-3}	200	3.33	25	14.4
4.14b	ZEUS	Ar	f/1.8	$\theta = 50^\circ$	1.31×10^{-3}	200	3.39	25	12.7

For each measurement, we obtain an image as shown in Figure 4.13c. We define $g(x, y)$ as the PSL value stored in each pixel of the image plate. While the vertical position (y) of the image plate on the rear surface of the spectrometer is constrained by design resulting in negligible uncertainty in vertical positioning, the horizontal positioning (x) is relatively less constrained.

To minimize the uncertainty in the analysis due to the uncertainty in horizontal positioning of the image plate, we first obtain a cumulative horizontal line profile, $h(x) = \int g(x, y)\,\mathrm{d}y$. We then use the peak of $h(x)$ as the center of the aperture in the horizontal direction. Finally, we obtain the cumulative vertical line profile, $h(y)$, which captures the displacement of electrons as $h(y) = \int_{x_1}^{x_2} g(x, y)\,\mathrm{d}x$. Centered on the x-coordinate corresponding to the peak of $h(x)$, we use $x_2 - x_1 = 4.5\ \mathrm{mm}$ as this corresponds to the width of the $3\text{-}\mathrm{mm}$ aperture when projected onto the image plate by extending rays from the focus through the diameter in the $\vec{B}_L$–$\vec{k}$ plane. This minimizes the inclusion of background noise due to secondary emissions recorded by the image plate outside the region of interest during the 200-shot measurement sequence. We present $h(y)$ for our measurements in Figure 4.14, where smaller displacement values imply higher electron energies. Thus, the horizontal axis is qualitatively an inversion of the energy axis used in Figure 4.12.



(a) (b)

Figure 4.14: The cumulative vertical line profile, $h(y)$ (see text), is shown for spectrometer measurements performed for Ar with (a) $\mathrm{f}/5$ and (b) $\mathrm{f}/1.8$. The blue (far-left), yellow and red (far-right) curves represent measurements with the spectrometer centered at $\theta = (35°, 40°, 45°)$ in (a) and $(35°, 42.5°, 50°)$ in (b), respectively. Measurement conditions detailed in Table 4.3.

First, we see that in both the $\mathrm{f}/5$ (Figure 4.14a) and $\mathrm{f}/1.8$ (Figure 4.14b) measurements,

the energy spectra for decreasing θ consistently appear to contain higher-energy electrons. Second, we observe that the $\mathrm{f}/5$ measurements have a consistently narrower spread in displacement, and thus energy, than those performed with $\mathrm{f}/1.8$. Both of these features are in qualitatively agreement with the behavior observed in Figures 4.12d–4.12f. However, to obtain a quantitative comparison of the most probable energies with the analytical expectation from Equation (2.23), we must convert $h(y)$ to $h(\gamma_f - 1)$. Due to the construction of our spectrometer, which resulted in a non-uniform $\vec{B}_S$ in the vicinity of the aperture, determining the mapping from $h(y)$ to $h(\gamma_f - 1)$ is less straightforward and is part of ongoing work. Nevertheless, we highlight that the measurements shown in Figure 4.14 provide a proof-of-concept for the dependence on w_0 predicted in Section 4.3.1.

4.4 Ultra-Relativistic Regime (Intensities Beyond 10^{22} $\mathrm{W/cm^2}$)

In this section, we present an outlook on the dynamics of electrons in the ultra-relativistic regime $\gamma_f - 1 \gg 1$ made accessible by state-of-the-art multi-petawatt lasers that can attain $I > 10^{22}$ $\mathrm{W/cm^2}$. At these intensities, electrons are ejected to exceedingly small θ ($< 5°$). It is therefore more useful to explore how γ_f varies with a_0 as measurements of θ become less useful at such intensities. As it is most likely that a gas with a large number of ionization stages densely spanning a wide range of ionization intensities will generate electrons that can closely sample the peak intensity, we simulate the interaction of a laser pulse with Xe for varying a_0 ($= 4.83, 48.3, 216$, which correspond to $I_0 = 5 \times 10^{19}, 5 \times 10^{21}, 1 \times 10^{23}$ $\mathrm{W/cm^2}$, respectively), and fixed τ ($= 30$ fs) and w_0 ($= 5$ μm). We show the initial positions of the most energetic electrons obtained at each a_0 for an effective pressure of 10^{-6} mbar in Figures 4.15a–4.15c.

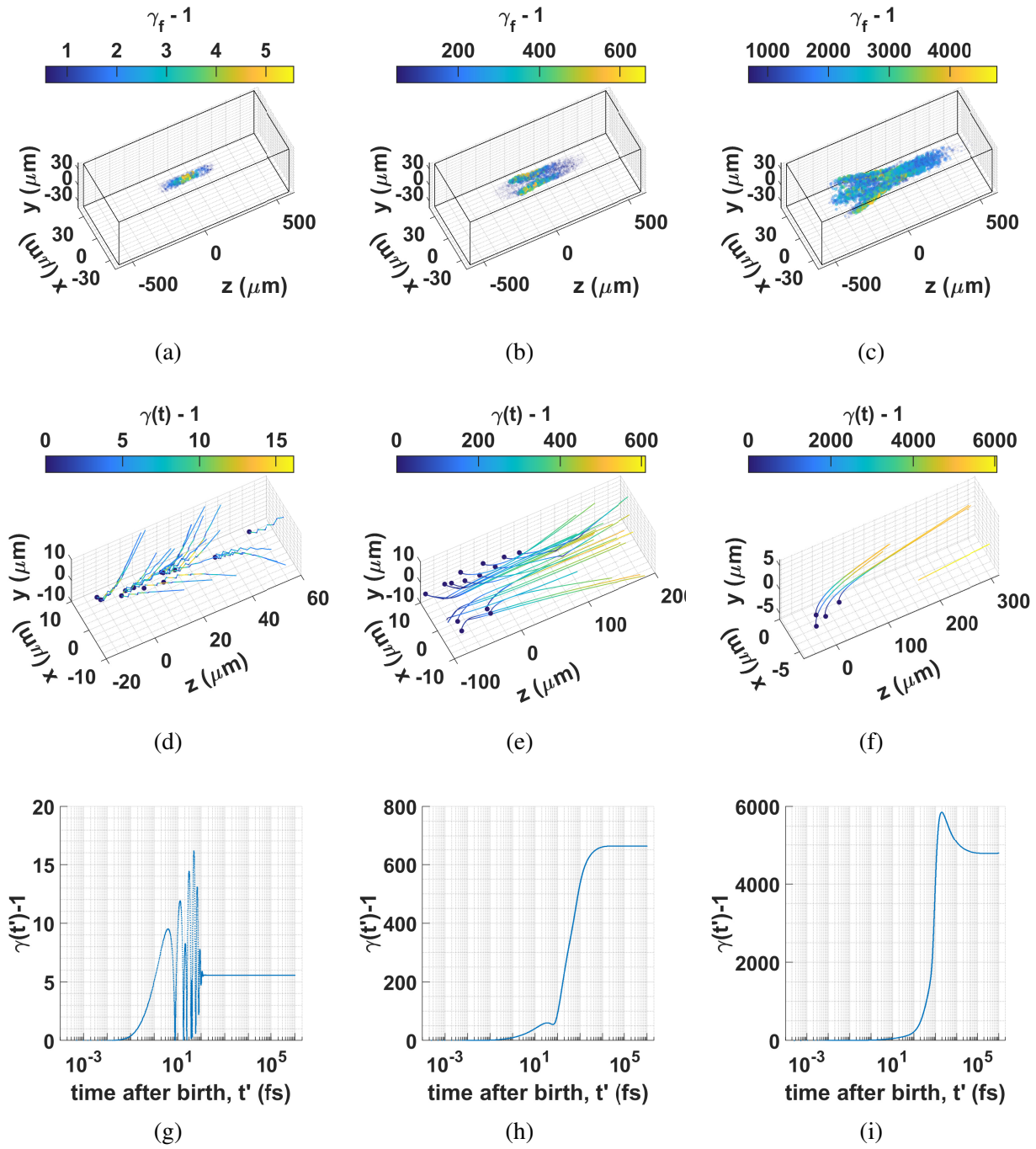


Figure 4.15: Initial positions of the most energetic electrons generated from $P = 10^{-6}$ mbar of Xe by a $\tau = 30$ fs, $w_0 = 5$ μm laser pulse with (a) $a_0 = 4.83$, (b) $a_0 = 48.3$ and (c) $a_0 = 216$, with color scale representing $\gamma_f - 1$. A representative sample of trajectories of electrons from (a)–(c) shown in (d)–(f), respectively, with color scale representing $\gamma(t) - 1$. The corresponding time dependence of $\gamma(t') - 1$ for the most energetic electron obtained is shown in (g)–(i), respectively.

We see that for low a_0, the most energetic electrons are generated near $r = 0$, which unsurprisingly corresponds to the vicinity of the peak field in a Gaussian beam. This implies that these electrons are generated in a region whose shape is similar to contours of fixed intensity. However, for very high a_0, we see that the most energetic electrons are born away from $r = 0$ and result in the formation of distinct ionization regions that are not similar to intensity contours of a Gaussian beam. To investigate this further, we recorded the corresponding trajectories of some of the most energetic electrons as shown in Figures 4.15d–4.15f and show $\gamma(t') - 1$ of the most energetic electron from each a_0 in Figures 4.15g–4.15i, respectively. We observe that as a_0 increases, the dynamics of the most energetic electrons appear less oscillatory or ponderomotive. This is because these electrons are accelerated to such high energies that they travel at nearly the speed of light in vacuum and thus undergo minimal phase lag with the laser pulse. In other words, they travel almost in phase with the laser field. A similar effect has been discussed in a slightly different context where electrons injected into the laser field with the right energy and momentum can be captured by the laser field and accelerated to large energies, also known as the Capture and Acceleration Scenario [156, 157]. The difference here, however, is that these electrons are born within the laser field at a specific phase that allows them to take such trajectories at these intensities. This results in the distinct ionization regions seen in Figure 4.15c for $a_0 = 216$, which does not reflect the intensity contour but rather a preferential-phase contour for optimal electron acceleration.

Naturally, these ionization regions depend on several factors such as the available ionization intensities and the spatiotemporal profile of the laser to name a few. It is therefore important to investigate the applicability of various ionization models at extreme intensities made available by multi-petawatt lasers as well as the accuracy of vector field models to describe a realistic laser

pulse for exploring electron dynamics in the ultra-relativistic regime. In addition, other effects such as radiation reaction may significantly affect electron dynamics as well. Finally, it is worth noting that for $I > 10^{24}$ $\mathrm{W/cm^2}$, protons start to get accelerated to relativistic speeds as its mass $m_p \approx 1836 m_e$ and $a_0 \propto 1/m$. Therefore, several aspects of relativistic electron dynamics explored herein may provide novel insight toward relativistic proton dynamics when such high intensities are made available in the future.

Chapter 5: Applications to Enabling Nonlinear QED Measurements

Portions of this chapter are adapted from:

- S. Ravichandran, M. Huault, R. Lera, C. Z. He, A. Longman, R. Fedosejevs, L. Roso, and W. T. Hill. "Imaging electron angular distributions to assess a full-power petawatt-class laser focus". *Physical Review A* 108.5 (Nov. 2023), p. 053101. *Copyright 2023 by the American Physical Society.*
- A. E. Raymond, S. Ravichandran, S.-W. Bahk, A. Longman, L. Roso, R. Fedosejevs, C. Mileham, I. A. Begishev, S. Qin, N. Dauphin, J. Shamlian, W. T. Hill, and H. G. Rinderknecht. "On-shot, high-intensity laser aberration measurements via ponderomotive electron ejection". *Physical Review A* 111.1 (Jan. 2025), p. 013121. *Copyright 2025 by the American Physical Society.*
- A. E. Raymond, S. Ravichandran, S.-W. Bahk, A. Longman, L. Roso, R. Fedosejevs, C. Mileham, I. A. Begishev, S. Qin, N. Dauphin, J. Shamlian, W. T. Hill III, and H. G. Rinderknecht. "Laser aberration signatures in expelled electrons from a tenuous gas". *Physics of Plasmas* 32.6 (June 2025), p. 062101, *with the permission of AIP Publishing.*
- S. Ravichandran, T. Cebriano, J. L. Henares, C. Mendez, J. A. Pérez-Hernández, L. Roso, R. Fedosejevs, and W. T. Hill III. "Ponderomotive expulsion: Toward creating an electron-free volume". *Physics of Plasmas* 32.9 (Sept. 2025), p. 092108, *with the permission of AIP Publishing.*

In this chapter, we review the features of electron dynamics that may be exploited to address challenges faced by precision measurements of nonlinear QED. We tackle the problem of measuring the peak laser intensity in Section 5.1, diagnosing the quality of the laser focus in Section 5.2 and creating an electron-free volume in Section 5.3.

5.1 Measuring the Peak Intensity

Here, we present a two-pronged approach to diagnose the peak intensity of the laser field in real time at full power. First, in Section 5.1.1, we employ the appearance of highly charged ion states that are associated with some appearance intensity based on an ionization model such as BSI (as tabulated in Appendix A). Second, in Section 5.1.2, we present a method to exploit

the intensity dependence of electrons ejected from the laser focus (as presented in Section 4.1) to infer the peak intensity. We performed these measurements during the same experimental campaign as in Section 4.1 using the VEGA-3 laser at CLPU.

5.1.1 Detecting Highly Charged Ions

We built a time of flight (TOF) detector that detects ions generated in the focal volume, as shown in Figure 5.1. The working principle of this detector is as follows. We apply an external electric field to accelerate ions generated by the laser in the focal volume toward a detector. These ions then travel through a field-free region with some constant speed that depends on their charge-to-mass ratio, which consequently dictates their temporal separation. We detect these ions using a microchannel plate (MCP) detector that provides the total charge deposited as a function of time. This allows us to identify various ions that have different charge-to-mass ratios appearing at different instants of time.

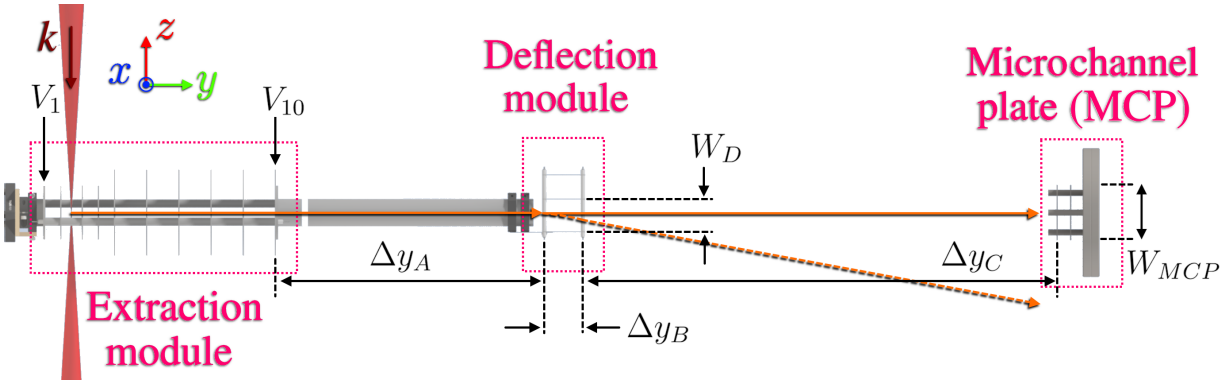


Figure 5.1: A schematic of the ion TOF detector comprising of an extraction module, deflection module and an MCP separated by field-free drift regions. A cartoon of trajectories for an ion of interest and an unwanted ion is shown by the solid and dashed orange lines, respectively. The laser focus is considered the origin, which is in between plates 2 and 3 of the extraction module. See Appendix C.3 for details about various components of the TOF detector

Specifically in our setup in Figure 5.1, we first extract ions generated in the focal volume

with the extraction module that applies an electric field along $\hat{y}$. The extraction module consists of 10 electrodes. Each electrode has a central hole to allow the ions to pass through and the i^{th} electrode is held at some constant electrostatic potential V_i such that the electric field within the volume traversed by the ions is uniform and constant. The laser focus is in between electrodes 2 and 3, and plate 10 is at some $y = y_{10}$ with $V_{10} = 0$ V. Thus, for some electrostatic potential V_F at the laser focus, the ions exit the extraction module with some kinetic energy U_{ion} and speed v_{ion} given by

$$U_{ion} = \frac{1}{2} m_{ion} v_{ion}^2 = q_{ion} V_F, \tag{5.1}$$

$$v_{ion} = \sqrt{\frac{2 q_{ion} V_F}{m_{ion}}}, \tag{5.2}$$

where m_{ion} and q_{ion} are the mass and charge of the ion, respectively. For the voltages we used, $V_F \approx 950$ V. Following the extraction module, these ions travel through a field-free region of length Δy_A until the deflection module that is effectively a parallel-plate capacitor of plate length Δy_B and separation W_D with one plate connected to ground and the other pulsed to some voltage V_D over a specific time interval. The deflection module thus applies a pulsed electric field along $-\hat{z}$ to expel unwanted ions that are readily ionized in the focal volume, such as H^+. We expel these ions to prevent damage to the MCP over repeated exposure to excessive charge deposition. We placed the MCP with diameter W_{MCP} after a second field-free region of length Δy_C due to geometric constraints associated with the vacuum chamber. As the speed of all ions along $\hat{y}$ remains unchanged following the extraction module, the time taken for an ion to travel through each stage of the TOF detector is

$$t_{ext} = y_{10}\sqrt{\frac{2m_{ion}}{q_{ion}V_F}}, \tag{5.3}$$

$$\Delta t_A = \Delta y_A \sqrt{\frac{m_{ion}}{2q_{ion}V_F}}, \tag{5.4}$$

$$\Delta t_B = \Delta y_B \sqrt{\frac{m_{ion}}{2q_{ion}V_F}}, \tag{5.5}$$

$$\Delta t_C = \Delta y_C \sqrt{\frac{m_{ion}}{2q_{ion}V_F}}, \tag{5.6}$$

resulting in a total travel time of

$$\begin{aligned} t_{tot} &= t_{ext} + \Delta t_A + \Delta t_B + \Delta t_C, \\ &= \frac{1}{\sqrt{2V_F}} \left(2\, y_{10} + \Delta y_A + \Delta y_B + \Delta y_C\right) \sqrt{\frac{m_{ion}}{q_{ion}}}. \end{aligned} \tag{5.7}$$

We provide the values used for the parameters associated with the TOF detector in Table 5.1.

Table 5.1: Summary of experimental parameters used for the TOF detector.

$\boldsymbol{V_F}$ (V)	$\boldsymbol{y_{10}}$ (mm)	$\boldsymbol{\Delta y_A}$ (mm)	$\boldsymbol{\Delta y_B}$ (mm)	$\boldsymbol{\Delta y_C}$ (mm)	$\boldsymbol{W_D}$ (mm)	$\boldsymbol{W_{MCP}}$ (mm)	$\boldsymbol{V_D}$ (V)
950	241	317	46	561	38	65	200

We determined the minimum deflection voltage for the unwanted ions as follows. To ensure that unwanted ions are displaced beyond the radius of the MCP, we need

$$|z_{f,u}| > W_{MCP}/2. \tag{5.8}$$

Within the deflection module, the ions experience a uniform electric field $E_D = V_D/W_D$, resulting in an acceleration $-q_{ion}E_D/m_{ion}\hat{z}$. During the time interval Δt_B, this produces an increase in velocity $q_{ion}E_D\Delta t_B/m_{ion}$ along $-\hat{z}$. Using Equations (5.5) and (5.6), the total displacement for an unwanted ion along $-\hat{z}$ may thus be written as

$$\begin{aligned} |z_{f,u}| &= \frac{1}{2}\frac{q_{ion}E_D}{m_{ion}}(\Delta t_B)^2 + \frac{q_{ion}E_D}{m_{ion}}\Delta t_B \Delta t_C, \\ &= \frac{1}{2}\frac{\Delta y_B}{W_D}\frac{V_D}{V_F}\left(\frac{\Delta y_B}{2} + \Delta y_C\right). \end{aligned} \tag{5.9}$$

Therefore, using Equations (5.8) and (5.9), we get

$$V_D > \frac{2W_{MCP}W_D}{\Delta y_B\left(\Delta y_B + 2\Delta y_C\right)}V_F \approx 87 \text{ V} \tag{5.10}$$

for the parameters specified in Table 5.1. We used $V_D \approx 200$ V for added clearance using a high-voltage switching circuit with rise and fall times < 60 ns when switching between 0 V and 200 V (see Appendix C.3 for more details).

We show the expected TOF based on Equation (5.7) in Figure 5.2a for ions of H, N, O. We see that as m_{ion}/q_{ion} is significantly smaller for H^+ than all other ions, it is notably separated from ions of N and O. We performed a measurement with a single laser shot ($U \approx 24$ J) and the deflection module turned off ($V_D = 0$ V) to locate the H^+ peak, shown in Figure 5.2b. We see reasonable agreement with the analytical expectation of ≈ 3.3 μs and the onset of the observed H^+ signal at ≈ 3.6 μs. Further, we observe that there are no other significant peaks in Figure 5.2b, plausibly due to the MCP being overloaded by the H^+ peak. We then turned on the deflection

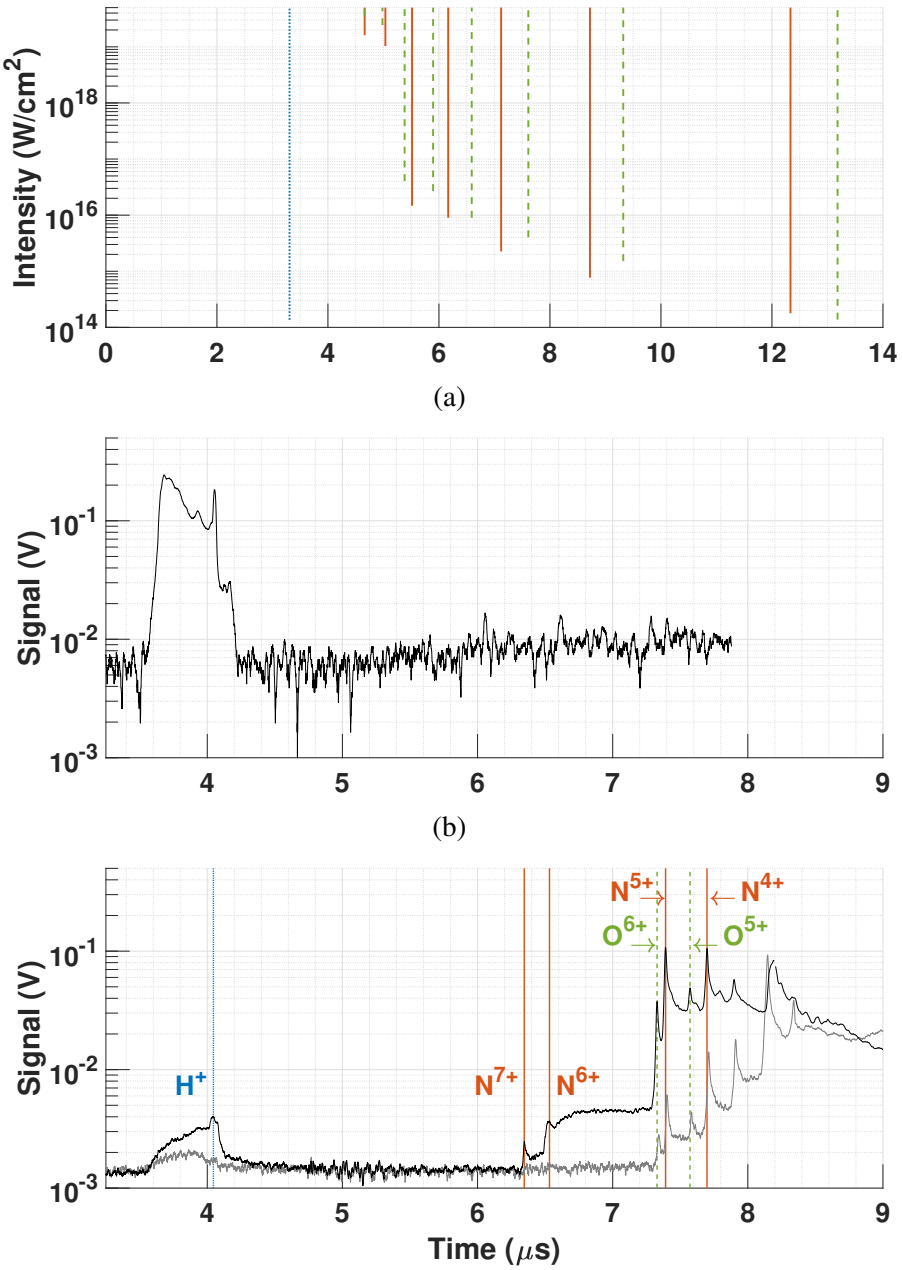


Figure 5.2: Analytically expected TOF in (a) for H^+, all ions of N and O shown by blue dotted, orange solid and green dashed lines, respectively, with the ionization stage decreasing from left to right starting with N^{7+} and O^{8+}. The starting point of each line represents the ionization intensity assuming BSI (Appendix A). Measured TOF signal (b) for a single laser shot with $U \approx 24$ J and deflection module turned off, and (c) averaged over 60 (26) shots with $U \approx 9.1$ J (0.96 J) shown by the black (gray) curve and deflection module turned on. Vertical lines denote the TOF of relevant ions (see text).

module ($V_D = 200$ V) for the following laser shots to deflect the excessive H^+ signal. We show the average signal obtained over 60 (26) laser shots using $U \approx 9.1$ J (0.96 J) with the chamber back filled with 5×10^{-5} (8×10^{-5} mbar) of ambient air in Figure 5.2c, after applying a temporal moving average noise filter with a 10 ns window.

We see that while the analytical expression predicts ion peaks from $\gtrsim 4.5$ μs (Figure 5.2a), we only observe distinct peaks from $\gtrsim 6.3$ μs (Figure 5.2c). While an ideal TOF spectrometer exhibits a time of flight scaling proportional to $\sqrt{m_{ion}/q_{ion}}$, deviations may arise in realistic implementation due to factors such as Coulomb explosion during strong-field ionization that imparts some initial energy spread. However, it is still possible to identify the peaks based on the following. Starting with the $U \approx 0.96$ J measurement, we see the presence of two pairs of peaks between ≈ 7.3 μs to 7.6 μs, with each pair containing a relatively weak and a relatively strong peak. As we know the ratio of N to O in air is $\sim 4:1$, it is straightforward to associate the stronger peaks with N and the weaker peaks with O. Further, we know from low-power measurements (Section 4.1.2.1) that assuming $I_0 \propto U$, even at $U \sim 1$ J, $I_{infer} \gg 10^{16}$ W/cm^2. This implies that with $U \approx 0.96$ J, we readily generate N^{5+} ($I_{th} \sim 10^{16}$ W/cm^2) over a large volume in the focus and it is therefore likely that we can detect N^{5+} for the measurement with $U \approx 0.96$ J. We see that when we ramp up the laser energy from ≈ 0.96 J to 9.1 J, however, while the time of arrival of most peaks largely remain unchanged as expected, two new peaks appear at ≈ 6.3 μs and 6.5 μs. As $I_{infer} \sim 7 \times 10^{19}$ W/cm^2 and 7×10^{18} W/cm^2 when $U \approx 9.1$ J and 0.96 J, respectively, the two new peaks when the pulse energy increases must correspond to N^{6+} and N^{7+} as their $I_{th} \sim 10^{19}$ W/cm^2. Therefore, with $U \sim 10$ J the TOF measurements show that we attain $I > 10^{19}$ W/cm^2.

5.1.2 Detecting Relativistic Electrons (With Scintillators)

While it is possible to obtain a reasonable lower bound on the peak intensity by detecting ions generated within the focal volume, employing a TOF detector is not straightforward and the diagnostics can be intrusive to the region near the focal volume. Therefore, it is beneficial to measure the peak intensity based on the intensity-dependence of electron dynamics discussed in Section 4.1. Here, we present a straightforward diagnostic that allows single-shot detection of electrons ejected from the focal volume using a scintillation detector placed in the $\vec{E}$-$\vec{k}$ plane as shown in Figure 5.3a.

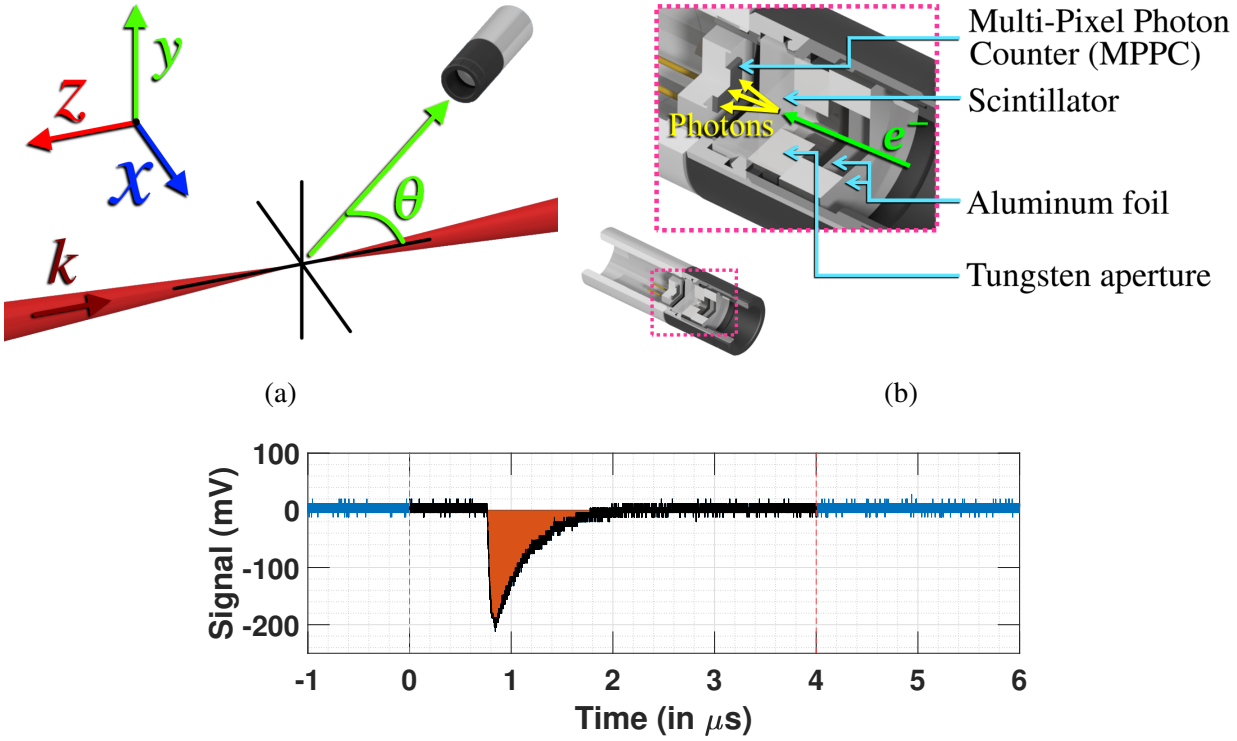


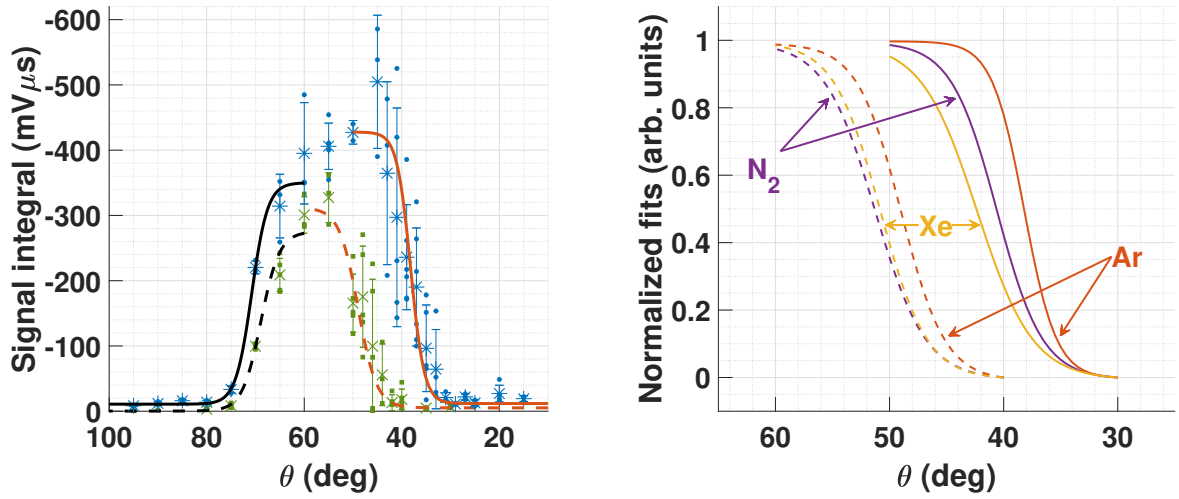
Figure 5.3: Experimental setup of the scintillation detector for electrons in (a), with individual components of the detector shown using a quarter-section view in (b). A representative measurement of the photon signal recorded by the MPPC for a single shot is shown in (c). The area under the curve (orange shaded region) represents the signal integral for the shot.

Table 5.2: Summary of experimental conditions used for measurements with the scintillation electron detectors. The U and τ reported here is the average value obtained over the corresponding sequence of shots. The techniques used to measure U and τ are detailed in Section 4.1.2.1.

Gas	**U (J)** **[±10%]**	**τ (fs)** **[±20%]**	**$a_{0,infer}$** **[±12%]**	**Pressure (mbar)**
N_2	10.6	35.6	6.2	5×10^{-5}
	26.9	40.4	9.2	3×10^{-5}
Ar	10.2	30.3	6.6	9×10^{-5}
	26.7	38.7	9.4	9×10^{-5}
Xe	10.0	31.5	6.4	4×10^{-5}
	26.4	49.7	8.2	4×10^{-5}

Figure 5.3b shows the composition of the detector. We placed a bismuth germanate scintillator crystal (thickness 3 mm) in front of a Hamamatsu MPPC (Multi-Pixel Photon Counter) [158] that records the photon signal generated in the scintillator upon irradiation by electrons. We used a tungsten disk (thickness 3 mm) with a 3 mm hole as an aperture to limit the acceptance angle from the focus to ≈ 0.37 msr for the detector placed ≈ 138 mm away, mounted such that we can vary θ at a fixed distance from the focus. We used two layers of Al foil (each with thickness 12 μm) to block scattered laser light and the abundant low-energy electrons $\lessapprox 70$ keV. In addition, we used a single layer of aluminized mylar (thickness 2 μm, coated with 100 nm of Al on each side) to cover the front of the detector for added light tightness. Figure 5.3c shows an example of the signal measured on a single shot, which we then integrate over an appropriate time interval to obtain the net response for each shot. We provide experimental conditions for the various measurements that we performed in Table 5.2.

In Figure 5.4a, we plot the signal integral for each laser shot at varying angular positions of the detector using Ar at low ($U \approx 10.2$ J) and high ($U \approx 26.7$ J) laser energy. By fitting a sigmoid for $\theta > 60^\circ$ (shown in black), we show that the large-angle falloff is independent



(a) (b)

Figure 5.4: Scintillation detector data from the Ar gas measurements in (a). The low (high) energy data are shown by green (blue) squares (dots), the average at each measurement position shown by "×" ("*") and corresponding standard deviations marked by the error bars. The dashed (solid) orange and black lines are sigmoid fits to the small and large angle falloff, respectively, for the low (high) energy measurement. Normalized and background subtracted sigmoid fits for the small angle falloff of measurements performed with N_2 (violet), Ar (orange) and Xe (yellow) in (b). The dashed (solid) curves correspond to low (high) energy measurements. The experimental conditions used for all measurements with the scintillation detector are given in Table 5.2.

of the laser intensity and is caused by the Al foil that blocks electrons with $\lessapprox 70$ keV [159]. This large-angle falloff at $\theta \approx 75^\circ$ is also roughly consistent with the energy predicted from Equation (2.23). We highlight the shift in the small-angle falloff with a sigmoid fit in the range $\theta < 60^\circ$ and $\theta < 50^\circ$ for the low and high energy cases, respectively. Figure 5.4b shows the sigmoid fits for the small-angle falloff for all the measurements in Table 5.2, which is consistent with the results from Section 4.1 in that the electrons are ejected at smaller angles for higher $a_{0,infer}$. The sensitivity of this method to shot-to-shot variations, as demonstrated in Figure 5.4a, thus holds promise for employment as a straightforward, real time diagnostic of the peak intensity at full power.

5.2 Diagnosing Laser Aberrations

As discussed briefly in Section 4.1, we see from image plate measurements over several shots in Figure 4.4 that consistent and distinct features appear in the spatial distribution of electrons (Figures 4.4a–4.4c) when the focal spot of the laser appears to contain aberrations (Figures 4.3a–4.3c). In contrast, when the focal spot appears relatively less aberrated (Figure 4.3d), the resulting spatial distribution of electrons appears to be more symmetric (Figure 4.4d). This indicates that measuring the spatial distribution of ejected electrons could potentially diagnose the spatial quality of the laser focus at full power [139]. To test this, we performed an experiment with the MTW laser at LLE (setup in Figure 4.7) to determine whether it is possible to reproducibly induce a feature in the spatial distribution of electrons by intentionally introducing a specific aberration to the laser profile.

To introduce specific aberrations at the focal plane, we employed a feedback mechanism

Table 5.3: Summary of experimental conditions used for measurements with varying laser aberrations. The nominal parameters applicable to all the measurements are $\mathrm{f}/2.8$, $\lambda_0 = 1.05\ \mu\mathrm{m}$, $\tau \approx 700\ \mathrm{fs}$ and $d = 25\ \mathrm{mm}$. All measurements were single shot. The Zernike index used here is based on the Fringe indexing scheme.

Fig.	**Aberration Name**	**Zernike Index**	**Gas**	**Pressure (mbar)**	**U (J)**
5.5a	Oblique astigmatism	6	N_2	6.67×10^{-4}	7.6
5.5b	Oblique astigmatism	6	N_2	6.67×10^{-4}	8.7
5.5c	Oblique astigmatism	6	N_2	6.67×10^{-4}	7.6
5.5d	Oblique astigmatism	6	Ar	1.13×10^{-3}	7.4
5.5e	Oblique astigmatism	6	Ar	1.13×10^{-3}	7.5
5.5f	Oblique astigmatism	6	Ar	1.13×10^{-3}	7.4
5.6a	Coma (parallel)	7	N_2	6.67×10^{-4}	7.3
5.6b	Coma (parallel)	7	N_2	6.67×10^{-4}	7.5
5.6c	Coma (parallel)	7	N_2	6.67×10^{-4}	7.5
5.6d	Coma (parallel)	7	Ar	1.13×10^{-3}	7.4
5.6e	Coma (parallel)	7	Ar	1.13×10^{-3}	7.4
5.6f	Coma (parallel)	7	Ar	1.13×10^{-3}	7.6

integrating the focal spot imaging system with a programmable spatial light modulator (PSLM), placed before the final amplifier and pulse compressor. In essence, the PSLM optimizes the weights of Zernike polynomials [160], which form a convenient basis set to describe aberrations in optics, based on the required output. For simplicity, we varied the amplitude of each polynomial individually. We provide the experimental parameters in Table 5.3 for measurements with varying magnitudes of oblique astigmatism in Figure 5.5 and coma parallel to the polarization axis in Figure 5.6. The focal spot images for these measurements is shown in Figure 3 of [154].

First, we see that the measurements performed with N_2 are relatively less populated compared to those with Ar. This is due to fewer electrons being available for ionization near the peak intensity with N ($n = 1$ shell) than in Ar ($n = 2$ shell), which contribute to the signal recorded at these angles, as discussed in Section 4.2. Second, we see that as the magnitude of the aber-

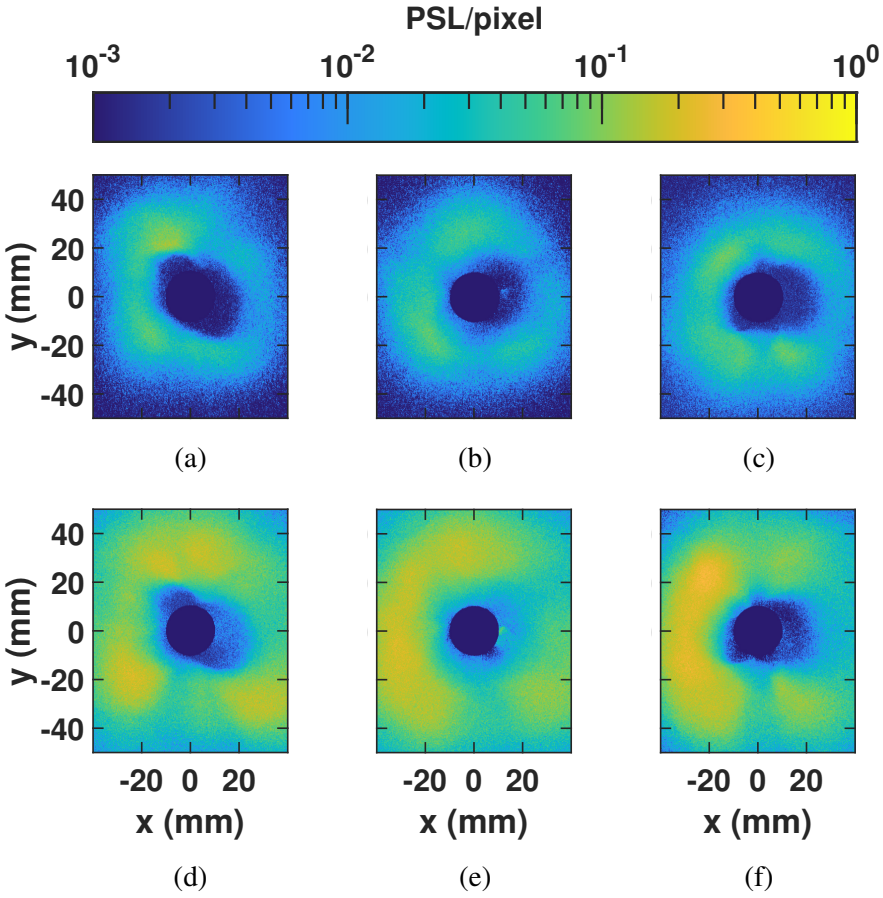


Figure 5.5: Image plate data captured for varying Astigmatism introduced at 45° to the polarization axis where the left, middle and right plots represent an aberration magnitude of $-\lambda_0/2, 0$ and $+\lambda_0/2$ in peak-to-peak wavefront distortion, while the top and bottom row represent measurements performed with N_2 and Ar, respectively. The color scale denotes the the PSL deposited in each 50×50 $\mu\mathrm{m}^2$ pixel across the plane. Polarization axis is along the vertical direction in each measurement.

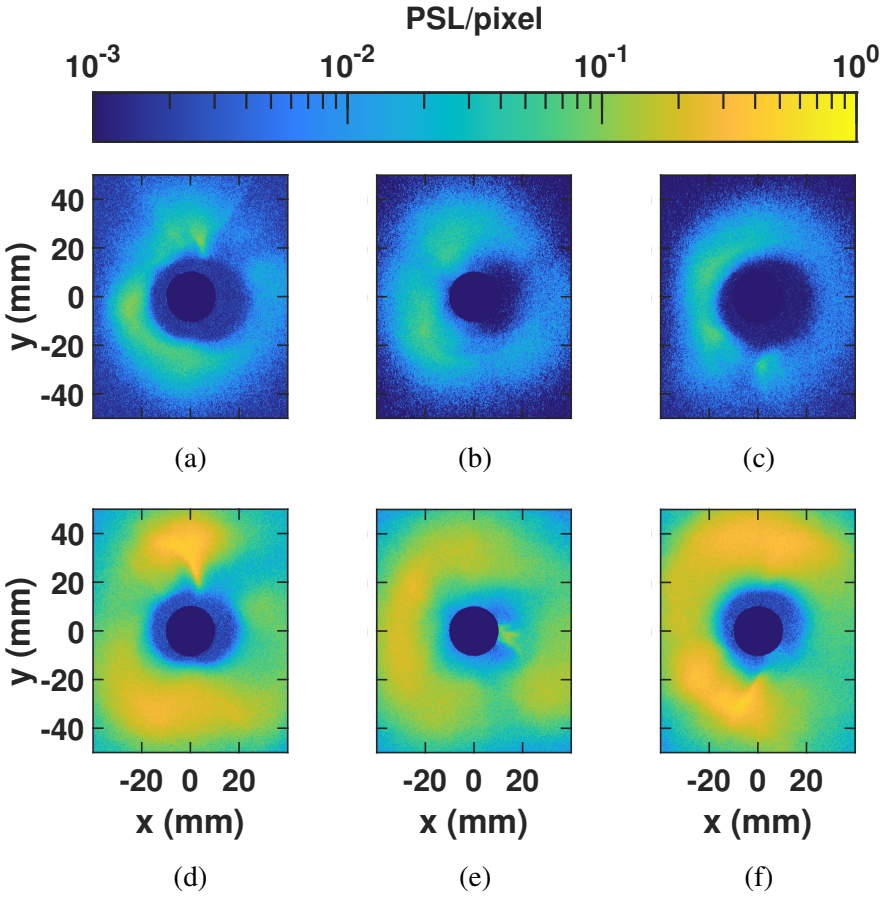


Figure 5.6: Image plate data captured for varying Coma introduced along the polarization axis where the left, middle and right plots represent an aberration magnitude of $-\lambda_0/2, 0$ and $+\lambda_0/2$ in peak-to-peak wavefront distortion, while the top and bottom row represent measurements performed with N_2 and Ar, respectively. The color scale denotes the the PSL deposited in each $50 \times 50\ \mu\mathrm{m}^2$ pixel across the plane. Polarization axis is along the vertical direction in each measurement.

ration varies within each row, the distribution has consistent features that appear in both N_2 and Ar across the two rows in each figure. Specifically in Figure 5.5, where we introduced oblique astigmatism, we see an elongation of the nominal ring-like distribution along the line $y = -x$ in both Figures 5.5a and 5.5d, and along the line $y = x$ in both Figures 5.5c and 5.5f. Similarly in Figure 5.6, where we introduced coma parallel to the polarization axis, we see a sharp pinching of electrons along $+\hat{y}$ in both Figures 5.6a and 5.6d, and along $-\hat{y}$ in both Figures 5.6c and 5.6f. This implies that the aberrations introduced in the focal spot directly affect the resultant spatial distribution of electrons. Conversely, the spatial distribution of electrons is directly influenced by the aberrations within the focal spot.

In the long-term, it may be possible to exploit this feature to develop machine learning algorithms that can solve the inverse problem of identifying aberrations in the focal spot based on the spatial distribution of electrons. This will require generating a vast library of electron distributions for various aberration types and magnitudes, which can then be used as training datasets. Therefore, measuring the spatial distribution of electrons ejected from the focal volume provides a path forward to enable real time measurement of the laser aberrations at full power.

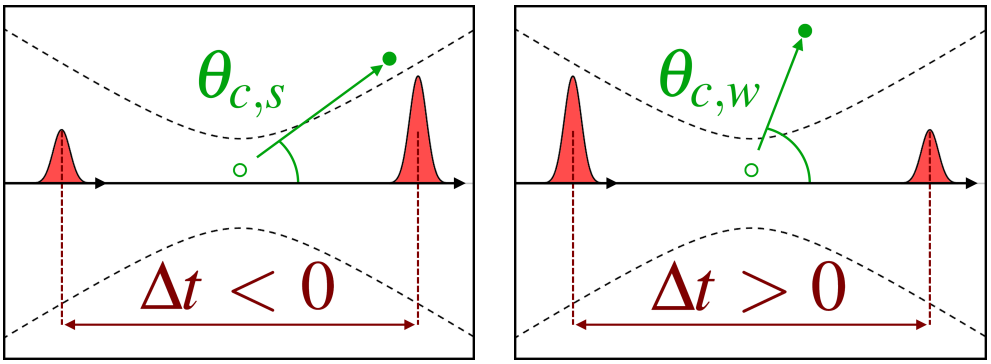
5.3 Creating an Electron-Free Volume Through Ponderomotive Expulsion

Creating a focal volume devoid of free electrons and incapable of producing any more prior to arrival of the main pulse(s) in QVAC experiments is a critical need to enable precision measurements of the QVAC as discussed in Section 1.2.1. One approach to expel electrons from rarefied gas particles is to allow a fraction of the laser energy to pass through the focus, known as a “pre-pulse” or “pedestal,” before the main pulse. It is expected that the pre-pulse or pedestal

of sufficient intensity will ionize and clear resultant electrons via ponderomotive expulsion. In this section, we demonstrate with experimental evidence a proof of concept to clear the laser focal volume of free electrons and disable their atomic and molecular sources using two pulses in copropagating geometry to mimic clearing with a pre-pulse [161].

5.3.1 Overview of Clearing Mechanism

As electrons are ejected from the focal volume due to a laser pulse, we can directly probe the number of electrons available within the focal volume by measuring the spatial distribution of the ejected electrons. Therefore, by deploying two copropagating laser pulses separated in time, we can observe the effect of allowing a pulse to pass through the focal volume before a trailing pulse. Through this, we can investigate the clearing mechanism of a pre-pulse, i.e., a fraction of the laser energy passing before the main pulse, and gain insights toward requirements for efficient clearing.



(a) (b)

Figure 5.7: A cartoon representing the minimum angle of ejection for the (a) strong pulse, $\theta_{c,s}$ and (b) weak pulse, $\theta_{c,w}$.

The first laser pulse liberates and accelerates electrons from rarefied gas ($\sim$ few $\times 10^{-4}$ mbar, $\gtrsim 90\%$ He) in the focal volume. The second laser pulse probes the focal volume a few

hundred femtoseconds later. This allows us to detect electrons that may have remained in the focal volume after the first pulse. Here, we use two pulses named strong and weak, separated by a time delay Δt. We define $\Delta t < 0$ ($\Delta t > 0$) when the strong (weak) pulse leads the weak (strong) as shown in Figure 5.7a (Figure 5.7b). The discernibility of electrons ejected from the focal volume in either case is based on the notable difference in peak intensities of the strong and weak pulses, I_{0s} and I_{0w}, respectively, i.e., $I_{0s} > I_{0w}$. Here, $I_{0w} \gg 10^{16}$ W/cm^2 $\sim$ the intensity required to doubly ionize He, implying that both laser pulses can deplete electrons from He over a large hourglass-like volume contained within $\rho \lesssim 13w_0$ and $|z| \lesssim 31z_R$, where ρ is the radial distance from the laser axis, z is the distance from the focal plane along the laser axis. When the strong pulse leads the weak, we expect that electrons liberated by the strong pulse are ejected at some $\theta \geq \theta_{c,s}$. When the weak pulse leads the strong, however, we expect that the weak pulse expels most electrons from the focal volume over $\theta \geq \theta_{c,w}$, leaving behind a paucity of electrons to be ejected by the strong pulse. As $\tan\theta_c \propto 1/\sqrt{I_0}$ and $I_{0w} < I_{0s}$, we expect that $\theta_{c,w} > \theta_{c,s}$ as depicted by the cartoon in Figures 5.7a and 5.7b. Therefore, we expect the yield of electrons for $\theta_{c,s} < \theta < \theta_{c,w}$ to be lower when the weak pulse leads the strong pulse, relative to when the strong pulse leads the weak pulse, or when the weak pulse is absent.

5.3.2 Observing Electron Clearing

5.3.2.1 Simulation

We demonstrate the design of the experiment by simulating the interaction of electrons generated from He with two copropagating laser pulses having Gaussian beam profiles using the approach detailed in Section 3.3. To describe two pulses with perfect overlap of focal volumes,

using Equations (3.16) and (3.17), we write the fields of the strong pulse as

$$\begin{aligned} \vec{E}_s(x,y,z,t) &= \vec{E}_L(x,y,z,t), \\ \vec{B}_s(x,y,z,t) &= \vec{B}_L(x,y,z,t), \end{aligned} \tag{5.11}$$

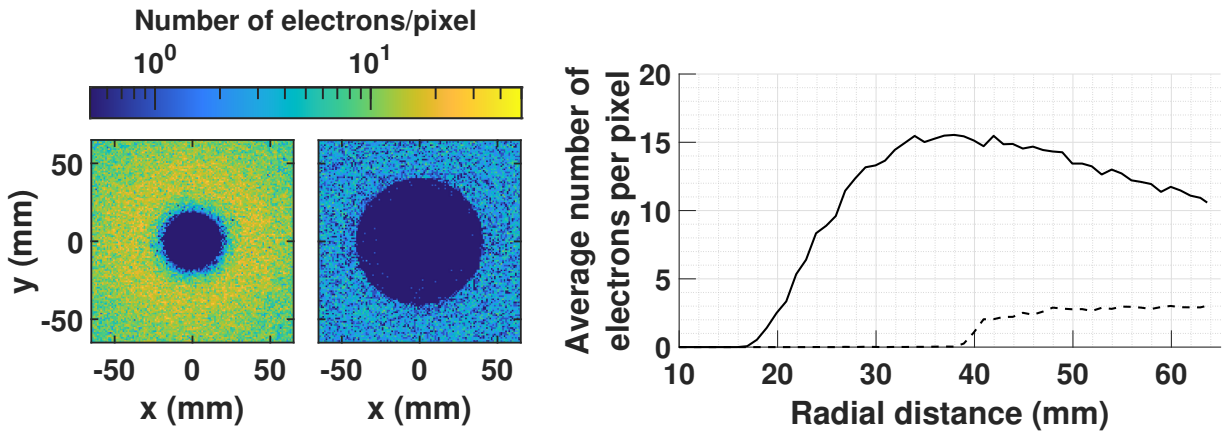
and those of the weak pulse as

$$\begin{aligned} \vec{E}_w(x,y,z,t) &= \frac{E_{0w}}{E_0}\,\vec{E}_L(x,y,z,t+\Delta t), \\ \vec{B}_w(x,y,z,t) &= \frac{E_{0w}}{E_0}\,\vec{B}_L(x,y,z,t+\Delta t). \end{aligned} \tag{5.12}$$

Here, $E_0 = \sqrt{2I_{0s}/(c\epsilon_0)}$, $E_{0w} = \sqrt{2I_{0w}/(c\epsilon_0)}$, and ϵ_0 is the permittivity of free space. For all simulations presented in this section (Section 5.3), we used $I_{0s} = 5 \times 10^{19}$ W/cm^2 and $I_{0w} = 1.25 \times 10^{19}$ W/cm^2. We assume the same beam waist $w_0 = 10$ μm for both beams for simplicity.

In Figures 5.8a and 5.8b we show the simulated spatial distribution of electrons captured by a plane, which is perpendicular to the laser axis ($\hat{z}$) and 30 mm after the laser focus, when the strong and weak pulse lead by 300 fs, respectively. We characterize each two-dimensional image of the electron distribution with $N_e(\Delta t, \rho)$ in Figure 5.8c. Here,

$$N_e(\Delta t, \rho) = \frac{1}{2\pi}\int_{\phi=0}^{\phi=2\pi} n_e(\Delta t, \rho, \phi)\,\mathrm{d}\phi \tag{5.13}$$



(a) (b) (c)

Figure 5.8: Spatial distribution of ejected electrons simulated when the (a) strong pulse and (b) weak pulse leads the other by 300 fs with perfect overlap of focal volumes. Distributions simulated 30 mm after the focus on a plane perpendicular to the laser axis passing through the origin. The color scale denotes the number of electrons in each 1×1 mm^2 pixel across the plane. The average number of electrons for varying distance from the laser axis is shown by the solid and dashed lines in (c) for simulations in (a) and (b), respectively.

is the average number of electrons deposited per pixel vs the radial distance ρ from the laser axis, where $n_e(\Delta t, \rho, \phi)$ is the number of electrons incident on a pixel at some (ρ, ϕ) on the image plate. We see that the electron yield is significantly reduced when the weak pulse leads the strong pulse. Therefore, our goal is to measure the spatial distribution of ejected electrons and compare the resulting ϕ-averaged line profiles for $\Delta t > 0$ (weak pulse leading) and $\Delta t < 0$ (strong pulse leading). A reduction in electron yield for varying θ when $\Delta t > 0$ relative to $\Delta t < 0$ will provide evidence of ponderomotive expulsion from the focal volume.

5.3.2.2 Experiment

We used the VEGA-3 laser beamline at CLPU [162] for our experiment (schematic in Figure 5.9a). The nominal pulse energy was ~ 25 J and duration ~ 40 fs. We split the fully amplified pulse before the pulse compressor using a Mach-Zehnder interferometer to create two copropa-

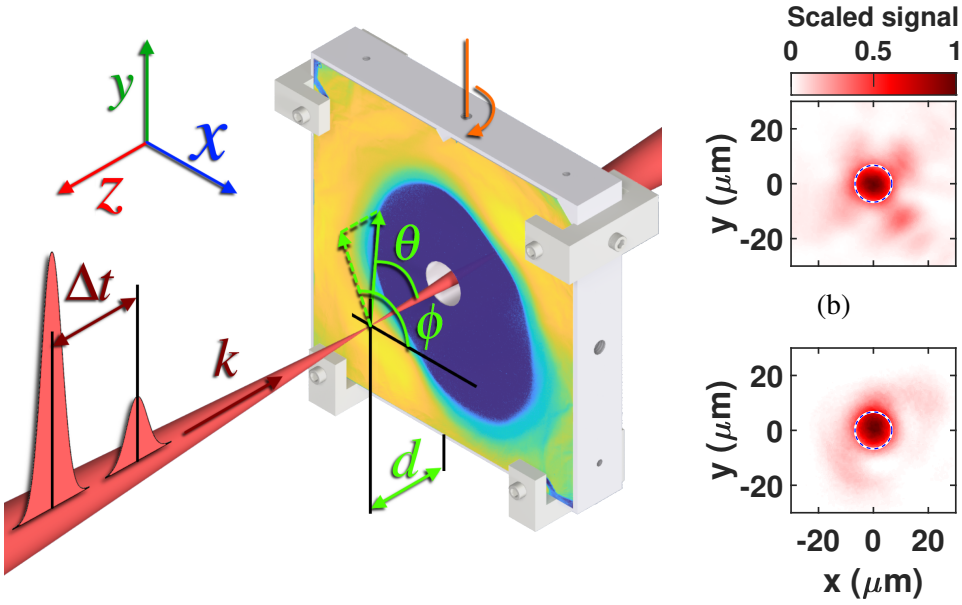


Figure 5.9: Schematic of the experimental setup (a) and typical isolated focal-spot images of the strong (b) and weak (c) pulses. The laser pulses propagate along $-\hat{z}$, polarized predominantly along $\hat{x}$ and separated in time by $\pm|\Delta t|$. The circular blue-white dashed line represents the full width at half maximum ($\approx 13.4\ \mu\mathrm{m}$) in (b) and (c). A pair of image plates are loaded onto the image-plate holder that can rotate about the vertical axis indicated in orange.

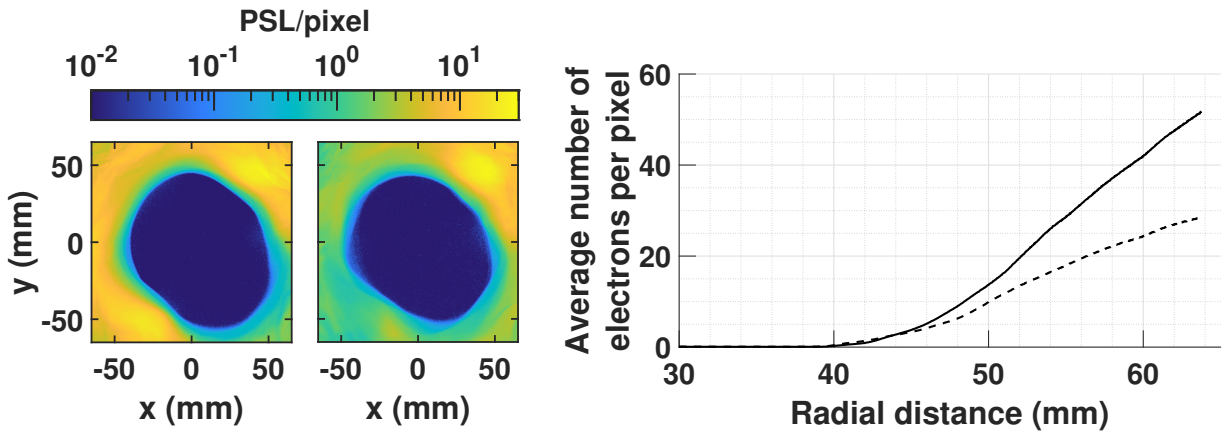
gating pulses with $\sim$ 10 J and 2.5 J (see Appendix C.4 for details). The beam transport system following the interferometer delivered $\sim 87\%$ of the energy to the focal plane. The nominal beam diameter at the Mach-Zehnder interferometer was ~ 10 cm. We used an apodizer of diameter 6 cm on the lower-energy beam arm to improve the spatial quality of the weak pulse at the focus. We verified spatial overlap of the two foci prior to each measurement by imaging a series of 20 shots at low power after setting the desired time delay. The relative spatial separation between the peaks of the two beams was less than the full width at half maximum (see Appendix C.4). We also used the autocorrelation measurement, which in the presence of two pulses contains a pair of secondary peaks spaced $\pm|\Delta t|$ away from the main peak, to verify that the set delay is delivered to the target chamber. We inferred the nominal peak intensities in the experiment, $I_{0s} \sim 6.6 \times 10^{19}$ W/cm^2 ($a_{0s} \approx 5.6$) and $I_{0w} \sim 7 \times 10^{18}$ W/cm^2 ($a_{0w} = 1.8$) for the strong and weak pulse by distributing the peak power over the focal spot images in Figure 5.9b and 5.9c, respectively, using the approach detailed previously in Section 4.1.2.1.

As He is fully ionized at non-relativistic intensities $\sim 10^{16}$ W/cm^2, which is sufficient to split H_2 into two protons and two electrons, we used He gas to mimic the gaseous composition of a high-vacuum environment where H_2 is most prevalent. We backfilled the chamber to $\approx$ 2.75×10^{-4} mbar of He from a base pressure $\sim$ a few $\times$ 10^{-5} mbar and used a residual gas analyzer to ensure that the partial pressure of He was $\gtrsim 90\%$ during operation, with other gases such as N_2, H_2O, O_2 making up the rest.

We used a Fujifilm BAS-MS image plate placed at a distance $d = 30$ mm after, and facing, the laser focus to detect ejected electrons on a plane perpendicular to the laser axis, $\vec{k}$, as shown in Figure 5.9. The size of the image plate was ≈ 148 mm $\times$ 148 mm with a 20-mm diameter hole cut in the center to allow the laser to pass through. We covered the image plate with an

aluminum foil (thickness 12 μm) to make it insensitive to laser light. We used a holder designed to accommodate two image plates at once such that one faces the laser focus during measurement while the other faces away. We made the holder using PEEK plastic of sufficient thickness, 25.4 mm, to ensure that the image plate facing away was not exposed to electrons from the focus during measurement. Each measurement sequence consisted of 50 shots, each of which included both pulses. After completing one measurement, we rotated the holder by 180° about an axis centered within the thickness of the holder intersecting the laser axis to interchange the image plates for the second measurement as shown in Figure 5.9. Then, we vented the vacuum chamber to scan the image plates. We made one measurement with $\Delta t = |\Delta t|$ (> 0) and another with $\Delta t = -|\Delta t|$ (< 0) within one vacuum cycle to minimize the role of systematic uncertainties, such as variations in pulse duration or focal spot quality, which can affect the peak intensity. Image plate measurements from a single vacuum cycle corresponding to $\Delta t = \pm 300$ fs are shown in Figures 5.10a and 5.10b.

To obtain $N_e(\Delta t, \rho)$ from our measurements we followed a two-step process: (i) obtain $n_e(\Delta t, \rho, \phi)$ by converting the PSL value per pixel into an estimate of the number of electrons per pixel, accounting for the angle-dependent electron energy and the response functions of the filters and image plates; and (ii) calculate $N_e(\Delta t, \rho)$ using Equation (5.13). To achieve (i), we perform the following procedure. We first define $g(\Delta t, \rho, \phi)$ as the PSL value stored in a pixel located at some (ρ, ϕ) on the image plate. We account for the acute incidence angle of electrons on the image plate that results in a larger PSL deposited relative to that under normal incidence by a factor of $1/\cos\theta$, where $\theta = \tan^{-1}(\rho/d)$. Under paraxial conditions, we assume Equation (2.23) to estimate the average energy lost by an electron with kinetic energy $(\gamma(\rho) - 1)m_e c^2$ passing through an Al filter of thickness $12\ \mu\text{m}/\cos\theta$. We use the continuous slowing down approxima-



(a) (b) (c)

Figure 5.10: Spatial distribution of ejected electrons measured when the (a) strong pulse and (b) weak pulse leads the other by 300 fs. Distributions measured 30 mm after the focus on a plane perpendicular to the laser axis passing through the origin. The color scale denotes the the PSL deposited in each 50×50 μm^2 pixel across the plane. The average number of electrons for varying distance from the laser axis is shown by the solid and dashed lines in (c) for measurements in (a) and (b), respectively.

tion range for Al [159, 163] and define the average loss in kinetic energy as $L_{KE}(\rho)$. We then find the PSL value that a single electron with an effective kinetic energy $\approx (\gamma(\rho)-1)m_ec^2 - L_{KE}(\rho)$ would deposit on average in a BAS-MS image plate, based on calibrations performed in [147] and call it $h(\rho,\phi)$. The number of electrons thus incident on a pixel at given ρ and ϕ may be estimated as $n_e(\Delta t,\rho,\phi) = g(\Delta t,\rho,\phi)\sqrt{1+\rho^2/d^2}/h(\rho,\phi)$. Figure 5.8c shows $N_e(-300\text{ fs},\rho)$ and $N_e(300\text{ fs},\rho)$ for measurements in Figures 5.10a and 5.10b, respectively.

5.3.2.3 Comparing Measurements with Theory

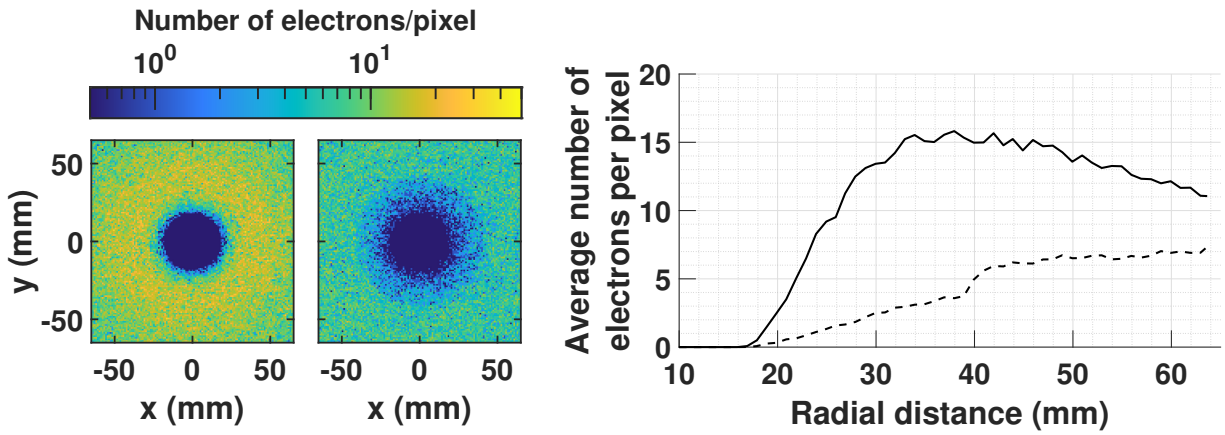
Electrons are cleared from the focal volume by the weak pulse if the ϕ-averaged line profile $N_e(\Delta t,\rho)$ is reduced when the weak pulse leads relative to when the strong pulse leads. This is shown both by simulation and experiment in Figures 5.8c and 5.10c, respectively, implying that clearing is observed at $|\Delta t| = 300$ fs. However, we see two features in Figure 5.8c that do not

accurately reflect the experiment. Namely, (i) N_e rises as early as $\rho \approx 17$ mm in Figure 5.8c while it rises at $\rho \approx 40$ mm in Figure 5.10c, and (ii) N_e appears distinctly different in Figure 5.8c depending on which pulse leads, i.e., rises at different ρ and shows significantly different signal strengths. This implies that realistic features, which are not captured in the simulations, play a major role in the experiment. These may be addressed as follows.

If the peak intensity of the strong pulse delivered in the experiment is lower than that used in the simulations, θ_c will be larger in the experiment than in the simulation, i.e., N_e will begin to rise at larger ρ in the experiment (as $\rho = d\tan\theta$), which can partly explain (i). Any relative spatial fluctuation of the focal volumes of the two beams leading to reduced overlap from shot to shot makes the observed electron distributions less distinct, which can partly explain (ii). This is because each pulse may interact with a volume of gas that is not affected by the other. We show this using simulations that model a randomized relative spatial fluctuation as follows. We included a relative spatial separation between the two laser axes on each shot by applying a shift of coordinates to the weak pulse prior to calculating the total field. The shift along the $\vec{x}$ and $\vec{y}$ axes are given by δx and δy, which vary randomly for different iterations of the simulation such that $\sqrt{(\delta x)^2 + (\delta y)^2} \leq 2w_0$, thus replacing Equation (5.12) with

$$\begin{aligned} \vec{E}_w(x,y,z,t) &= \frac{E_{0w}}{E_0}\,\vec{E}(x+\delta x, y+\delta y, z, t+\Delta t), \\ \vec{B}_w(x,y,z,t) &= \frac{E_{0w}}{E_0}\,\vec{B}(x+\delta x, y+\delta y, z, t+\Delta t). \end{aligned} \tag{5.14}$$

This models a weak pulse whose center is separated from the center of the strong pulse at most by $2w_0$ at arbitrary ϕ along the transverse plane on each shot.



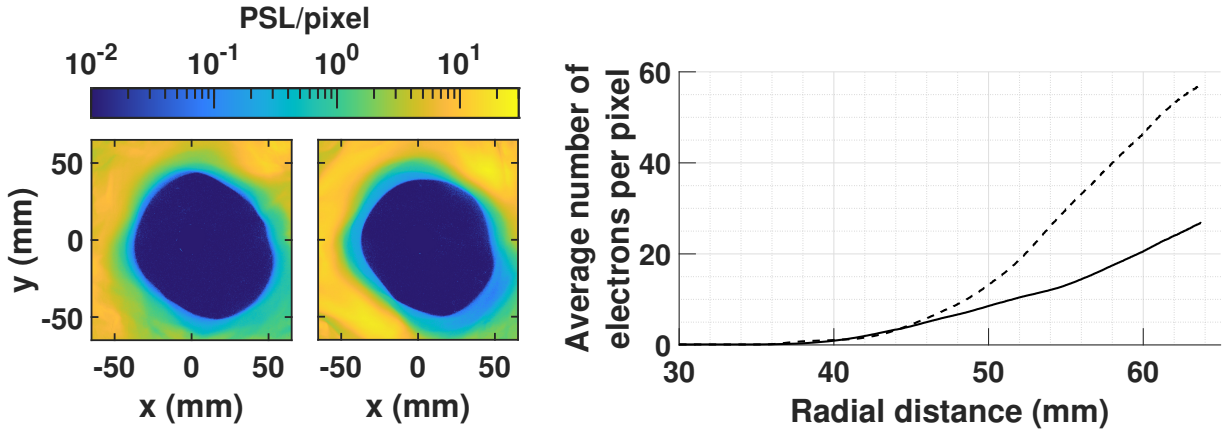
(a) (b) (c)

Figure 5.11: Spatial distribution of ejected electrons simulated when the (a) strong pulse and (b) weak pulse leads the other by 300 fs with randomized relative spatial separation of $\leq 2w_0$ between the laser axes. Distributions simulated 30 mm after the focus on a plane perpendicular to the laser axis passing through the origin. The color scale denotes the number of electrons in each 1×1 mm^2 pixel across the plane. The average number of electrons for varying distance from the laser axis is shown by the solid and dashed lines in (c) for simulations in (a) and (b), respectively.

We show the corresponding distributions in Figures 5.11a and 5.11b, with their $N_e(\pm 300 \text{ fs}, \rho)$ in Figure 5.11c. We see that this results in N_e rising at the same ρ associated with that of the strong pulse. This also increases the overall strength of $N_e(300 \text{ fs})$ (weak pulse leading), making it more similar to $N_e(-300 \text{ fs})$ (strong pulse leading). This is because the strong pulse may now liberate and interact with electrons from He atoms that were not doubly ionized by the weak pulse, and eject them down to $\theta_c = \theta_{c,s}$ regardless of whether the weak pulse leads. In summary, although we observed clearing for $|\Delta t| = 300$ fs, the differences observed in the experiment and idealized simulations highlight the need to tackle issues such as relative spatial fluctuation between focal volumes. One possible way to address this would be to use different beam geometries that minimize the role of spatial misalignment, such as using a larger clearing beam.

5.3.3 Time Taken to Clear the Focal Volume

To obtain insights on how long it takes to clear electrons from the focal volume, which can inform the timing sequence for QVAC experiments, we investigated electron clearing for a shorter time delay of $\Delta t = \pm 150$ fs. We present the measurements in Figures 5.12a and 5.12b when the strong pulse and weak pulse leads the other, respectively.



(a) (b) (c)

Figure 5.12: Spatial distribution of ejected electrons measured when the (a) strong pulse and (b) weak pulse leads the other by 150 fs. Distributions measured 30 mm after the focus on a plane perpendicular to the laser axis passing through the origin. The color scale denotes the PSL deposited in each 50×50 μm^2 pixel across the plane. The average number of electrons for varying distance from the laser axis is shown by the solid and dashed lines in (c) for measurements in (a) and (b), respectively.

We see from the corresponding line profiles $N_e(\pm 150 \text{ fs}, \rho)$ in Figure 5.12c that the behavior at 150 fs is contrary to that at 300 fs (Figure 5.10c) in that N_e is stronger when the weak pulse leads. This indicates that the passing of the weak pulse through the focal volume increases the number of electrons available for the strong pulse to interact with over a span of 150 fs. This also contradicts behavior predicted by corresponding simulations with a Gaussian laser profile at 150 fs, presented in Figures 5.13a and 5.13b. However, we see from Figure 5.9c that the focal

spot image of the weak pulse has a distinct ring-like feature outside the central spot, which is expected for a focused flattop or super-Gaussian. This ring-like secondary maximum outside the central spot has sufficient intensity to ionize He and thus can potentially contribute to the overall electron population within the focal volume of the strong pulse by expelling electrons toward the laser axis. Note that the volume of the ring-like feature is larger than the central spot and thus a large number of electrons could be generated therein.

To better understand the dynamics involved, we simulated this interaction replacing the weak pulse with a Laguerre-Gauss $l = 0,\ p = 1$ of same a_{0w} and w_0 as the Gaussian. We used this as an approximation to recreate the ring-like feature outside the central spot in Figure 5.9c while maintaining the characteristic peak intensity of the weak pulse. The fields of the weak pulse thus replace Equation (5.14) as [136]

$$\begin{aligned}\vec{E}_w(x,y,z,t) &= E_{0w}\left[\hat{x} + \frac{xy(1+4L_1)}{2\mathcal{Z}^2}\,\hat{y} - i\,\frac{x(1+2L_1)}{\mathcal{Z}}\,\hat{z}\right]\psi_{p=1}^{l=0}(x,y,z)\,f(t+\Delta t),\\ \vec{B}_w(x,y,z,t) &= \frac{E_{0w}}{c}\left[\frac{xy(1+4L_1)}{2\mathcal{Z}^2}\,\hat{x} + \hat{y} - i\,\frac{y(1+2L_1)}{\mathcal{Z}}\,\hat{z}\right]\psi_{p=1}^{l=0}(x,y,z)\,f(t+\Delta t).\end{aligned} \tag{5.15}$$

where $L_1 = (z_R/\mathcal{Z}^*)/\left[1 - 2(x^2+y^2)/w(z)^2\right]$ and $\psi_{p=1}^{l=0}$ is the spatial profile given by

$$\psi_{p=1}^{l=0} = \frac{w_0}{w(z)}\left(1 - \frac{2(x^2+y^2)}{w(z)^2}\right)\exp\left(-\frac{k(x^2+y^2)}{2\mathcal{Z}}\right)\exp\left(-3i\tan^{-1}\frac{z}{z_R}\right). \tag{5.16}$$

We show the resultant electron distributions in Figures 5.13c and 5.13d. It is evident that when the weak pulse with an $l = 0,\ p = 1$ mode leads the strong pulse (Figure 5.13d), the num-

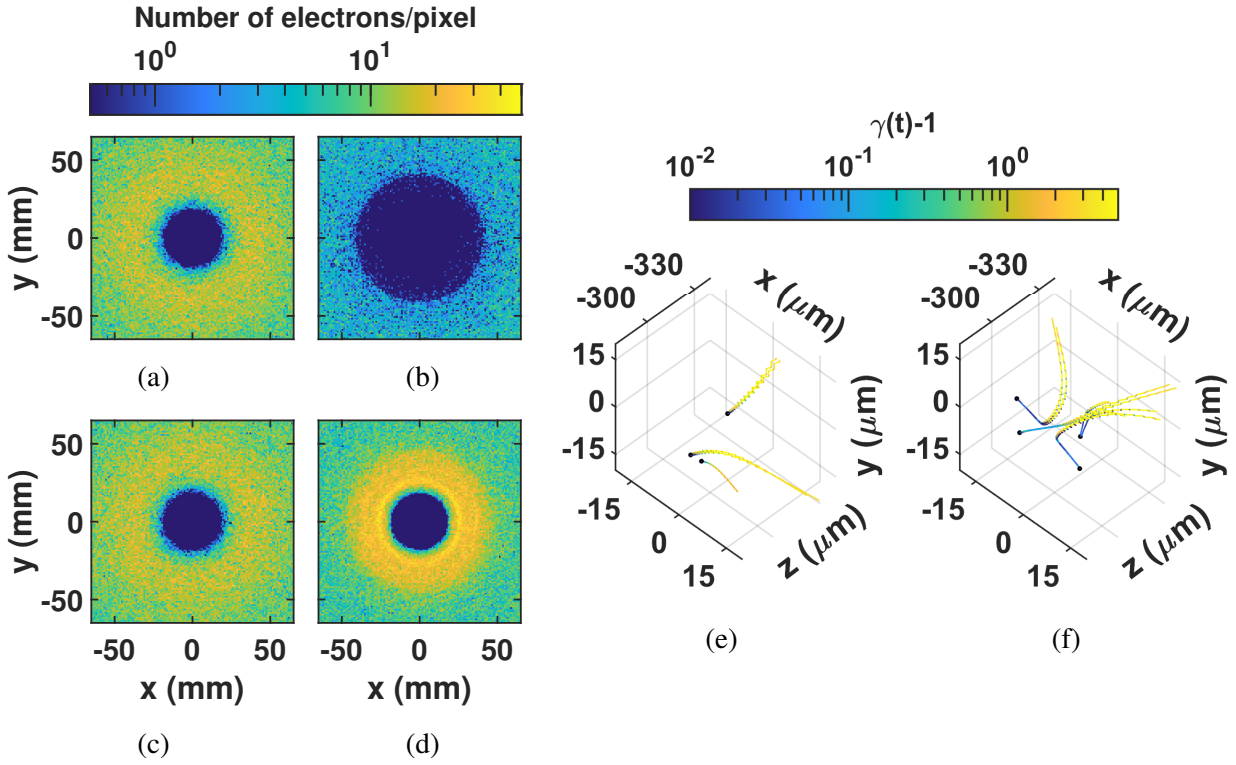


Figure 5.13: Spatial distribution of ejected electrons simulated with $l = 0,\ p = 0$ Laguerre-Gauss mode beams with (a) strong pulse leading and (b) weak pulse leading the other by 150 fs. Corresponding distributions when the weak pulse is replaced with an $l = 0,\ p = 1$ mode in (c) and (d), respectively. Color scale denotes number of electrons deposited in each $1 \times 1\ \mathrm{mm}^2$ pixel. Trajectories of the electrons with some of the smallest θ (see text) in (c) and (d) shown in (e) and (f), respectively. Birth positions denoted by black points. Color scale denotes the instantaneous $\gamma - 1$ through their trajectory.

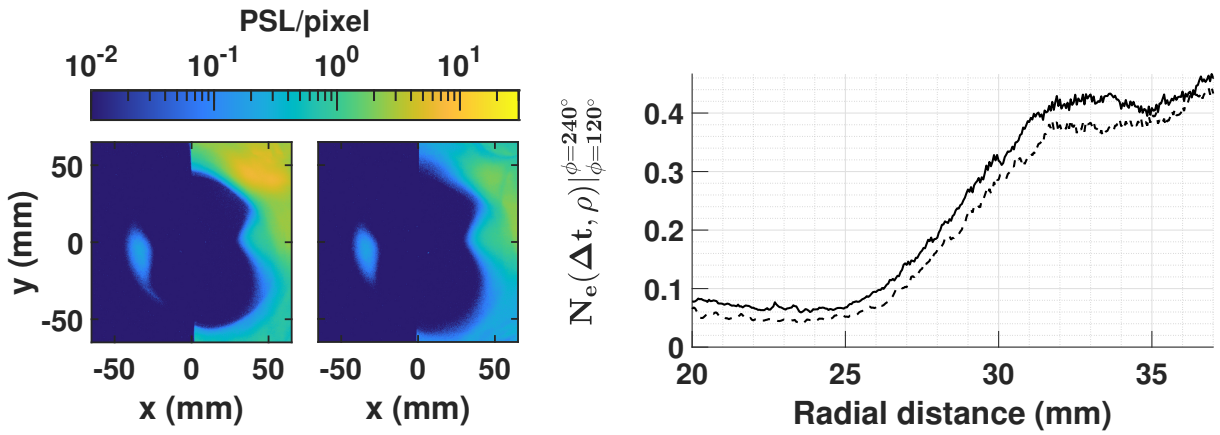
ber of electrons ejected onto the observation plane at small angles is larger than that when the strong pulse leads (Figure 5.13c). This implies that there is indeed a larger number of electrons that remain in the focal volume over 150 fs after the passing of the weak pulse, which are subsequently ejected by the following strong pulse toward small angles. In comparison, such electrons do not appear in the absence of a ring-like feature in the weak pulse, resulting in the lack of electrons being ejected at small angles (Figure 5.13b). This may be further explained using the trajectories of electrons appearing at small angles ($\theta \sim 35°$), corresponding to final $\gamma - 1 \sim 4.5$ in Figures 5.13c and 5.13d, shown in Figures 5.13e and 5.13f, respectively. Here, $(\gamma - 1) \times 0.511$ MeV is the kinetic energy of the electron. We see in Figure 5.13e that when the strong pulse leads, electrons are ponderomotively accelerated and ejected radially outward from the focal volume. However, we see in Figure 5.13f that when the more realistic weak pulse leads, electrons that are ejected at similar angles are born at larger ρ from the ring-like feature, injected inward with non-relativistic energies ($\gamma - 1 \lesssim 0.1$) and subsequently ejected radially outward by the strong pulse with $\gamma - 1 \sim 4.5$. It is straightforward to calculate the drift length for these electrons during the initial 150 fs after ionization as $\gamma = 1/\sqrt{1 - v^2/c^2}$. Using $\gamma - 1 \sim 0.02$ to 0.1, we get a drift length $\sim 9 - 18\ \mu\mathrm{m}$ that is in agreement with Figure 5.13f. This implies that electrons ionized by secondary maxima of the weak pulse can potentially cause a temporary increase in the number of electrons within the focal volume, which is counterproductive to ponderomotive clearing. Over the longer time scale of 300 fs, most of these electrons pass through and leave the central focal volume. This highlights that although it is possible to clear the focal volume with ponderomotive clearing, it is less straightforward to achieve efficient clearing, which depends on various features of the clearing beam and could vary for different time delays.

5.3.4 Role of High-Z Gases

While H_2 is most prevalent in a high-vacuum environment, the potential presence of high-Z gases such as N_2 and O_2 could pose a significant risk to achieving a truly electron-free focal volume. This is because each N_2 molecule can release up to 7 times as many electrons as each H_2. It is therefore important to understand the role of such gases in the dynamics of ponderomotive clearing. In this section, we report on how N_2 can affect the availability of electrons within the focal volume following the clearing pulse.

To achieve this, we backfilled the chamber with 9×10^{-4} mbar of N_2. We used $\Delta t = \pm 600$ fs to allow sufficient time for electrons ionized by the weak pulse to evacuate the focal volume. In addition, due to the possibility of high energy electrons from the $1s$ shell of N_2 that ionize at $I_{th} \sim 10^{19}$ W/cm^2 (see Table A.3), we used an added layer of Al (thickness 520 μm) placed directly in contact with the image plate surface facing the laser focus. We covered only $x < 0$ (or $\phi \in (\pi/2, 3\pi/2]$) with this added layer to allow a simultaneous comparison of electron distributions on two halves of each image plate, with each half blocking electrons with energies $\lesssim 0.5$ MeV for $x < 0$ and $\lesssim 50$ keV for $x > 0$. We present the measurements in Figures 5.14a and 5.14b when the strong pulse and the weak pulse lead to the other, respectively.

We observe a clear difference between the measurements performed with N_2 (Figures 5.14a and 5.14b) and those performed with He (Figures 5.10a and 5.10b). In the N_2 measurements, the distributions exhibit an additional lobe-like feature concentrated near $y = 0$, corresponding to the $\vec{E}$-$\vec{k}$ plane. Further, it is worth noting that this feature predominantly consists high-energy electrons (> 0.5 MeV) that are not filtered by the added layer of Al for $x < 0$. To investigate this further, we obtain a ϕ-averaged line profile for $\phi \in (2\pi/3, 4\pi/3]$ by modifying Equation (5.13)



(a) (b) (c)

Figure 5.14: Spatial distribution of ejected electrons measured when the (a) strong pulse and (b) weak pulse leads the other by 600 fs. Distributions measured 30 mm after the focus on a plane perpendicular to the laser axis passing through the origin. The color scale denotes the PSL deposited in each 50×50 μm^2 pixel across the plane. The average number of electrons for varying distance from the laser axis for $\phi \in (2\pi/3, 4\pi/3]$ is shown by the solid and dashed lines in (c) for measurements in (a) and (b), respectively.

as

$$N_e(\Delta t, \rho)\big|_{\phi=2\pi/3}^{\phi=4\pi/3} = \frac{1}{2\pi/3} \int_{\phi=2\pi/3}^{\phi=4\pi/3} n_e(\Delta t, \rho, \phi)\, \mathrm{d}\phi, \tag{5.17}$$

as shown in Figure 5.14c. From this, we see that the number of electrons contained in this lobe-like feature is nearly identical between Figures 5.14a and 5.14b. This implies that there is a group of high-energy electrons that are ejected to effectively the same ϕ and θ independent of the ordering of the two laser pulses.

As electrons from the $n = 2$ shell of N_2 are generated at $I_{th} \sim 10^{16}$ W/cm^2, which is similar to that of the two electrons in He, it is plausible that these high-energy electrons are likely due to the newly-introduced presence of electrons that ionize at $I_{th} \sim 10^{19}$ W/cm^2 from the $n = 1$ shell of N_2. Further, we note that the nominally-inferred intensities of the two pulses are

$I_{0s} \sim 6.6 \times 10^{19}$ and $I_{0w} \sim 7 \times 10^{18}$ $\mathrm{W/cm^2}$. This implies that while the strong pulse may readily ionize the $1s$ shell of N_2, the rate at which the weak pulse may liberate electrons from the $1s$ shell is significantly lower as this mostly relies on tunnel ionization. Therefore, this could explain why the lobe-like feature appears to be independent of the ordering of the pulses because these electrons are almost solely ionized and ejected by the strong pulse, while the weak pulse has no effect. This highlights that for efficient clearing of the focal volume prior to the main pulse of a QVAC experiment, the clearing pulse must have some $I_0 > I_{th,max}$, where $I_{th,max}$ is the intensity required to fully ionize the species with the highest electron binding energy.

We also note that, unlike electrons ionized at $I_{th} \ll I_{0s}$, which are distributed across all ϕ, electrons that are ionized at $I_{th} \lesssim I_{0s}$ appear confined to a much narrower range of ϕ centered around $\phi \approx 0$ and $\phi \approx \pi$. This is consistent with the fact that electrons liberated near the peak of the field likely experience only a short interaction time with the longitudinal component of the field that is responsible for driving them out of the $\vec{E}$-$\vec{k}$ plane. Consequently, these electrons are not displaced significantly out of the $\vec{E}$-$\vec{k}$ plane. To illustrate this effect, we performed idealized test simulations with a single Gaussian beam for varying ionization thresholds relative to the peak intensity. For simplicity, we assumed a sharp ionization threshold. We used $a_0 = 4.84$, $\tau = 40$ fs and $I_{th} = \delta_{th} I_0$, where $\delta_{th} \in \mathbb{R}^+$. We show the resulting spatial distribution of electrons for $w_0 = 5$ and 3 μm for varying δ_{th} in Figures 5.15a–5.15c and Figures 5.15d–5.15f, respectively.

We see that as $I_{th} \to I_0$, in addition to a reduction in the number of ejected electrons due to a decrease in the ionization volume, the electron density appears stronger along the $\vec{E}$-$\vec{k}$ plane and weaker along the $\vec{B}$-$\vec{k}$ plane. This is a direct consequence of electrons being prematurely ejected after ionization with an insufficient interaction time with the longitudinal component of the field that contributes to angular broadening in ϕ. This is especially evident for the tighter

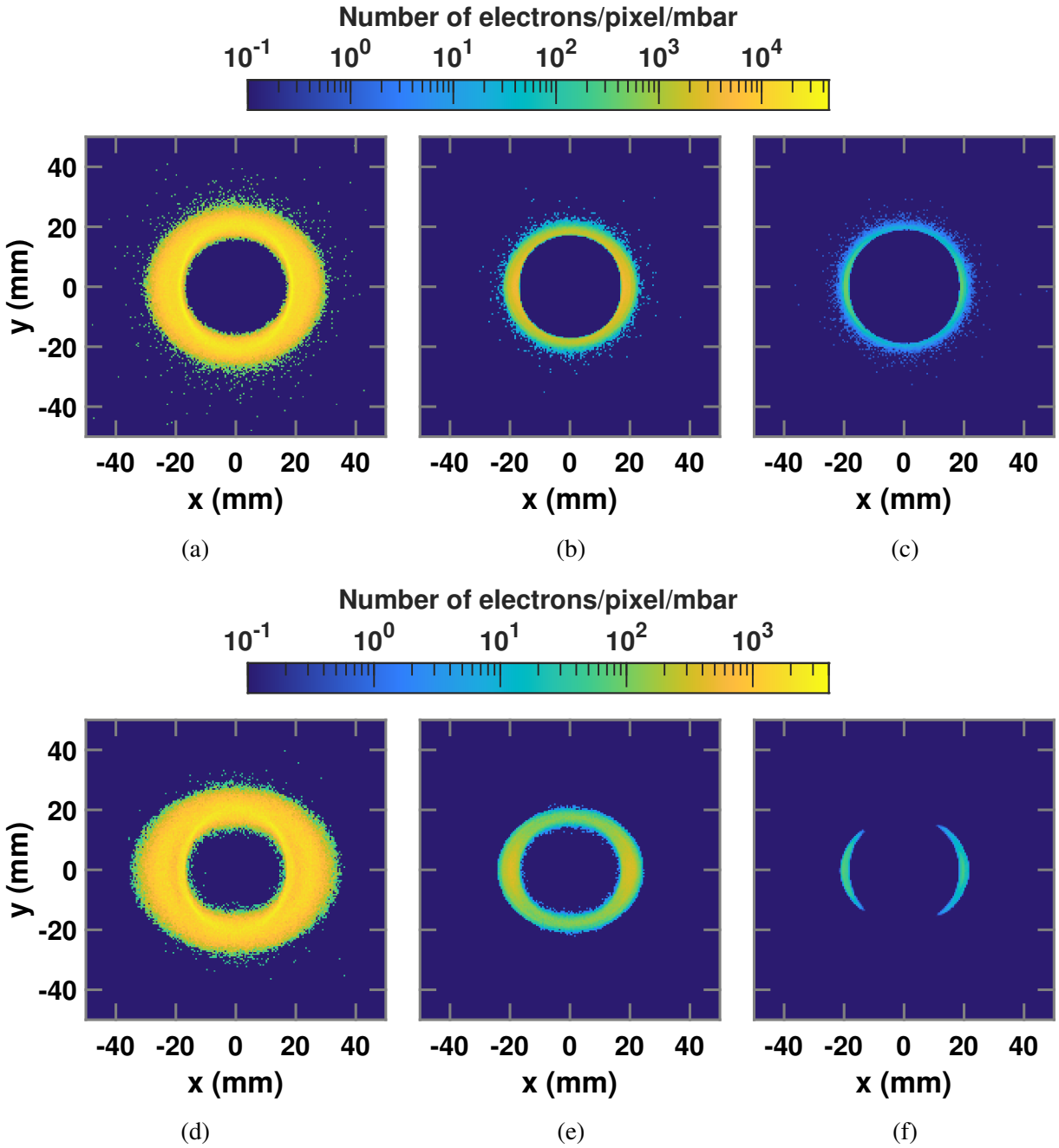


Figure 5.15: Spatial distribution of ejected electrons simulated with a single beam ($a_0 = 4.84$, $\tau = 40$ fs) and sharp ionization threshold $I_{th} = \delta_{th} I_0$ for (a) $w_0 = 5\ \mu$m, $\delta_{th} = 0.75$, (b) $w_0 = 5\ \mu$m, $\delta_{th} = 0.95$, (c) $w_0 = 5\ \mu$m, $\delta_{th} = 0.99$, (d) $w_0 = 3\ \mu$m, $\delta_{th} = 0.75$, (e) $w_0 = 3\ \mu$m, $\delta_{th} = 0.95$ and (f) $w_0 = 3\ \mu$m, $\delta_{th} = 0.99$. Color scale denotes number of electrons deposited in each 0.5×0.5 mm^2 pixel per mbar.

focus (smaller w_0) that results in a smaller focal volume, which facilitates premature ejection resulting in two distinct features around $\phi \approx 0$ and $\phi \approx \pi$ similar to that in Figure 5.14. Thus, the observed angular confinement of ejected electrons in ϕ from our measurements in Figure 5.14 aligns with the expectation that these electrons originate from the $n = 1$ shell of N_2. Although we qualitatively observe this effect with simulations for test cases, we note that achieving quantitative agreement with the measurements may require incorporating other factors such as a non-Gaussian spatial profile of a realistic beam and more robust ionization models.

Chapter 6: Summary and Outlook

6.1 Summary

Lasers with peak power in the multi-petawatt regime and above enable novel routes to probe fundamental physical phenomena in the universe, such as QVAC effects, within a controlled environment in the laboratory. The need to address challenges faced by precision measurements of the QVAC, which include diagnosing properties of the focal volume directly at peak intensity and minimizing noise sources for highly sensitive measurements, motivated the work presented in this dissertation. Through a series of experiments and computational exercises, we explored the dynamics of electrons liberated from rarefied gas in the focal volume and subsequently expelled at acute angles relative to the direction of laser propagation. We identified key features of the spatial and energy distributions of ejected electrons that depend on various parameters such as the inferred laser intensity, pulse duration, focusing, and the parent gas species. We showed that the dynamics of these electrons is highly relevant to addressing the above challenges.

In Chapter 1, we provided a brief historical overview of the development of state-of-the-art laser systems capable of creating extreme conditions in a laboratory, and the variety of physical phenomena and applications made accessible by these lasers (Section 1.1). We reviewed the need, and various ways, to measure nonlinear QED phenomena (Section 1.2). We presented some of the challenges that must be overcome to perform these measurements (Section 1.2.1) and a brief

overview of how improving our understanding of electron dynamics in extreme laser fields can benefit these measurements (Section 1.2.2).

In Chapter 2, we reviewed the theoretical background required for the work presented in this dissertation. This included describing the physical environment experienced by the electrons, beginning with a review of ionization in strong fields (Section 2.1) and a comparison between the magnitude of the laser field and that of nearby charged particles, thereby justifying the treatment of the electrons as being influenced solely by the laser (Section 2.2). The chapter concluded with descriptions of simplistic models of the ensuing electron dynamics in non-relativistic (Section 2.3) and relativistic fields (Section 2.4). We explained the reason why electrons are ejected from the focal volume at acute angles in relativistic fields, and reviewed analytic relationships between the kinetic energy of the electrons, ejection angle of the electrons and the laser intensity within the plane-wave approximation.

In Chapter 3, we presented a description of our approach to numerically simulate the dynamics of electrons in relativistic fields. We described how we initialize and ionize atoms within the focal volume (Section 3.1.1), how we numerically solve the equations of motion and extract observable quantities such as the ejection angle and the final kinetic energy (Section 3.1.2), and the field equations that we used to achieve this (Section 3.2). We detailed our approach to model multiple laser pulses (Section 3.3) and to estimate optimal computational parameters that maximize efficiency while ensuring the physical validity of our simulations (Section 3.4).

In Chapter 4, we detailed our exploration of how spatial and energy distributions of ejected electrons depend on various parameters. Specifically, in Section 4.1, we showed in the range of $a_0 \sim 4$ to 12 that the minimum angle of ejection for a paraxial laser focus scales with the inferred laser intensity in a way that is consistent with the plane-wave model discussed in Chapter 2, and

discussed potential factors that affect the constant of proportionality such as the presence of aberrations. In Section 4.2, we explored the dependence of the maximum kinetic energies of ejected electrons on the pulse duration through computation, and preliminary measurements performed with ~ 40 fs and ~ 700 fs laser pulses for two different gas species (N_2 and Ar). We found that as the pulse duration increases to several hundreds of fs, electrons mostly experience intensities similar to that at their birth and are thus not accelerated to energies that are characteristic of the peak intensity. We then investigated the role of focusing conditions in Section 4.3 by varying the $f/\#$ and showed that tighter focusing conditions (smaller $f/\#$) result in increased energy spread for a given observation angle, potentially limiting the use of analytical models for non-paraxial beams. Finally, in Section 4.4, we presented a brief outlook on the dynamics of electrons at intensities $> 10^{22}$ W/cm^2 using simulations.

In Chapter 5, we showed how the features of electron dynamics explored in Chapter 4 may be exploited to address challenges in precision measurements of the QVAC. In conjunction with detecting highly charged ion states as a fiducial (Section 5.1.1), we presented the potential of scintillation-based electron detection as an on-shot diagnostic of the peak intensity (Section 5.1.2). We then showed how the spatial distribution of the ejected electrons is influenced by aberrations introduced in the focal spot, which implies that measuring the ejected electron distribution presents a novel route to detect aberrations at full power (Section 5.2). Using a pump-probe setup that employed two co-propagating laser pulses, we showed that it is possible to deplete the number of electrons in the focal volume using a clearing pulse prior to the main laser pulses of a QVAC measurement (Section 5.3). We explored the role of features such as relative spatial fluctuation of the beams, airy-ring structures that affect the clearing efficiency, in addition to the role of heavier gases such as N_2 that could potentially inject electrons in the

presence of the main pulse if the clearing pulse does not fully ionize such species over the desired focal volume.

6.2 Outlook

6.2.1 Improving Measurements of Peak Intensity with Electron Dynamics

In Section 4.1, we hypothesized that a laser focus that appears less aberrated likely results in reduced intensity degradation at full power and is more favorable for electron acceleration, resulting in $\eta \approx \sqrt{2}$, which is in good agreement with simulations and Equation 2.25. Thus, it would be worthwhile to measure η for a paraxial beam with $\tau < 100$ fs and different aberrations through a similar exercise to vary the inferred intensity. Such an experiment could employ either a deformable mirror [164] or a PSLM as used in Section 5.2, both of which were unfortunately unavailable to us during the experiment in Section 4.1, to maximize the symmetry of the electron distribution. Through this, we could test whether we can quantitatively show that $\eta \to \sqrt{2}$ for a less aberrated beam, of which we currently have preliminary evidence through one single measurement (Figure 4.4d).

Based on our measurements in Section 5.1.2, we know that the electron distributions are sensitive to shot-to-shot fluctuations. Therefore, it is worth exploiting this fact with a more advanced detector that is capable of on-shot measurements of the spatial distribution of electrons, such as the Advacam WidePIX detector [165], which can electronically record the distribution in real time unlike image plates that must be removed from the chamber and scanned.

As angular measurements have limited use beyond $I_0 \gtrsim 10^{21}$ W/cm^2 due to the asymptotic behavior of $\tan\theta$ as $\theta \to 0$, further investigations of γ_f are required for higher intensities, at least

until protons become relativistic and enable novel proton-based intensity measurements. Such experiments at $I_0 > 10^{22}$ W/cm^2 can be illustrative for both charged-particle dynamics in strong fields as well as testing ionization models in unprecedented regimes.

6.2.2 Next Steps for Measuring Aberrations with Electron Distributions

As briefly mentioned in Section 5.2, the natural next step for employing electron distributions as a real time, full-power diagnostic of beam aberrations in the focus is to generate large datasets of electron distributions for various focal spot aberrations and train machine learning algorithms to identify the aberration as a function of the electron distribution.

Another interesting investigation would be to diagnose the focal spot resulting from the use of a plasma mirror [166]. Plasma-based optics hold promise for ushering in the next generation of high-intensity lasers, as they are inherently unaffected by laser-induced damage thresholds that limit the capabilities of current optical components [167]. Therefore, it is important to test the quality of the beam following reflections from plasma mirrors to check whether they induce any significant aberrations that can be detrimental to maximizing the peak intensity. Measuring the electron distribution from a laser focus with and without a plasma mirror as one of the optical components prior to focusing can help compare the extent of aberrations induced by a plasma mirror.

6.2.3 Quantifying Ponderomotive Clearing Efficiency

As our aim in Section 5.3 was to demonstrate a proof of concept to deplete electrons from the focal volume, we chose to employ a copropagating beam geometry to maximize the proba-

bility of overlapping focal volumes. Naturally, a follow up measurement to quantify the clearing efficiency would require employing the two beams at an angle, such as in perpendicular geometry, which would allow spatial separation of ejected electrons and thus their detection on different planes. In addition, such an experiment may require improved modeling capabilities to accurately represent the laser field and account for the influence of airy-ring structures, which we showed can affect residual electron availability for a few hundred fs following the clearing pulse. Follow-up experiments to quantify the clearing effect may also be informative for future experiments capable of employing clearing beams with $I_0 > 10^{23}\ \mathrm{W/cm^2}$ that can expel protons in addition to electrons. If such clearing beams are employed in conjunction with an ultra-high vacuum where the only residual gas species is $\mathrm{H_2}$, this could result in a near-ideal vacuum that is highly desirable for QVAC measurements.

Appendix A: Tables of Ionization Intensities Assuming BSI

In this Chapter, we provide the ionization intensities I_{th} for various atomic species of interest calculated based on Equation (2.3), using U_{th} values obtained from the Atomic Spectra Database of the National Institute of Standards and Technology [128].

A.1 Hydrogen

Table A.1: I_{th} for H.

Ion. stage	Ion. energy (eV)	I_{th} ($\mathrm{W/cm^2}$)
1	13.6	1.36×10^{14}

A.2 Helium

Table A.2: I_{th} for He.

Ion. stage	Ion. energy (eV)	I_{th} ($\mathrm{W/cm^2}$)
1	24.6	1.46×10^{15}
2	54.4	8.77×10^{15}

A.3 Nitrogen

Table A.3: I_{th} for N.

Ion. stage	Ion. energy (eV)	I_{th} ($\mathrm{W/cm^2}$)
1	14.5	1.78×10^{14}
2	29.6	7.68×10^{14}
3	47.4	2.25×10^{15}
4	77.5	9.00×10^{15}
5	97.9	1.47×10^{16}
6	552	1.03×10^{19}
7	667	1.62×10^{19}

A.4 Oxygen

Table A.4: I_{th} for O.

Ion. stage	Ion. energy (eV)	I_{th} ($\mathrm{W/cm^2}$)
1	13.6	1.38×10^{14}
2	35.1	1.52×10^{15}
3	54.9	4.05×10^{15}
4	77.4	8.98×10^{15}
5	113	2.69×10^{16}
6	138	4.04×10^{16}
7	739	2.44×10^{19}
8	871	3.60×10^{19}

A.5 Argon

Table A.5: I_{th} for Ar.

Ion. stage	Ion. energy (eV)	I_{th} $(\mathrm{W/cm^2})$
1	15.8	2.47×10^{14}
2	27.6	5.83×10^{14}
3	40.7	1.22×10^{15}
4	59.6	3.15×10^{15}
5	74.8	5.02×10^{15}
6	91.3	7.72×10^{15}
7	124	1.96×10^{16}
8	144	2.65×10^{16}
9	423	1.58×10^{18}
10	480	2.12×10^{18}
11	540	2.82×10^{18}
12	619	4.08×10^{18}
13	686	5.23×10^{18}
14	755	6.64×10^{18}
15	856	9.52×10^{18}
16	918	1.11×10^{19}
17	4120	3.99×10^{21}
18	4426	4.74×10^{21}

A.6 Krypton

Table A.6: I_{th} for Kr.

Ion. stage	Ion. energy (eV)	I_{th} ($\mathrm{W/cm^2}$)
1	14.0	1.53×10^{14}
2	24.4	3.52×10^{14}
3	35.8	7.33×10^{14}
4	50.8	1.67×10^{15}
5	64.7	2.80×10^{15}
6	78.5	4.22×10^{15}
7	109	1.16×10^{16}
8	125	1.57×10^{16}
9	233	1.46×10^{17}
10	268	2.06×10^{17}
11	308	2.97×10^{17}
12	350	4.17×10^{17}
13	391	5.53×10^{17}
14	446	8.08×10^{17}
15	492	1.04×10^{18}
16	540	1.33×10^{18}
17	591	1.69×10^{18}
18	640	2.07×10^{18}
19	785	4.21×10^{18}
20	832	4.78×10^{18}
21	883	5.51×10^{18}
22	945	6.59×10^{18}
23	999	7.53×10^{18}
24	1042	8.19×10^{18}
25	1155	1.14×10^{19}
26	1205	1.25×10^{19}
27	2928	4.03×10^{20}
28	3072	4.54×10^{20}
29	3228	5.16×10^{20}
30	3380	5.80×10^{20}
31	3584	6.87×10^{20}
32	3752	7.74×10^{20}
33	3971	9.13×10^{20}
34	4109	9.86×10^{20}
35	17296	2.92×10^{23}
36	17936	3.19×10^{23}

A.7 Xenon

Table A.7: I_{th} for Xe.

Ion. stage	Ion. energy (eV)	I_{th} ($\mathrm{W/cm^2}$)
1	12.1	8.66×10^{13}
2	21.0	1.94×10^{14}
3	31.0	4.13×10^{14}
4	42.2	7.93×10^{14}
5	54.1	1.37×10^{15}
6	66.7	2.20×10^{15}
7	91.6	5.75×10^{15}
8	106	7.88×10^{15}
9	180	5.17×10^{16}
10	202	6.66×10^{16}
11	230	9.09×10^{16}
12	255	1.17×10^{17}
13	281	1.48×10^{17}
14	314	1.98×10^{17}
15	343	2.46×10^{17}
16	374	3.06×10^{17}
17	404	3.69×10^{17}
18	434	4.38×10^{17}
19	549	1.01×10^{18}
20	582	1.15×10^{18}
21	616	1.31×10^{18}
22	650	1.48×10^{18}
23	700	1.82×10^{18}
24	736	2.04×10^{18}
25	818	2.87×10^{18}
26	857	3.19×10^{18}
27	1493	2.73×10^{19}
28	1571	3.11×10^{19}
29	1653	3.55×10^{19}
30	1742	4.09×10^{19}
31	1826	4.63×10^{19}
32	1919	5.30×10^{19}
33	2023	6.15×10^{19}
34	2113	6.90×10^{19}
35	2209	7.78×10^{19}
36	2300	8.64×10^{19}
37	2556	1.25×10^{20}
38	2637	1.34×10^{20}
39	2726	1.45×10^{20}
40	2811	1.56×10^{20}
41	2975	1.86×10^{20}
42	3068	2.01×10^{20}
43	3243	2.39×10^{20}
44	3333	2.55×10^{20}
45	7660	6.80×10^{21}
46	7889	7.32×10^{21}
47	8144	7.97×10^{21}
48	8382	8.57×10^{21}
49	8971	1.08×10^{22}
50	9243	1.17×10^{22}
51	9581	1.30×10^{22}
52	9810	1.37×10^{22}
53	40271	3.75×10^{24}
54	41299	3.99×10^{24}

Appendix B: Details of Computational Approach Used for Simulations

In Section 3.1.2, we briefly specified our approach to solve the equations of motion for electrons. In this Chapter, we detail our reason for choosing an ODE solver to perform our numerical simulations. We first establish the background necessary to characterize the system that we simulate in Section B.1. Then, we review two potential approaches to performing the simulation in Section B.2 and compare results from implementing these two approaches for various test cases in Section B.3.

B.1 Characterizing the System

It is important to first characterize the system that we intend to simulate before finding appropriate methods to solve the equations of motion. We know from Section 2.2 that we can treat electrons as single particles solely influenced by the laser field that is explicitly specified independent of the positions of all charged particles. This is because the energy transferred to the electrons from the laser is an insignificant fraction of the laser energy (see Eq. (2.9)). Therefore, although the laser and the electrons combined form a closed system in reality, we can numerically isolate the electrons as an open system while prescribing the field externally for any point in space and time. This allows us to employ approaches to solve the equations of motion without being constrained by the need to preserve the symplectic structure of the system, i.e., without being

forced to use methods that conserve total energy despite the electrons gaining energy over time.

B.2 Methods to Solve Equations of Motion

A relatively robust metric to compare different methods when we are interested in the trajectories of electrons is to check for the convergence of trajectories and the final state of electrons for varying tolerances, rather than simply check for energy conservation. Here, we compare two methods that are at our disposal to solve the equations of motion for the electrons

- Pusher algorithms: In these algorithms, the positions and momenta of charged particles are advanced from an initial to a final time in discrete steps with fixed size $\mathrm{d}t$, with each particle's update corresponding to the same global time advance. These algorithms are the preferred choice when the electromagnetic fields are self-consistent, i.e., depend on the instantaneous positions and momenta of the particles, which requires synchronization of all particles at each time step and thus limits parallelization over particles. Common examples include the Boris [168] and Vay [169] pusher algorithms that are ubiquitously used in particle-in-cell programs for plasma physics. For particles attaining relativistic energies, as is the case here, the Vay pusher is known to be more accurate the Boris pusher, which can exhibit significant errors when computing trajectories [169].

- Parallelized particle tracking with ode45: In this approach, each particle's trajectory is computed independently by integrating its equations of motion with a general-purpose ODE solver. The solver employs adaptive time stepping, so individual particles may be evaluated at different intermediate time points. This enables straightforward parallelization over particles. The choice of ODE solver typically depends on whether the system of

ODEs is stiff or non-stiff. A system is considered stiff when numerical stability requirements impose time steps that are much smaller than those dictated by the physical time scales of interest. However, for the problem herein, the limiting time step is determined by the oscillation period of the laser field, which is a physically relevant timescale. Therefore, we employ the native MATLAB® ODE solver, ode45 [133], which is appropriate for non-stiff problems. This solver uses an explicit Runge-Kutta (4,5) algorithm [134, 135] with a variable time step.

B.3 Comparing Results From Different Methods for Various Test Cases

Here, we present numerical solutions to the system of ODEs in Equations (3.9) and (3.10) for three different scenarios, achieved using the Vay pusher algorithm and parallelized particle tracking with ode45. The parameters that control the temporal resolution of the numerical solutions are the predetermined step size $\mathrm{d}t$ for the Vay pusher and the permissible tolerances RelTol and AbsTol [170] that affect the adaptive step size for the ode45 solver. For simplicity of comparing the performance of the two methods while minimizing the number of independent parameters, we define and vary Tol under the constraint $\mathrm{Tol} = \mathrm{RelTol} = \mathrm{AbsTol}$.

B.3.1 Constant Magnetic Field

In this problem, we initialize a test particle with charge $+e$ and initial speed $\vec{v}_i = c\sqrt{1 - 1/\gamma_0^2}\,\hat{x}$ in a region with constant magnetic field $\vec{B} = B_0\,\hat{z}$. We know analytically that this results in circular motion on the x-y plane centered at $(0, -R_G, 0)$, where R_G is the radius of gyration given by

Table B.1: Summary of B_0 and γ_0 used for simulating an electron in a constant magnetic field, with corresponding R_G and T_G calculated analytically.

$\boldsymbol{B_0}$ (T)	$\boldsymbol{\gamma_0}$	$\boldsymbol{R_G}$ ($\boldsymbol{\mu}$m)	$\boldsymbol{T_G}$ (ps)
40	10	424.07	8.931
	20	851.36	17.863
	50	2130.64	44.658

$$R_G = \frac{m_e c}{eB_0}\sqrt{\gamma_0^2 - 1}. \tag{B.1}$$

We also know that the gyration period is

$$T_G = \gamma_0 \frac{2\pi m_e}{eB_0}. \tag{B.2}$$

For reference, we provide the analytically calculated values for R_G and T_G in Table B.1 for $B_0 = 40$ T and three different γ_0. We show the numerical solutions to $x(t)$ and $y(t)$ in Figure B.1, obtained over a 60 ps time interval that is typically sufficient for electrons to reach steady state in the original problem of an electron solely interacting with a sub-ps focused laser pulse. Here, we used $\mathrm{d}t = 0.0267$ fs $\ll 60$ ps for the Vay pusher method, and $\mathrm{Tol} = 10^{-6}$ for the ode45 method.

We see in Figure B.1 that the numerical solutions obtained from the Vay pusher method (Figures B.1a, B.1c and B.1e) are practically identical to the corresponding solutions obtained with the ode45 method (Figures B.1b, B.1d and B.1f). Further, each is consistent with the analytically estimated values for R_G and T_G. To quantify the numerical stability of each method,

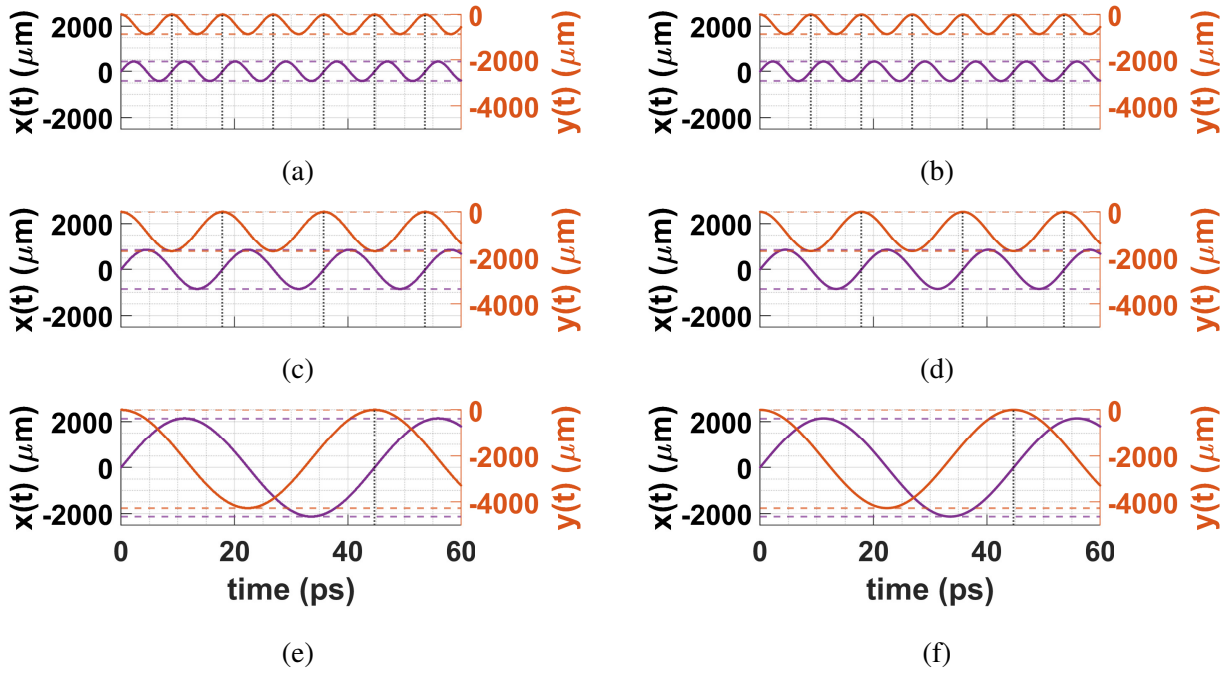


Figure B.1: Numerical solutions to the equations of motion for an electron in a constant magnetic field ($B_0 = 40$ T). The top, middle and bottom row correspond to $\gamma = 10, 20$ and 50, while the left and right columns represent simulations performed using the Vay pusher algorithm and the ode45 solver, respectively. The violet (orange) curve plotted on the primary (secondary) axis represents $x(t)$ ($y(t)$). The horizontal dashed violet (orange) lines represent the analytically estimated peak-to-peak amplitude, i.e., $2R_G$. The vertical black dotted lines are plotted to represent integral multiples of the gyration period T_G.

we evaluated γ explicitly at each time point from Figure B.1, and show the resultant $\gamma(t)$ in Figure B.2.

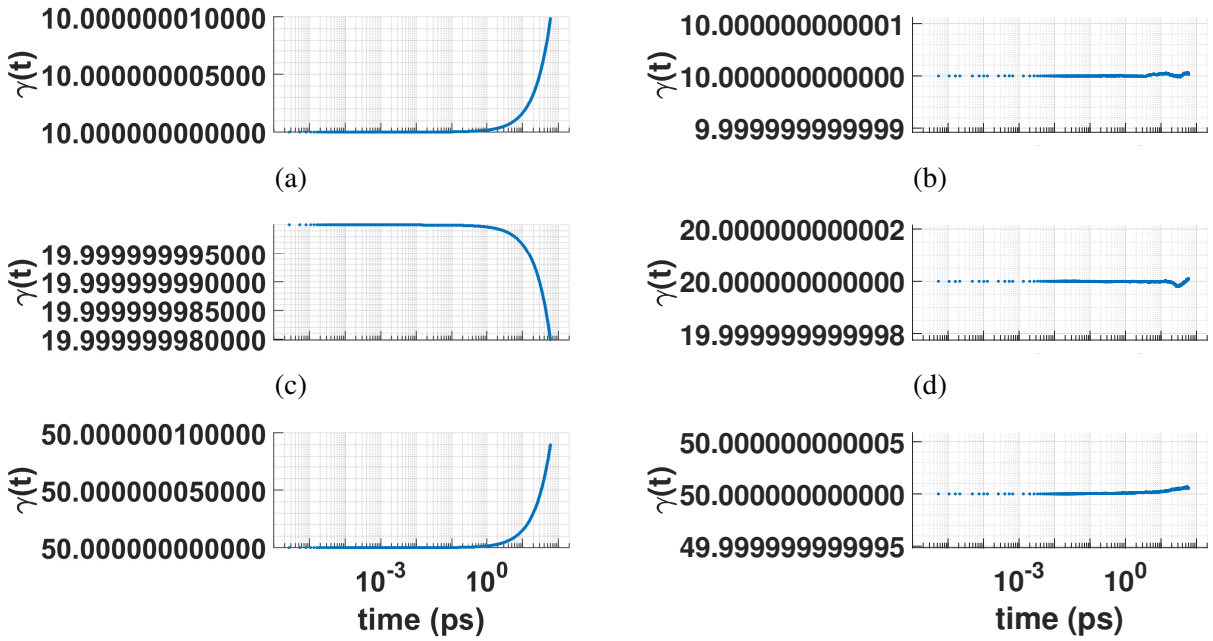


Figure B.2: Variation of γ over time due to numerical computation error for an electron in a constant magnetic field ($B_0 = 40$ T). The top, middle and bottom row correspond to $\gamma = 10, 20$ and 50, while the left and right columns represent simulations performed using the Vay pusher algorithm and the ode45 solver, respectively.

We know that the magnetic field does no work on the electron. Therefore, analytically, $\gamma(t) = \gamma_0 \, \forall \, t$. We see in Figure B.2 that for all practical purposes, both methods result in a constant γ. Specifically, the variation in $\gamma(t)$ over the simulated 60 ps interval for the Vay pusher method is $\delta\gamma \sim 10^{-8}$ and for the ode45 method is $\delta\gamma \sim 10^{-12}$ in this case.

B.3.2 Focused Laser Field with $a_0 = 10$ and $a_0 = 200$

We now simulate the problem relevant to this dissertation, i.e., an electron solely influenced by a focused laser field such as that specified in Section 3.2. To test the accuracy of our

Table B.2: Summary of initial conditions for the representative electron trajectories presented.

Fig.	a_0	$\vec{r}_i$ (μm)	t_i (fs)	**Residual ion**
B.3	10	$(0.767, -0.083, -93.38)$	-351.34	Ar^{16+}
B.4	200	$(-8.19, -5.35, -3.52)$	-17.11	Ar^{17+}

simulations across different kinds of electron trajectories discussed in Section 4.4, i.e., rapid phase lag (highly oscillatory) versus minimal phase lag (barely oscillatory) with the laser field, we performed simulations with $a_0 = 10$ and $a_0 = 200$, respectively, for a laser pulse with $\lambda_0 = 0.8\ \mu\text{m},\ w_0 = 8\ \mu\text{m}$ and $\tau = 40$ fs. We then picked one electron with a representative trajectory for the two a_0 with initial conditions summarized in Table B.2.

We plot $\gamma(t') - 1$ for $a_0 = 10$ in Figure B.3 and $a_0 = 200$ in Figure B.4. Here, t' is the time elapsed after the birth of the electron at some global time t_i, i.e., $t' = t - t_i$. We note that at $t = 0$, the pulse is centered at $z = 0$. Therefore, t_i may be negative if the electron is born before the pulse crosses $z = 0$. We performed simulations for $t \in [t_i,\ t_{end}]$, which corresponds to $t' \in [0,\ t'_{end}]$, where $t'_{end} = t_{end} - t_i$. We used $t_{end} = 60$ ps for $a_0 = 10$ as the electron reaches steady state relatively quickly (< 1 ps). For $a_0 = 200$, we found that 60 ps was insufficient as the electron interacts with the laser for much longer times due to minimal phase lag. Thus, we attempted to simulate $a_0 = 200$ for up to $t_{end} = 100$ ps, which was feasible when recording the trajectory with the ode45 method due to adaptive time stepping minimizing the total size of the generated data. However, due to limitations in file size handling in case of the Vay pusher method that uses a fixed time step, we could only record the trajectory up to $t_{end} = 60$ ps. To compare the performance of the Vay pusher and the ode45 solver method, we varied step size $\mathrm{d}t$ and Tol within the respective methods. This allows us to check whether γ_f converges for decreasing $\mathrm{d}t$

Table B.3: Summary of results from simulations with varying $\mathrm{d}t$ and Tol for the representative electron trajectories presented.

Fig.	a_0	**Numerical method**	t'_{obs} (ps)	$\gamma(t'_{obs})$	t'_{end} (ps)	$\gamma(t'_{end})$
B.3a	10	Vay ($\mathrm{d}t = T_L/100$)	1	11.4987	60.351	11.4987
B.3b	10	Vay ($\mathrm{d}t = T_L/1000$)	1	12.4640	60.351	12.4640
B.3c	10	Vay ($\mathrm{d}t = T_L/2000$)	1	12.5257	60.351	12.5257
B.3d	10	ode45 ($\mathrm{Tol} = 10^{-6}$)	1	12.5883	60.351	12.5883
B.3e	10	ode45 ($\mathrm{Tol} = 10^{-8}$)	1	12.5883	60.351	12.5883
B.3f	10	ode45 ($\mathrm{Tol} = 10^{-10}$)	1	12.5884	60.351	12.5884
B.4a	200	Vay ($\mathrm{d}t = T_L/100$)	60	4771.2721	60.017	4771.2413
B.4b	200	Vay ($\mathrm{d}t = T_L/1000$)	60	5324.4523	60.017	5324.4233
B.4c	200	Vay ($\mathrm{d}t = T_L/2000$)	60	5330.6700	60.017	5330.6413
B.4d	200	ode45 ($\mathrm{Tol} = 10^{-6}$)	60	5334.0439	100.017	4819.6666
B.4e	200	ode45 ($\mathrm{Tol} = 10^{-8}$)	60	5334.0440	100.017	4819.6670
B.4f	200	ode45 ($\mathrm{Tol} = 10^{-10}$)	60	5334.0439	100.017	4819.6670

or Tol within each method and thus to estimate a suitable value for the relevant parameter that constrains the accuracy of the method. We represent $\mathrm{d}t$ in units of the field oscillation period $T_L = \lambda_0/c \approx 2.67$ fs.

We see from both Figures B.3 and B.4 that $\gamma(t') - 1$ simulated by the Vay pusher method with $\mathrm{d}t = T_L/100$ (Figures B.3a and B.4a) appears notably distinct from those performed with the Vay pusher method with $\mathrm{d}t = T_L/1000$ and $\mathrm{d}t = T_L/2000$. Meanwhile, we also see that in the ode45 method (Figures B.3d–B.3f and B.4d–B.4f), the temporal structure of $\gamma(t') - 1$ is consistent and well preserved across the range of values used here for Tol. To quantify these observations, we recorded $\gamma(t')$ at some $t' = t'_{obs} < t'_{end}$ for a single value of t'_{obs} across all the solver configurations within each a_0. We summarize the resulting $\gamma(t'_{obs})$ as well as $\gamma(t'_{end} = t_{end} - t_i)$ in Table B.3.

As $\gamma(t'_{obs}) = \gamma(t'_{end}) = \gamma_f$ for $a_0 = 10$, which is evident from Figure B.3 where $\gamma(t') - 1$

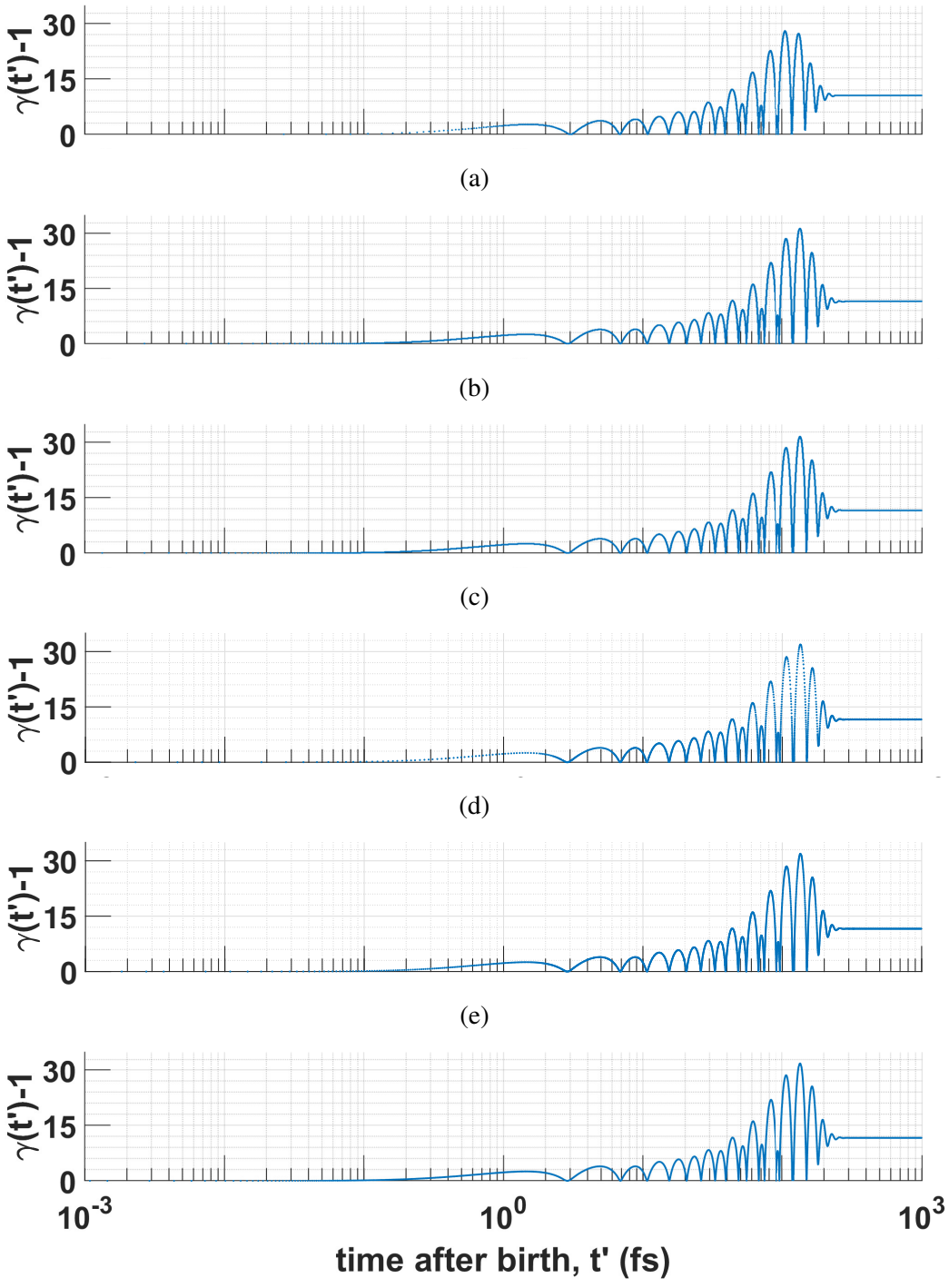


Figure B.3: Normalized kinetic energy $(\gamma(t')-1)$ as a function of time after birth t' for an electron in a Gaussian laser field with $a_0 = 10,\ \lambda_0 = 0.8\ \mu\text{m},\ w_0 = 8\ \mu\text{m},\ \tau = 40$ fs, solved using the Vay pusher with (a) $\mathrm{d}t = T_L/100$, (b) $\mathrm{d}t = T_L/1000$ and (c) $\mathrm{d}t = T_L/2000$, and the ode45 solver with (d) $\text{Tol} = 10^{-6}$, (e) $\text{Tol} = 10^{-8}$ and (f) $\text{Tol} = 10^{-10}$.

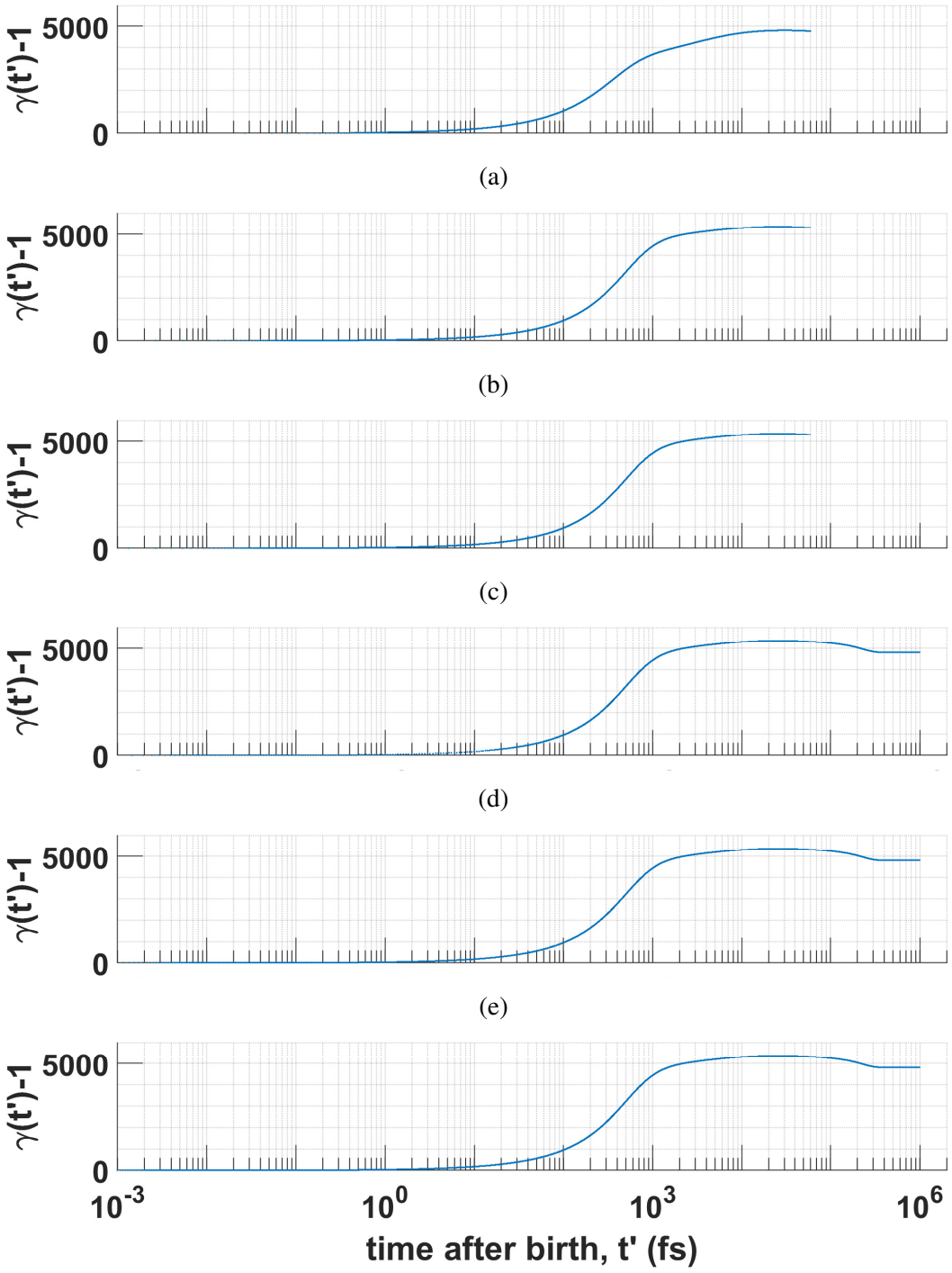


Figure B.4: Normalized kinetic energy $(\gamma(t')-1)$ as a function of time after birth t' for an electron in a Gaussian laser field with $a_0 = 200,\ \lambda_0 = 0.8\ \mu\text{m},\ w_0 = 8\ \mu\text{m},\ \tau = 40$ fs, solved using the Vay pusher with (a) $\mathrm{d}t = T_L/100$, (b) $\mathrm{d}t = T_L/1000$ and (c) $\mathrm{d}t = T_L/2000$, and the ode45 solver with (d) $\text{Tol} = 10^{-6}$, (e) $\text{Tol} = 10^{-8}$ and (f) $\text{Tol} = 10^{-10}$.

appears to attain steady state by $t' \approx 200$ fs, we can infer from comparing $\gamma(t'_{obs})$ across solver configurations that the Vay pusher method with $\mathrm{d}t = T_L/100$ ($T_L/1000$) results in γ_f that is $\approx$ 91% (99%) of that with $\mathrm{d}t = T_L/2000$. Therefore, $\mathrm{d}t = T_L/100$ ($T_L/1000$) appears insufficient (sufficient) to resolve the dynamics of a highly oscillatory electron trajectory. Meanwhile, we see that there is effectively no difference between γ_f obtained with ode45 using $\mathrm{Tol} = 10^{-6}, 10^{-8}$, and 10^{-10}. Further, the fact that γ_f obtained with the Vay pusher with $\mathrm{d}t = T_L/2000 \approx$ that obtained with ode45, coupled with the near-identical trajectories of the respective simulations imply that both methods are in agreement when sufficiently stringent computational parameters are chosen.

For $a_0 = 200$, it is evident that $\gamma(t'_{obs}) \neq \gamma_f$ as $\gamma(t') - 1$ appears to attain steady state only by $t' \approx 300$ ps. Therefore, comparing $\gamma(t'_{obs})$ does not hold the same physical significance as it does for $a_0 = 10$ because it is now sampled at an arbitrary moment within the evolution of $\gamma(t')$. Nonetheless, it is still worthwhile to highlight that the trend in convergence is qualitatively similar to that observed with $a_0 = 10$ in that for the Vay pusher, $\mathrm{d}t = T_L/100$ is insufficient to capture the dynamics as accurately as that with $\mathrm{d}t \leq T_L/1000$ and/or any of the ode45 simulations with $\mathrm{Tol} \leq 10^{-6}$.

B.4 Summary

We see from our comparison of numerical solutions achieved with the Vay pusher method and the ode45 method (Section B.3) that both are capable of accurately solving the equations of motion in Equations (3.9) and (3.10). However, for our specific problem, the ode45 method offers the following benefits: (i) relative ease of parallelization over particles, which enables the use of

multi-core processing on high-performance computers and (ii) adaptive time-stepping, which produces consistent results efficiently without being constrained by extremely small time steps throughout the simulation period. Therefore, we choose to employ the ode45 method with $\mathrm{Tol} \leq 10^{-6}$ for all our simulations. However, we note that the Vay pusher method offers the distinct benefit of enabling the implementation of these simulations on platforms outside MATLAB®, such as on open-source compilers that employ Python.

Appendix C: Details of experimental setup

In this chapter, we discuss the details of experimental setups that may be relevant for multiple experiment campaigns either already covered within this dissertation or yet to be performed in the future.

C.1 Focal Spot Diagnostics

In this section, we provide key insights for extracting useful information from focal spot images measured at low power for an arbitrary imaging setup at a laser facility.

C.1.1 Focal Spot Image File Format

We typically capture focal spot images using a charge-coupled device camera in grayscale and store these images in the TIFF file format, which has the file extension `.tiff`. We use a minimum bit depth of $N_b = 8$ bits. Ideally, a higher bit depth of 12 or 16 bits provides enhanced dynamic range by increasing the number of available quantization levels. This is because each pixel can store integer values $\in [0, 2^{N_b} - 1]$. Consequently, a grayscale image comprised of M rows and N columns of pixels can represent pixel intensities $\in [0, 255]$ for an 8-bit image and $\in [0, 65535]$ for a 16-bit image. Thus, any inherent electronic noise of ± 1 count, for example, has a relatively adverse effect on an 8-bit image than it does on a 16-bit image. This makes it more

straightforward to minimize uncertainties due to background subtraction with 16-bit images than it is with 8-bit images. It is therefore beneficial to obtain images with higher bit depth.

C.1.2 Choosing the Appropriate Exposure Level

The exposure level of the recorded image can typically be controlled either using neutral density filters in the imaging setup or by setting the gain value of the camera. As we evaluate the peak intensity by distributing the peak power across the focal spot image, it is important to ensure that the image is neither underexposed nor overexposed as this can lead to significant error in inferring the peak intensity. To illustrate this, we show representative focal spot images captured with an 8-bit camera in Figure C.1.

We captured the focal spot images across three different laser shots with an internal gain setting of 15 dB, 19 dB and 24 dB. We set an empirically estimated value of 3 counts for the background level due to scattered light. Figures C.1a–C.1c show the images after background subtraction, while Figures C.1d–C.1f show the corresponding raw images before background subtraction. We see that when the image is underexposed (Figures C.1a and C.1d) the portion of the focal spot distribution that lies above the background level is underrepresented. This results in distributing the fixed peak power over a smaller area integral and thus overestimating the peak intensity. Meanwhile, when the image is overexposed (Figures C.1c and C.1f), the image saturates and results in the misrepresentation of the intensity distribution near the peak. It is thus desirable to adjust the exposure level to optimally utilize the available bit depth of the camera.

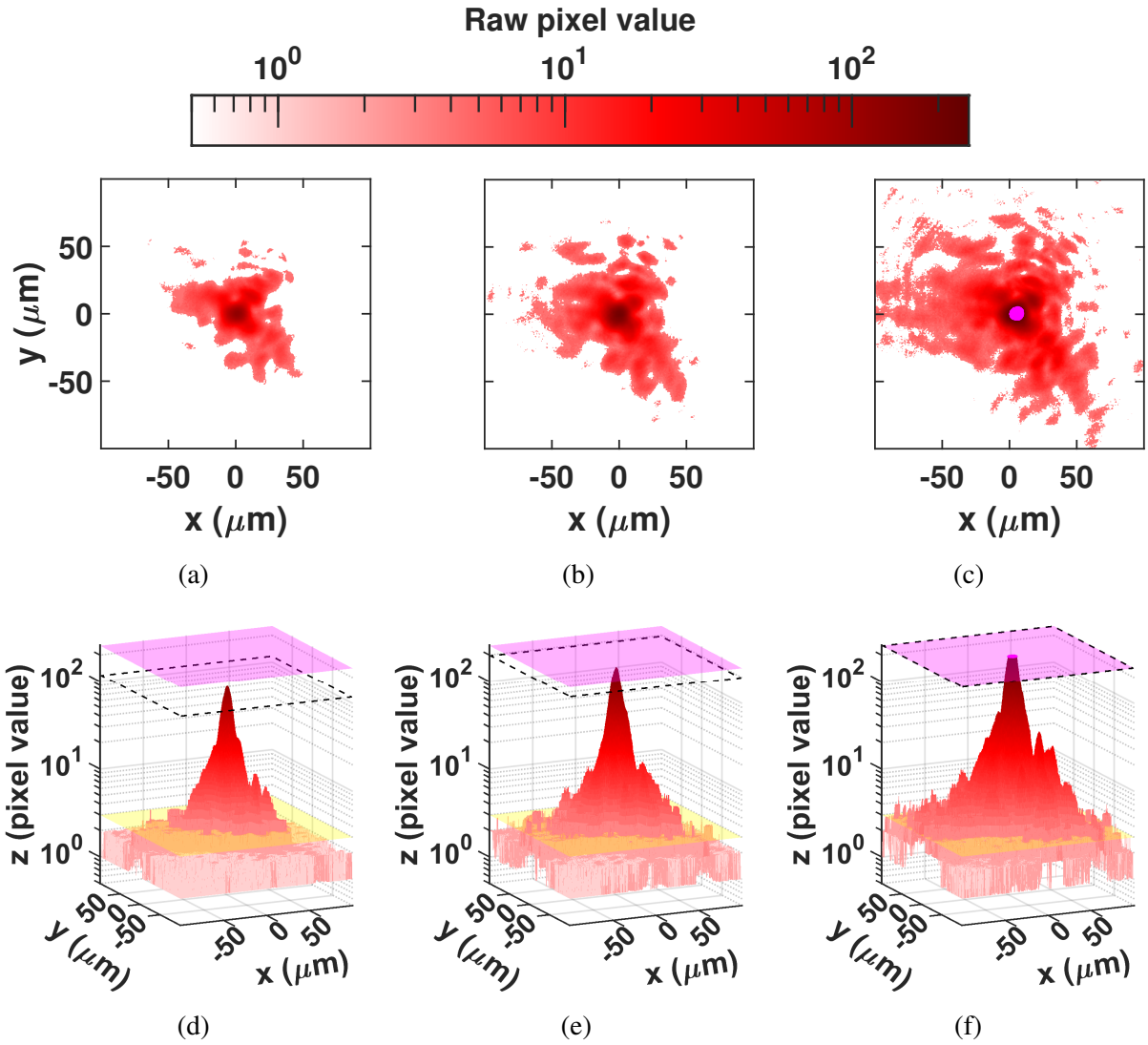


Figure C.1: Representative focal spot images captured across three different laser shots with an 8-bit camera for varying gain of (a) 15 dB, (b) 19 dB and (c) 24 dB. The color scale represents the raw value stored in each pixel. Three-dimensional view of (a)–(c) is shown in (d)–(f) where the height corresponds to the pixel value. The yellow and magenta planes represent the fixed value used to subtract the background and the maximum possible value, which are 3 and 255 here, respectively. The transparent plane with a black dashed outline represents the maximum pixel value stored in the corresponding image.

C.1.3 Establishing Image Orientation

As each focal spot image is essentially stored as a two-dimensional array where each array element is the integral value $\in [0, 2^{N_b} - 1]$ recorded in a pixel, it may be parsed differently across various image viewers or processing software used. Therefore, it is critical to establish the orientation of the recorded image with physical references as it is not straightforward to achieve this solely with ray tracing from the laser focus for any realistic imaging setup that involves several optical elements. A straightforward approach to achieve this in a pre-aligned imaging setup with an alignment laser is as follows

- Step 1: Establish the direction of the laser beam relative to geographic directions, i.e., North, South, East, and West. As an example, we consider a laser beam approximately traveling from North to South.

- Step 2: Using an opaque object with a well-defined straight edge, block a fraction of the imaged area on the focal plane along a specific direction on the horizontal axis and record an image. Take note of the blocking orientation chosen. In our example, this could mean choosing to block either from West to East or from East to West. Then, take note of the orientation in which this block appears on the image acquisition software. For example, if the imaging setup and/or the acquisition software introduces a rotation of 90° or 180°, the block may appear either along the vertical direction (up–down) or appear laterally inverted.

- Step 3: Repeat Step 2 for a specific direction of choice along the vertical axis.

- Step 4: Use the images recorded in Step 2 and 3 as reference images when opening the image on any software. For example, if the goal is to visualize the focal spot such that

the laser goes into the page while preserving up–down the same as that in the lab, identify the rotations and/or inversions that must be applied within the software for the reference images to be visualized along the required direction from their default orientation when opened with the software. Then, applying the same rotations and/or inversions in the same sequence to any focal spot image recorded with the same setup will provide the desired orientation of the focal spot.

C.1.4 Evaluating Energy Delivered to the Focal Plane for an Apodized Beam

The use of apodizers to vary the diameter of the collimated beam immediately preceding a focusing optic allows us to vary the $\mathrm{f}/\#$ of the optic with fixed focal length as the $\mathrm{f}/\#$ is simply the ratio of the focal length to the beam diameter. This is highly beneficial when it is desirable to switch between a tight (small $\mathrm{f}/\#$) and loose focus (large $\mathrm{f}/\#$) without needing to replace the focusing optic, which is both cumbersome and time-consuming. However, apodizing the beam implies that the energy delivered to the focal plane changes simultaneously as only some fraction of the laser energy is transmitted past the apodizer. One approach to fix the laser energy past the apodizer is to operate with reduced laser energy without the apodizer and increase the laser energy when the apodizer is in use. However, when it is critical to achieve the maximum possible peak intensity, we simply operate the laser with full energy. In this case, it is important to account for the loss in laser energy when inferring the peak intensity on the focal plane with the apodizer in use.

While the most ideal way to achieve this is to measure the total energy before and after the apodizer, such a measurement may not always be feasible for technical reasons. In such a

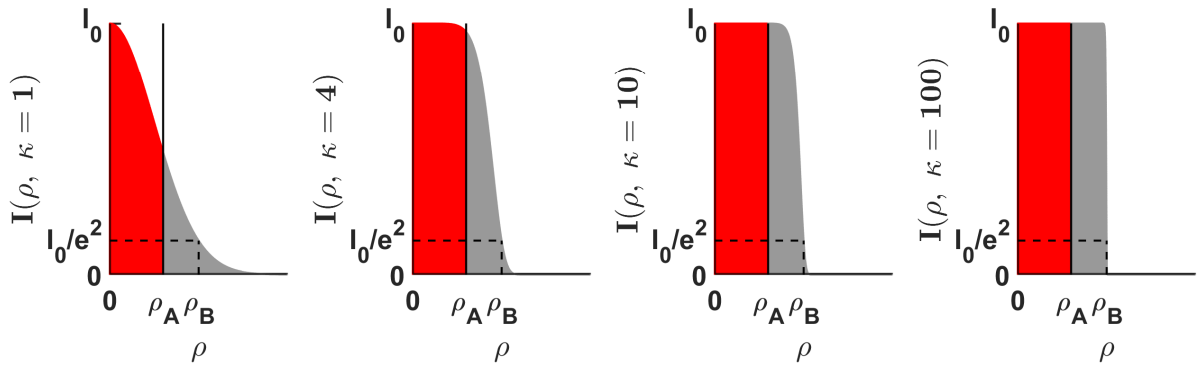


Figure C.2: Intensity profile of a super-Gaussian beam (Eq. (C.1)) with radius ρ_B for order (a) $\kappa = 1$, (b) $\kappa = 4$, (c) $\kappa = 10$, and (d) $\kappa = 100$. The red (gray) shaded region represents the part of the beam transmitted past (discarded by) a circular apodizer with radius ρ_A centered on the beam.

situation, it is possible to analytically infer the fraction of the laser energy delivered on the focal plane. Petawatt-class laser systems typically aim to employ a flat-top spatial profile to maximize the energy delivered while minimizing damage to optical components [171]. In practice, however, the spatial profile is often best approximated as a super-Gaussian with order $\kappa \approx 4$ to 10. For a collimated beam with a $1/e^2$ radius ρ_B, the spatial profile is thus

$$I(\rho,\ \kappa) = I_0\ \exp\left[-2\left(\frac{\rho}{\rho_B}\right)^{2\kappa}\right], \tag{C.1}$$

where $\kappa = 1$ represents a simple Gaussian. We show $I(\rho, \kappa)$ for a few relevant cases in Figure C.2. For a circular apodizer with radius ρ_A centered on the beam, we can thus calculate the fraction of the laser energy transmitted as

$$\mathcal{U} = \frac{\int_0^{\rho_A} \exp\left[-2\left(\frac{\rho}{\rho_B}\right)^{2\kappa}\right] \mathrm{d}\rho}{\int_0^{\infty} \exp\left[-2\left(\frac{\rho}{\rho_B}\right)^{2\kappa}\right] \mathrm{d}\rho}. \tag{C.2}$$

In our experiment in Section 4.3.2, we used a circular apodizer with radius $1.8\ \mathrm{cm}$ to apodize the collimated beam (diameter $10\ \mathrm{cm}$) before the focusing mirror (focal length $180\ \mathrm{mm}$) to produce an $\mathrm{f}/5$ focus. Thus, $\rho_A = 1.8\ \mathrm{cm}$ and $\rho_B = 5\ \mathrm{cm}$. For a realistic range of $\kappa = 4$ to 10, we get the ratio of energy transmitted through the apodizer as $\mathcal{U} \approx 0.17$ to 0.15. Therefore, we assume that the use of the apodizer reduced the energy delivered to the focal plane to $\approx 16\%$ of that without the apodizer.

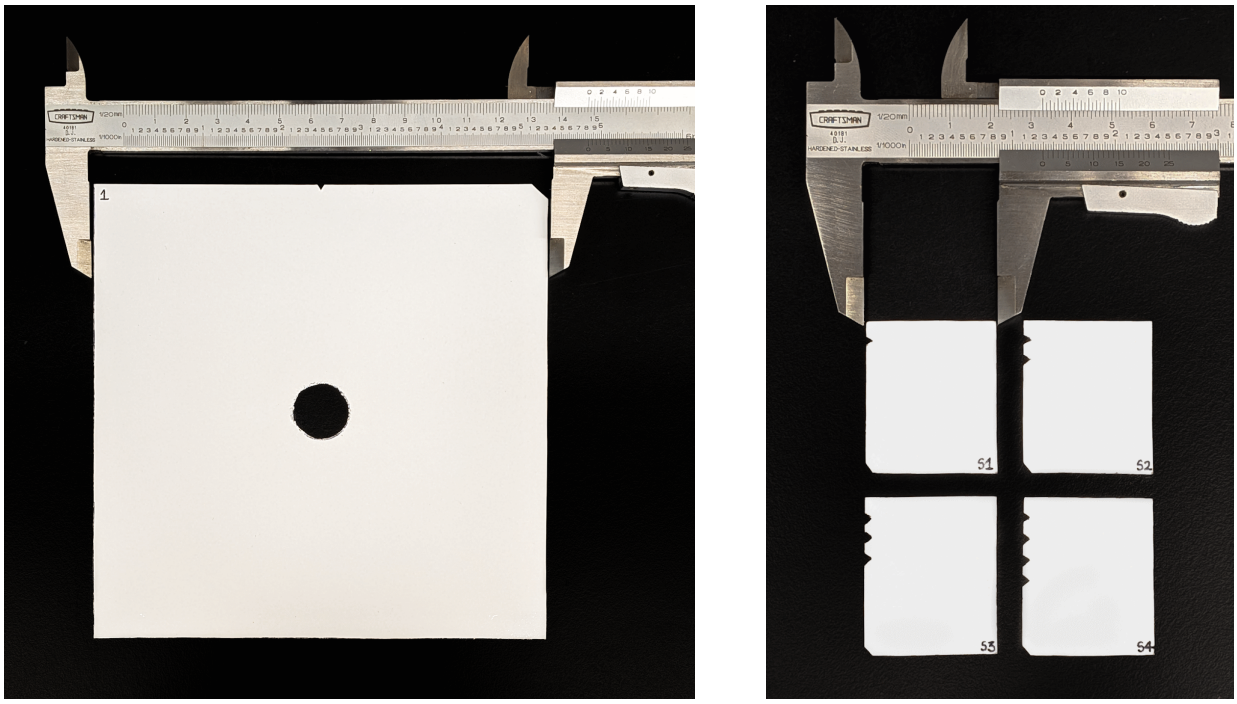
C.2 Image Plate Handling

In this section, we provide key details relevant for handling image plates to record the spatial distribution of electrons.

C.2.1 Preparing an Image Plate

Commercial image plates such as the Fujifilm BAS-MS or BAS-SR that we use are often manufactured in fixed dimensions that may be larger than necessary for our specific application. We thus cut the image plates to the desired shape and size. In this process, it is important to create features on the image plates that can help both identify the image plate as well as its orientation when used and scanned. We typically cut a triangular feature along an edge that represents the numbering of the image plate and one consistent corner across all the image plates used in any

given experiment, as shown in Figure C.3. These two features together help uniquely correlate the orientation of the plate between the chamber and the scanner even if the image plate is symmetric along multiple axes such as a square.



(a) (b)

Figure C.3: Image plates used to measure (a) the spatial distributions of electrons in CLPU, April 2024 (Section 5.3) and (b) energy distribution through the magnetic spectrometer in ZEUS, June 2024 (Section 4.3.2).

Before placing the image plate in the chamber, we erase any residual data stored in the image plate by exposing it to ambient light, or a flash lamp if available, for $\approx$ 15 to 20 minutes. We then wrap the image plate with aluminum foil to prevent the scattered light in the target chamber from erasing the data recorded after the laser shot. We verify that the foil is sufficiently uniform and free of tiny holes or wrinkles that could compromise light-tightness or cause artifacts in the recorded distribution. We wrap the image plate only shortly before placing it in the chamber to prevent the accumulation of energy deposited by cosmic rays, which constantly traverse the

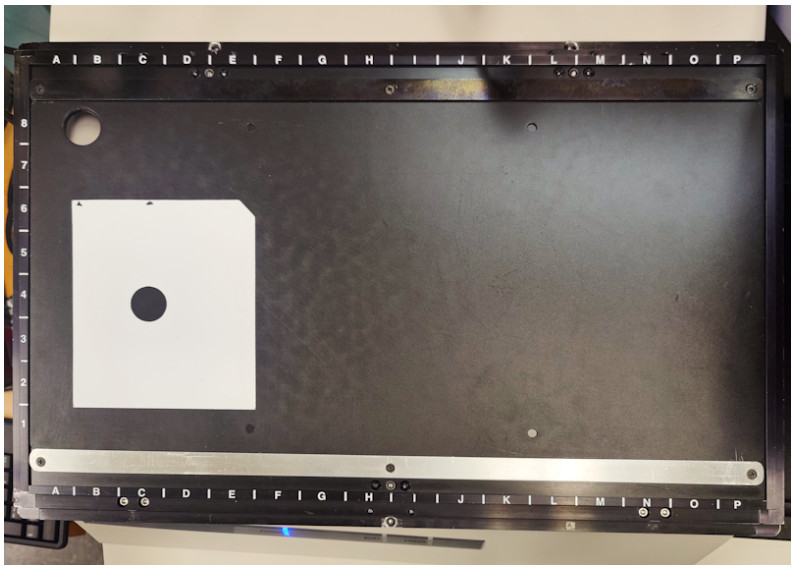
Earth's surface. The energy deposited by cosmic rays can contribute to significant background noise if the image plate remains unexposed for several hours.

C.2.2 Analyzing an Image Plate

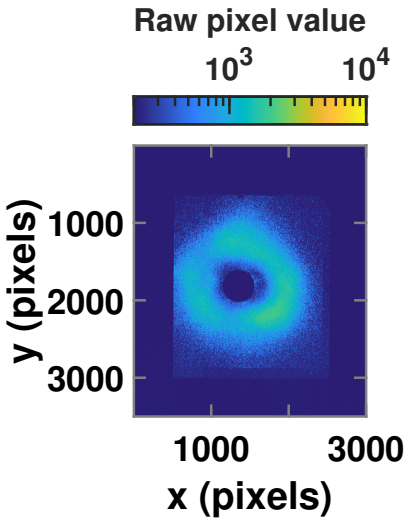
Following exposure to the radiation of interest, in this case electrons, we place the magnetic back surface of the image plate in contact with the magnetic surface of the scanner tray as shown in Figure C.4a and place the scanner tray inside the image plate scanning system. Based on the position of the image plate on the scanner tray, we select a region to scan that is sufficiently clear of the edges of the image plate. In Figure C.4a, this corresponds to the region `F7`. We then choose the desired scan settings that are important for extracting PSL values from the raw scan recorded in a `.gel` file. These include the resolution $\mathcal{R}$, sensitivity parameter $\mathcal{S}$ and latitude $\mathcal{L}$. The PSL value stored in each pixel is given by [148]

$$\mathrm{PSL} = \left(\frac{G}{2^{16}-1}\right)^2 \left(\frac{\mathcal{R}\,(\mu\mathrm{m})}{100}\right)^2 \frac{4000}{\mathcal{S}}\, 10^{\mathcal{L}/2}, \tag{C.3}$$

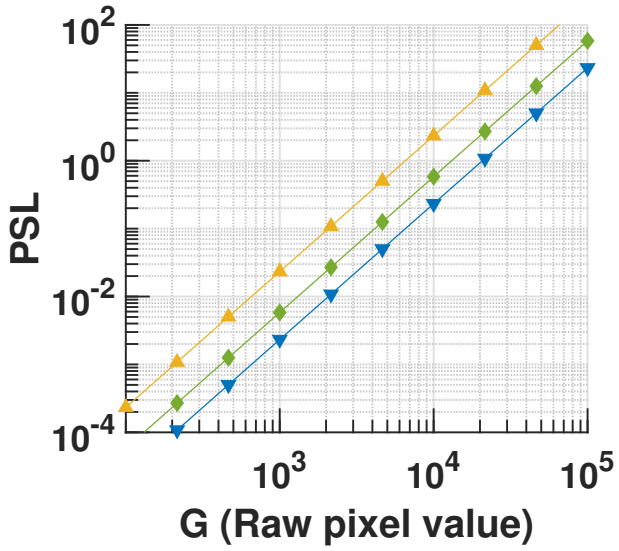
where G is the raw value stored in a pixel. Typically, we set $\mathcal{S} = 4000$ or 10000 and $\mathcal{L} = 5$. While some scanners allow the setting of $\mathcal{S}$ directly, other scanners only allow the setting of the bias voltage in the internal photomultiplier tube (PMT). In that case, we estimate the sensitivity parameter based on calibrations that map the PMT voltage to $\mathcal{S}$, such as those performed in [148]. Once the PSL value is obtained, additional processing may be performed as necessary to correct for factors such as signal fading over time between measurement and scanning [147].



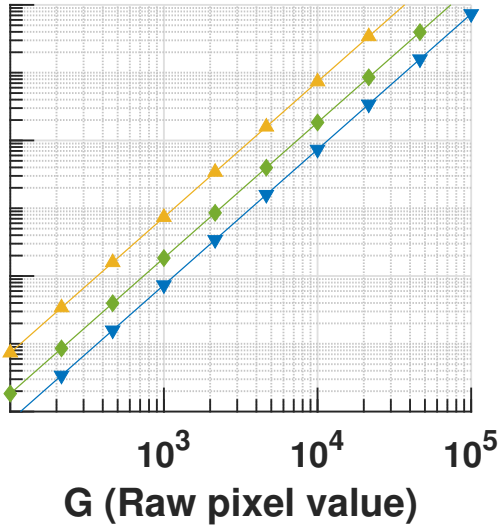
(a)



(b)



(c)



(d)

Figure C.4: Image plate placed on a scanner tray in (a) and a representative scan in (b) where the color axis represents the raw value recorded in each 50×50 μm^2 pixel, when $\mathcal{S} = 4000$ and $\mathcal{L} = 5$ (see text). PSL values corresponding to a range of raw values stored in a 50×50 μm^2 pixel shown for (c) $\mathcal{L} = 4$ and (d) $\mathcal{L} = 5$. The blue, green and yellow lines marked by the downward triangle, diamond and upward triangle correspond to $\mathcal{S} = 10000, 4000$ and 1000, respectively.

C.3 Time of Flight Detector

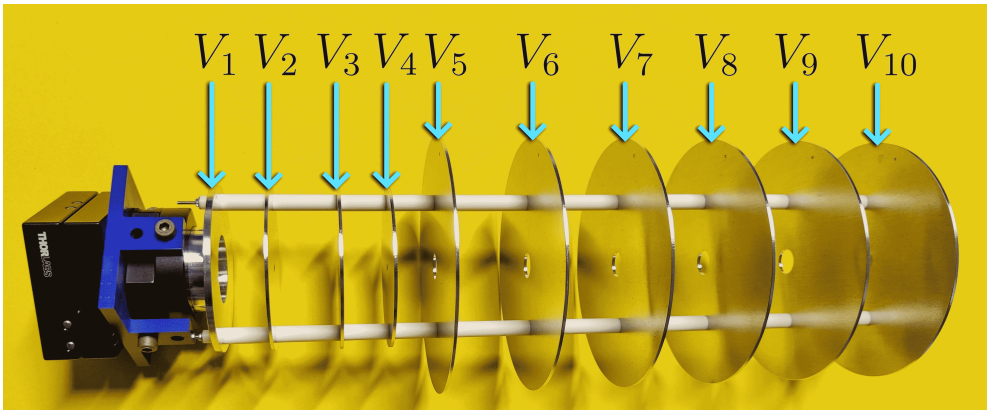
In this section, we provide key details relevant to the assembly and operation of components in the TOF detector used in Section 5.1.1.

C.3.1 Assembling the Extraction and Deflection Modules

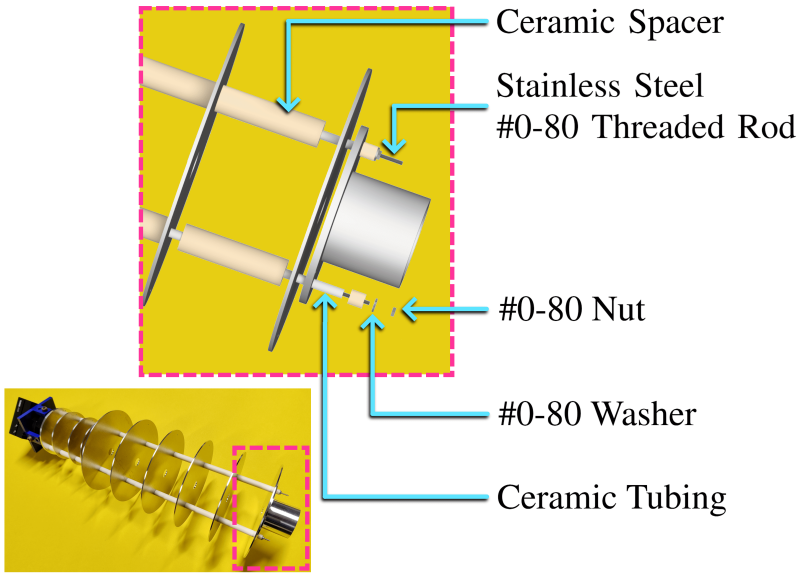
We provide an image of the fully-assembled extraction module in Figure C.5a. It consists of 10 electrodes, which are essentially plates made of aluminum, labeled 1 through 10 with corresponding voltages V_1 through V_{10}. The plates are held together by two pillars whose components are shown in Figure C.5b. A $\#0$-80 threaded rod made of stainless steel forms the skeletal structure of the pillar that is held together on both sides by compression using a $\#0$-80 nut and washer. A ceramic tube surrounds the stainless steel rod to prevent electrical contact between the rod and the electrodes. We used ceramic spacers to set the desired spacing between each consecutive pair of electrodes as well as on the outside of plates 1 and 10 to maximize the area of contact for the washer to apply compression. In addition, we placed a commercially available stainless-steel mesh in electrode 10 between the flat disc-like plate and the part that resembles a top-hat, which are in direct contact to form electrode 10. The mesh was made of thin wires of diameter $\approx 30\,\mu\mathrm{m}$ spaced $\approx 0.51\,\mathrm{mm}$ apart to maximize ion transmission through the electrode while maximizing flatness of the field at the end electrode.

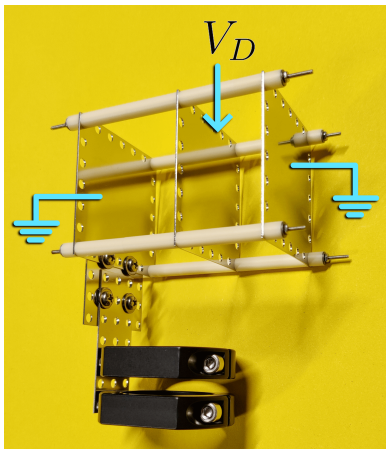
The deflection module, pictured in Figure C.5c, consists of a similar structure that holds together three electrodes made of commercially available stainless steel plates, where the plates on the ends are held at ground and the plate in the center is pulsed to some voltage V_D.

Each electrode in both the extraction and deflection modules is electrically connected with a



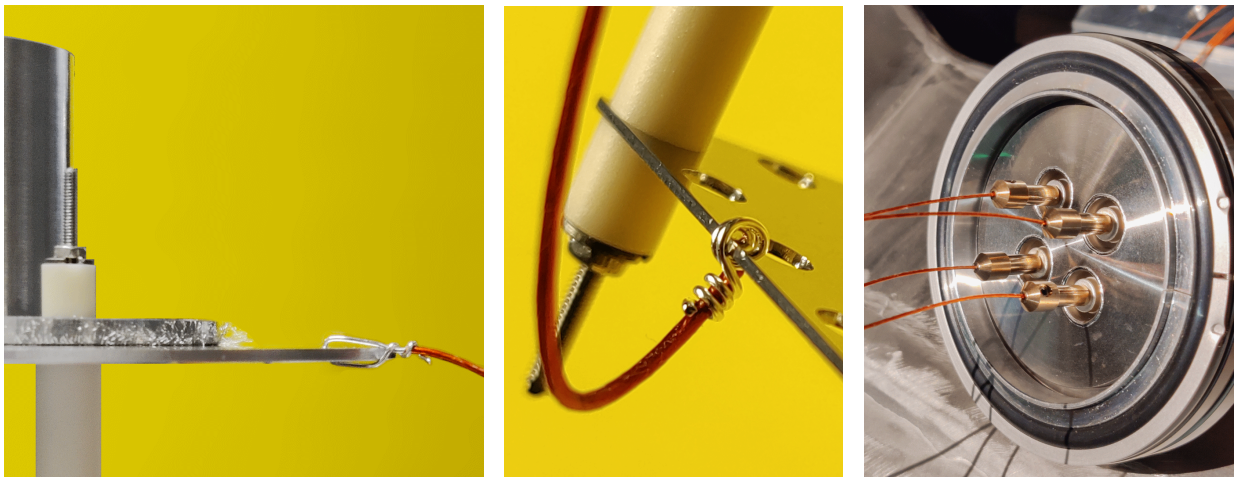
(a)





(b) (c)

Figure C.5: Components of the TOF detector. The fully constructed extraction module is shown in (a) and a deconstructed close-up view is shown in (b). The laser focus is between plates 2 and 3. The deflection module is shown in (c).



(a) (b) (c)

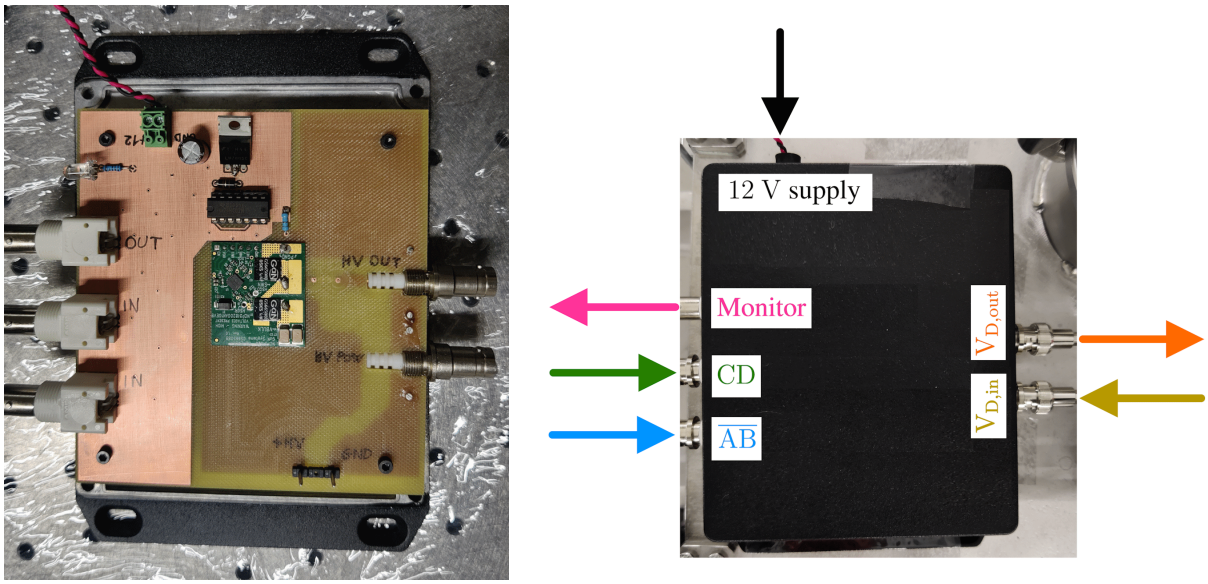
Figure C.6: Wiring connected to (a) a plate on the extraction module, (b) a plate on the deflection module and (c) the flange on the vacuum chamber.

Kapton insulated wire (gauge 24 AWG) with a silver-plated copper core as shown in Figures C.6a and C.6b. The diameters of the wire and its core are $\approx 0.76\,\mathrm{mm}$ and $\approx 0.51\,\mathrm{mm}$, respectively. We connect the other end of the wire to the internal side of a feedthrough using a commercially available pin connector as shown in Figure C.6c. The external side of the feedthrough has SHV connectors to allow the use of high voltage signals.

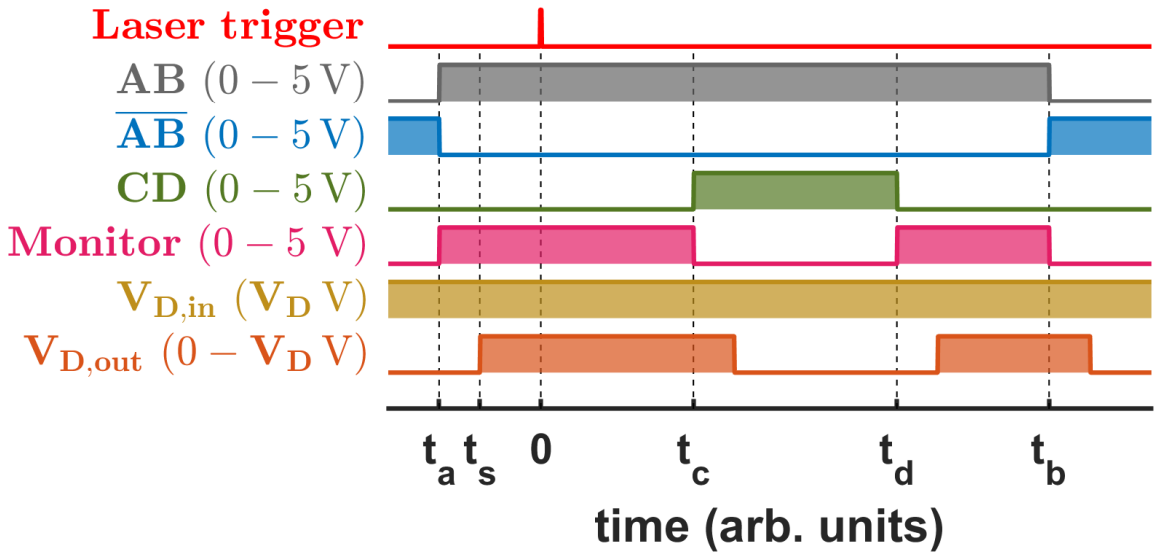
C.3.2 Deflection Circuit

We built a high voltage switch circuit to pulse the deflection voltage through the deflection module. We incorporated the evaluation board of an NCP51820 Half-Bridge Gate Driver from onsemi (formerly ON Semiconductor), pictured in Figure C.7a, with an integrated circuit hosting logic gates on a custom-built printed circuit board. We show the input and output signals of the deflection circuit in Figure C.7b and describe the timing schematic of the signals (shown in Figure C.7c) below.

We obtain an electronic trigger from the laser system that allows us to generate trigger



(a) (b)



(c)

Figure C.7: Operation of the deflection circuit. Components are shown in (a), input and output signals are shown in (b), and timing schematic (not to scale) for the signals is shown in (c), where time increases to the right, i.e., $t_b > t_a$.

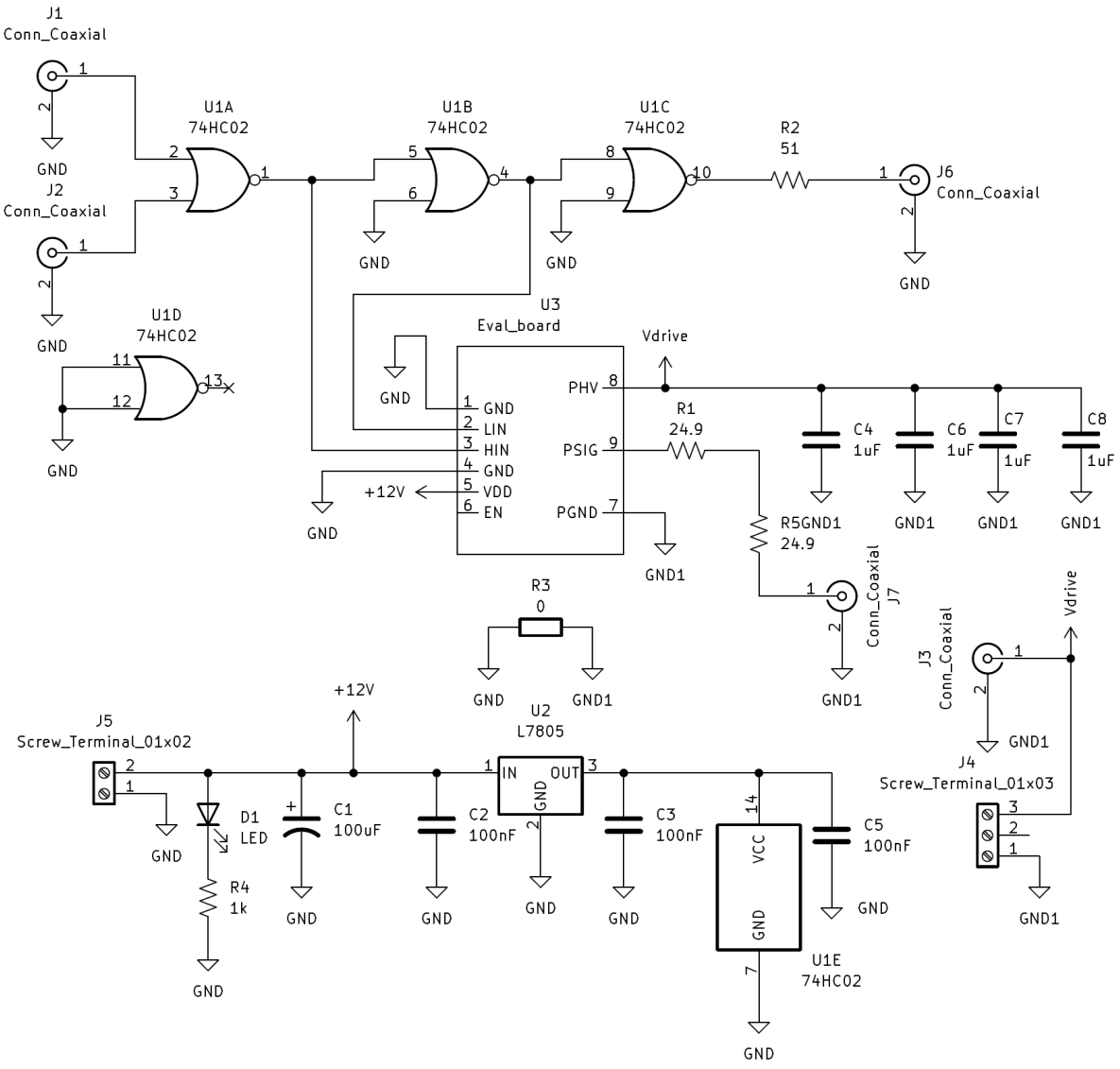


Figure C.8: Schematic diagram of the deflection circuit.

pulses relative to the laser pulse using a Digital Delay Generator that produces two independent pulse outputs, AB and CD. Signal AB (CD) rises at t_a (t_c) and falls at t_b (t_d). We supply $\overline{\mathrm{AB}}$ and CD as inputs and the deflection circuit performs an XNOR operation to produce the Monitor signal that we feed into an oscilloscope to monitor the output. The pulse CD thus acts as the temporal window for the transmission of unaffected ions through the deflection module. We supply a constant voltage input of $V_{D,in} = V_D\,\mathrm{V}$ to scale the monitor signal from a maximum voltage of $5\,\mathrm{V}$ to $V_D\,\mathrm{V}$, subject to an inherent system delay of $95\,\mathrm{ns}$, i.e., the output signal that is fed to the deflection module electrode is delayed such that its rise time is $t_s = t_a + 95\,\mathrm{ns}$. We provide a schematic diagram of the deflection circuit in Figure C.8 for reference.

C.4 Two-beam setup

In this section, we present details relevant to the experimental realization of the two-beam setup used in Section 5.3. We implemented a Mach-Zehnder interferometer to split the single beam from the final amplifier into two beams with variable time delay as shown in Figure C.9a. We did this before the compressor as a temporally compressed pulse can exceed the damage threshold for transmissive optical components used in the interferometer, i.e., the beam splitters. To split the incoming beam into two beams with notably different pulse energies, $\mathrm{BS1}$ was 80% reflective and 20% transmissive. Thus, the beam in the $\mathrm{M1}$-$\mathrm{M2}$ ($\mathrm{M3}$-$\mathrm{M4}$) arm contained 80% (20%) of the incoming beam from the final amplifier. Mirrors $\mathrm{M1}$ and $\mathrm{M2}$ were placed on a motorized translation stage to vary the time delay between the two pulses as $\Delta t = \Delta l/c$ for a difference in path length of Δl between the two beam paths. The translation stage had a total travel range of $300\ \mathrm{mm}$ with a minimum step size of $0.1\ \mu\mathrm{m}$ and repeatability $< 2\ \mu\mathrm{m}$. This

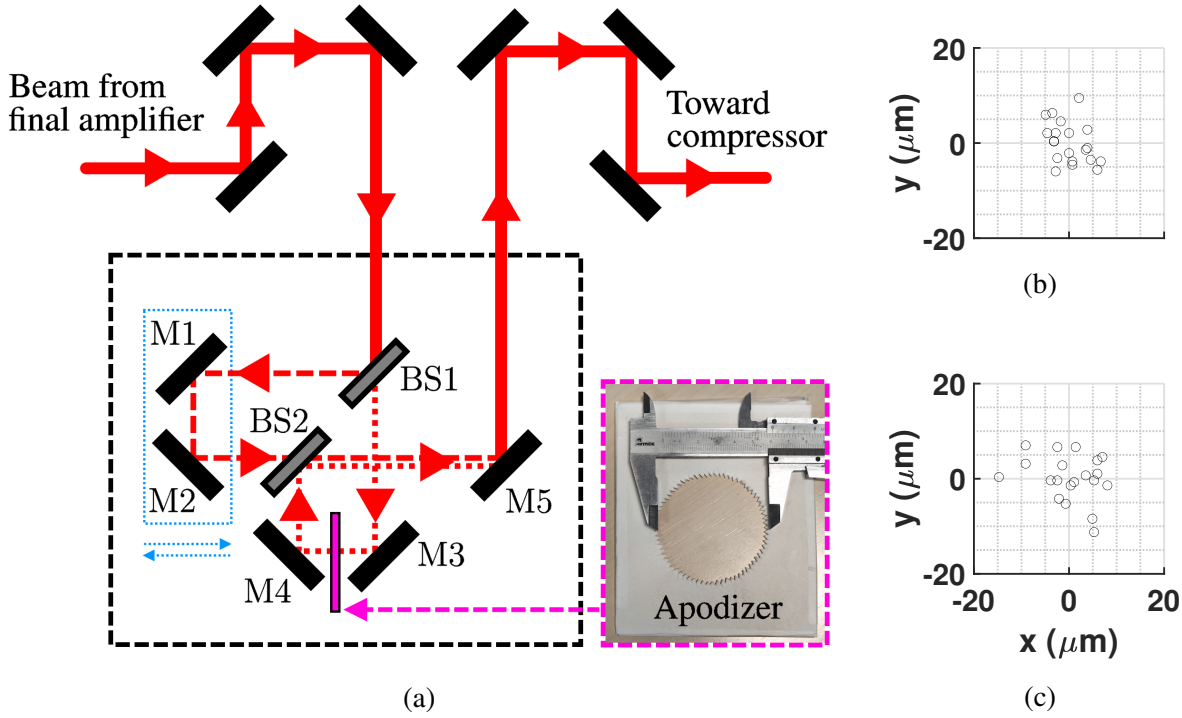


Figure C.9: Schematic diagram of the two-beam setup (not to scale) employed in CLPU, April 2024, for the ponderomotive-expulsion experiment (Section 5.3) in (a). The black dashed boundary represents the Mach-Zehnder setup. Plane mirrors are marked 'M1' through 'M5', beam splitters are marked 'BS1' and 'BS2'. The two beams resulting from BS1 are represented by the red dashed and dotted rays, which overlap following BS2. The blue dotted boundary around M1 and M2 represents a motorized translation stage. The 6-cm apodizer was placed between M3 and M4. Pointing fluctuation on the focal plane in the target chamber is shown for the strong (b) and weak (c) beams over a series of 20 shots per beam imaged at low power.

allowed us to introduce path length differences with repeatability $< 4\ \mu\mathrm{m}$, corresponding to $\lesssim 13\ \mathrm{fs}$, due to both $\mathrm{M1}$ and $\mathrm{M2}$ being on the translation stage. We placed the apodizer of width $6\ \mathrm{cm}$ between $\mathrm{M3}$ and $\mathrm{M4}$ in the path of the weak beam. We then recombined the beam paths using $\mathrm{BS2}$, which was 50% reflective and 50% transmissive, thus discarding half the energy within each individual arm and allowing them to subsequently copropagate toward the compressor.

We quantified the relative spatial fluctuation of the beams on the focal plane in the target chamber as follows. When both beams were delivered to the target chamber, we first optimized the overlap of the two beams visually using low-power images by performing minor motorized adjustments to the position of the focusing optic. This allowed the peaks of the two beams to appear overlapped to an extent where the peak of the weak beam was indistinguishable from the secondary maxima or hot spots of the strong beam. Then, we recorded a 20-shot series of focal-spot images for each beam while the other was blocked in the Mach-Zehnder interferometer. For each series, we determined the coordinates (x_j, y_j) of the maximum intensity in the j^{th} image. We defined the effective center of the series as the mean position of these maxima,

$$\langle x \rangle = \frac{1}{20} \sum_{j=1}^{20} x_j, \tag{C.4}$$

$$\langle y \rangle = \frac{1}{20} \sum_{j=1}^{20} y_j. \tag{C.5}$$

We show the position of the peak in each image relative to $(\langle x \rangle, \langle y \rangle)$ as the center for the strong and weak beam in Figures C.9b and C.9c, respectively. We calculated the root-mean-square displacement as

$$\sigma_{RMS} = \sqrt{\frac{1}{20}\sum_{j=1}^{20}((x_j - \langle x \rangle)^2 + (y_j - \langle y \rangle)^2)}, \tag{C.6}$$

obtaining $\sigma_{RMS} \approx 5.5\ \mu\mathrm{m}$ and $7.6\ \mu\mathrm{m}$ for the strong and weak beam, respectively. This implies that the relative spatial fluctuation between the peaks of the two beams was $\lesssim$ the FWHM of the individual peaks.

References

[1] F. J. McClung and R. W. Hellwarth. “Giant Optical Pulsations from Ruby”. *Journal of Applied Physics* 33.3 (Mar. 1962), pp. 828–829. ISSN: 0021-8979. DOI: 10.1063/1.1777174.

[2] L. E. Hargrove, R. L. Fork, and M. A. Pollack. “LOCKING OF He–Ne LASER MODES INDUCED BY SYNCHRONOUS INTRACAVITY MODULATION”. *Applied Physics Letters* 5.1 (July 1964), pp. 4–5. ISSN: 0003-6951. DOI: 10.1063/1.1754025.

[3] D. Strickland and G. Mourou. “Compression of amplified chirped optical pulses”. *Optics Communications* 55.6 (Oct. 1985), pp. 447–449. ISSN: 0030-4018. DOI: 10.1016/0030-4018(85)90151-8.

[4] C. Danson, D. Hillier, N. Hopps, and D. Neely. “Petawatt class lasers worldwide”. *High Power Laser Science and Engineering* 3 (Jan. 2015), e3. ISSN: 2095-4719, 2052-3289. DOI: 10.1017/hpl.2014.52.

[5] C. N. Danson, C. Haefner, J. Bromage, T. Butcher, J.-C. F. Chanteloup, E. A. Chowdhury, A. Galvanauskas, L. A. Gizzi, J. Hein, D. I. Hillier, N. W. Hopps, Y. Kato, E. A. Khazanov, R. Kodama, G. Korn, R. Li, Y. Li, J. Limpert, J. Ma, C. H. Nam, D. Neely, D. Papadopoulos, R. R. Penman, L. Qian, J. J. Rocca, A. A. Shaykin, C. W. Siders, C. Spindloe, S. Szatmári, R. M. G. M. Trines, J. Zhu, P. Zhu, and J. D. Zuegel. “Petawatt and exawatt class lasers worldwide”. *High Power Laser Science and Engineering* 7 (Jan. 2019), e54. ISSN: 2095-4719, 2052-3289. DOI: 10.1017/hpl.2019.36.

[6] C. N. Danson, L. A. Gizzi, and D. Hillier. “High Power Laser Science and Engineering Editorial – a celebration of ultra-high-power lasers”. *High Power Laser Science and Engineering* 14 (Jan. 2026), e1. ISSN: 2095-4719, 2052-3289. DOI: 10.1017/hpl.2025.10102.

[7] C. A. Haynam, P. J. Wegner, J. M. Auerbach, M. W. Bowers, S. N. Dixit, G. V. Erbert, G. M. Heestand, M. A. Henesian, M. R. Hermann, K. S. Jancaitis, K. R. Manes, C. D. Marshall, N. C. Mehta, J. Menapace, E. Moses, J. R. Murray, M. C. Nostrand, C. D. Orth, R. Patterson, R. A. Sacks, M. J. Shaw, M. Spaeth, S. B. Sutton, W. H. Williams, C. C. Widmayer, R. K. White, S. T. Yang, and B. M. Van Wonterghem. “National Ignition Facility laser performance status”. *Applied Optics* 46.16 (June 2007), p. 3276. ISSN: 0003-6935, 1539-4522. DOI: 10.1364/AO.46.003276.

[8] A. Casner, T. Caillaud, S. Darbon, A. Duval, I. Thfouin, J. Jadaud, J. LeBreton, C. Reverdin, B. Rosse, R. Rosch, N. Blanchot, B. Villette, R. Wrobel, and J. Miquel. “LMJ/PETAL laser facility: Overview and opportunities for laboratory astrophysics”. *High Energy Den-*

sity Physics 17 (Dec. 2015), pp. 2–11. ISSN: 15741818. DOI: 10.1016/j.hedp.2014.11.009.

[9] W. Zheng, X. Wei, Q. Zhu, F. Jing, D. Hu, J. Su, K. Zheng, X. Yuan, H. Zhou, W. Dai, W. Zhou, F. Wang, D. Xu, X. Xie, B. Feng, Z. Peng, L. Guo, Y. Chen, X. Zhang, L. Liu, D. Lin, Z. Dang, Y. Xiang, and X. Deng. "Laser performance of the SG-III laser facility". *High Power Laser Science and Engineering* 4 (Jan. 2016), e21. ISSN: 2095-4719, 2052-3289. DOI: 10.1017/hpl.2016.20.

[10] F. Wang, S. Jiang, Y. Ding, S. Liu, J. Yang, S. Li, T. Huang, Z. Cao, Z. Yang, X. Hu, W. Miao, J. Zhang, Z. Wang, G. Yang, R. Yi, Q. Tang, L. Kuang, Z. Li, D. Yang, Y. Li, X. Peng, K. Ren, and B. Zhang. "Recent diagnostic developments at the 100 kJ-level laser facility in China". *Matter and Radiation at Extremes* 5.3 (May 2020), p. 035201. ISSN: 2468-2047. DOI: 10.1063/1.5129726.

[11] T. R. Boehly, D. L. Brown, R. S. Craxton, R. L. Keck, J. P. Knauer, J. H. Kelly, T. J. Kessler, S. A. Kumpan, S. J. Loucks, S. A. Letzring, F. J. Marshall, R. L. McCrory, S. F. B. Morse, W. Seka, J. M. Soures, and C. P. Verdon. "Initial performance results of the OMEGA laser system". *Optics Communications* 133.1 (Jan. 1997), pp. 495–506. ISSN: 0030-4018. DOI: 10.1016/S0030-4018(96)00325-2.

[12] D. Zhao, L. Wan, Z. Lin, P. Shao, and J. Zhu. "SG-II-Up prototype final optics assembly: optical damage and clean-gas control". *High Power Laser Science and Engineering* 3 (Jan. 2015), e7. ISSN: 2095-4719, 2052-3289. DOI: 10.1017/hpl.2015.1.

[13] C. Radier, O. Chalus, M. Charbonneau, S. Thambirajah, G. Deschamps, S. David, J. Barbe, E. Etter, G. Matras, S. Ricaud, V. Leroux, C. Richard, F. Lureau, A. Baleanu, R. Banici, A. Gradinariu, C. Caldararu, C. Capiteanu, A. Naziru, B. Diaconescu, V. Iancu, R. Dabu, D. Ursescu, I. Dancus, C. A. Ur, K. A. Tanaka, and N. V. Zamfir. "10 PW peak power femtosecond laser pulses at ELI-NP". *High Power Laser Science and Engineering* 10 (Jan. 2022), e21. ISSN: 2095-4719, 2052-3289. DOI: 10.1017/hpl.2022.11.

[14] W. Li, Z. Gan, L. Yu, C. Wang, Y. Liu, Z. Guo, L. Xu, M. Xu, Y. Hang, Y. Xu, J. Wang, P. Huang, H. Cao, B. Yao, X. Zhang, L. Chen, Y. Tang, S. Li, X. Liu, S. Li, M. He, D. Yin, X. Liang, Y. Leng, R. Li, and Z. Xu. "339 J high-energy Ti:sapphire chirped-pulse amplifier for 10 PW laser facility". *Optics Letters* 43.22 (Nov. 2018), p. 5681. ISSN: 0146-9592, 1539-4794. DOI: 10.1364/OL.43.005681.

[15] X. Liang, Y. Leng, R. Li, and Z. Xu. "Recent Progress on the Shanghai Superintense Ultrafast Laser Facility (SULF) at SIOM". In: *OSA High-brightness Sources and Light-driven Interactions Congress 2020 (EUVXRAY, HILAS, MICS)*. Washington, DC: Optica Publishing Group, 2020, HTh2B.2. ISBN: 978-1-943580-73-6. DOI: 10.1364/HILAS.2020.HTh2B.2.

[16] X. Zeng, K. Zhou, Y. Zuo, Q. Zhu, J. Su, X. Wang, X. Wang, X. Huang, X. Jiang, D. Jiang, Y. Guo, N. Xie, S. Zhou, Z. Wu, J. Mu, H. Peng, and F. Jing. "Multi-petawatt laser facility fully based on optical parametric chirped-pulse amplification". *Optics Letters* 42.10 (May 2017), p. 2014. ISSN: 0146-9592, 1539-4794. DOI: 10.1364/OL.42.002014.

[17] *ELI's L4 ATON Laser Achieves 5 Petawatt — ELI's L4 ATON Laser Achieves 5 Petawatt*. URL: https://www.eli-laser.eu/news/eli-s-l4-aton-laser-achieves-5-petawatt/.

[18] *LASER L4 ATON — ELI Beamlines – Dolní Břežany*. URL: https://www.eli-beams.eu/facility/lasers/laser-4-aton-10-pw-2-kj/.

[19] J. W. Yoon, Y. G. Kim, I. W. Choi, J. H. Sung, H. W. Lee, S. K. Lee, and C. H. Nam. "Realization of laser intensity over 10^{23} W/cm^2". *Optica* 8.5 (May 2021), p. 630. ISSN: 2334-2536. DOI: 10.1364/OPTICA.420520.

[20] F. Gobert, Y. Ayoul, A. Beluze, D. Mataja, A. Fréneaux, N. Lebas, M. Chabanis, M. Dumergue, P. Audebert, D. N. Papadopoulos, and F. Mathieu. "The Apollon laser facility : operational aspects of the multi-PW beam line". In: *High-Brightness Sources and Light-Driven Interactions Congress*. Vienna: Optica Publishing Group, 2024, JTu4A.10. ISBN: 978-1-957171-35-7. DOI: 10.1364/EUVXRAY.2024.JTu4A.10.

[21] W. Yao, R. Lelièvre, I. Cohen, T. Waltenspiel, A. Allaoua, P. Antici, Y. Ayoul, A. Beck, A. Beluze, C. Blancard, D. Cavanna, M. Chabanis, S. N. Chen, E. Cohen, P. Cossé, Q. Ducasse, M. Dumergue, F. E. Hai, C. Evrard, E. Filippov, A. Freneaux, D. C. Gautier, F. Gobert, F. Goupille, M. Grech, L. Gremillet, Y. Heller, E. d'Humières, H. Lahmar, L. Lancia, N. Lebas, L. Lecherbourg, S. Marchand, D. Mataja, G. Meyniel, D. Michaeli, D. Papadopoulos, F. Perez, S. Pikuz, I. Pomerantz, P. Renaudin, L. Romagnani, F. Trompier, E. Veuillot, T. Vinchon, F. Mathieu, and J. Fuchs. "Characterization and performance of the Apollon main short-pulse laser beam following its commissioning at 2 PW level". *Physics of Plasmas* 32.4 (Apr. 2025), p. 043106. ISSN: 1070-664X. DOI: 10.1063/5.0252874.

[22] J. Hartmann, T. F. Rösch, F. Balling, M. Berndl, L. Doyle, L. Flaig, S. Gerlach, L. Tischendorf, and J. Schreiber. "Commissioning of the laser-driven ion acceleration beamline at the Centre for Advanced Laser Applications". In: *Laser Acceleration of Electrons, Protons, and Ions VI*. Vol. 11779. SPIE, Apr. 2021, pp. 44–49. DOI: 10.1117/12.2592407.

[23] A. Maksimchuk, J. Nees, B. Hou, R. Anthony, J. Bae, F. Bayer, M. Burger, P. T. Campbell, J. Cardarelli, V. Contreras, N. Ernst, F. Falcoz, R. Fitzgarrald, I. Jovanovic, G. Kalinchenko, C. Kuranz, J. Latham, Y. Ma, A. McKelvey, T. Nutting, Q. Qian, B. K. Russell, G. Sucha, A. G. R. Thomas, R. Van Camp, E. Viges, L. Willingale, G. Young, Q. Zhang, and K. Krushelnick. "The ZEUS multi-petawatt laser system". *Physics of Plasmas* 32.10 (Oct. 2025), p. 103107. ISSN: 1070-664X. DOI: 10.1063/5.0283440.

[24] K. Nakamura, H.-S. Mao, A. J. Gonsalves, H. Vincenti, D. E. Mittelberger, J. Daniels, A. Magana, C. Toth, and W. P. Leemans. "Diagnostics, Control and Performance Parameters for the BELLA High Repetition Rate Petawatt Class Laser". *IEEE Journal of Quantum Electronics* 53.4 (Aug. 2017), pp. 1–21. ISSN: 1558-1713. DOI: 10.1109/JQE.2017.2708601.

[25] N. Blanchot, G. Béhar, J. C. Chapuis, C. Chappuis, S. Chardavoine, J. F. Charrier, H. Coïc, C. Damiens-Dupont, J. Duthu, P. Garcia, J. P. Goossens, F. Granet, C. Grosset-Grange, P. Guerin, B. Hebrard, L. Hilsz, L. Lamaignere, T. Lacombe, E. Lavastre, T. Longhi, J. Luce, F. Macias, M. Mangeant, E. Mazataud, B. Minou, T. Morgaint, S. Noailles, J. Neauport, P. Patelli, E. Perrot-Minnot, C. Present, B. Remy, C. Rouyer, N. Santacreu, M. Sozet, D. Valla, and F. Laniesse. "1.15 PW–850 J compressed beam demonstration using the PETAL facility". EN. *Optics Express* 25.15 (July 2017), pp. 16957–16970. ISSN: 1094-4087. DOI: 10.1364/OE.25.016957.

[26] H. Li, K. Liu, X. Wang, X. Liu, X. Meng, Y. Liu, L. Song, Y. Leng, and R. Li. "Timing fluctuation correction for the front end of a 100-PW laser". *High Power Laser Science and Engineering* 11 (Jan. 2023), e52. ISSN: 2095-4719, 2052-3289. DOI: 10.1017/hpl.2023.41.

[27] A. Wang, P. Xue, X. Liu, X. Wang, L. Yu, X. Liang, Y. Leng, and R. Li. "Characteristics of broadband OPCPA based on DKDP crystals with different deuterations for the SEL-100 PW laser system". EN. *Optics Express* 32.3 (Jan. 2024), pp. 3597–3605. ISSN: 1094-4087. DOI: 10.1364/OE.505937.

[28] Y. Li, L. Chen, M. Chen, F. Liu, Y. Gu, B. Guo, J. Hua, T. Huang, Y. Leng, F. Li, L. Li, R. Li, C. Lin, W. Lu, Z. Lyu, W. Ma, X. Ning, Y. Peng, Y. Wan, J. Wang, Z. Wang, Z. Wei, X. Yan, J. Zhang, B. Zhao, Z. Zhao, C. Zhou, K. Zhou, W. Zhou, J. Zhu, and P. Zhu. "High-intensity lasers and research activities in China". *High Power Laser Science and Engineering* 13 (Jan. 2025), e12. ISSN: 2095-4719, 2052-3289. DOI: 10.1017/hpl.2024.69.

[29] I. Y. Kostyukov, E. A. Khazanov, A. A. Shaikin, A. G. Litvak, and A. M. Sergeev. "International Exawatt Center for Extreme Light Studies (XCELS): Laser System and Experiment Program". *Bulletin of the Lebedev Physics Institute* 50.6 (Oct. 2023), S635–S640. ISSN: 1934-838X. DOI: 10.3103/S1068335623180136.

[30] J. Bromage, S.-W. Bahk, M. Barczys, A. Bolognesi, C. Dorrer, N. Ekanayake, C. Feng, E. Hill, C. Jeon, M. Krieger, B. Kruschwitz, J. Kwiatkowski, E. Power, B. Webb, and J. D. Zuegel. "Laser system design and critical technologies for the NSF OPAL project". In: *High-power, High-energy Lasers, and Ultrafast Optical Technologies II*. Vol. 13532. SPIE, June 2025, pp. 20–22. DOI: 10.1117/12.3055413.

[31] C. Hernandez-Gomez, J. Collier, C. Armstrong, V. Aleksandrov, N. Booth, T. Butcher, D. Carrol, R. Clarke, H. Crespo, T. F. Pinto, M. De-vido, K. Glize, J. Green, R. Heathcote, P. Oliveira, M. Oliver, P. Mason, R. Pattathil, G. Quinn, C. Spindloe, N. Stuart, D. Symes, and T. Winstone. "Status of the new high intensity laser facilities under construction in the UK: Extreme Photonics Application Centre and Vulcan 20-20". In: *High-power, High-energy Lasers, and Ultrafast Optical Technologies II*. Vol. PC13532. SPIE, June 2025, PC135320F. DOI: 10.1117/12.3061905.

[32] Committee on the Assessment of High Energy Density Science, Board on Physics and Astronomy, Division on Engineering and Physical Sciences, and National Academies of Sciences, Engineering, and Medicine. *Fundamental Research in High Energy Density Science*. Pages: 26728. Washington, D.C.: National Academies Press, June 2023. ISBN: 978-0-309-69414-8. DOI: 10.17226/26728.

[33] D. G. Hicks, T. R. Boehly, J. H. Eggert, J. E. Miller, P. M. Celliers, and G. W. Collins. "Dissociation of Liquid Silica at High Pressures and Temperatures". *Physical Review Letters* 97.2 (July 2006), p. 025502. DOI: 10.1103/PhysRevLett.97.025502.

[34] R. S. McWilliams, D. K. Spaulding, J. H. Eggert, P. M. Celliers, D. G. Hicks, R. F. Smith, G. W. Collins, and R. Jeanloz. "Phase Transformations and Metallization of Magnesium Oxide at High Pressure and Temperature". *Science* 338.6112 (Dec. 2012), pp. 1330–1333. DOI: 10.1126/science.1229450.

[35] M. Millot, N. Dubrovinskaia, A. Černok, S. Blaha, L. Dubrovinsky, D. G. Braun, P. M. Celliers, G. W. Collins, J. H. Eggert, and R. Jeanloz. "Shock compression of stishovite and melting of silica at planetary interior conditions". *Science* 347.6220 (Jan. 2015), pp. 418–420. DOI: 10.1126/science.1261507.

[36] M. Millot, S. Hamel, J. R. Rygg, P. M. Celliers, G. W. Collins, F. Coppari, D. E. Fratanduono, R. Jeanloz, D. C. Swift, and J. H. Eggert. "Experimental evidence for superionic water ice using shock compression". *Nature Physics* 14.3 (Mar. 2018), pp. 297–302. ISSN: 1745-2481. DOI: 10.1038/s41567-017-0017-4.

[37] S. Brygoo, P. Loubeyre, M. Millot, J. R. Rygg, P. M. Celliers, J. H. Eggert, R. Jeanloz, and G. W. Collins. "Evidence of hydrogen-helium immiscibility at Jupiter-interior conditions". *Nature* 593.7860 (May 2021), pp. 517–521. ISSN: 1476-4687. DOI: 10.1038/s41586-021-03516-0.

[38] S. P. Hatchett, C. G. Brown, T. E. Cowan, E. A. Henry, J. S. Johnson, M. H. Key, J. A. Koch, A. B. Langdon, B. F. Lasinski, R. W. Lee, A. J. Mackinnon, D. M. Pennington, M. D. Perry, T. W. Phillips, M. Roth, T. C. Sangster, M. S. Singh, R. A. Snavely, M. A. Stoyer, S. C. Wilks, and K. Yasuike. "Electron, photon, and ion beams from the relativistic interaction of Petawatt laser pulses with solid targets". *Physics of Plasmas* 7 (May 2000). ADS Bibcode: 2000PhPl....7.2076H, pp. 2076–2082. ISSN: 1070-664X. DOI: 10.1063/1.874030.

[39] R. A. Snavely, M. H. Key, S. P. Hatchett, T. E. Cowan, M. Roth, T. W. Phillips, M. A. Stoyer, E. A. Henry, T. C. Sangster, M. S. Singh, S. C. Wilks, A. MacKinnon, A. Offenberger, D. M. Pennington, K. Yasuike, A. B. Langdon, B. F. Lasinski, J. Johnson, M. D. Perry, and E. M. Campbell. "Intense High-Energy Proton Beams from Petawatt-Laser Irradiation of Solids". *Physical Review Letters* 85.14 (Oct. 2000), pp. 2945–2948. DOI: 10.1103/PhysRevLett.85.2945.

[40] S. C. Wilks, A. B. Langdon, T. E. Cowan, M. Roth, M. Singh, S. Hatchett, M. H. Key, D. Pennington, A. MacKinnon, and R. A. Snavely. "Energetic proton generation in ultra-intense laser–solid interactions". *Physics of Plasmas* 8.2 (Feb. 2001), pp. 542–549. ISSN: 1070-664X. DOI: 10.1063/1.1333697.

[41] A. Macchi, M. Borghesi, and M. Passoni. "Ion acceleration by superintense laser-plasma interaction". *Reviews of Modern Physics* 85.2 (May 2013), pp. 751–793. DOI: 10.1103/RevModPhys.85.751.

[42] R. Jeanloz, P. M. Celliers, G. W. Collins, J. H. Eggert, K. K. M. Lee, R. S. McWilliams, S. Brygoo, and P. Loubeyre. "Achieving high-density states through shock-wave loading of precompressed samples". *Proceedings of the National Academy of Sciences* 104.22 (May 2007), pp. 9172–9177. DOI: 10.1073/pnas.0608170104.

[43] T. Tajima and J. M. Dawson. "Laser Electron Accelerator". *Physical Review Letters* 43.4 (July 1979), pp. 267–270. DOI: 10.1103/PhysRevLett.43.267.

[44] C. Aniculaesei, T. Ha, S. Yoffe, L. Labun, S. Milton, E. McCary, M. M. Spinks, H. J. Quevedo, O. Z. Labun, R. Sain, A. Hannasch, R. Zgadzaj, I. Pagano, J. A. Franco-Altamirano, M. L. Ringuette, E. Gaul, S. V. Luedtke, G. Tiwari, B. Ersfeld, E. Brunetti, H. Ruhl, T. Ditmire, S. Bruce, M. E. Donovan, M. C. Downer, D. A. Jaroszynski, and B. M. Hegelich. "The acceleration of a high-charge electron bunch to 10 GeV in a 10-cm nanoparticle-assisted wakefield accelerator". *Matter and Radiation at Extremes* 9.1 (Nov. 2023), p. 014001. ISSN: 2468-2047. DOI: 10.1063/5.0161687.

[45] E. Rockafellow, J. E. Shrock, B. Miao, A. J. Sloss, M. S. Le, S. W. Hancock, S. Zahedpour, R. C. Hollinger, S. Wang, J. King, P. Zhang, J. Šišma, G. M. Grittani, R. Versaci, D. F. Gordon, G. J. Williams, B. A. Reagan, J. J. Rocca, and H. M. Milchberg. "High charge laser acceleration of electrons to 10 GeV". *Nuclear Instruments and Methods in Physics Research Section A: Accelerators, Spectrometers, Detectors and Associated Equipment* 1077 (Aug. 2025), p. 170586. ISSN: 0168-9002. DOI: 10.1016/j.nima.2025.170586.

[46] F. Albert. "Principles and applications of x-ray light sources driven by laser wakefield acceleration". *Physics of Plasmas* 30.5 (May 2023), p. 050902. ISSN: 1070-664X. DOI: 10.1063/5.0142033.

[47] N. Blanchot, C. Rouyer, I. Allais, D. Husson, É. Mazataud, M. Nail, A. Pierre, C. Sauteret, and A. Migus. "Production and characterization of multi 1019 W/cm2 intensities using 300 fs, 30 TW pulses generated in a gain shaped Ti:Sapphire / Nd-doped mixed glasses set-up". In: *High Field Interactions and Short Wavelength Generation*. St. Malo: Optica Publishing Group, 1994, MA3. DOI: 10.1364/HRFTS.1994.MA3.

[48] C. Rouyer, N. Blanchot, I. Allais, E. Mazataud, J. L. Miquel, M. Nail, A. Pierre, C. Sauteret, and A. Migus. "Production and characterization of intensities above 2×10^{19} W/cm^2, obtained with 30-TW 300-fs pulses generated in a Ti:sapphire/Nd-doped mixed-glass chain". EN. *JOSA B* 13.1 (Jan. 1996), pp. 55–58. ISSN: 1520-8540. DOI: 10.1364/JOSAB.13.000055.

[49] A. Modena, Z. Najmudin, A. E. Dangor, C. E. Clayton, K. A. Marsh, C. Joshi, V. Malka, C. B. Darrow, C. Danson, D. Neely, and F. N. Walsh. "Electron acceleration from the breaking of relativistic plasma waves". *Nature* 377.6550 (Oct. 1995), pp. 606–608. ISSN: 1476-4687. DOI: 10.1038/377606a0.

[50] P. A. Norreys, M. Zepf, S. Moustaizis, A. P. Fews, J. Zhang, P. Lee, M. Bakarezos, C. N. Danson, A. Dyson, P. Gibbon, P. Loukakos, D. Neely, F. N. Walsh, J. S. Wark, and A. E. Dangor. "Efficient Extreme UV Harmonics Generated from Picosecond Laser Pulse Interactions with Solid Targets". *Physical Review Letters* 76.11 (Mar. 1996), pp. 1832–1835. ISSN: 0031-9007, 1079-7114. DOI: 10.1103/PhysRevLett.76.1832.

[51] D. L. Burke, R. C. Field, G. Horton-Smith, J. E. Spencer, D. Walz, S. C. Berridge, W. M. Bugg, K. Shmakov, A. W. Weidemann, C. Bula, K. T. McDonald, E. J. Prebys, C. Bamber, S. J. Boege, T. Koffas, T. Kotseroglou, A. C. Melissinos, D. D. Meyerhofer, D. A. Reis, and W. Ragg. "Positron Production in Multiphoton Light-by-Light Scattering". *Physical Review Letters* 79.9 (Sept. 1997), pp. 1626–1629. ISSN: 0031-9007, 1079-7114. DOI: 10.1103/PhysRevLett.79.1626.

[52] S. P. Le Blanc, M. C. Downer, R. Wagner, S.-Y. Chen, A. Maksimchuk, G. Mourou, and D. Umstadter. "Temporal Characterization of a Self-Modulated Laser Wakefield". *Physical Review Letters* 77.27 (Dec. 1996), pp. 5381–5384. ISSN: 0031-9007, 1079-7114. DOI: 10.1103/PhysRevLett.77.5381.

[53] Committee on Opportunities in the Science, Applications, and Technology of Intense Ultrafast Lasers, Board on Physics and Astronomy, Division on Engineering and Physical Sciences, and National Academies of Sciences, Engineering, and Medicine. *Opportunities in Intense Ultrafast Lasers: Reaching for the Brightest Light*. Pages: 24939. Washington, D.C.: National Academies Press, Jan. 2018. ISBN: 978-0-309-46769-8. DOI: 10.17226/24939.

[54] M. D. Perry, D. Pennington, B. C. Stuart, G. Tietbohl, J. A. Britten, C. Brown, S. Herman, B. Golick, M. Kartz, J. Miller, H. T. Powell, M. Vergino, and V. Yanovsky. "Petawatt laser pulses". *Optics Letters* 24.3 (Feb. 1999), p. 160. ISSN: 0146-9592, 1539-4794. DOI: 10.1364/OL.24.000160.

[55] S.-W. Bahk, P. Rousseau, T. A. Planchon, V. Chvykov, G. Kalintchenko, A. Maksimchuk, G. A. Mourou, and V. Yanovsky. "Generation and characterization of the highest laser intensities (10^22 W/cm^2)". *Optics Letters* 29.24 (Dec. 2004), p. 2837. ISSN: 0146-9592, 1539-4794. DOI: 10.1364/OL.29.002837.

[56] V. Yanovsky, V. Chvykov, G. Kalinchenko, P. Rousseau, T. Planchon, T. Matsuoka, A. Maksimchuk, J. Nees, G. Cheriaux, G. Mourou, and K. Krushelnick. "Ultra-high intensity- 300-TW laser at 0.1 Hz repetition rate". *Optics Express* 16.3 (2008), p. 2109. ISSN: 1094-4087. DOI: 10.1364/OE.16.002109.

[57] J. W. Yoon, C. Jeon, J. Shin, S. K. Lee, H. W. Lee, I. W. Choi, H. T. Kim, J. H. Sung, and C. H. Nam. "Achieving the laser intensity of 5.5×10^{22} W/cm^2 with a wavefront-corrected multi-PW laser". EN. *Optics Express* 27.15 (July 2019), pp. 20412–20420. ISSN: 1094-4087. DOI: 10.1364/OE.27.020412.

[58] S. Augst, D. D. Meyerhofer, D. Strickland, and S. L. Chin. "Laser ionization of noble gases by Coulomb-barrier suppression". EN. *JOSA B* 8.4 (Apr. 1991), pp. 858–867. ISSN: 1520-8540. DOI: 10.1364/JOSAB.8.000858.

[59] P. A. M. Dirac. "The quantum theory of the electron". *Proceedings of the Royal Society of London. Series A, Containing Papers of a Mathematical and Physical Character* 117.778 (Feb. 1928), pp. 610–624. ISSN: 0950-1207. DOI: 10.1098/rspa.1928.0023.

[60] P. A. M. Dirac. "A theory of electrons and protons". *Proceedings of the Royal Society of London. Series A, Containing Papers of a Mathematical and Physical Character* 126.801 (Jan. 1930), pp. 360–365. ISSN: 0950-1207. DOI: 10.1098/rspa.1930.0013.

[61] C. D. Anderson. "The Apparent Existence of Easily Deflectable Positives". *Science* 76.1967 (1932), pp. 238–239. ISSN: 0036-8075. URL: https://www.jstor.org/stable/1658257.

[62] Z. Medin and D. Lai. "Pair cascades in the magnetospheres of strongly magnetized neutron stars". *Monthly Notices of the Royal Astronomical Society* 406.2 (Aug. 2010), pp. 1379–1404. ISSN: 0035-8711. DOI: 10.1111/j.1365-2966.2010.16776.x.

[63] A. K. Harding, Z. Wadiasingh, and M. G. Baring. "Pair Cascades in Magnetar Magnetospheres". *The Astrophysical Journal* 991.2 (Sept. 2025), p. 178. ISSN: 0004-637X. DOI: 10.3847/1538-4357/adfa06.

[64] A. K. Harding, A. G. Muslimov, and B. Zhang. "Regimes of Pulsar Pair Formation and Particle Energetics". *The Astrophysical Journal* 576.1 (Sept. 2002), p. 366. ISSN: 0004-637X. DOI: 10.1086/341633.

[65] R. Peierls. "The vacuum in Dirac's theory of the positive electron". *Proceedings of the Royal Society of London. Series A, Containing Papers of a Mathematical and Physical Character* 146.857 (Sept. 1934), pp. 420–441. ISSN: 0950-1207. DOI: 10.1098/rspa.1934.0164.

[66] G. Breit and J. A. Wheeler. "Collision of Two Light Quanta". *Physical Review* 46.12 (Dec. 1934), pp. 1087–1091. DOI: 10.1103/PhysRev.46.1087.

[67] H. Bethe and W. Heitler. "On the stopping of fast particles and on the creation of positive electrons". *Proceedings of the Royal Society of London. Series A, Containing Papers of a Mathematical and Physical Character* 146.856 (Aug. 1934), pp. 83–112. ISSN: 0950-1207. DOI: 10.1098/rspa.1934.0140.

[68] H. J. Bhabha. "The creation of electron pairs by fast charged particles". *Proceedings of the Royal Society of London. A. Mathematical and Physical Sciences* 152.877 (Nov. 1935), pp. 559–586. ISSN: 0080-4630. DOI: 10.1098/rspa.1935.0208.

[69] G. Racah. "Sulla nascita di coppie per urti di particelle elettrizzate". it. *Il Nuovo Cimento (1924-1942)* 13.2 (Feb. 1936), pp. 66–73. ISSN: 1827-6121. DOI: 10.1007/BF02961178.

[70] R. N. Lee, A. A. Lyubyakin, and V. A. Smirnov. "Total Born cross section of e+e–pair production by an electron in the Coulomb field of a nucleus". *Physics Letters B* 848 (Jan. 2024), p. 138408. ISSN: 0370-2693. DOI: 10.1016/j.physletb.2023.138408.

[71] M. Camac. "Pair Production by Electrons". *Physical Review* 88.4 (Nov. 1952), pp. 745–750. ISSN: 0031-899X. DOI: 10.1103/PhysRev.88.745.

[72] G. Alexander, J. Barley, Y. Batygin, S. Berridge, V. Bharadwaj, G. Bower, W. Bugg, F. .-. Decker, R. Dollan, Y. Efremenko, K. Flöttmann, V. Gharibyan, C. Hast, R. Iverson, H. Kolanoski, J. W. Kovermann, K. Laihem, T. Lohse, K. T. McDonald, A. A. Mikhailichenko, G. A. Moortgat-Pick, P. Pahl, R. Pitthan, R. Pöschl, E. Reinherz-Aronis, S. Riemann, A. Schälicke, K. P. Schüler, T. Schweizer, D. Scott, J. C. Sheppard, A. Stahl, Z. Szalata, D. R. Walz, and A. Weidemann. "Undulator-based production of polarized positrons". *Nuclear Instruments and Methods in Physics Research Section A: Accelera-*

tors, Spectrometers, Detectors and Associated Equipment 610.2 (Nov. 2009), pp. 451–487. ISSN: 0168-9002. DOI: 10.1016/j.nima.2009.07.091.

[73] A. Di Piazza, C. Müller, K. Z. Hatsagortsyan, and C. H. Keitel. "Extremely high-intensity laser interactions with fundamental quantum systems". *Reviews of Modern Physics* 84.3 (Aug. 2012), pp. 1177–1228. DOI: 10.1103/RevModPhys.84.1177.

[74] A. Gonoskov, T. Blackburn, M. Marklund, and S. Bulanov. "Charged particle motion and radiation in strong electromagnetic fields". *Reviews of Modern Physics* 94.4 (Oct. 2022), p. 045001. DOI: 10.1103/RevModPhys.94.045001.

[75] V. I. Ritus. "Quantum effects of the interaction of elementary particles with an intense electromagnetic field". *Journal of Soviet Laser Research* 6.5 (Sept. 1985), pp. 497–617. ISSN: 1573-8760. DOI: 10.1007/BF01120220.

[76] F. Sauter. "Über das Verhalten eines Elektrons im homogenen elektrischen Feld nach der relativistischen Theorie Diracs". de. *Zeitschrift für Physik* 69.11 (Nov. 1931), pp. 742–764. ISSN: 0044-3328. DOI: 10.1007/BF01339461.

[77] W. Heisenberg and H. Euler. "Folgerungen aus der Diracschen Theorie des Positrons". de. *Zeitschrift für Physik* 98.11 (Nov. 1936), pp. 714–732. ISSN: 0044-3328. DOI: 10.1007/BF01343663.

[78] J. Schwinger. "On Gauge Invariance and Vacuum Polarization". *Physical Review* 82.5 (June 1951), pp. 664–679. DOI: 10.1103/PhysRev.82.664.

[79] H. R. Reiss. "Absorption of Light by Light". *Journal of Mathematical Physics* 3.1 (Jan. 1962), pp. 59–67. ISSN: 0022-2488. DOI: 10.1063/1.1703787.

[80] A. I. Nikishov and V. I. Ritus. "QUANTUM PROCESSES IN THE FIELD OF A PLANE ELECTROMAGNETIC WAVE AND IN A CONSTANT FIELD. PART I". Russian. *Zh. Eksperim. i Teor. Fiz.* 46.2 (1964). Institution: Lebedev Inst. of Physics, Moscow, p. 776. URL: https://www.osti.gov/biblio/4032026.

[81] A. I. Nikishov and V. I. Ritus. "Pair Production by a Photon and Photon Emission by an Electron in the Field of an Intense Electromagnetic Wave and in a Constant Field". *Soviet Journal of Experimental and Theoretical Physics* 25 (Dec. 1967). ADS Bibcode: 1967JETP...25.1135N, p. 1135. ISSN: 1063-7761. URL: https://ui.adsabs.harvard.edu/abs/1967JETP...25.1135N.

[82] H. R. Reiss. "Production of Electron Pairs from a Zero-Mass State". *Physical Review Letters* 26.17 (Apr. 1971), pp. 1072–1075. DOI: 10.1103/PhysRevLett.26.1072.

[83] V. N. Baier, A. I. Mil'shtein, and V. M. Strakhovenko. "Interaction between a photon and an intense electromagnetic wave". *Sov. Phys. JETP* 42 (1975), pp. 961–965.

[84] A. Golub, S. Villalba-Chávez, and C. Müller. "Nonlinear Breit-Wheeler pair production in collisions of bremsstrahlung $\ensuremath{\gamma}$ quanta and a tightly focused laser pulse". *Physical Review D* 105.11 (June 2022), p. 116016. DOI: 10.1103/PhysRevD.105.116016.

[85] H. Hu, C. Müller, and C. H. Keitel. "Complete QED Theory of Multiphoton Trident Pair Production in Strong Laser Fields". *Physical Review Letters* 105.8 (Aug. 2010), p. 080401. DOI: 10.1103/PhysRevLett.105.080401.

[86] A. Ilderton. “Trident Pair Production in Strong Laser Pulses”. *Physical Review Letters* 106.2 (Jan. 2011), p. 020404. DOI: 10.1103/PhysRevLett.106.020404.

[87] F. Mackenroth and A. Di Piazza. “Nonlinear trident pair production in an arbitrary plane wave: A focus on the properties of the transition amplitude”. *Physical Review D* 98.11 (Dec. 2018), p. 116002. DOI: 10.1103/PhysRevD.98.116002.

[88] L. S. Brown and T. W. B. Kibble. “Interaction of Intense Laser Beams with Electrons”. *Physical Review* 133.3A (Feb. 1964), A705–A719. DOI: 10.1103/PhysRev.133.A705.

[89] I. I. Goldman. “Intensity effects in compton scattering”. *Physics Letters* 8.2 (Jan. 1964), pp. 103–106. ISSN: 0031-9163. DOI: 10.1016/0031-9163(64)90728-0.

[90] C. Bamber, S. J. Boege, T. Koffas, T. Kotseroglou, A. C. Melissinos, D. D. Meyerhofer, D. A. Reis, W. Ragg, C. Bula, K. T. McDonald, E. J. Prebys, D. L. Burke, R. C. Field, G. Horton-Smith, J. E. Spencer, D. Walz, S. C. Berridge, W. M. Bugg, K. Shmakov, and A. W. Weidemann. “Studies of nonlinear QED in collisions of 46.6 GeV electrons with intense laser pulses”. *Physical Review D* 60.9 (Oct. 1999), p. 092004. ISSN: 0556-2821, 1089-4918. DOI: 10.1103/PhysRevD.60.092004.

[91] A. R. Bell and J. G. Kirk. “Possibility of Prolific Pair Production with High-Power Lasers”. *Physical Review Letters* 101.20 (Nov. 2008), p. 200403. DOI: 10.1103/PhysRevLett.101.200403.

[92] X.-L. Zhu, T.-P. Yu, Z.-M. Sheng, Y. Yin, I. C. E. Turcu, and A. Pukhov. “Dense GeV electron–positron pairs generated by lasers in near-critical-density plasmas”. *Nature Communications* 7.1 (Dec. 2016). Number: 1, p. 13686. ISSN: 2041-1723. DOI: 10.1038/ncomms13686.

[93] T. Grismayer, M. Vranic, J. L. Martins, R. A. Fonseca, and L. O. Silva. “Seeded QED cascades in counterpropagating laser pulses”. *Physical Review E* 95.2 (Feb. 2017), p. 023210. DOI: 10.1103/PhysRevE.95.023210.

[94] M. Tamburini, A. Di Piazza, and C. H. Keitel. “Laser-pulse-shape control of seeded QED cascades”. *Scientific Reports* 7.1 (July 2017), p. 5694. ISSN: 2045-2322. DOI: 10.1038/s41598-017-05891-z.

[95] M. Jirka, O. Klimo, M. Vranic, S. Weber, and G. Korn. “QED cascade with 10 PW-class lasers”. eng. *Scientific Reports* 7.1 (Nov. 2017), p. 15302. ISSN: 2045-2322. DOI: 10.1038/s41598-017-15747-1.

[96] A. Sampath and M. Tamburini. “Towards realistic simulations of QED cascades: Non-ideal laser and electron seeding effects”. *Physics of Plasmas* 25.8 (Aug. 2018), p. 083104. ISSN: 1070-664X. DOI: 10.1063/1.5022640.

[97] C. Slade-Lowther, D. Del Sorbo, and C. P. Ridgers. “Identifying the electron–positron cascade regimes in high-intensity laser-matter interactions”. *New Journal of Physics* 21.1 (Jan. 2019), p. 013028. ISSN: 1367-2630. DOI: 10.1088/1367-2630/aafa39.

[98] A. A. Mironov, S. S. Bulanov, A. Di Piazza, M. Grech, L. Lancia, S. Meuren, J. Palastro, C. Riconda, H. G. Rinderknecht, P. Tzeferacos, and G. Gregori. "Testing strong-field QED with the avalanche precursor". *Physics of Plasmas* 32.9 (Sept. 2025), p. 093302. ISSN: 1070-664X. DOI: 10.1063/5.0283438.

[99] F. Karbstein, C. Sundqvist, K. S. Schulze, I. Uschmann, H. Gies, and G. G. Paulus. "Vacuum birefringence at x-ray free-electron lasers". *New Journal of Physics* 23.9 (Sept. 2021), p. 095001. ISSN: 1367-2630. DOI: 10.1088/1367-2630/ac1df4.

[100] N. Ahmadiniaz, C. Bähtz, A. Benediktovitch, C. Bömer, L. Bocklage, T. E. Cowan, J. Edwards, S. Evans, S. F. Viñas, H. Gies, S. Göde, J. Görs, J. Grenzer, U. H. Acosta, T. Heinzl, P. Hilz, W. Hippler, L. G. Huang, O. Humphries, F. Karbstein, P. Khademi, B. King, T. Kluge, C. Kohlfürst, D. Krebs, A. Laso-García, R. Lötzsch, A. J. Macleod, B. Marx-Glowna, E. A. Mosman, M. Nakatsutsumi, G. G. Paulus, S. V. Rahul, L. Randolph, R. Röhlsberger, N. Rohringer, A. Sävert, S. Sadashivaiah, R. Sauerbrey, H.-P. Schlenviogt, S. M. Schmidt, U. Schramm, R. Schützhold, J.-P. Schwinkendorf, D. Seipt, M. Šmíd, T. Stöhlker, T. Toncian, M. Valialshchikov, A. Wipf, U. Zastrau, and M. Zepf. "Towards a vacuum birefringence experiment at the Helmholtz International Beamline for Extreme Fields (Letter of Intent of the BIREF@HIBEF Collaboration)". *High Power Laser Science and Engineering* 13 (Jan. 2025), e7. ISSN: 2095-4719, 2052-3289. DOI: 10.1017/hpl.2024.70.

[101] M. Šmíd, P. Khademi, N. Ahmadiniaz, M. Andrzejewski, C. Baehtz, E. Brambrink, J. Bulička, T. Burian, S. D. D. Cafiso, J. Chalupský, T. E. Cowan, S. Göde, J. Grenzer, V. Hájková, P. Hilz, W. Hippler, H. Höppner, A. Horynová, L. Huang, O. Humphries, Š. Jelínek, L. Juha, F. Karbstein, C. Kohlfürst, A. L. Garcia, R. Lötzsch, M. Masruri, A. Matheron, M. Nakatsutsumi, G. G. Paulus, A. Pelka, T. R. Preston, S. V. Rahul, L. Randolph, A. Sävert, H.-P. Schlenvoigt, R. Schützhold, J. P. Schwinkendorf, T. Stöhlker, M. Toncian, T. Toncian, M. Valialshchikov, V. Vozda, E. Weckert, C. Wessel, J. Wild, U. Zastrau, and M. Zepf. "Proof-of-principle experiment for the dark-field detection concept for measuring vacuum birefringence". *Physical Review A* 112.6 (Dec. 2025), p. 063512. DOI: 10.1103/xpxy-ntwz.

[102] R. Karplus and M. Neuman. "The Scattering of Light by Light". *Physical Review* 83.4 (Aug. 1951), pp. 776–784. ISSN: 0031-899X. DOI: 10.1103/PhysRev.83.776.

[103] V. Costantini, B. De Tollis, and G. Pistoni. "Nonlinear effects in quantum electrodynamics". *Il Nuovo Cimento A (1965-1970)* 2.3 (Apr. 1971), pp. 733–787. ISSN: 1826-9869. DOI: 10.1007/BF02736745.

[104] E. Lundström, G. Brodin, J. Lundin, M. Marklund, R. Bingham, J. Collier, J. T. Mendonça, and P. Norreys. "Using High-Power Lasers for Detection of Elastic Photon-Photon Scattering". *Physical Review Letters* 96.8 (Mar. 2006), p. 083602. DOI: 10.1103/PhysRevLett.96.083602.

[105] D. Tommasini, A. Ferrando, H. Michinel, and M. Seco. "Precision tests of QED and non-standard models by searching photon-photon scattering in vacuum with high power lasers". *Journal of High Energy Physics* 2009.11 (Nov. 2009), p. 043. ISSN: 1126-6708. DOI: 10.1088/1126-6708/2009/11/043.

[106] D. Tommasini and H. Michinel. "Light by light diffraction in vacuum". *Physical Review A* 82.1 (July 2010), p. 011803. DOI: 10.1103/PhysRevA.82.011803.

[107] B. King and C. H. Keitel. "Photon–photon scattering in collisions of intense laser pulses". *New Journal of Physics* 14.10 (Oct. 2012), p. 103002. ISSN: 1367-2630. DOI: 10.1088/1367-2630/14/10/103002.

[108] H. Gies, F. Karbstein, and C. Kohlfürst. "All-optical signatures of strong-field QED in the vacuum emission picture". *Physical Review D* 97.3 (Feb. 2018), p. 036022. DOI: 10.1103/PhysRevD.97.036022.

[109] H. Gies, F. Karbstein, C. Kohlfürst, and N. Seegert. "Photon-photon scattering at the high-intensity frontier". *Physical Review D* 97.7 (Apr. 2018), p. 076002. DOI: 10.1103/PhysRevD.97.076002.

[110] H. Gies, F. Karbstein, and L. Klar. "All-optical quantum vacuum signals in two-beam collisions". *Physical Review D* 106.11 (Dec. 2022), p. 116005. DOI: 10.1103/PhysRevD.106.116005.

[111] A. V. Berezin and A. M. Fedotov. "Analytical formula for signal optimization in stimulated photon-photon scattering setup with three laser pulses". *Physical Review D* 110.1 (July 2024), p. 016009. DOI: 10.1103/PhysRevD.110.016009.

[112] L. Roso, R. Lera, S. Ravichandran, A. Longman, C. Z. He, J. A. Pérez-Hernández, J. I. Apiñaniz, L. D. Smith, R. Fedosejevs, and W. T. Hill. "Towards a direct measurement of the quantum-vacuum Lagrangian coupling coefficients using two counterpropagating super-intense laser pulses". *New Journal of Physics* 24.2 (Mar. 2022), p. 025010. ISSN: 1367-2630. DOI: 10.1088/1367-2630/ac51a7.

[113] H. G. Rinderknecht, E. Dill, A. J. MacLeod, B. King, K. Sow, S.-W. Bahk, I. A. Begishev, F. Karbstein, J. Schreiber, M. Zepf, and A. Di Piazza. "On measuring stimulated photon–photon scattering using multiple ultraintense lasers". *Physics of Plasmas* 32.8 (Aug. 2025), p. 083301. ISSN: 1070-664X. DOI: 10.1063/5.0272791.

[114] J. Bromage, S.-W. Bahk, D. Irwin, J. Kwiatkowski, A. Pruyne, M. Millecchia, M. Moore, and J. D. Zuegel. "A focal-spot diagnostic for on-shot characterization of high-energy petawatt lasers". EN. *Optics Express* 16.21 (Oct. 2008), pp. 16561–16572. ISSN: 1094-4087. DOI: 10.1364/OE.16.016561.

[115] C. Z. He, A. Longman, J. A. Pérez-Hernández, M. de Marco, C. Salgado, G. Zeraouli, G. Gatti, L. Roso, R. Fedosejevs, and W. T. Hill. "Towards an in situ, full-power gauge of the focal-volume intensity of petawatt-class lasers". *Optics Express* 27.21 (Oct. 2019), p. 30020. ISSN: 1094-4087. DOI: 10.1364/OE.27.030020.

[116] S. C. Park, H. Yun, J. W. Yoon, S. K. Lee, J. H. Sung, I. W. Choi, C. H. Nam, and K. T. Kim. "Random pinhole attenuator for high-power laser beams". *High Power Laser Science and Engineering* 12 (2024), e34. ISSN: 2095-4719, 2052-3289. DOI: 10.1017/hpl.2024.15.

[117] S. Howard, J. Esslinger, N. Weiße, J. Schröder, C. Eberle, R. H. W. Wang, S. Karsch, P. Norreys, and A. Döpp. "Single-shot spatiotemporal vector field measurements of petawatt laser pulses". *Nature Photonics* 19.8 (Aug. 2025), pp. 898–905. ISSN: 1749-4893. DOI: 10.1038/s41566-025-01698-x.

[118] C. Benvenuti and P. Chiggiato. "Obtention of pressures in the 10^{-14} torr range by means of a Zr-V-Fe non evaporable getter". *Vacuum*. Special Issue Selected Proceedings of the 12th International Vacuum Congress (IVC-12) 8th International Conference on Solid Surfaces (ICSS-8) 44.5 (May 1993), pp. 511–513. ISSN: 0042-207X. DOI: 10.1016/0042-207X(93)90084-N.

[119] C. N. Harvey. "*In situ* characterization of ultraintense laser pulses". *Physical Review Accelerators and Beams* 21.11 (Nov. 2018), p. 114001. ISSN: 2469-9888. DOI: 10.1103/PhysRevAccelBeams.21.114001.

[120] J. Gao. "Laser intensity measurement by Thomson scattering". *Applied Physics Letters* 88.9 (Feb. 2006), p. 091105. ISSN: 0003-6951. DOI: 10.1063/1.2180869.

[121] O. Har-Shemesh and A. Di Piazza. "Peak intensity measurement of relativistic lasers via nonlinear Thomson scattering". *Optics Letters* 37.8 (Apr. 2012), p. 1352. ISSN: 0146-9592, 1539-4794. DOI: 10.1364/OL.37.001352.

[122] A. Link, E. A. Chowdhury, J. T. Morrison, V. M. Ovchinnikov, D. Offermann, L. Van Woerkom, R. R. Freeman, J. Pasley, E. Shipton, F. Beg, P. Rambo, J. Schwarz, M. Geissel, A. Edens, and J. L. Porter. "Development of an in situ peak intensity measurement method for ultraintense single shot laser-plasma experiments at the Sandia Z petawatt facility". *Review of Scientific Instruments* 77.10 (Oct. 2006), 10E723. ISSN: 0034-6748. DOI: 10.1063/1.2336469.

[123] M. F. Ciappina, S. V. Popruzhenko, S. V. Bulanov, T. Ditmire, G. Korn, and S. Weber. "Progress toward atomic diagnostics of ultrahigh laser intensities". *Physical Review A* 99.4 (Apr. 2019), p. 043405. ISSN: 2469-9926, 2469-9934. DOI: 10.1103/PhysRevA.99.043405.

[124] A. L. Galkin, M. P. Kalashnikov, V. K. Klinkov, V. V. Korobkin, M. Y. Romanovsky, and O. B. Shiryaev. "Electrodynamics of electron in a superintense laser field: New principles of diagnostics of relativistic laser intensity". *Physics of Plasmas* 17.5 (May 2010), p. 053105. ISSN: 1070-664X, 1089-7674. DOI: 10.1063/1.3425864.

[125] M. Kalashnikov, A. Andreev, K. Ivanov, A. Galkin, V. Korobkin, M. Romanovsky, O. Shiryaev, M. Schnuerer, J. Braenzel, and V. Trofimov. "Diagnostics of peak laser intensity based on the measurement of energy of electrons emitted from laser focal region". *Laser and Particle Beams* 33.3 (Sept. 2015), pp. 361–366. ISSN: 0263-0346, 1469-803X. DOI: 10.1017/S0263034615000403.

[126] K. A. Ivanov, I. N. Tsymbalov, O. E. Vais, S. G. Bochkarev, R. V. Volkov, V. Y. Bychenkov, and A. B. Savel'ev. "Accelerated electrons for in situ peak intensity monitoring of tightly focused femtosecond laser radiation at high intensities". *Plasma Physics and Controlled Fusion* 60.10 (Sept. 2018), p. 105011. ISSN: 0741-3335. DOI: 10.1088/1361-6587/aada60.

[127] F. Mackenroth, A. R. Holkundkar, and H.-P. Schlenvoigt. "Ultra-intense laser pulse characterization using ponderomotive electron scattering". *New Journal of Physics* 21.12 (Dec. 2019), p. 123028. ISSN: 1367-2630. DOI: 10.1088/1367-2630/ab5c4d.

[128] A. Kramida, Y. Ralchenko, J. Reader, K. Olsen, and R. Ibacache. *Atomic Spectra Database*. Last Modified: 2025-02-24T15:28-05:00. July 2009. URL: https://www.nist.gov/pml/atomic-spectra-database.

[129] E. S. Sarachik and G. T. Schappert. "Classical Theory of the Scattering of Intense Laser Radiation by Free Electrons". *Physical Review D* 1.10 (May 1970), pp. 2738–2753. DOI: 10.1103/PhysRevD.1.2738.

[130] C. I. Moore, J. P. Knauer, and D. D. Meyerhofer. "Observation of the Transition from Thomson to Compton Scattering in Multiphoton Interactions with Low-Energy Electrons". *Physical Review Letters* 74.13 (Mar. 1995), pp. 2439–2442. ISSN: 0031-9007, 1079-7114. DOI: 10.1103/PhysRevLett.74.2439.

[131] B. Quesnel and P. Mora. "Theory and simulation of the interaction of ultraintense laser pulses with electrons in vacuum". *Physical Review E* 58.3 (Sept. 1998), pp. 3719–3732. ISSN: 1063-651X, 1095-3787. DOI: 10.1103/PhysRevE.58.3719.

[132] W. L. Erikson and S. Singh. "Polarization properties of Maxwell-Gaussian laser beams". *Physical Review E* 49.6 (June 1994), pp. 5778–5786. ISSN: 1063-651X, 1095-3787. DOI: 10.1103/PhysRevE.49.5778.

[133] *ode45 - Solve nonstiff differential equations — medium order method - MATLAB*. URL: https://www.mathworks.com/help/matlab/ref/ode45.html.

[134] J. R. Dormand and P. J. Prince. "A family of embedded Runge-Kutta formulae". *Journal of Computational and Applied Mathematics* 6.1 (Mar. 1980), pp. 19–26. ISSN: 0377-0427. DOI: 10.1016/0771-050X(80)90013-3.

[135] L. F. Shampine and M. W. Reichelt. "The MATLAB ODE Suite". *SIAM Journal on Scientific Computing* 18.1 (Jan. 1997), pp. 1–22. ISSN: 1064-8275. DOI: 10.1137/S1064827594276424.

[136] A. Longman and R. Fedosejevs. "Modeling of high intensity orbital angular momentum beams for laser–plasma interactions". *Physics of Plasmas* 29.6 (June 2022), p. 063109. ISSN: 1070-664X. DOI: 10.1063/5.0093067.

[137] J. Peatross, M. Berrondo, D. Smith, and M. Ware. "Vector fields in a tight laser focus: comparison of models". EN. *Optics Express* 25.13 (June 2017), pp. 13990–14007. ISSN: 1094-4087. DOI: 10.1364/OE.25.013990.

[138] S. Ravichandran, M. Huault, R. Lera, C. Z. He, A. Longman, R. Fedosejevs, L. Roso, and W. T. Hill. "Imaging electron angular distributions to assess a full-power petawatt-class laser focus". *Physical Review A* 108.5 (Nov. 2023), p. 053101. DOI: 10.1103/PhysRevA.108.053101.

[139] A. Longman, S. Ravichandran, L. Manzo, C. Z. He, R. Lera, N. McLane, M. Huault, G. Tiscareno, D. Hanggi, P. Spingola, N. Czapla, R. L. Daskalova, L. Roso, R. Fedosejevs, and W. T. Hill III. "Toward direct spatial and intensity characterization of ultra-high-intensity laser pulses using ponderomotive scattering of free electrons". *Physics of Plasmas* 30.8 (Aug. 2023), p. 082110. ISSN: 1070-664X. DOI: 10.1063/5.0160195.

[140] *Technical features of the VEGA laser*. URL: https://www.clpu.es/en/facilties-vega-features/.

[141] C. Méndez, O. Varela, E. García, I. Hernández, J. Ajates, J. D. Pisonero, J. L. Sagredo, M. Olivar, and L. Roso. "VEGA laser facility beamlines management for pump-probe experiments". In: *Fourth International Conference on Applications of Optics and Photonics*. Vol. 11207. SPIE, Oct. 2019, pp. 431–436. DOI: 10.1117/12.2527481.

[142] *Scarlet Laser System — High Energy Density Physics Scarlet Laser Facility*. URL: https://hedp.osu.edu/facilities/scarlet.

[143] P. L. Poole, C. Willis, R. L. Daskalova, K. M. George, S. Feister, S. Jiang, J. Snyder, J. Marketon, D. W. Schumacher, K. U. Akli, L. V. Woerkom, R. R. Freeman, and E. A. Chowdhury. "Experimental capabilities of 0.4 PW, 1 shot/min Scarlet laser facility for high energy density science". EN. *Applied Optics* 55.17 (June 2016), pp. 4713–4719. ISSN: 2155-3165. DOI: 10.1364/AO.55.004713.

[144] K. Takahaahi, K. Kohda, and J. Niyaltara. "MECHANISM OF PHOTOSTIMULATEO LUMINESCENCE IN BaFX:Eu (X˜Cl,Nr) PHOSPHORS" (), p. 3.

[145] K. Takahashi, J. Miyahara, and Y. Shibahara. "Photostimulated Luminescence (PSL) and Color Centers in BaFX : Eu2 + (X = Cl , Br , I) Phosphors". *Journal of The Electrochemical Society* 132.6 (June 1985), p. 1492. ISSN: 1945-7111. DOI: 10.1149/1.2114149.

[146] J. Miyahara, K. Takahashi, Y. Amemiya, N. Kamiya, and Y. Satow. "A new type of X-ray area detector utilizing laser stimulated luminescence". *Nuclear Instruments and Methods in Physics Research Section A: Accelerators, Spectrometers, Detectors and Associated Equipment* 246.1 (May 1986), pp. 572–578. ISSN: 0168-9002. DOI: 10.1016/0168-9002(86)90156-7.

[147] G. Boutoux, N. Rabhi, D. Batani, A. Binet, J.-E. Ducret, K. Jakubowska, J.-P. Nègre, C. Reverdin, and I. Thfoin. "Study of imaging plate detector sensitivity to 5-18 MeV electrons". *Review of Scientific Instruments* 86.11 (Nov. 2015), p. 113304. ISSN: 0034-6748. DOI: 10.1063/1.4936141.

[148] G. J. Williams, B. R. Maddox, H. Chen, S. Kojima, and M. Millecchia. "Calibration and equivalency analysis of image plate scanners". *Review of Scientific Instruments* 85.11 (Nov. 2014), 11E604. ISSN: 0034-6748. DOI: 10.1063/1.4886390.

[149] *Stopping-Power & Range Tables for Electrons, Protons, and Helium Ions*. Last Modified: 2024-10-11T12:05-04:00. Oct. 2009. URL: https://www.nist.gov/pml/stopping-power-range-tables-electrons-protons-and-helium-ions.

[150] T. Bonnet, M. Comet, D. Denis-Petit, F. Gobet, F. Hannachi, M. Tarisien, M. Versteegen, and M. M. Aléonard. "Response functions of imaging plates to photons, electrons and 4He particles". *Review of Scientific Instruments* 84.10 (Oct. 2013), p. 103510. ISSN: 0034-6748. DOI: 10.1063/1.4826084.

[151] I. Ouatu, B. T. Spiers, R. Aboushelbaya, Q. Feng, M. W. von der Leyen, R. W. Paddock, R. Timmis, C. Ticos, K. M. Krushelnick, and P. A. Norreys. "Ionization states for the multipetawatt laser-QED regime". *Physical Review E* 106.1 (July 2022), p. 015205. DOI: 10.1103/PhysRevE.106.015205.

[152] V. Leroux, T. Eichner, and A. R. Maier. "Description of spatio-temporal couplings from heat-induced compressor grating deformation". EN. *Optics Express* 28.6 (Mar. 2020), pp. 8257–8265. ISSN: 1094-4087. DOI: 10.1364/OE.386112.

[153] A. E. Raymond, S. Ravichandran, S.-W. Bahk, A. Longman, L. Roso, R. Fedosejevs, C. Mileham, I. A. Begishev, S. Qin, N. Dauphin, J. Shamlian, W. T. Hill, and H. G. Rinderknecht. "On-shot, high-intensity laser aberration measurements via ponderomotive electron ejection". *Physical Review A* 111.1 (Jan. 2025), p. 013121. DOI: 10.1103/PhysRevA.111.013121.

[154] A. E. Raymond, S. Ravichandran, S.-W. Bahk, A. Longman, L. Roso, R. Fedosejevs, C. Mileham, I. A. Begishev, S. Qin, N. Dauphin, J. Shamlian, W. T. Hill III, and H. G. Rinderknecht. "Laser aberration signatures in expelled electrons from a tenuous gas". *Physics of Plasmas* 32.6 (June 2025), p. 062101. ISSN: 1070-664X. DOI: 10.1063/5.0272444.

[155] I. A. Begishev, V. Bagnoud, S.-W. Bahk, W. A. Bittle, G. Brent, R. Cuffney, C. Dorrer, D. H. Froula, D. Haberberger, C. Mileham, P. M. Nilson, A. V. Okishev, J. L. Shaw, M. J. Shoup, C. R. Stillman, C. Stoeckl, D. Turnbull, B. Wager, J. D. Zuegel, and J. Bromage. "Advanced laser development and plasma-physics studies on the multiterawatt laser". EN. *Applied Optics* 60.36 (Dec. 2021), pp. 11104–11124. ISSN: 2155-3165. DOI: 10.1364/AO.443548.

[156] P. X. Wang, Y. K. Ho, X. Q. Yuan, Q. Kong, N. Cao, A. M. Sessler, E. Esarey, and Y. Nishida. "Vacuum electron acceleration by an intense laser". *Applied Physics Letters* 78.15 (Apr. 2001), pp. 2253–2255. ISSN: 0003-6951, 1077-3118. DOI: 10.1063/1.1359486.

[157] Y. I. Salamin and C. H. Keitel. "Electron Acceleration by a Tightly Focused Laser Beam". *Physical Review Letters* 88.9 (Feb. 2002), p. 095005. ISSN: 0031-9007, 1079-7114. DOI: 10.1103/PhysRevLett.88.095005.

[158] *MPPCs (SiPMs) / MPPC arrays — Hamamatsu Photonics*. URL: https://www.hamamatsu.com/us/en/product/optical-sensors/mppc/mppc_mppc-array.html.

[159] *Stopping Power and Range Tables for Electrons*. URL: https://physics.nist.gov/cgi-bin/Star/e_table.pl.

[160] R. J. Noll. "Zernike polynomials and atmospheric turbulence*". *Journal of the Optical Society of America* 66.3 (Mar. 1976), p. 207. ISSN: 0030-3941. DOI: 10.1364/JOSA.66.000207.

[161] S. Ravichandran, T. Cebriano, J. L. Henares, C. Mendez, J. A. Pérez-Hernández, L. Roso, R. Fedosejevs, and W. T. Hill III. "Ponderomotive expulsion: Toward creating an electron-free volume". *Physics of Plasmas* 32.9 (Sept. 2025), p. 092108. ISSN: 1070-664X. DOI: 10.1063/5.0278383.

[162] *CLPU. Centro de Láseres Pulsados*. URL: https://www.clpu.es/en/.

[163] *NIST: Appendix for ESTAR, PSTAR, and ASTAR*. URL: https://physics.nist.gov/PhysRefData/Star/Text/appendix.html.

[164] V. Samarkin, A. Alexandrov, G. Borsoni, T. Jitsuno, P. Romanov, A. Rukosuev, and A. Kudryashov. "Wide aperture piezoceramic deformable mirrors for aberration correction in high-power lasers". *High Power Laser Science and Engineering* 4 (Jan. 2016), e4. ISSN: 2095-4719, 2052-3289. DOI: 10.1017/hpl.2016.3.

[165] *WidePIX CHROMATIC 25: Large area detector with exceptional dynamic range and an outstanding frame rate*. URL: https://advacam.com/camera/widepix-chromatic-25/.

[166] C. Thaury, F. Quéré, J.-P. Geindre, A. Levy, T. Ceccotti, P. Monot, M. Bougeard, F. Réau, P. d'Oliveira, P. Audebert, R. Marjoribanks, and P. Martin. "Plasma mirrors for ultrahigh-intensity optics". *Nature Physics* 3.6 (June 2007), pp. 424–429. ISSN: 1745-2481. DOI: 10.1038/nphys595.

[167] V. Scutelnic, M. Speicher, A. Fazzini, P. Ghenuche, D. Doria, A. Ailincutei, B. Gonzalez-Izquierdo, T. Asavei, S. Balascuta, J. J. Bekx, P. G. Bleotu, G. Bodini, C. Braganza, A. Brodersen, A. Cavalli, O. Chalus, G. Cojocaru, J. D'mello, I. Dancus, C. Derycke, F. Deurvorst, M. Ehrmanntraut, D. Gengenbach, D. Ghita, L. Giuffrida, M. Gugiu, M. Guenther, O. Juina, K. Kenney, S. Kumar, M. Martinez-Pacheco, I. M. Bacho, S. Norbaev, N. Poetranto, H. Ruhl, E. Schork, M. Stein, S. Steinke, A.-M. Talposi, A. Toma, M. Tosca, A. Ubarhande, L. Vasescu, E. Gaul, D. Rivas, M. Schollmeier, and G. Korn. "Implementation of a spherical double-plasma-mirror telescope for a multi-petawatt laser". *High Power Laser Science and Engineering* 13 (Jan. 2025), e100. ISSN: 2095-4719, 2052-3289. DOI: 10.1017/hpl.2025.10076.

[168] J. P. Boris and R. A. Shanny. *Proceedings of the Conference on the Numerical Simulation of Plasmas (4th) Held at the Naval Research Laboratory, Washington, D.C. on 2, 3 November 1970:* tech. rep. Fort Belvoir, VA: Defense Technical Information Center, July 1971. DOI: 10.21236/ADA023511.

[169] J.-L. Vay. "Simulation of beams or plasmas crossing at relativistic velocity". *Physics of Plasmas* 15.5 (May 2008). ISSN: 1070-664X. DOI: 10.1063/1.2837054.

[170] *odeset - Create or modify options structure for ODE and PDE solvers - MATLAB*. URL: https://www.mathworks.com/help/matlab/ref/odeset.html.

[171] T. A. Laurence, D. A. Alessi, E. Feigenbaum, R. A. Negres, S. R. Qiu, C. W. Siders, T. M. Spinka, and C. J. Stolz. "Mirrors for petawatt lasers: Design principles, limitations, and solutions". *Journal of Applied Physics* 128.7 (Aug. 2020). ISSN: 0021-8979. DOI: 10.1063/1.5131174.